der Bundeswehr
Universität München

A computational framework for balloon angioplasty and stented arteries based on mixed-dimensional modeling

Nora Hagmeyer

Vollständiger Abdruck der von der Fakultät für Bauingenieurwesen und Umweltwissenschaften der Universität der Bundeswehr München zur Erlangung des akademischen Grades eines

Doktor-Ingenieurs (Dr.-Ing.)

angenommenen Dissertation.

Gutachter:
1. Univ.-Prof. Dr.-Ing. Alexander Popp
2. Prof. Stéphane Cotin, Ph.D., HDR
3. Prof. Paolo Zunino, Ph.D.

Die Dissertation wurde am 12. April 2023 bei der Universität der Bundeswehr München eingereicht und durch die Fakultät für Bauingenieurwesen und Umweltwissenschaften am 21. August 2023 angenommen. Die mündliche Prüfung fand am 04. September 2023 statt.

Abstract

Cardiovascular diseases (CVDs), a group of disorders impeding the blood supply to heart, brain, or arms and legs, represent the leading cause of death worldwide. The high number of deaths motivates the desire for minimally invasive procedures and accounts for the success of image-guided catheter-based treatment procedures such as balloon angioplasty and stent insertion. However, the risk of post-surgical complications and follow-up surgeries due to pathological tissue responses such as restenosis is relatively high. This motivates computational methods as a tool to enhance the understanding of the underlying causes and for the computer-aided design of new endovascular devices in order to prevent post-operative complications in the future. Especially because of their complex geometry, high slenderness, and large deformations during insertion, the efficient simulation of stent structures and the interaction with their surroundings still pose a challenge.

Within this thesis, a reduced-dimensional model to represent the stent structure, based on geometrically exact beam theory, is adopted, and the applicability of a mixed-dimensional framework in the context of balloon angioplasty and stented arteries is investigated. In particular, a novel coupling of 1-dimensional (1D) geometrically exact beam equations to a 3-dimensional (3D) background fluid mesh is developed, and arising numerical and algorithmic challenges connected to its multi-physics nature and large dimensionality gap are addressed. The high efficiency gained by the employment of a reduced-dimensional model allows the design of an efficient mixed-dimensional model taking into account the interactions between all components of a stented artery, namely the blood flow, the stent structure, and the vessel wall, making it the first model of its kind.

In the first part of this thesis, the computational framework for the embedding of geometrically exact beam theory in 3-dimensional fluid flow is presented. The consequently arising truly mixed-dimensional 1D-3D coupling scheme constitutes a novel numerical strategy that naturally necessitates consistent discretization methods and specifically tailored algorithmic solution schemes to ensure accurate and efficient computational treatment. Two state-of-the-art interface discretization methods, a Gauss-Point-to-Segment (GPTS) and a mortar-type method, as well as a specially-tailored strongly-coupled Quasi-Newton based partitioned solution algorithm for applications involving fibers with high slenderness ratios, are presented. The influence of all employed algorithmic and numerical parameters on efficiency and results of the solution procedure as well as the limit of the method's modeling assumptions are studied through appropriate examples. Finally, the convergence of the mixed-dimensional problem solution under uniform mesh refinement is demonstrated and the method's capabilities in capturing flow phenomena at large scale are illustrated. Further, an extension of the proposed fluid-beam interaction (FBI) method to a full fluid-

beam-structure interaction (FBSI) framework, allowing the representation of additional effects in regard to the interaction of fluid flow with 3D continuum structures, is presented.

Next, the focus lies on the mixed-dimensional modeling of balloon angioplasty based on state-of-the-art approaches to beam-to-solid-surface (BTSS) interactions and mortar finite element-based contact mechanics. The model is validated by chosen numerical examples and used as the foundation for the proposal of a novel patient-specific balloon-catheter technology for the stenting of curved or asymmetrically stenosed arteries. An optimization procedure for the automated adaptation of the proposed technology to patient-specific geometries is presented, and the benefit of the improved devices is demonstrated through numerical experiments.

Eventually, the core capabilities of the newly developed solution algorithm for mixed-dimensional multi-physics problems and the mixed-dimensional structure model for balloon angioplasty are combined to form a novel fluid-beam-structure interaction framework that takes beam-to-solid-surface mesh tying into account, and the resulting procedure is applied to an idealized model of a stented artery. All in all, the results obtained in this thesis demonstrate the substantial potential of mixed-dimensional modeling not only in the context of balloon angioplasty but as a general-purpose tool for the interaction of slender structures with 3-dimensional continua. Possible extensions and exciting future application scenarios are outlined at the end of this thesis.

Zusammenfassung

Herz-Kreislauf-Erkrankungen stellen eine Gruppe von Erkrankungen dar, die die Blutversorgung des Herzens, des Gehirns oder der Arme und Beine beeinträchtigen, und sind die häufigste Todesursache weltweit. Die hohe Zahl der Todesfälle motiviert das Streben nach minimal-invasiven Verfahren zu ihrer Behandlung und erklärt den Erfolg Katheter-gestützter Behandlungsverfahren wie der Ballonangioplastie und dem Einsetzen von Stents. Bedauerlicherweise ist für diese Behandlungen das Risiko von postoperativen Komplikationen und Folgeoperationen aufgrund von pathologischen Gewebereaktionen wie Restenose noch immer relativ hoch. Der Einsatz von Computersimulationen als Instrument zur Verbesserung des Verständnisses der zugrundeliegenden Ursachen und zur Computer-gestützten Entwicklung neuer endovaskulärer Geräte hat das Potential Abhilfe zu schaffen und postoperative Komplikationen in Zukunft zu vermeiden. Aufgrund der komplexen Geometrie, der hohen Schlankheit und der großen Verformungen während des Einsetzens stellt die effiziente Simulation von Stentstrukturen und ihrer Interaktion mit umgebenden Materialien noch immer eine Herausforderung dar.

In dieser Arbeit wird ein reduziert-dimensionales Modell, basierend auf geometrisch exakter Balkentheorie, zur Repräsentation der Stentstruktur verwendet und die Anwendbarkeit gemischt-dimensionaler Methoden im Kontext von Ballonangioplastie und gestenteter Arterien untersucht. Insbesondere wird eine neuartige Kopplungsmethode für die Einbettung von eindimensionalen (1D) geometrisch exakten Balkengleichungen in eine dreidimensionale (3D) Fluidströmung entwickelt und die sich daraus ergebenden numerischen und algorithmischen Herausforderungen, die mit der Multiphysik und den unterschiedlichen Dimensionalitäten zusammenhängen, werden behandelt. Die hohe Effizienz, die durch die Verwendung eines reduziert-dimensionalen Modells erreicht wird, ermöglicht die Entwicklung eines effizienten gemischt-dimensionalen Modells, das die Wechselwirkungen zwischen allen Komponenten einer gestenteten Arterie, nämlich der Blutströmung, der Stentstruktur und der Gefäßwand, berücksichtigt und somit das erste Modell seiner Art darstellt.

Im ersten Teil dieser Arbeit wird das numerische Modell für die Einbettung geometrisch exakter Balkentheorie in dreidimensionale Fluidströmungen vorgestellt. Das sich hieraus ergebende gemischt-dimensionale 1D-3D-Kopplungsschema stellt eine neuartige numerische Strategie dar, die konsistente Diskretisierungsmethoden und speziell zugeschnittene algorithmische Lösungsschemata erfordert, um eine genaue und effiziente Behandlung zu gewährleisten. Zwei hochmoderne Diskretisierungsmethoden für das Kopplungsgebiet, eine Gauß-Punkt-zu-Segment-Methode (GPTS) und eine Mortar-ähnliche Methode, sowie ein speziell zugeschnittener, stark gekoppelter, auf Quasi-Newton-Methoden

basierender partitionierter Lösungsalgorithmus für Anwendungen, die höchst schlanke Fasern enthalten, werden vorgestellt. Der Einfluss aller verwendeten algorithmischen und numerischen Parameter auf die Effizienz und die Lösungen des Verfahrens sowie die Modellgrenzen der Methode werden anhand geeigneter Beispiele untersucht. Anschließend wird die Konvergenz der Lösung des gemischt-dimensionalen Problems unter uniformer Netzverfeinerung demonstriert und die Anwendbarkeit der numerischen Implementierung auf große Probleme veranschaulicht. Des Weiteren wird eine Erweiterung der vorgeschlagenen Fluid-Balken Interaktionsmethode (FBI) zu einem vollständigen Fluid-Balken-Struktur Interaktionsmodell (FBSI), das die Erfassung zusätzlicher Effekte in Bezug auf die Interaktion von Fluidströmungen mit 3D-Kontinuumsstrukturen ermöglicht, vorgestellt.

Im Weiteren, wird der Schwerpunkt auf die gemischt-dimensionale Modellierung von Ballonangioplastie auf der Grundlage modernster Ansätze zur Balken-Festkörper Interaktion und zur voll aufgelösten Kontaktmechanik gelegt. Das Modell wird anhand ausgewählter numerischer Beispiele validiert und als Grundlage für die Vorstellung einer neuartigen patienten-spezifischen Ballonkathetertechnologie für das Stenting von gekrümmten oder asymmetrisch verengten Arterien verwendet. Ein Optimierungsverfahren für die automatische Anpassung der vorgeschlagenen Technologie an patienten-spezifische Geometrien wird vorgestellt und der Nutzen der verbesserten Geräte wird durch numerische Experimente demonstriert.

Schließlich werden die Kernstücke des neu entwickelten gemischt-dimensionalen Multiphysik-Problems und des gemischt-dimensionalen Strukturmodells für die Ballonangioplastie zu einer neuartigen Fluid-Balken-Struktur Interaktionsmethode unter Berücksichtigung von Balken-Festkörper Interaktion kombiniert und das resultierende Verfahren wird auf ein idealisiertes Modell einer gestenteten Arterie angewendet. Insgesamt zeigen die in dieser Arbeit erzielten Ergebnisse das erhebliche Potenzial des gemischt-dimensionalen Modellierungansatzes, nicht nur im Kontext der Ballonangioplastie, sondern als verallgemeinertes Werkzeug zur Abbildung der Interaktion von schlanken Strukturen mit 3-dimensionalen Kontinua. Weitere mögliche Erweiterungen und interessante zukünftige Anwendungsszenarien werden am Ende dieser Arbeit skizziert.

Contents

List of Figures

List of Tables

Nomenclature

Operators and Symbols

$(\cdot)^T$	Transpose of a matrix
$(\cdot)^{-1}$	Inverse of a matrix
$(\cdot)^{-T}$	Transpose of the inverse of a matrix
$\times$	Cross product
$\circ$	Concatination of functions
$\mathbf{I}$	Identity matrix
$\det$	Determinant
$\boldsymbol{\nabla}$	Gradient operator
$\boldsymbol{\nabla} \cdot (\cdot)$	Divergence operator
$\dot{(\cdot)}$	Derivative with respect to time
$(\cdot)'$	Derivative with respect to space
$\mathbf{S}(\cdot)$	Skew-symmetric tensor for an axial vector
$\langle \cdot, \cdot \rangle_{W^*,W}$	Dual pairing on the dual space W^* to W
$(\cdot, \cdot)_W$	Inner product on the Hilbert space W
$\|\cdot\|_W$	Norm on the Hilbert space W
$(\cdot, \cdot)_\Omega$	L^2-inner product in the domain Ω
$\|\cdot\|_\Omega$	L^2-norm in the domain Ω
$(\cdot)\|_{\partial\Omega}$	Restriction of a function to the boundary $\partial\Omega$
$\langle \cdot \rangle$	Macauley bracket
$\mathcal{B}$	Operation on the beam partition
$\mathcal{F}$	Operation on the fluid partition
$\mathcal{S}$	Operation on the structure partition

Superscripts and Subscripts

$(\cdot)_N$	Quantities related to Neumann boundary conditions
$(\cdot)_D$	Quantities related to Dirichlet boundary conditions
$(\cdot)_{in}$	Quantities related to the fluid's inflow boundary
$(\cdot)_{out}$	Quantities related to the fluid's outflow boundary
$(\cdot)_h$	Spatially discretized quantities
$(\cdot)^{\mathcal{F}}$	Right hand side vectors related to the fluid field
$(\cdot)^f$	Functions and nodal values related to the fluid field
$(\cdot)_f$	Material parameter for the fluid field

$(\cdot)_{\mathcal{F}}$	Matrices related to fluid degrees of freedom
$(\cdot)^{b}$	Functions and nodal values related to the beam equations
$(\cdot)^{\mathcal{B}}$	Right hand side vectors related to the beam equations
$(\cdot)_{\mathcal{B}}$	Matrices related to beam degrees of freedom
$(\cdot)^{s}$	Functions and nodal values related to the structure field
$(\cdot)^{\mathcal{S}}$	Right hand side vectors related to the structure field
$(\cdot)^{0}$	Quantities related to the initial or reference configuration
$(\cdot)_{s}$	Material parameter for the structure field
$(\cdot)_{\mathcal{S}}$	Matrices related to structural degrees of freedom
$(\cdot)^{1}$	Quantities related to body 1
$(\cdot)^{2}$	Quantities related to body 2
$(\cdot)^{c}$	Quantities related to contact mechanics
$(\cdot)_{c}$	Numerical parameter for contact mechanics
$(\cdot)^{lm}$	Quantities related to Lagrange multiplier
$(\cdot)^{\Lambda}$	Right hand side vectors related to the mortar method
$(\cdot)^{ale}$	Quantities related to the Arbitrary-Lagrangian Eulerian approach
$(\cdot)_{\mathcal{A}}$	Matrices related to mesh motion
$(\cdot)^{fsi}$	Functions and vectors related to fluid-structure interaction
$(\cdot)^{fbi}$	Functions and vectors related to fluid-beam interaction
$(\cdot)_{btss}$	Quantities related to beam-to-solid-surface coupling

Domains and Boundaries

Ω_s	Structure configuration
Ω_s^0	Structural reference configuration
Γ_N^s	Neumann boundary on the structure configuration
Γ_D^s	Dirichlet boundary on the structure configuration
Ω_b	Image of the beam's centerline
Ω_f	Fluid configuration
Γ_N^f	Neumann boundary on the fluid configuration
Γ_D^f	Dirichlet boundary on the fluid configuration
Γ_c	Contact boundary
Γ_{fsi}	Fluid-structure interaction interface
Γ_{btss}	Beam-to-solid-surface coupling interface
Γ_{in}	Inflow boundary on the fluid configuration
Γ_{out}	Outflow boundary on the structure configuration
Γ_{opt}	Integration boundary for the goal function

Function Spaces & Groups

$\mathcal{W}_{\mathcal{S}}$	Function space of admissible time-dependent structure displacements
$SO\,(3)$	Special orthogonal group
$\mathcal{V}_{\mathcal{B}}$	Function space for the beam state
$\mathcal{V}_r^1$, $\mathcal{V}_r^2$	Function space for the beam centerline
$\mathcal{V}_\theta$	Function space for the beam cross-section rotations
$\mathcal{W}_{\mathcal{B}}$	Function space of admissible time-dependent beam states
$\mathcal{V}_p$	Function space of normalized fluid pressure solutions
$\mathcal{W}_{\mathcal{F}}^p$	Function space of admissible time-dependent fluid pressure solutions
$\mathcal{W}_{\mathcal{F}}^v$	Function space of admissible time-dependent fluid velocity solutions
$\mathcal{M}$	Function space for the Lagrange multiplier in contact mechanics
$\mathcal{W}_{\mathcal{F}}^u$	Function space of admissible time-dependent fluid mesh motion displacement solutions

Kinematics

$\mathbf{v}^f$	Fluid velocity
p^f	Fluid pressure
$\boldsymbol{\mathcal{E}}\,(\cdot)$	Fluid strain rate tensor
$\mathbf{r}$	Beam centerline
$\boldsymbol{\eta}^b$	Beam state
$\mathbf{v}^b$	Beam velocity
s	Parametrization of the beam centerline
$\mathbf{u}^s$	Structure displacement
$\mathbf{v}^s$	Structure velocity
$\mathbf{X}_s$	Point in the reference configuration
$\mathbf{x}_s$	Point in the current configuration
$\mathbf{S}$	Second Piola-Kirchhoff stress tensor
$\mathbf{P}$	First Piola-Kirchhoff stress tensor
$\mathbf{F}$	Deformation gradient
$\mathbf{C}$	Right Cauchy Green tensor
$\bar{\mathbf{C}}$	Modified right Cauchy Green tensor
ψ, ξ	Parametrization of a surface in reference configuration
$\boldsymbol{u}^f$	Fluid mesh motion displacement
$\boldsymbol{v}^{\text{ale}}$	Mesh motion velocity
$\boldsymbol{h}^f$	Traction on the fluid interface
$\boldsymbol{h}^s$	Traction on the structure interface
g_n	Gap function
p_c	Contact pressure

Constraints enforcement

ϵ	Penalty parameter
$\mathbf{n}$	Normal vector
$\boldsymbol{\lambda}^{\text{c}}$	Contact mechanics Lagrange multiplier
χ	Projection operator

$\boldsymbol{\mathcal{A}}$	Arbitrary-Lagrangian Eulerian mapping
$\boldsymbol{\lambda}^{fsi}$	Fluid-structure interaction Lagrange multiplier
Π	Projection operator
$\boldsymbol{\lambda}^{\text{fbi}}$	Fluid-beam interaction Lagrange multiplier

Constitutive Parameter

ρ	Density
ν	Poisson's ratio or dynamic fluid viscosity

Indices

i, j	Index for degrees of freedom
k	Index for FSI iterations or degrees of freedom
l	Length of a beam in the initial configuration
m	Index for Quasi-Netwon iterations
n	Number of degrees of freedom or index for time steps

The Finite Element Method

N	Finite element shape functions
H	Hermite centerline shape functions
Φ	Lagrange multiplier shape functions
$\mathbf{u}_h^s$	Finite element approximation of the structure displacement
$\hat{\mathbf{u}}_h^s$	Vector of structure displacement nodal values
$\hat{\mathbf{u}}_h^{s,i}$	Nodal structure displacement values
$\mathbf{v}_h^s$	Finite element approximation of the structure velocity
$\hat{\mathbf{v}}_h^s$	Vector of structure velocity nodal values
$\mathbf{f}_h^{\mathcal{S}}$	Right-hand side vector for the structure field
$\mathbf{r}_h$	Finite element approximation of the beam centerline
$\hat{\mathbf{r}}_h$	Vector of beam centerline nodal values
$\hat{\mathbf{d}}_h^j$	Nodal positional beam centerline values
$\hat{\mathbf{t}}_h^j$	Nodal tangential beam centerline values
$\boldsymbol{\eta}_h^b$	Finite element approximation of the beam state
$\hat{\boldsymbol{\eta}}_h^b$	Vector of beam state nodal values
$\mathbf{v}_h^b$	Finite element approximation of the beam velocity
$\hat{\mathbf{v}}_h^b$	Vector of beam velocity nodal values
$\hat{\mathbf{v}}_h^{b,i}$	Nodal beam velocity values
$\mathbf{f}_h^{\mathcal{B}}$	Right-hand side vector for the beam equations
$\mathbf{v}_h^f$	Finite element approximation of the fluid velocity
$\hat{\mathbf{v}}_h^f$	Vector of fluid velocity nodal values
$\hat{\mathbf{v}}_h^{f,i}$	Nodal fluid velocity values
p_h^f	Finite element approximation of the fluid pressure
$\hat{\mathbf{p}}_h^f$	Vector of fluid pressure nodal values

$\hat{p}_h^{f,i}$	Nodal fluid pressure values
$\mathbf{f}_h^{\mathcal{F}}$	Right-hand side vector for the fluid field
$\boldsymbol{\lambda}^{\mathrm{c}}$	Contact Lagrange multiplier
$\boldsymbol{\lambda}_h^{\mathrm{c}}$	Finite element approximation of the contact Lagrange multiplier
$\hat{\boldsymbol{\lambda}}_h^{\mathrm{c}}$	Vector of contact Lagrange multiplier nodal values
$\hat{\boldsymbol{\lambda}}_h^{\mathrm{c},k}$	Nodal contact Lagrange multiplier values
$\hat{\boldsymbol{u}}_h^{f}$	Vector of fluid mesh motion displamcent nodal values
$\hat{\boldsymbol{v}}^{\mathrm{ale}}$	Vector of fluid mesh motion velocity nodal values
$\boldsymbol{\lambda}^{fsi}$	Vector of fluid-structure interaction Lagrange multiplier nodal values
$\hat{\boldsymbol{\lambda}}^{fsi}$	Vector of fluid-structure interaction Lagrange multiplier nodal values
$\mathbf{f}_h^{s,fsi}$	Vector of fluid-structure interaction force values on structural nodes
$\mathbf{f}_h^{f,fsi}$	Vector of fluid-structure interaction force values on fluid nodes
τ	Parameter relating displacements and velocities
$\boldsymbol{\lambda}^{\mathrm{fbi}}$	Fluid-beam interaction Lagrange multiplier
$\boldsymbol{\lambda}_h^{\mathrm{fbi}}$	Finite element approximation of the fluid-beam interaction Lagrange multiplier
$\hat{\boldsymbol{\lambda}}_h^{\mathrm{fbi}}$	Vector of fluid-beam interaction Lagrange multiplier nodal values
$\hat{\boldsymbol{\lambda}}_h^{\mathrm{fbi},k}$	Nodal fluid-beam interaction Lagrange multiplier values
$\mathbf{f}_h^{\mathcal{F},fbi}$	Fluid-beam interaction force acting on the fluid
$\mathbf{f}_h^{\mathcal{B},fbi}$	Fluid-beam interaction force acting on the beam
$\mathbf{f}_h^{fbsi}$	Vector of fluid-beam-structure interaction force values on fluid nodes

Linear Forms

$\mathbf{a}(\cdot;\cdot)$	Semi-linear form
$b(\cdot)$	Linear form
$\mathbf{c}(\cdot,\cdot)$	Bi-linear form

Matrices and Vectors

$\mathbf{A}$	Nonlinear or linear operator
$\mathbf{D}$, $\mathbf{M}$	Matrix arising from the mortar finite element method
$\mathbf{x}^{fbsi}$	Vector containing all FBSI related states
$\mathbf{f}$	Right hand side vector

Partitioned fluid-structure interaction algorithm

$\mathbf{r}^{fbi}$	Fluid-beam interaction residual
$\mathbf{f}_h^{fbi}$	Fluid-beam interaction force
$\tilde{\mathbf{J}}_{fbi}^k$	Jacobian
γ	Step size parameter for finite differences approximations
δy	Step size for finite differences approximations

Abbreviations

0D	0-dimensional
1D	1-dimensional
2D	2-dimensional
3D	3-dimensional
a.e.	almost everywhere
AMG	Algebraic multigrid
BFGS	Broyden-Fletcher-Goldfarb-Shanno
BTSS	Beam-to-solid-surface
CT	Computed tomography
CVD	Cardiovascular disease
DES	Drug-eluding Stent
DoF	Degree of freedom
FBI	Fluid-beam interaction
FBSI	Fluid-beam-structure interaction
FD	Finite differences
FE	Finite element
FEM	Finite element method
FSI	Fluid-structure interaction
GPTS	Gauss-point-to-Segment
HPC	High performance computing
IBM	Immersed boundary method
L-BFGS	limited-memory Broyden-Fletcher-Goldfarb-Shanno
LAD	Left anterior descending artery
LBB	Ladyzhenskaya-Babuška-Brezzi
LCx	left curcumflex artery
LMS	Left main stem
MFNK	Matrix-free Newton Krylov
MMPDE	Mesh motion partial differential equation
MULF	Modified updated Lagrangian formulation
NURBS	Non-uniform rational B-splines
PDE	Partial differential equation
PSPG	pressure-stabilizing Petrov-Galerkin
SR	Simo-Reissner
STS	Segment-to-Segment
SUPG	streamline-upwind Petrov-Galerkin
TF	Torsion-free
WHO	World Health Organization
WSS	Wall shear stress

1. Introduction

1.1. Motivation

"An estimated 17.9 million people died from [cardiovascular diseases] in 2019, representing 32% of all global deaths" according to the World Health Organization (WHO) [3]. This makes cardiovascular diseases (CVDs) the leading cause of death worldwide, cf. Figure 1.1a, and the number is increasing from year to year as shown in Figure 1.1b. CVDs are a group of disorders involving the heart and/or blood vessels. Examples include cerebrovascular, coronary heart, and peripheral arterial diseases, which impede the blood supply to brain, heart, and arms and legs, respectively. The high number of deaths motivates the desire for minimally invasive procedures that reduce the risk of peri-operative complications during arterial and coronary repairs. This accounts for the success of image-guided catheter-based minimally invasive treatment procedures, or interventional radiology, as these interventional surgeries may represent a low-risk treatment option and an alternative to established open vascular surgical procedures [96].

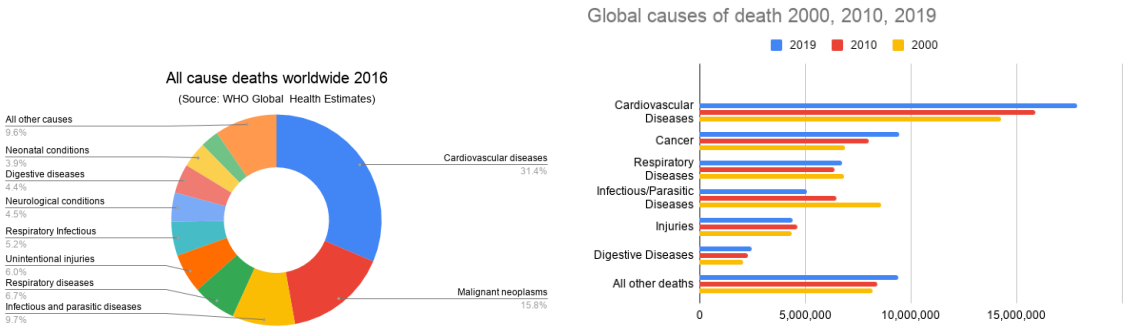

(a) Leading causes of death worldwide 2016. Taken from [3].

(b) Trend in global cause of death. Taken from [2].

Figure 1.1.: Data on cardiovascular diseases provided by the World Health organization

One such intervention, which is used to treat coronary artery disease and atherosclerosis, is balloon angioplasty. During balloon angioplasty, a catheter with a small balloon is guided through the artery to the blockage and is inflated in order to widen narrowed or blocked arteries. Often a wire-like structure, a bare-metal stent or, more recently, a drug eluding stent (DES), is placed inside the artery to keep the vessel open after the balloon is removed. The process is shown in Figure 1.2 for a DES. Even though the minimally invasive nature of this procedure generally reduces the risk of peri-operative complications compared to traditional bypass procedures, the risk of post-surgical complications and required follow-

up surgeries due to:

- damage to the arterial wall,
- stent migration, where the stent becomes loose and starts moving through the artery,
- restenosis and renarrowing, where the artery grows shut again,
- and artery rupture,

is still relatively high.

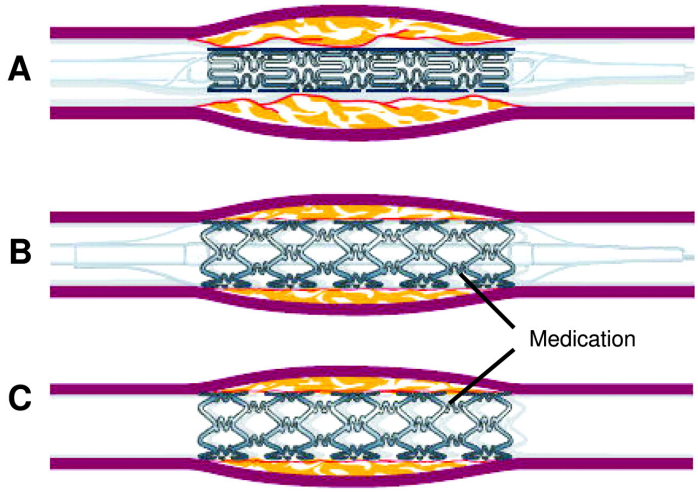

Figure 1.2.: The process of balloon angioplasty. Insertion of the stent (top), expansion of balloon and stent (middle), deflation of the balloon (bottom). Taken from [127].

In a study of $1,058$ patients the rate of failure for a standard bare-metal stent was found to be 21.0 %, and 8.6 % for a DES [140]. Adverse wall shear stress (WSS) and arterial injury during stenting have been found to be contributing factors. However, the reasons for these complications and pathological tissue responses are not fully understood yet.

Avoiding these unfavorable outcomes still represents a challenge, thus, motivating computational methods as a tool to enhance the understanding of the underlying causes and for the computer-based training of surgeons to prevent post-operative complications in the future [38, 40]. Furthermore, simulating the interaction of the stent with the arterial system may benefit the process of image-based surgery planning by reducing the necessity of taking undesirably frequent images for catheter guidance [121]. In addition, a great variety of stent and balloon catheter products is currently available on the market. Seeing that in many instances stent design may have a larger influence on thrombosis and restenosis than the stent deployment procedure itself, cf. [162], numerical experiments to choose the one best suited for a specific patient or situation may prove advantageous in terms of long-term outcomes of interventions. Last but not least, computer-aided design of new endovascular devices based on the understanding of post-operative complications may provide a useful tool in the future.

1.2. Numerical modeling of balloon angioplasty and stented arteries

The idea of using numerical experiments based on the finite element method (FEM) as a tool to aid in the design phase of engineering products in general, and the design of endovascular devices specifically, is not new. For instance, in [13], numerical investigation is used to propose new stent designs that reduce adverse WSS with the goal to reduce WSS-related in-stent restenosis. Further works, such as [94, 147], study the influence of stent design on hemodynamic features associated with restenosis with the goal of finding the best stent design characteristics to improve long-term outcomes of balloon angioplasty. Another mechanism generally associated with restenosis is stenting-induced arterial wall injury. [115] stipulates that the reduction of stent-induced arterial wall injury needs to play an essential part in the design of new endovascular devices. This topic is picked up by works such as [80], where a strong effect of stent design on stenting-induced damage is demonstrated. Based on that, works such as [139] adopt numerical simulation as a tool to propose novel stent designs that lead to reduced peak stresses, thus, demonstrating the potential of computer-aided design for endovascular devices. However, not only the design of stents but also their material has an influence on its mechanical behavior. Materials and coatings generally influence the expansion and recoil behavior as well as the build-up of micro stresses that may further affect the longevity of stents [170, 168]. Furthermore, the stent is not the only component influencing the outcome of balloon angioplasty. The outcome of interventions is also affected by the specific patient's vessel geometry and the composition of plaque and stenosed regions [170, 169].

However, complete modeling of the effects of balloon angioplasty leads to very complex systems incorporating not only fluid-structure interaction (FSI) of the medical device with the hemodynamics but a multitude of additional interactions. These interactions include contact between the stent structures and the arterial wall and the interaction between the vessel walls and the pulsatile blood flow. The high complexity of the mechanics governing balloon angioplasty generally necessitates the incorporation of simplifications for the numerical simulations to yield results in adequate time. Frequently applied modeling simplifications include the assumption of symmetry and symmetric expansion behavior of the stent [49, 206, 147, 33], the use of generic pipe geometries instead of patient-specific ones to assess new stent designs [80, 206, 59, 147], the analysis of the stent's free expansion behavior without any interactions with the vessel wall [103], the neglect of blood flow [103, 139, 49, 80, 206] or pre-stressing [139], as well as the assumption of rigid vessels [59, 147] and the simplification of the considered constitutive laws [49, 206, 33]. While these simplifications lead to valid approaches for many research questions, there are other phenomena that one may only capture via modeling the interplay of a multitude, or even all, of the interactions and complexities characterizing balloon angioplasty.

One highly complex component of balloon angioplasty models is the stent structure itself. Because of their intricate geometries, high slenderness, and the large deformations during insertion, the stent meshes generally require a large number of 3-dimensional (3D) finite elements (FEs). To address this issue, in [183], Tambača et al. propose a general 1-dimensional vascular stent model, which is utilized in [184] to efficiently simulate the

behavior of coronary stents under physiologically reasonable conditions. As an extension of that, the behavior of this 1-dimensional (1D) stent model is compared to the results of a fully resolved 3-dimensional simulation in [215]. A difference of less than 6% in the displacement magnitude at a complexity reduction, in terms of degrees of freedom (DoFs), of more than 400 is observed. These results motivate the use of a reduced-dimensional model, which exhibits desirable properties addressing the aforementioned challenges of 3D modeling, for the stent structure. In particular, within this thesis, the stent is modeled as a 1D Cosserat structure, governed by geometrically exact beam theory, embedded in 3D space.

In the case of balloon angioplasty, not only the behavior of the stent but especially its interaction with the arterial wall, be it chemical in the case of DESs, or mechanical in nature, is of interest. In general, this necessitates mixed-dimensional models to capture the interaction between the 1D beam equations with classical 3D continuum-based models describing the blood flow and the mechanics of the vessel wall. The upcoming section gives an overview of recent developments in reduced-dimensional models and their interaction with continuum fields.

1.3. Reduced- & mixed-dimensional modeling

The application of dimensionally-reduced models to adequately describe complex behaviors of slender bodies has a long-standing history. The formulations in this paper greatly build on the extension of such models to the nonlinear regime of finite deformations in three dimensions. Important to mention in this context is the extension to a finite strain problem in 3D by Simo in [175] based on the work by Reissner in [158]. The formulations proposed in these works fall in the group of geometrically exact beam theories and constitute the basis of computationally efficient and rather well-posed problems for systems of slender bodies. The actual beam implementations used in the remainder of this thesis are described in detail in [134, 135, 133].

These reduced-dimensional formulations can be used to model highly complex systems of slender structures. To further capture their interaction with their surroundings, mixed-dimensional modeling approaches are required. Such mixed-dimensional models are not restricted to endovascular devices but naturally arise in a multitude of applications that include structures with high slenderness ratios. Applications of mixed-dimensional models in the literature include the coupling of water reservoirs with wells [30], the modeling of blood vessels within tumors [110], and reaction-diffusion as well as action potential models [37, 167, 20]. Nevertheless, the most prominent examples are the coupling of beam theory with solid and fluid continua.

The interaction of rod-like structures with fluid flow plays an important role in a broad spectrum of applications varying from biomechanical to industrial processes. Applications in which immersed fibers have a significant impact on the fluid flow include the modeling of optimal flow control. In [114], an experimental analysis of different coatings of hairy flaps to control vertex shedding behind an immersed cylinder is reported, and in [55], a homogenized model is used to model the hairy coating. A similarly global effect on the

(a) The schematics of a submerged canopy. Taken from [15].

(b) The geometry of a stent-graft. Taken from [78].

Figure 1.3.: Examples of slender structures interacting with 3D continua

flow can be observed in the case of terrestrial canopies and submerged vegetation. Even though one immersed fiber does not affect the fluid flow considerably, the movement and interaction of a large patch of fibers has a significant impact on the vorticity of the overall flow [192, 193, 145, 54]. In this context, the application of mixed-dimensional models, such as [198, 193], leads to a more accurate solution than homogenized methods, cf. [29, 44, 204], while simultaneously leading to computationally more efficient methods than fully resolved ones [145, 54].

In contrast, the interaction of rod-like structures with structural continuum equations has, first and foremost, been studied in the context of fiber-reinforced materials. In [150, 32, 48, 155, 67, 97] string-like models have been placed into solid continua with limited incorporation of modes of deformation such as bending and torsion. Such methods have been extended to couplings of full beam theories with structural continua more recently, e.g., in [177, 43, 179, 98]. However, little research exists on the interaction of beams with 2-dimensional (2D) surfaces of structural bodies. While node collision methods can generally be used to model the interaction of slender structures with surfaces [16], methods specifically tailored to the mixed-dimensional interaction of 2D surfaces with 1D beams are still rare [109, 176].

The solution to all these mixed-dimensional interaction problems leads to new challenges compared to equal-dimensional formulations. General assurance of well-posedness of mixed-dimensional problems as well as recovering theoretical optimal convergence are still elusive topics of interest [19, 84, 113, 118, 27, 167, 138]. From a numerical perspective, some of the most prominent research questions include the challenge of how to couple 3D variables with 1D stress resultants and how to transfer values between unavoidably geometrically non-matching meshes. In the realm of FSI, [91] represents one of the first contributions on mixed-dimensional coupling methods for 1D equations with 3D fluid flow. The coupling is based on an immersed boundary-type (IBM) method. The beam is coupled with the Navier-Stokes equations on the reconstructed beam's surface, making it

a surface-to-volume coupling scheme as categorized in [177]. Within surface-to-volume coupling approaches, the slender body is modeled using 1D equations, the fluid domain consists of the entire simulation domain, and the fluid-beam interaction (FBI) quantities are coupled on the beam's reconstructed surface. This makes it necessary to reconstruct the beam's surfaces to be coupled with the fluid equations, and in turn, to exchange relevant data between the beam's· surface and its centerline. As a result, the fluid domain has to be massively refined in order to resolve the surface mesh tying, and also the coupling procedure itself rapidly grows more complex in terms of computational efficiency. This reduces the computational advantages of employing a reduced-dimensional beam model. The work of Tschisgale et al. [192] represents an intermediate step since the beam's surface does not have to be reconstructed. Instead, classical regularized delta functions, which depend on the beam's radius, are used to add FBI forces to the overall problem. This method, nevertheless, also necessitates the use of finely resolved background meshes in order for the delta functions to have a width of multiple fluid elements. A truly mixed-dimensional FBI method, that directly couples the two fields on the 1D beam centerline and, therefore, allows for relatively coarse background meshes, was discussed only in [205]. Here, the coupling was applied to the simulation of a transcatheter heart valve. The computational results of the biomechanical problem look promising, however, no numerical study of the necessary assumptions for the validity of the method nor its limitations are presented.

1.4. Research objectives

The aim of this thesis is to provide an efficient computational framework for the investigation of long-term outcomes of balloon angioplasty and stent insertion based on mixed-dimensional finite element modeling. To target this goal, two work packages can be identified:

- the development of a novel fluid-beam interaction (FBI) approach that can be used to capture the interaction of stents with blood flow, and that can be applied to applications beyond that,
- and the design of an efficient, accurate computational model for the simulation of balloon angioplasty based on mixed-dimensional interactions.

As outlined in Section 1.3, the application of reduced-dimensional models and their coupling to fluid flow has been studied for many years. However, a truly mixed-dimensional 1D-3D coupling approach under an explicit statement of its model assumptions and analysis of its limitations is still missing. While the true 1D-3D coupling raises a multitude of questions and challenges, this type of coupling is essential for the resulting method of maintaining the efficiency benefits of employing a reduced-dimensional structure model. For a truly efficient mixed-dimensional framework, the fluid mesh is required to be independent of the beam geometry in the sense that the finite element size should not be required to be smaller than the beam's diameter. Such a dependence leads to a disproportionate complexity for the envisioned application regime, where applications may contain large numbers of very slender interacting fibers. Further, to be able to model complex geometries such as stents, the method should not have any requirements when it comes to

the position of the fibers relative to the background mesh.

Moreover, it is not uncommon for slender fibers in general, and stents during balloon angioplasty in particular, to display large displacements. The FBI approach is, thus, required to be robust with respect to large displacements of the immersed fibers and their interaction. Especially in the case of balloon angioplasty with stent insertion, the interaction of the stent with blood flow is not the only phenomenon worth capturing. Rather, the FBI approach has to be sufficiently flexible to be extended to include additional complex interaction effects. Such effects include the contact of the stent with the arterial wall, interactions between individual stent struts, and interaction of the arterial wall with the flow. The method, thus, has to be able to also handle unstructured as well as moving meshes.

Furthermore, as the goal of this thesis is the development of a FBI framework specifically tailored to the interaction of very slender bodies with 3D fluid flow, the application regime and underlying assumptions have to be clearly stated and the accuracy and limitations of the approach have to be well analyzed.

Last but not least, a unified framework of specifically tailored mixed-dimensional models as an efficient simulation tool that is able to capture the various mechanical interactions that occur during balloon angioplasty is still missing. To aid in the design of new endovascular devices and to find solutions on a patient-specific basis, high accuracy, efficiency, and simplicity of the model setup are crucial requirements for a useful computational framework.

1.5. Scientific novelties

This thesis describes a novel mixed-dimensional interaction framework that addresses all aforementioned requirements which, to the best of the author's knowledge, makes it the first of its kind. The novel highly accurate mixed-dimensional methods are applied in the context of balloon angioplasty. A model based on geometrically exact beam theory is proposed to significantly reduce the number of required DoFs without an unacceptable loss of accuracy. Mixed-dimensional methods are used to model the interaction of the stent with fluid flow, cf. [75] and Chapter 7, and for the interaction of the stent with the balloon and vessel wall, cf. [176] and Chapter 5. The contact interactions between the balloon and the vessel wall are modeled using state-of-the-art mortar finite element methods. To showcase the robustness of the novel mixed-dimensional and general interaction methods with respect to physically meaningful parameters and situations, highly accurate constitutive artery models, pre-stressing and as pre-stretching is included in the considered simulations of balloon angioplasty-related simulations. The capability of the applied methods in the context of biomedical applications is illustrated by their ability to answer common research questions as well as their validation with respect to real-life observations and fully resolved numerical examples. To the author's knowledge, this constitutes the first application of a truly mixed-dimensional model to the simulation of balloon angioplasty. Finally, based on the developed angioplasty model, a novel balloon-catheter technology for the use in patient-specific, curved, and asymmetric vessels is proposed and its usefulness is demonstrated by numerical examples.

To summarize, this work constitutes:

- the first successful application of a mortar-type discretization approach to couple 1D fibers embedded into a fluid continuum,
- the first implementation of a mixed-dimensional coupling scheme on a moving fluid mesh,
- the first analysis of the modeling assumptions and limitations of a true 1D-3D coupling approach in the context of fluid-structure interaction,
- the first application of a mixed-dimensional model to the simulation of balloon angioplasty,
- and the first time a balloon-catheter model based on an anisotropic material is proposed to address asymmetric arterial geometry features.

1.6. Outline

The remainder of this thesis is structured as follows: In Chapter 2 the relevant governing equations for a mixed-dimensional model of balloon angioplasty, namely for nonlinear solid mechanics, geometrically exact beam theory, and fluid mechanics, are recounted. In addition, the main mathematical concepts of weak solutions, the finite element method (FEM), constraint enforcement techniques and their spatial discretization, and optimal control problems are briefly reviewed. Afterward, state-of-the-art numerical formulations and important algorithmic details for contact mechanics and FSI are summarized.

The subsequent developments of a mixed-dimensional model for balloon angioplasty and stented arteries are structured into three distinct parts. In Part I, a computational FBI framework is developed. In Chapter 3, a mixed-dimensional approach to couple geometrically exact beam theory with fluid flow on a fixed background mesh is introduced. The weak forms for two different constraint enforcement techniques are presented and the nonlinear systems of equations arising from application of the FEM are stated. Subsequently, a novel partitioned algorithm strategy specifically tailored to the FBI methodology is proposed. In the end, numerical examples validate the proposed approach and illustrate its envisioned application regime as well as its limitations. In Chapter 4, the introduced FBI approach is extended to fluid flow on moving meshes. In particular, an algorithm is outlined which allows capturing the FBI on a fluid mesh which is updated by a moving mesh partial differential equation (MMPDE) based on the fluid's interaction with a 3D structure. The algorithm, therefore, allows to capture FBI related phenomena and classical FSI within the same simulation. The approach is validated by a numerical example.

Part II focuses on a mixed-dimensional structural model to simulate the process of balloon angioplasty and stent insertion. Chapter 5 introduces the mixed-dimensional model problem including the employed numerical method to represent the stent's interaction with balloon and artery. The model is validated by demonstrating the its ability to capture well-known phenomena from literature and medical practice. In Chapter 6, the developed model is applied to the computer-aided design of endovascular devices. Specifically, a

novel patient-specific technology for balloon angioplasty in curved blood vessels is proposed. As a proof of concept, optimal control concepts are applied to optimize the novel balloon design for the treatment of generic curved vessels and vessels with asymmetric cross-sections. In the end, a numerical experiment, which compares the optimized device's behavior to that of classical balloons, is conducted.

Finally, in Part III the results from Parts I and II are consolidated and a model to analyze the influence of stent placement on blood flow including FBI, FSI as well as interactions of the stent with the vessel wall, is presented. The model is validated by demonstrating its ability to capture effects known from the literature and medical practice.

To conclude the thesis, the novelties and achievements therein are summarized and an outlook on ongoing and future research is given.

2. Governing equations & numerical methods

The simulation of balloon angioplasty and stent insertion necessitates the accurate modeling of a multitude of individual components as well as their interactions. Within this chapter, first, some of the most important definitions and theorems that build the basis of the FEM for the solution of Partial Differential Equations (PDEs) are reviewed. In order to provide a basis for the treatment of interface and optimization problems, the fundamentals of constraint enforcement optimal control techniques are supplied before reviewing the single field equations used within the remainder of this thesis. The formulations include the applied nonlinear solid continuum model, the incompressible Navier-Stokes equations, and the used variants of geometrically exact beam theory. Then, the computational contact and FSI frameworks used in subsequent chapters are stated. This chapter is not intended to give an elaborate review of the finite element methods and continuum mechanics. Instead, throughout this chapter, the interested reader is referred to more extensive literature on the discussed topics.

2.1. Mathematical concepts for weak solutions & the finite element method

Within this section, some of the mathematical basics of the finite element method are recounted. In particular, the definition of the most important function spaces used within the remainder of this work as well as important theorems ensuring well-posedness for classical applications, are recapitulated. The following definitions and theorems are based on the introductions in [82].

The finite element method is based on the so-called weak form of the balance equations. In general, existence of a solution that fulfills the equations in a strong, or point-wise, sense cannot be guaranteed. However, depending on the problem and its geometry, the existence of a solution that fulfills the equations in a weak, or integral, manner can be proven. For the weak form, the requirements on the regularity of the solutions can be loosened. In order to define the weak forms of the continuum equations, and the form of their solutions, within this work, some useful function spaces are defined here. Furthermore, some important properties that will be used within subsequent chapters are recapitulated.

Definition 2.1 (Lebesgue Spaces) *For $0 \leq p < \infty$, let the spaces of equivalence classes for Lebesgue measurable functions be*

$$L^p(\Omega) := \left\{ w : \Omega \to \mathbb{R} \text{ Lebesgue measurable} : \left(\int_\Omega |w|^p \, d\Omega \right)^{\frac{1}{p}} < \infty \right\} \Big/ \sim, \tag{2.1}$$

with the equivalence relation

$$w \sim v \Leftrightarrow \left(\int_\Omega |w - v|^p \, d\Omega \right)^{\frac{1}{p}} = 0 \Leftrightarrow w = v \quad \text{almost everywhere (a.e).} \tag{2.2}$$

Here, almost everywhere is defined as everywhere in the integration domain up to a domain of measure zero. Then, the function spaces can be equipped with the norm

$$\|\cdot\|_{L^p(\Omega)} := \left(\int_\Omega |\cdot|^p \, d\Omega \right)^{\frac{1}{p}}. \tag{2.3}$$

Additionally, the space $L^2(\Omega)$ can be equipped with the inner product

$$(w, v)_{L^2(\Omega)} := \int_\Omega w \cdot v \, d\Omega. \tag{2.4}$$

The function space $L^2(\Omega)$ is required in the following to ensure that all equations developed in the remainder of this thesis are well-defined.

In addition to the function w, PDEs generally contain the function's partial derivatives. In order to allow for a lower regularity of the weak solution, as compared to the classical strong form, the concept of weak derivatives is introduced.

Definition 2.2 *For $k \in \mathbb{N}_0$, let the function space of "nice" infinitely often differentiable functions with compact support in Ω be denoted by*

$$C_c^\infty(\Omega) := \left\{ w \in C^\infty\left(\bar{\Omega}\right) : \text{ supp}(w) \subset \Omega \text{ is compact} \right\}. \tag{2.5}$$

Definition 2.3 (Weak Derivatives) *Let Ω be an open domain and, for all $K \subset \Omega$ compact, let $u \in L^1(K)$ be a function. If there exists a function $w \in L^1(K)$, for all $K \subset \Omega$ compact, such that*

$$\int_\Omega (v \cdot \psi) \, d\Omega = (-1)^{|\alpha|} \int_\Omega \left(w \cdot \frac{\partial^{|\alpha|} \psi}{\partial^{\alpha_1} x_1 \, ... \, \partial^{\alpha_n} x_n} \right) d\Omega \quad \forall \quad \psi \in C_c^\infty(\Omega), \tag{2.6}$$

then v is called the $|\alpha|$-th weak derivative of w and denoted as $D^\alpha w := v$ within this chapter.

The concept of a weak derivative can then be used to define the Sobolev spaces:

Definition 2.4 (Sobolev Spaces) *Under the same requirements as above, the Sobolev space $W^{k,p}(\Omega)$ can be defined as:*

$$W^{k,p}(\Omega) := \{w \in L^p(\Omega) : D^\alpha w \in L^p(\Omega) \quad \forall \quad |\alpha| \leq k\}, \tag{2.7}$$

and its inner product takes the form

$$(w, v)_{H^k(\Omega)} := \sum_{|\alpha| \leq k} (D^\alpha w, D^\alpha v)_{L^2(\Omega)}. \tag{2.8}$$

Further, the following notation will be used in the remainder of this thesis: $H^k(\Omega) := W^{k,2}(\Omega)$.

The Sobolev spaces will be used to ensure well-posedness of the subsequent weak solutions. A drawback of Lebesgue and Sobolev spaces is the fact that functions are only defined up to a subset of measure zero. This poses a problem when it comes to boundary conditions, i.e., if a certain displacement or velocity fields needs to be prescribed on a boundary. Since boundaries represent a subset of measure zero, boundary conditions are a priori not well-defined. The upcoming definition and theorem represent a mathematical technique to still enable the imposition of boundary conditions under specific prerequisites.

Definition 2.5 *For $k \in \mathbb{N}_0$, let the closure of $C_c^\infty(\Omega)$ in $H^k(\Omega)$ be denoted as $H_0^k(\Omega)$.*

The space $H_0^k(\Omega)$ can be interpreted as the space of all functions in $H^k(\Omega)$ that are zero themselves, and that posses k weak derivatives that are zero, on the boundary $\partial\Omega$. All other, non-zero, boundary conditions can be recovered by adding a function conforming with the weak problem, and the desired values on the boundary, to the solution. The well-posedness of this action is ensured by the use of a trace operator. For Lipschitz boundaries $\partial\Omega$, the existence of a trace is postulated by the trace theorem:

Theorem 2.6 (Trace Theorem) *Assume that $\Omega \subset \mathbb{R}^n$ is open and bounded with Lipschitz boundary $\partial\Omega$. Then for all $p \in (0, \infty)$ there exists a unique bounded linear operator*

$$T : W^{1,p}(\Omega) \to L^p(\partial\Omega) \tag{2.9}$$

such that

$$Tw = w|_{\partial\Omega} \quad \forall \quad w \in W^{1,p}(\Omega) \cap C\left(\bar{\Omega}\right), \tag{2.10}$$

where $w|_{\partial\Omega}$ represents the restriction of w to the boundary $\partial\Omega$. Then, Tw is called the trace of w on $\partial\Omega$.

The trace theorem ensures that boundary conditions are well defined. This is not necessarily the case if the above requirements are not fulfilled, particularly if the boundary $\partial\Omega$ does not represent a Lipschitz boundary of a domain Ω. Theorem 2.6 also enables the definition of the trace space $H^{\frac{1}{2}}(\partial\Omega)$ as the space of traces of the functions contained in $H^1(\Omega)$.

Definition 2.7 *Under the assumptions of Theorem 2.6, the trace space of $H^1(\Omega)$ can be defined as the image of the trace operator, i.e.,*

$$H^{\frac{1}{2}}(\partial\Omega) := \left\{ Tw \mid w \in H^1(\Omega) \right\}. \tag{2.11}$$

The definition of trace spaces is essential for the well-posedness of interface problems. Further, the concept of dual spaces and dual pairings will be necessary in order to define the constraint enforcement techniques in Section 2.2:

Definition 2.8 (Dual Pairing) *Let X be a Banach space. Further, let X^* denote the space of bounded linear functionals on X, i.e.,*

$$X^* := \left\{ f : X \to \mathbb{R} \text{ linear} \; : \sup_{\|w\|_X = 1} |f(w)|_{\mathbb{R}} < \infty \right\} \tag{2.12}$$

Then, X^* is called the dual space of X, and the dual pairing of $w^* \in X^*$ and $w \in X$ is defined as

$$\langle w^*, w \rangle_{X^*,X} := w^*(v). \tag{2.13}$$

Dual pairings, thus, represent the evaluation of a linear functional. In the subsequent chapters, particularly the dual space $H^{-\frac{1}{2}}(\partial\Omega)$ of $H^{\frac{1}{2}}(\partial\Omega)$, and the dual space $H^{-1}(\Omega)$ of $H_0^1(\Omega)$ will be required. To simplify the notation in the remainder of this thesis, and to ensure consistency with other scientific works, the following theorem will be implicitly utilized:

Theorem 2.9 (Riesz Representation Theorem) *Let X be a Hilbert space. For every $v \in X$ there exists a linear functional $w^* \in X^*$ such that*

$$\langle w^*, w \rangle_{X^*,X} = (v, w)_X \quad \forall w \in X, \tag{2.14}$$

and it holds $\|w^*\|_{X^*} = \|v\|_X$.

Vice versa, for every $w^* \in X^*$ there exists $v \in X$ such that (2.14) *holds and $\|w^*\|_{X^*} = \|v\|_X$.*

The implicit application of the Riesz representation theorem allows the use of the inner product to denote the dual pairing of $w \in X$ and $v \in X^*$ in the remainder of this thesis, as it is common practice.

With these basic building blocks, the general idea of the finite element method can be summarized, starting from the weak form. In order for the equilibrium equations $q(w)$ to be fulfilled a.e., the continuum equations have to hold on any smooth non-zero subset of $\Omega \subset \mathbb{R}^3$, i.e.,

$$(q(w), \psi)_{L^2(\Omega)} = 0 \quad \forall \quad \psi \in L^2(\Omega), \tag{2.15}$$

where ψ can be interpreted as the density of a measure $\mathrm{d}\psi$ such that $\mathrm{d}\psi = \psi \cdot \mathrm{d}\Omega$. The equation can, thus, be interpreted as enforcement of the equations on any smooth non-zero subset of Ω. For nonlinear equations $q(w)$, (2.15) generally leads to an operator $a : W \times L^2(\Omega) \to \mathbb{R}$, which is nonlinear in the first and linear in the second argument. Such operators are denoted as semi-linear forms in the remainder of this work. In general, more regularity on the test functions ψ is imposed in order to shave off regularity requirements on the solution w, i.e., $w \in H^1(\Omega)$.

The idea of the finite element method is to find the (best) solution in a finite dimensional function space V_h with dimension N and basis ψ_h^i, $i \in [N]$. In this case, a general function $w_h \in V_h$ can be written as

$$w_h := \sum_{i=0}^{N} w_h^i \psi_h^i(x), \tag{2.16}$$

where the function is uniquely determined by the coefficients w_h^i, $i \in [N]$.

With such a finite dimensional basis of the employed function space, the test functions in V_h can be represented as linear combination of finitely many basis functions, leading to the discretized relation

$$\left(a_h(w_h), \psi_h^i\right)_{L^2(\Omega_h)} = 0 \quad \forall \quad \psi_h^i \in V_h. \tag{2.17}$$

In the case of the finite element method, this space is generally chosen in such a way that functions can be approximated by piece-wise polynomial functions. The basis itself is, thus, fully determined by the chosen finite element technology and the employed finite element mesh. A comprehensive review of the finite element method can be found in [214].

Within the remainder of this work the weak form of the problems at hand is chosen as the starting point. Where appropriate, the interface conditions are stated in strong form before being incorporated into the overall system. For the discretization in time, a finite differencing (FD) scheme is applied to all considered problem descriptions. In the following, the finite differencing schemes are assumed to be representable as a linear combination of the state during two successive time steps n and $n+1$, respectively. For the sake of a compact notation, the discrete systems of equations are, thus, only given for the state of one time step $[\cdot]_{n+1}$.

Remark 2.10 *In the remainder of this work, to be consistent with the notation found in literature, the weak derivative $D^\alpha w$ is denoted as $\dfrac{\partial^\alpha w}{\partial x^\alpha}$.*

Furthermore, for a given domain Ω, the notation $(\cdot,\cdot)_\Omega := (\cdot,\cdot)_{L^2(\Omega)}$ is frequently used to denote the L^2 inner product on the domain Ω, and, for the reader's convenience, vector-valued variables and operators are denoted by a bold symbol.

2.2. Methods of constraint enforcement

The solution of interface problems as they are considered within this thesis requires the fulfillment of interface constraints. In general, such types of constraint problems can be interpreted as cases of constrained optimization, i.e., as the minimization of a potential function

$$\begin{aligned} \min_{\mathbf{w}\in W} \mathcal{Q}(\mathbf{w}), \\ \boldsymbol{\mathcal{G}}(\mathbf{w}) = 0, \end{aligned} \tag{2.18}$$

where $\mathcal{Q} : W \to \mathbb{R}$ represents a positive definite potential that depends on the variable $\mathbf{w} \in W$ and $\boldsymbol{\mathcal{G}} : W \to \mathbb{R}$ denotes a constraint on $\mathbf{w}$.

In the following, two mathematical techniques commonly used to incorporate the constraint $\boldsymbol{\mathcal{G}}$ into the finite element system are presented. The remainder of this section follows the review given in the thesis [152].

2.2.1. Lagrange multiplier method

The Lagrange multiplier method represents a stat-of-the-art method for the exact enforcement of interface constraints, cf. [105, 9, 130, 177, 153], among others. The Lagrange multiplier method introduces an additional variable $\boldsymbol{\lambda} \in W^*$ to the constrained problem. The Lagrange multiplier variable is used to combine the constraint function and the potential functional into the constrained functional

$$\mathcal{Q}_{lm}(\mathbf{w}) := \mathcal{Q}(\mathbf{w}) + \langle \boldsymbol{\lambda}, \boldsymbol{\mathcal{G}}(\mathbf{w}) \rangle_{W^*,W}. \tag{2.19}$$

Building the Gateaux derivative of $\mathcal{Q}_{lm}$ in direction $(\delta\mathbf{w}, \delta\boldsymbol{\lambda}) \in W \times W^*$ leads to the following system of equations to be solved:

$$\left(\frac{\partial \mathcal{Q}(\mathbf{w})}{\partial \mathbf{w}} + \left\langle \boldsymbol{\lambda}, \frac{\partial \boldsymbol{\mathcal{G}}(\mathbf{w})}{\partial \mathbf{w}} \right\rangle_{W^*,W} \right) \delta\mathbf{w} + \langle \delta\boldsymbol{\lambda}, \boldsymbol{\mathcal{G}}(\mathbf{w}) \rangle_{W^*,W} = 0. \tag{2.20}$$

The application of Lagrange multipliers gives rise to a primal-dual problem, meaning that the optimization can be viewed as a minimization with respect to the primal variable $\mathbf{w}$, and as a maximization problem with respect to the dual variable $\boldsymbol{\lambda}$. The overall problem can, therefore, be viewed as a saddle point problem of the general form

$$\begin{aligned} \mathbf{a}(\mathbf{w}; \delta\mathbf{w}) + \mathbf{c}(\delta\mathbf{w}, \boldsymbol{\lambda}) = 0, \\ \mathbf{c}(\mathbf{w}, \delta\boldsymbol{\lambda}) = 0, \end{aligned} \tag{2.21}$$

where $\mathbf{a}(\mathbf{w}; \delta\mathbf{w})$ represents a generic semi-linear form and $\mathbf{c}(\delta\mathbf{w}, \boldsymbol{\lambda})$ denotes a bi-linear form. To guarantee a stable solution, such saddle point problems have to adhere to the

Ladyzhenskaya-Babuška-Brezzi (LBB), or inf-sup, condition [23]. For the inf-sup condition to be fulfilled, the function spaces $W \ni \mathbf{w}$ and $M \ni \boldsymbol{\lambda}$ must be chosen in a way such that the relation

$$\inf_{\mathbf{w}\in W} \sup_{\boldsymbol{\lambda}\in M} \frac{\mathbf{c}\left(\mathbf{w},\boldsymbol{\lambda}\right)}{\|\mathbf{w}\|_W \|\boldsymbol{\lambda}\|_M} \geq \gamma, \tag{2.22}$$

holds for a $\gamma > 0$. Here, $\|\cdot\|_W$ and $\|\cdot\|_M$ are norms on the function spaces W and M, respectively.

Within the remainder of this work, the inf-sup condition will be frequently brought up and the LBB-stability, or its circumvention, will be discussed for all considered interface problems and their discretizations.

2.2.2. Penalty method

Another frequently applied method of constraint enforcement is the penalty method [126]. For the penalty method, a penalty potential is added to the functional to be minimized such that the overall potential takes the form

$$\mathcal{Q}_{pen}\left(\mathbf{w}\right) = \mathcal{Q}\left(\mathbf{w}\right) + \frac{\epsilon}{2}\boldsymbol{\mathcal{G}}\left(\mathbf{w}\right)\cdot\boldsymbol{\mathcal{G}}\left(\mathbf{w}\right). \tag{2.23}$$

The method can be interpreted as a penalization of violations of the constraint $\mathcal{G}\left(\mathbf{W}\right)$ via scaling with the penalty parameter $\epsilon > 0$. Building the Gateaux derivative in direction $\delta\mathbf{w} \in W$ gives rise to the following system of equations to be solved:

$$\frac{\partial \mathcal{Q}_{pen}\left(\mathbf{w}\right)}{\partial \mathbf{w}} = \left(\frac{\partial \mathcal{Q}\left(\mathbf{w}\right)}{\partial \mathbf{w}} + \epsilon\boldsymbol{\mathcal{G}}\left(\mathbf{w}\right)\frac{\partial \boldsymbol{\mathcal{G}}\left(\mathbf{w}\right)}{\partial \mathbf{w}}\right)\delta\mathbf{w} = 0. \tag{2.24}$$

Constraint enforcement via the penalty method, generally, leads to a more or less moderate violation of the enforced constraint for any $\epsilon > 0$ and can only be interpreted as exact for the limit case $\epsilon \to \infty$. Besides the violation of the constraint, in the general case, a further drawback is the deterioration of the condition number of the arising system matrix, especially as $\epsilon \to \infty$. These two opposing challenges, reducing the constraint violation while keeping the condition number of the problem rather low, make the choice of a reasonable penalty parameter non-trivial. However, for suitable penalty parameters ϵ, the penalty method represents a simple and robust approach for the enforcement of constraints.

Remark 2.11 *The penalty method as a constraint enforcement method is often described as inferior to the Lagrange multiplier approach as, for any penalty parameter $\epsilon > 0$, the constraint is never exactly fulfilled. Nevertheless, the regularization parameter can also be interpreted as a modeling parameter to allow for some penetration. An example is given by the modeling of micro-scale roughness of the surface, as presented in the author's own work in [18].*

2.2.3. Discrete enforcement of constraints & numerical integration

Analogously to the various methods of constraint enforcement in the continuous regime presented above, there also exist numerous methods for their numerical and computational realization. This section is dedicated to giving some remarks on the manner in which the discretized constraints are enforced and on the integration procedure applied to the arising coupling contributions. In general, all coupling approaches considered within this work are applicable to non-matching meshes. The numerical integration of these coupling contributions, therefore, requires the choice of a suitable integration domain as well as the decision on how to enforce fulfillment of the constraint $\boldsymbol{\mathcal{G}}(\mathbf{w})$ in the discrete regime.

An obvious strategy for the integration of the coupling contributions, with respect to a chosen integration mesh, is the **element-wise integration**. However, this approach introduces integration errors due to weak discontinuities at the finite element boundaries of the projected mesh. In contrast, within a **segment-wise integration** approach, numerical integration is applied to each segment on the integration mesh, or slave side, corresponding to exactly one finite element on the projected mesh, or master side. This approach requires a segmentation of the integration side but also leads to smaller integration errors. Especially for meshes moving relative to each other, as is the case for contact mechanics and IBM-type approaches, segment-wise integration leads to a more consistent method compared to element-wise integration.

Remark 2.12 *In the case of beams interacting with a continuum field, Figure 2.1 illustrates both cases, element-wise as well as segment-wise integration. In the remainder of this thesis, if not stated otherwise, the more accurate segment-based integration approach is adopted from [177] to evaluate any beam-to-continuum field contributions.*

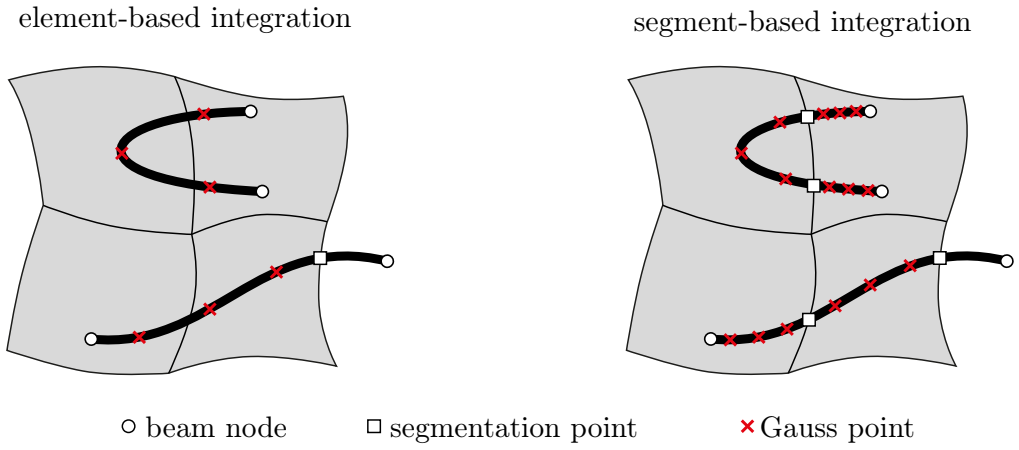

Figure 2.1.: Segmentation of the beam element for stable and accurate numerical integration as presented in [177]: circles and crosses denote beam nodes and quadrature points, respectively. The squares subdivide the beam into integration segments, such that an integration cell on the beam does not cross element boundaries of the fluid mesh to not integrate across weak discontinuities.

Closely related to the question of numerical integration is the choice of where to enforce the constraint in the discrete case. A classical method is the **Gauss-Point-to-Segment** (GPTS) approach. For GPTS-type approaches, the coupling contributions are integrated over the integration mesh but the constraint is only enforced on distinct Gauss points on the projected mesh. The satisfaction of patch tests can in general not be guaranteed. In contrast, when employing the **Segment-to-Segment** (STS) approach, the constraints are enforced in a weak sense on the whole coupling domain. This type of method, most recently the mortar finite element method [202, 153], enables a rather smooth representation of the contact forces while requiring the introduction of a separate discretization field, e.g., for the Lagrange multipliers introduced in Section 2.2.1.

Given conforming surfaces, the **mortar finite element method** ensures a straightforward choice of shape functions for the Lagrange multiplier field to obtain an inf-sup stable mixed finite element formulation. Namely, the shape functions for the Lagrange multiplier field can be chosen as the shape functions of the primal field on the surface of one of the interacting bodies.

Remark 2.13 *Note that the above stated simple choice of shape functions for the Lagrange multiplier field only leads to an inf-sup stable mixed finite element formulation in the case of conforming surfaces. This requirement does not hold in the case of immersed meshes nor in the case of complex geometries, for which the discretized geometry additionally depends on the choice of finite element shape functions. In these cases, the surfaces are in general not conforming. Nevertheless, the mortar finite element method constitutes the first mesh coupling method that passes patch tests and, therefore, represents the state of the art when it comes to discretization methods for mesh tying and computational contact mechanics.*

2.3. Optimal control

Optimal control describes the problem of finding a control that optimizes a given dynamical system with respect to a quantity of interest. This quantity of interest is described by the so-called goal function. In general, such a goal function depends on the state of the system as well as the control itself. Using the state $\mathbf{w}$ and the control $\mathbf{p}$, the goal function is denoted as $J(\mathbf{p}, \mathbf{w})$. The objective is to find the optimal parameter $\mathbf{p}$ within a given set of parameters $\mathcal{P}$ such that the state of the investigated system exhibits some desired behavior. The goal function has to represent a positive definite functional in order for the optimal control problem

Problem 2.14

$$\begin{aligned} &\min_{\mathbf{p}\in\mathcal{P}} J(\mathbf{p}, \mathbf{w}), \\ &\mathbf{a}(\mathbf{p}, \mathbf{w}) = 0, \end{aligned} \tag{2.25}$$

to be solvable. Here, $\mathbf{a}(\mathbf{p}, \mathbf{w})$ represents the state equation of the system. The state equation serves as a dynamic constraint that relates the control $\mathbf{p}$ to the state $\mathbf{w}$. For simplicity, within this thesis the control $\mathbf{p}$ is assumed to contain a finite number of parameters.

If $\mathbf{a}$ is such that it allows for a unique solution $(\mathbf{p}, \mathbf{w})$, the state of the system can be rewritten in dependence of the control $\mathbf{p}$ as $\mathbf{w} := \mathbf{w}(\mathbf{p})$, and the reduced goal functional

$$j(\mathbf{p}) := J(\mathbf{p}, \mathbf{w}(\mathbf{p})), \tag{2.26}$$

can be defined. A solution to Problem 2.14 (within the interior of the domain $\mathcal{P}$) is then given as solution of

$$\frac{\partial j(\mathbf{p})}{\partial \mathbf{p}} = 0. \tag{2.27}$$

In general, the reduced goal functional $j(\mathbf{p})$ represents a nonlinear problem. Within the remainder of this work, some variant of the Broyden-Fletcher-Goldfarb-Shanno (BFGS) algorithm will be applied to treat that nonlinearity without having to explicitly compute the Hesse matrix $\frac{\partial^2 j(\mathbf{p})}{\partial \mathbf{p}^2}$. The BFGS algorithm can be classified as a quasi-Newton algorithm meaning that the solution of the system is found by finding the root of (2.27) using an approximation of the Hessian matrix.

2.4. Structure field

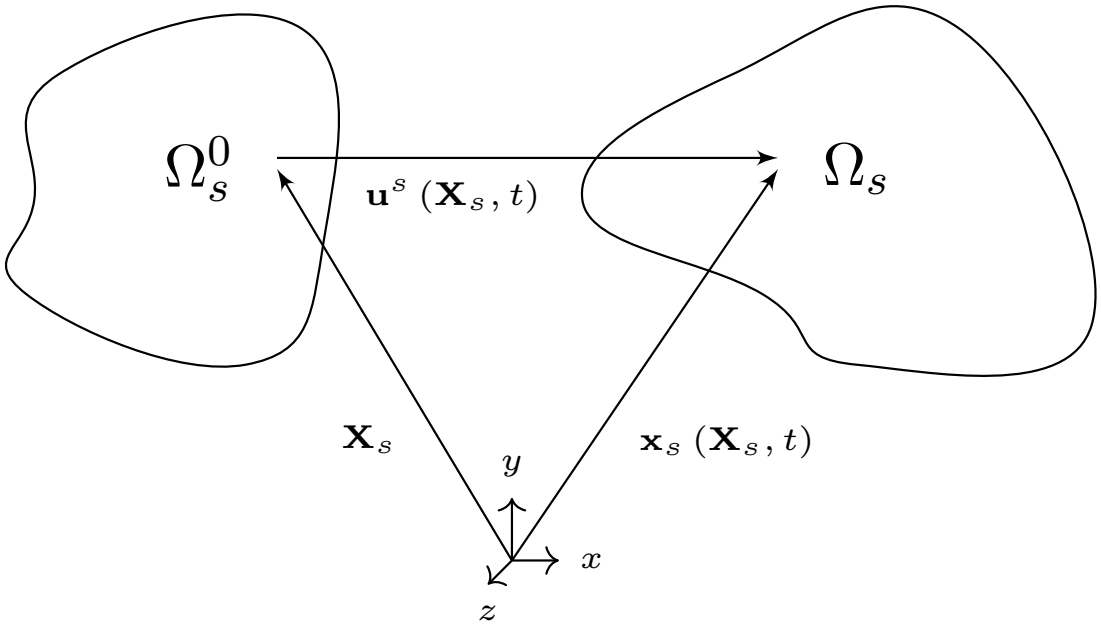

Figure 2.2.: Kinematics of nonlinear solid mechanics and the relationship between the initial configuration Ω_s^0 and the current configuration Ω_s

For nonlinear solid mechanics a Lagrangian description in material coordinates $\mathbf{X}_s$, where $\mathbf{X}_s$ is contained in the reference configuration $\Omega_s^0 \subset \mathbb{R}^3$, is used. Every point in the refer-

ence configuration is related to its current position $\mathbf{x}_s \in \Omega_s$ using the displacement field $\mathbf{u}^s\left(t, \mathbf{X}_s\right)$ via the relation

$$\mathbf{x}_s\left(t, \mathbf{X}_s\right) = \mathbf{X}_s + \mathbf{u}^s\left(t, \mathbf{X}_s\right). \tag{2.28}$$

This relation is illustrated in Figure 2.2. Furthermore, based on the displacement, the deformation gradient can be specified as

$$\mathbf{F} = \frac{\partial \mathbf{x}_s\left(t, \mathbf{X}_s\right)}{\partial \mathbf{X}_s} = \mathbf{I} + \frac{\partial \mathbf{u}^s\left(t, \mathbf{X}_s\right)}{\partial \mathbf{X}_s}, \tag{2.29}$$

where $\mathbf{I} \in \mathbb{R}^{3\times3}$ denotes the identity matrix. The deformation gradient represents a fundamental measure for the deformation in nonlinear continuum mechanics and relates infinitesimal line elements in the reference configuration to their counterparts in the current configuration. The deformation gradient can, therefore, be used to define strain measures. In particular, within the remainder of this thesis the Green-Lagrange strain tensor

$$\boldsymbol{E} = \frac{1}{2}\left(\boldsymbol{F}^T\boldsymbol{F} - \boldsymbol{I}\right), \tag{2.30}$$

is employed to describe finite strains. The Green-Lagrange strain tensor is an objective strain measure, i.e., it is independent of rigid body modes including rotations, making it well suited for various nonlinear application scenarios. Its energy conjugate stress tensor is the second Piola-Kirchhoff stress tensor $\mathbf{S}$. Based on the right Cauchy-Green tensor $\mathbf{C} = \mathbf{F}^T\mathbf{F}$, and assuming a hyperelastic constitutive behavior with strain energy function $\boldsymbol{\Psi}$, the second Piola-Kirchhoff stress tensor is given by the relationship

$$\mathbf{S} = 2\frac{\partial \boldsymbol{\Psi}}{\partial \mathbf{C}}. \tag{2.31}$$

In the remainder of this work, the first Piola-Kirchhoff stress tensor $\boldsymbol{P}$ will be used, which can be expressed as

$$\boldsymbol{P} = \mathbf{F}\mathbf{S}. \tag{2.32}$$

With these considerations, the semi-linear form for the nonlinear continuum model in weak form can be written as

$$\mathbf{a}^s\left(\mathbf{u}^s; \delta\mathbf{u}^s\right) := \rho_s\left(\frac{\partial^2 \mathbf{u}^s}{\partial t^2}, \delta\mathbf{u}^s\right)_{\Omega_s} + \left(\mathbf{P}, \nabla\delta\mathbf{u}^s\right)_{\Omega_s}, \tag{2.33}$$

and, for a Neumann boundary $\Gamma_N^s \subset \partial\Omega_s$ and corresponding value $\mathbf{h}_s$ as well as the body force $\mathbf{f}_s$, the linear form defaults to

$$\mathbf{b}^s\left(\delta\mathbf{u}^s\right) := -\left(\mathbf{f}_s, \delta\mathbf{u}^s\right)_{\Omega_s} - \left(\mathbf{h}_s, \delta\mathbf{u}^s\right)_{\Gamma_N^s}. \tag{2.34}$$

For a function $\mathbf{u}_D^s$ that conforms to the Dirichlet boundary condition on the Dirichlet boundary $\Gamma_D^s \subset \partial\Omega_s$, and the function space of admissible structure displacement solutions on the time interval $I := (0, T)$

$$\mathcal{W}_{\mathcal{S}} := \left\{ \mathbf{u} \in L^2\left(I, H_0^1\left(\Omega_s\right)^3 + \mathbf{u}_D^s\right) : \frac{\partial^2 \mathbf{u}}{\partial t^2} \in L^2\left(I, L^2\left(\Omega_s\right)^3\right) \right\},$$

the state of a solid body is given by the solution of the following problem:

Problem 2.15 *Find* $\mathbf{u}^s \in \mathcal{W}_{\mathcal{S}}$ *such that*

$$\int_0^t \mathbf{a}^s\left(\mathbf{u}^s; \delta\mathbf{u}^s\right) - \mathbf{b}^s\left(\delta\mathbf{u}^s\right) \mathbf{d}t = 0 \tag{2.35}$$

for all $\delta\mathbf{u}^s \in L^2\left(I, H_0^1\left(\Omega_s\right)^3\right)$.

Using the finite element method, the discretized solution of the solid displacement can be approximated as the sum of the finite element shape functions N_i, $i \in [n^s]$, multiplied with the nodal displacement values $\hat{\mathbf{u}}_h^{s,i}$, $i \in [n^s]$, i.e.,

$$\mathbf{u}_h^s := \sum_{i=1}^{n^s} N_i \hat{\mathbf{u}}_h^{s,i}. \tag{2.36}$$

Insertion of (2.36) into the discretized version of Problem 2.15 and subsequent numerical integration leads to the following system of nonlinear equations

$$\boldsymbol{A}_{\mathcal{SS}}\left(\hat{\mathbf{u}}_h^s\right) \hat{\mathbf{u}}_h^s = \mathbf{f}_h^{\mathcal{S}}. \tag{2.37}$$

Here, $\hat{\mathbf{u}}_h^s$ is made up of the nodal displacement values $\hat{\mathbf{u}}_h^{s,i}$, $\boldsymbol{A}_{\mathcal{SS}}\left(\hat{\mathbf{u}}_h^s\right)$ represents the nonlinear equations arising from the discretization of the semi-linear form $\mathbf{a}^s\left(\cdot;\cdot\right)$, and $\mathbf{f}_h^{\mathcal{S}}$ contains all nodal contributions of the external forces and body loads acting on the solid.

Remark 2.16 *To distinguish structural components satisfying the above equations of nonlinear solid mechanics from reduced-dimensional models, in the remainder of this thesis such bodies will frequently be denoted as solids and continuum-based, or 3D, structures.*

2.5. Geometrically exact beam theory

The applied beam models constitute geometrically exact beam models in the sense that "the relationships between the configuration and the strain measures are consistent with the virtual work principle and the equilibrium equations at a deformed state regardless of the magnitude of displacements, rotations and strain" [36, p. 1126]. The two geometrically exact beam formulations treated within this work fall into the category of semi-induced beam theories, meaning that the kinematic equations are consistently derived from the three-dimensional continuum theory while the constitutive equations are directly postulated on the one-dimensional geometry. In contrast to fully induced methods this approach ensures the fulfillment of important mechanical principles such as the equilibrium of forces [134].

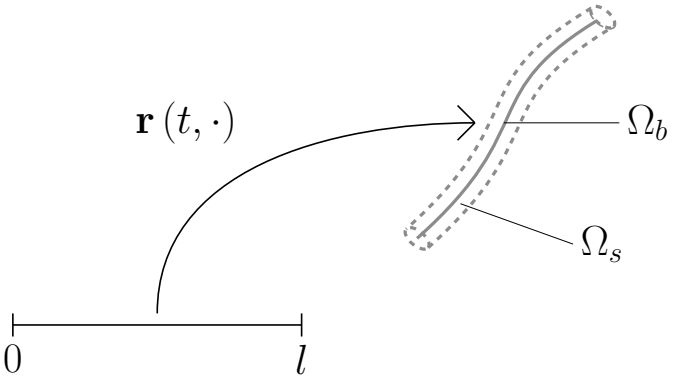

Figure 2.3.: Depiction of a beam and its centerline representation by a curve

In order to write the two particular beam formulations in the upcoming subsections, namely the Simo-Reissner (SR) model and a torsion-free (TF) variant, in a compact form, let

$$\mathcal{V}_{\mathcal{B}}^{\mathrm{p}} := \left\{ v : [0,l] \to \mathbb{R}^3 : \left\| \frac{\partial^\alpha v}{\partial s} \right\|_{\mathcal{B}} < \infty, \alpha \leq p \right\} \qquad \text{for} \quad p \in \{1,2\}, \tag{2.38}$$

be two different spaces of curves on $[0,l]$ with additional requirements on the smoothness of higher order derivatives of the contained curves. Both spaces shall be endowed with the inner product $(\cdot,\cdot)_{\mathcal{B}} := \int_{\mathbb{R}} (\cdot,\cdot)_{\mathbb{R}^3} \, \mathrm{d}s$ and the associated norm $\|\cdot\|_{\mathcal{B}} := \sqrt{(\cdot,\cdot)_{\mathcal{B}}}$. Analogously, $(\cdot,\cdot)_{\mathbb{R}^3}$ denotes the scalar product of two vectors in 3D and its associated norm $\|\cdot\|_{\mathbb{R}^3} := \sqrt{(\cdot,\cdot)_{\mathbb{R}^3}}$ will be used throughout the remainder of this thesis. Furthermore, in the upcoming subsections, the cross product of two vectors $\mathbf{a}$ and $\mathbf{b}$ will be denoted by cross product operator $\boldsymbol{S}(\boldsymbol{a})\,\boldsymbol{b} := \mathbf{a} \times \mathbf{b}$.

In general, the state of a beam at each time $t \in I := [0,T]$ can be characterized by the position of its centerline $\boldsymbol{r}(t,\cdot) \in \mathcal{V}_r^{\mathrm{p}} := \mathcal{V}_{\mathcal{B}}^{\mathrm{p}}$, for $p \in \{1,2\}$, and the cross-section rotation vector $\boldsymbol{\psi}(t,\cdot) \in \mathcal{V}_\theta := \mathcal{V}_{\mathcal{B}}^1$. With the help of Rodrigues' rotation formula, the rotation vector can be used to define a rotation matrix $\boldsymbol{\Lambda} = \boldsymbol{\Lambda}(\boldsymbol{\psi}(t,s)) \in SO(3)$ in the special orthogonal group $SO(3)$ for all $s \in [0,l]$, $t \in I$. Figure 2.3 visualizes the image of the centerline curve $\Omega_b := \Omega_b(t) := \mathbf{r}(t,[0,l]) \subset \mathbb{R}^3$, as well as the 3-dimensional domain $\Omega_s := \Omega_s(t) \subset \mathbb{R}^3$ denoting the beam's current configuration, at a specific time t.

To maintain a compact notation where possible, the solution state $\boldsymbol{\eta}^b \in \mathcal{V}_{\mathcal{B}}$ summarizing all relevant unknowns, such as the centerline position $\mathbf{r}$ and the rotation vector $\boldsymbol{\psi}$, is introduced to represent the state of the regarded beam. The exact form of $\boldsymbol{\eta}^b$ and $\mathcal{V}_{\mathcal{B}}$ depends on basic modeling assumptions and therefore differs for the two beam models, which will be introduced in the upcoming subsections.

For now, using the presented general notation, the general beam problem can be completed by introducing the Dirichlet boundary conditions $\boldsymbol{\eta}_D$, an initial state $\boldsymbol{\eta}_0$, and the function space of admissible solutions

$$\mathcal{W}_{\mathcal{B}} := \left\{ \boldsymbol{\eta} \in L^2(I, \mathcal{V}_{\mathcal{B}} + \boldsymbol{\eta}_D) : \ddot{\mathbf{r}} \in L^2\left(I, L^2([0,l])\right) \right\}$$

Then, the state of the beam can be characterized as solution $\boldsymbol{\eta}^b$ of the following problem:

Problem 2.17 *Find $\boldsymbol{\eta}^b \in \mathcal{W}_{\mathcal{B}}$ such that*

$$\int_0^T \mathbf{a}^b\left(\boldsymbol{\eta}^b; \delta\boldsymbol{\eta}^b\right) - \mathbf{b}^b\left(\delta\boldsymbol{\eta}^b\right)\, dt = 0, \tag{2.39}$$

for all $\delta\boldsymbol{\eta}^b \in L^2\left(I, \mathcal{V}_{\mathcal{B}}\right)$ and with $\boldsymbol{\eta}^b = \boldsymbol{\eta}_0$ a. e. for $t = 0$, and $\left\|\mathbf{r}'\left(0,\cdot\right)\right\|_{\mathbb{R}^3} = 1$ a. e. on $[0, l]$.

The exact form of the semi-linear form $\boldsymbol{a}^b\left(\boldsymbol{\eta}^b; \delta\boldsymbol{\eta}^b\right)$, the linear form $\boldsymbol{b}^b\left(\delta\boldsymbol{\eta}^b\right)$, and the corresponding solution space $\mathcal{V}_{\mathcal{B}}$ will be given in the upcoming subsections for two particular beam models.

Remark 2.18 *In problem 2.17, the additional condition $\left\|\mathbf{r}'\left(0,\cdot\right)\right\|_{\mathbb{R}^3} = 1$ means that $\mathbf{r}\left(0,\cdot\right)$ represents an arc-length parameterized curve on $[0, l]$, or, in other words, l defines the initial length of the beam.*

2.5.1. Simo-Reissner beam model

The Simo-Reissner (SR) model is based on the assumptions of plane, rigid cross-sections, but does not introduce any additional kinematic constraints on the beam. For further details on the derivation, see e.g., [175].

For the density ρ_b, shear and Young's modulus G_b and E_b, respectively, the cross-section area A, the reduced cross-section values A_1 and A_2, the torsional moment of inertia I_T, and the principal moments of inertia I_2, I_3, the constitutive matrices $\boldsymbol{C}_M$, $\boldsymbol{C}_F$, and the inertia tensor $\boldsymbol{C}_\rho$ are given as follows:

$$\begin{aligned} \boldsymbol{C}_M &:= \begin{pmatrix} G_b I_T & 0 & 0 \\ 0 & E_b I_2 & 0 \\ 0 & 0 & E_b I_3 \end{pmatrix}, \boldsymbol{C}_F := \begin{pmatrix} E_b A & 0 & 0 \\ 0 & G_s A_2 & 0 \\ 0 & 0 & G_s A_3 \end{pmatrix}, \\ \text{and } \boldsymbol{C}_\rho &:= \begin{pmatrix} \rho_b\left(I_2 + I_3\right) & 0 & 0 \\ 0 & \rho_b I_2 & 0 \\ 0 & 0 & \rho_b I_3 \end{pmatrix}. \end{aligned} \tag{2.40}$$

With the deformation measures $\boldsymbol{\Gamma} := \boldsymbol{\Lambda}^T\mathbf{r}' - \mathbf{e}_1$, and the solution state $\boldsymbol{\eta}^b := (\mathbf{r}, \boldsymbol{\psi})$, the semi-linear form in Problem 2.17 is defined as

$$\begin{aligned} \mathbf{a}^b\left(\boldsymbol{\eta}^b; \delta\boldsymbol{\eta}^b\right) := &\left(\rho_b \mathbf{A}\ddot{\mathbf{r}}, \delta\mathbf{r}\right)_{\mathcal{B}} + \left(\boldsymbol{\Lambda}\mathbf{C}_F\boldsymbol{\Gamma}, \delta\mathbf{r}'\right)_{\mathcal{B}} \\ &+ \left(\boldsymbol{\Lambda}\boldsymbol{C}_M\boldsymbol{\Omega}, \delta\boldsymbol{\theta}'\right)_{\mathcal{B}} - \left(\boldsymbol{\Lambda}\boldsymbol{C}_F\boldsymbol{\Gamma}, \mathbf{S}\left(\delta\boldsymbol{\theta}\right)\mathbf{r}'\right)_{\mathcal{B}} \\ &+ \left(\mathbf{S}\left(\mathbf{w}\right)\mathbf{c}_\rho\mathbf{w} + \mathbf{c}_\rho\dot{\mathbf{w}}, \delta\boldsymbol{\theta}\right)_{\mathcal{B}}, \end{aligned} \tag{2.41}$$

and the linear form defaults to

$$\mathbf{b}^b\left(\delta\boldsymbol{\eta}^b\right) := (\mathbf{f}, \delta\mathbf{r})_{\mathcal{B}} + \left[\tilde{\mathbf{f}}^T\delta\mathbf{r}\right|_0^l + (\mathbf{m}, \delta\boldsymbol{\theta})_{\mathcal{B}} + \left[\tilde{\mathbf{m}}^T\delta\boldsymbol{\theta}\right|_0^l. \tag{2.42}$$

Here, the external forces $\mathbf{f}$, the external moments $\mathbf{m}$, the point forces $\tilde{\mathbf{f}}$, the point moments $\tilde{\mathbf{m}}$, the angular velocity vector $\mathbf{w}$ such that $\mathbf{S}(\mathbf{w}) = \dot{\boldsymbol{\Lambda}}\boldsymbol{\Lambda}^T$, and the material curvature vector $\boldsymbol{\Omega}$ such that $\mathbf{S}(\boldsymbol{\Omega})\,\mathbf{a} = \boldsymbol{\Lambda}^T\boldsymbol{\Lambda}'\mathbf{a}$ for all $\mathbf{a} \in \mathbb{R}^3$, are used.

For the above integrals to be well defined, the appropriate function space for test and trial functions has to take the form of the product space $\mathcal{V}_{\mathcal{B}} := \mathcal{V}_r^1 \times \mathcal{V}_\theta$.

2.5.2. Torsion-free beam model

In the case of initially straight beams with isotropic cross-section, under the assumption of vanishing shear strains, and assuming that torsional components of distributed and discrete external moments acting on the beam are negligible, the SR beam formulation can be simplified to a torsion-free (TF) model. The following formulation was originally introduced in [135] for static problems, and extended to transient problem types in [133].

The above assumptions lead to exactly vanishing torsion only in static problems. Nevertheless, it is suggested in [133] that under the mentioned restrictions, torsional values are "very small" also in dynamic applications. Thus, the kinematic assumptions of the beam can be reformulated such that the unknown vector of rotations $\boldsymbol{\psi}$ can be removed from the system and only the unknowns $\boldsymbol{\eta}^b := \mathbf{r}$ remain. The semi-linear form then takes the form

$$\begin{aligned}\mathbf{a}^b\left(\boldsymbol{\eta}^b; \delta\boldsymbol{\eta}^b\right) := {} & (\rho_b\mathbf{A}\ddot{\mathbf{r}}, \delta\mathbf{r})_{\mathcal{B}} + \left(E_bA\frac{(\|\mathbf{r}'\| - 1)\,\mathbf{r}'}{\|\mathbf{r}'\|}, \delta\mathbf{r}'\right)_{\mathcal{B}} \\ & + \left(\frac{E_bI}{\|\mathbf{r}'\|^4}\mathbf{S}\left(\mathbf{r}'\right)\mathbf{r}'', \mathbf{S}\left(\delta\mathbf{r}'\right)\mathbf{r}'' + \mathbf{S}\left(\mathbf{r}'\right)\delta\mathbf{r}''\right)_{\mathcal{B}} \\ & - \left(\frac{2E_bI}{\|\mathbf{r}'\|^6}\mathbf{S}\left(\mathbf{r}'\right)\mathbf{r}'', \delta\left(\mathbf{r}'^T\mathbf{r}\right)\mathbf{S}\left(\mathbf{r}'\right)\mathbf{r}''\right)_{\mathcal{B}} - \left(\mathbf{m}, \frac{\mathbf{S}\left(\mathbf{r}'\right)}{\|\mathbf{r}'\|^2}\delta\mathbf{r}'\right)_{\mathcal{B}} \\ & - \left[\frac{\tilde{\mathbf{m}}\mathbf{S}\left(\mathbf{r}'\right)\delta\mathbf{r}'}{\|\mathbf{r}'\|^2}\right|_0^l,\end{aligned} \tag{2.43}$$

and the linear form is defined by

$$\mathbf{b}^b\left(\delta\boldsymbol{\eta}^b\right) := (\mathbf{f}, \delta\mathbf{r})_{\mathcal{B}} + \left[\tilde{\mathbf{f}}^T\delta\mathbf{r}\right|_0^l. \tag{2.44}$$

The removal of rotational unknowns from the system of PDEs through enforcement of the TF constraint comes with the cost of additionally required smoothness of the centerline curves, namely $\mathbf{r} \in \mathcal{V}_{\mathcal{B}} := \mathcal{V}_r^2$.

2.5.3. Discretization of the beam centerline

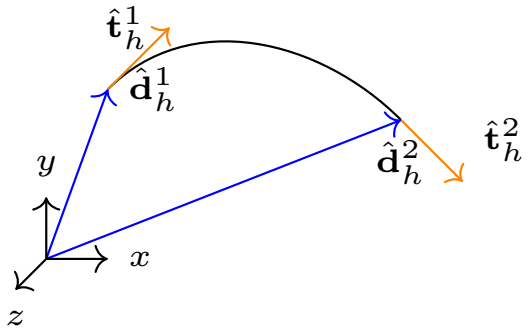

Figure 2.4.: Visualization of a Hermite beam centerline interpolation

The beam centerline and velocity discretization applied in this contribution is exclusively based on 3rd-order C^1-continuous Hermite shape functions as suggested in [135, 133]. C^1-continuity is required to capture the beam's curvature and, thus, for the torsion-free beam formulation presented above to be well-defined. Based on the nodal positions $\hat{\mathbf{d}}_h^j$, the nodal tangents $\hat{\mathbf{t}}_h^j$, the initial length l_{ele}^0 of the finite element, and the corresponding positional and tangential shape functions H_j^d and H_j^t, respectively, the semi-discrete centerline position and beam velocity fields can be expressed as

$$\mathbf{r}_h := \sum_{j=1}^{n^b} H_j^d \hat{\mathbf{d}}_h^j + \frac{l_{ele}^0}{2} \sum_{j=1}^{n^b} H_j^t \hat{\mathbf{t}}_h^j, \quad \mathbf{v}_h^b := \dot{\mathbf{r}}_h. \tag{2.45}$$

Within the FBI framework proposed in Chapter 3 as well as the applied variant of the beam-to-solid-surface coupling method employed in Chapter 5, only the centerline terms will be coupled. As the centerline terms are independent of the employed beam theory, the details of the cross-sectional rotation discretization will be skipped here. The interested reader may be referred to [133] for details on the applied Petrov-Galerkin method for discretization in space.

Insertion of (2.45) into (2.39) and subsequent spatial integration leads to the nonlinear system

$$\mathbf{A}_{\mathcal{BB}}\left(\hat{\boldsymbol{\eta}}_h^b\right)\hat{\mathbf{r}}_h = \mathbf{f}_h^{\mathcal{B}}. \tag{2.46}$$

Here, $\hat{\mathbf{r}}_h$ contains all beam-related degrees of freedom (DoFs) including positional and tangential unknowns, and accordingly so do the system of nonlinear equations $\mathbf{A}_{\mathcal{BB}}\left(\hat{\boldsymbol{\eta}}_h^b\right)$ and the vector $\mathbf{f}_h^{\mathcal{B}}$.

In the remainder of this thesis, the time evolution of the torsion-free variant is discretized using a Generalized-α time integration scheme [34] with the spectral radius set to $\rho_\infty = 1$, and all parameters set accordingly to produce a second-order accurate time stepping scheme. For the Lie-group Generalized-α time stepping scheme, based on multiplicative

updates of the rotational degrees of freedom of the employed beam finite elements, the interested reader is referred to [24, 25].

2.6. Fluid field

To model the fluid field, the instationary, isothermal incompressible Navier-Stokes equations for Newtonian fluids on fixed meshes are used. Within this section, the weak form of the Navier-Stokes equations, their spatial discretization with finite elements, and the arising nonlinear system of equations, is recounted. For a more comprehensive overview of challenges and methods in the context of the finite element discretization for the incompressibe Navier-Stokes equations, the interested reader is referred to [156].

2.6.1. Weak form of the Navier-Stokes equations

To define the weak form of the Navier-Stokes equations, the standard Sobolev space on the fluid domain Ω_f with zero trace on the boundary $\partial\Omega_f$, $H_0^1(\Omega_f)$ is used. The fluid boundary $\partial\Omega_f = \Gamma_N^f \cup \Gamma_D^f$ can be partitioned into a Neumann boundary Γ_N^f and a Dirichlet boundary Γ_D^f. On the Neumann boundary Γ_N^f, a traction $\mathbf{h}^f$ is prescribed, and a function $\mathbf{v}_D^f$ with prescribed velocity values on Γ_D^f is introduced as Dirichlet boundary condition. Further, let $\mathcal{V}_p := \left\{ p \in L^2(\Omega_f) \,|\, \|p\|_{L^2(\Omega^f)} = 0 \right\}$ be the space of normalized pressure solutions, $\mathcal{W}_{\mathcal{F}}^p := L^2(I, \mathcal{V}_p)$ the space of admissible pressure solutions, and

$$\mathcal{W}_{\mathcal{F}}^v := \left\{ \mathbf{v} \in L^2\left(I, H_0^1(\Omega_f)^3 + \mathbf{v}_D\right) : \frac{\partial v}{\partial t} \in L^2\left(I, H^1(\Omega_f)^3\right) \right\},$$

the space of admissible fluid velocity solutions.

For the fluid field, the semi-linear form takes the form

$$\begin{aligned} \mathbf{a}^f\left(\mathbf{v}^f, p^f; \delta\mathbf{v}^f, \delta p^f\right) := \rho_f \left(\frac{\partial \mathbf{v}^f}{\partial t}, \delta\mathbf{v}^f \right)_{\Omega_f} + 2\gamma_f \left(\boldsymbol{\mathcal{E}}\left(\mathbf{v}^f\right), \boldsymbol{\nabla}\mathbf{v}^f \right)_{\Omega_f} - \left(p^f, \boldsymbol{\nabla} \cdot \delta\mathbf{v}^f \right)_{\Omega_f} \\ + \rho_f \left(\left(\mathbf{v}^f \cdot \boldsymbol{\nabla}\right)\mathbf{v}^f, \delta\mathbf{v}^f \right)_{\Omega_f} + \left(\boldsymbol{\nabla} \cdot \mathbf{v}^f, \delta p^f \right)_{\Omega_f}, \end{aligned} \tag{2.47}$$

and the linear form is defined by

$$\mathbf{b}^f\left(\delta\mathbf{v}^f\right) := \rho_f \left(\mathbf{f}^f, \delta\mathbf{v}^f \right)_{\Omega_f} + \left(\mathbf{h}^f, \delta\mathbf{v}^f \right)_{\Gamma_N^f}, \tag{2.48}$$

with the strain rate tensor $\boldsymbol{\mathcal{E}}\left(\mathbf{v}^f\right) = \frac{1}{2}\left(\nabla\mathbf{v}^f + \left(\nabla\mathbf{v}^f\right)^T\right)$, a body force $\mathbf{f}^f$, the dynamic viscosity γ_f, and the fluid density ρ_f, respectively.

In the case of a divergence-free initial velocity field $\mathbf{v}_0^f$, the behavior of the fluid on the domain Ω_f is fully described by

Problem 2.19 *Find* $\left(\mathbf{v}^f, p^f\right) \in \mathcal{W}_{\mathcal{F}}^p \times \mathcal{W}_{\mathcal{F}}^v$, *with* $\mathbf{v}^f = \mathbf{v}_0$ *a. e. for* $t = 0$, *such that*

$$\int_0^T \mathbf{a}^f \left(\mathbf{v}^f, p^f; \delta\mathbf{v}^f, \delta p^f\right) - \mathbf{b}^f \left(\delta\mathbf{v}^f\right) \, dt = 0, \tag{2.49}$$

for all $\left(\delta\mathbf{v}^f, \delta p^f\right) \in L^2\left(I, H_0^1\left(\Omega_f\right)^3\right) \times L^2\left(I, \mathcal{V}_p\right)$.

2.6.2. Discretization of the Navier-Stokes equations

Discretization of the Navier-Stokes equations leads to a mixed finite element formulation in the fluid velocity and pressure, with the velocity as the primal variable and the pressure representing a dual variable that ensures a divergence-free flow. Instead of the employment of inf-sup stable finite elements for the velocity-pressure pairs, stabilization terms are added to the system in order to circumvent the LBB condition. This makes it possible to use simple, equal-order P1/P1 shape functions for the fluid solution pairs, i.e.,

$$\mathbf{v}_h^f := \sum_{i=1}^{n^f} N_i \hat{\mathbf{v}}_h^{f,i}, \quad p_h^f := \sum_{i=1}^{n^f} N_i \hat{p}_h^{f,i}. \tag{2.50}$$

Within the remainder of this thesis, a PSPG stabilization is applied to the Navier-Stokes equations to circumvent the inf-sup condition [189]. To further improve the numerical properties of the resulting system of equations a div-grad stabilization term, and the SUPG method to prevent instabilities in convection-dominated flows, are added [77, 57, 171]. To specify the additional stabilization terms for the inf-grad, and SUPG/PSPG term, respectively, the discrete residuals, $\mathbf{r}_h^M$ for the momentum, and $\mathbf{r}_h^C$ for the continuity equation, are introduced as

$$\mathbf{r}_h^M = \rho_f \frac{\partial \mathbf{v}_h^f}{\partial t} + 2\gamma_f \boldsymbol{\mathcal{E}}\left(\mathbf{v}_h^f\right) - \boldsymbol{\nabla} p_h^f + \rho_f \left(\mathbf{v}_h^f \cdot \boldsymbol{\nabla}\right) \mathbf{v}_h^f, \tag{2.51}$$

and

$$\mathbf{r}_h^C = \boldsymbol{\nabla} \cdot \mathbf{v}_h^f. \tag{2.52}$$

With these definitions, the overall stabilized (time-continuous) nonlinear fluid system reads

$$\begin{aligned}
\mathbf{a}_h^f \left(\mathbf{v}_h^f, p_h^f, \delta\mathbf{v}_h^f, \delta p_h^f\right) := {} & \rho^f \left(\frac{\partial \mathbf{v}_h^f}{\partial t}, \delta\mathbf{v}_h^f\right)_{\Omega_f^h} + 2\gamma^f \left(\boldsymbol{\mathcal{E}}\left(\mathbf{v}_h^f\right), \boldsymbol{\nabla}\mathbf{v}_h^f\right)_{\Omega_f^h} \\
& - \left(p_h^f, \boldsymbol{\nabla} \cdot \delta\mathbf{v}_h^f\right)_{\Omega_f^h} + \rho^f \left(\left(\mathbf{v}_h^f \cdot \boldsymbol{\nabla}\right) \mathbf{v}_h^f, \delta\mathbf{v}_h^f\right)_{\Omega_f^h} + \left(\boldsymbol{\nabla} \cdot \mathbf{v}_h^f, \delta p_h^f\right)_{\Omega_f^h} \\
& + \rho_f \left(\tau_M \mathbf{r}_h^M, \mathbf{v}_h^f \cdot \delta\mathbf{v}_h^f\right)_{\Omega_f^h} + \left(\tau_C \mathbf{r}_h^C, \boldsymbol{\nabla} \cdot \delta\mathbf{v}_h^f\right)_{\Omega_f^h} + \left(\tau_M \mathbf{r}_h^M, \nabla \delta p_h^f\right)_{\Omega_f^h}.
\end{aligned} \tag{2.53}$$

Here, τ_C and τ_M represent suitable stabilization parameters according to the definitions in [187, 201]. Evaluation of the integrals over the trial and test functions in (2.53) leads to the nonlinear system of equations

$$\boldsymbol{A}_{\mathcal{FF}}\left(\hat{\mathbf{v}}_h^f\right)\begin{pmatrix}\hat{\mathbf{v}}_h^f\\ \hat{\mathbf{p}}_h^f\end{pmatrix}=\mathbf{f}^{\mathcal{F}}, \tag{2.54}$$

where the vectors $\hat{\mathbf{v}}_h^f$ and $\hat{\mathbf{p}}_h^f$ are made up of the components $\hat{\mathbf{v}}_h^{f,i}$ and $\hat{p}_h^{f,i}$, respectively, as defined in (2.50). $\boldsymbol{A}_{\mathcal{FF}}\left(\hat{\mathbf{v}}_h^f\right)$ is obtained by evaluation of (2.53), and $\mathbf{f}^{\mathcal{F}}$ contains all nodal contributions of the applied forces introduced in (2.48).

2.7. Contact mechanics

Within this section, frictionless normal contact between two interacting bodies is presented. In the following, the two structural bodies are denoted as $\Omega_{s,1}\subset\mathbb{R}^3$ and $\Omega_{s,2}\subset\mathbb{R}^3$, and the superscripts $(\cdot)_1$ and $(\cdot)_2$ are used to denote quantities related to the first and second body, respectively. An extension to multi-body contact can be realized straightforwardly. Furthermore, let $\Gamma_c:=\Gamma_{c,1}\subset\partial\Omega_s^1$ be the potential contact area on $\partial\Omega_{s,1}$. Γ_c is in general not the actual contact area. For a comprehensive review of computational contact and impact mechanics, modeling and discretization approaches, the interested reader is referred to [119, 12].

2.7.1. Contact conditions

The modeling of contact mechanics leads to a highly nonlinear problem based on inequality constraints. In contrast to equality constraints such as introduced in Section 2.2, inequality constraints only contribute to the system of equations when the solution variable lies on a multi-dimensional surface of the region of admissible solutions. This distinction is already obvious from the continuous constraint equations for frictionless normal contact in strong form, which are described by the Hertz-Signorini-Moreau conditions:

$$\begin{aligned} g_n &\geq 0 \quad \text{on } \Gamma_c,\\ p_c &< 0 \quad \text{on } \Gamma_c,\\ g_n\cdot p_c &= 0 \quad \text{on } \Gamma_c. \end{aligned} \tag{2.55}$$

Here, p_c denotes the contact pressure in normal direction and the gap function g_n describes the minimal distance of one point $\mathbf{X}_{s,1}$ on body $\Omega_{s,1}$ to body $\Omega_{s,2}$, i.e.,

$$g_n\left(t,\mathbf{X}_{s,1}\right):=-\mathbf{n}_{c,1}\cdot\left(\mathbf{x}_{s,1}\left(t,\mathbf{X}_{s,1}\right)\right)\cdot\left(\mathbf{x}_{s,1}\left(t,\mathbf{X}_{s,1}\right)-\bar{\mathbf{x}}_{s,2}\left(\mathbf{x}_{s,1}\left(t,\mathbf{X}_{s,1}\right)\right)\right), \tag{2.56}$$

where $\mathbf{n}_{c,1}\left(\mathbf{x}_{s,1}\left(\mathbf{X}_{s,1},t\right)\right)$ represents the outward-facing normal on $\partial\Omega_{s,1}$ at $\mathbf{x}_{s,1}$, and the contact point $\bar{\mathbf{x}}_{s,2}\in\partial\Omega_{s,2}$ is defined via the closest point projection

$$\bar{\mathbf{x}}_{s,2}\left(\mathbf{x}_{s,1}\right) := \arg \min_{\mathbf{x}_{s,2} \in \partial\Omega_{s,2}} \left\| \mathbf{x}_{s,1} - \mathbf{x}_{s,2} \right\|. \tag{2.57}$$

In the primal-dual system given by (2.55), the gap function g_n represents the primal variable and the contact pressure p_c acts as the dual variable. Considering the physical interpretation of (2.55), the conditions ensure non-penetration, the absence of adhesive stresses, and represent a complementary condition.

2.7.2. Weak form of the contact problem

Following the approach in [153], a Lagrange multiplier-based constraint enforcement is applied to model the contact between the two interacting bodies. Due to the inequality constraint, the function space M_λ of admissible Lagrange multipliers takes the form of a cone, i.e.,

$$M_\lambda := \left\{ \boldsymbol{\mu} \in H^{-\frac{1}{2}}\left(\Gamma_c\right)^3 \,|\, \langle \boldsymbol{\mu}, \mathbf{w} \rangle_{H^{-\frac{1}{2}}(\Gamma_c)^3, H^{\frac{1}{2}}(\Gamma_c)^3} \leq 0 \quad \forall \quad \mathbf{w} \in H^{\frac{1}{2}}\left(\Gamma_c\right)^3 \right\}. \tag{2.58}$$

In the following, the semi-linear forms for body $\Omega_{s,1}$ and body $\Omega_{s,2}$ containing the structural equations presented in (2.33) are denoted as $\boldsymbol{a}_1^s\left(\mathbf{u}_1^s; \delta\mathbf{u}_1^s\right)$ and $\boldsymbol{a}_2^s\left(\mathbf{u}_2^s; \delta\mathbf{u}_2^s\right)$, respectively. Furthermore, the linear forms for body $\Omega_{s,1}$ and body $\Omega_{s,2}$ containing the forces acting on the two structures, as introduced in (2.34), are denoted as $\boldsymbol{b}_1^s\left(\delta\mathbf{u}_1^s\right)$ and $\boldsymbol{b}_2^s\left(\delta\mathbf{u}_2^s\right)$, respectively. Additionally, $\mathcal{W}_{\mathcal{S},1}$ and $\mathcal{W}_{\mathcal{S},2}$ denote the function spaces of admissible displacement solutions for $\Omega_{s,1}$ and $\Omega_{s,2}$, respectively, and $\chi^s : \mathbf{x}_{s,1} \rightarrow \bar{\mathbf{x}}_{s,2}$ denotes the closest point projection (2.57). Using (2.58) and the above defined notation, the problem of two contacting bodies looks as follows:

Problem 2.20 *Find* $\left(\mathbf{u}_1^s, \mathbf{u}_2^s, \boldsymbol{\lambda}^c\right) \in \mathcal{W}_{\mathcal{S},1} \times \mathcal{W}_{\mathcal{S},2} \times L^2\left(I, M_\lambda\right)$ *such that*

$$\begin{aligned}
\int_0^t \boldsymbol{a}_1^s\left(\mathbf{u}_1^s; \delta\mathbf{u}_1^s\right) - \boldsymbol{b}_1^s\left(\delta\mathbf{u}_1^s\right) - \left(\boldsymbol{\lambda}^c, \delta\mathbf{u}_1^s\right)_{\Gamma_c} \, dt = 0 \\
\int_0^t \boldsymbol{a}_2^s\left(\mathbf{u}_2^s; \delta\mathbf{u}_2^s\right) - \boldsymbol{b}_2^s\left(\delta\mathbf{u}_2^s\right) - \left(\boldsymbol{\lambda}^c, \delta\mathbf{u}_2^s \circ \chi^s\right)_{\Gamma_c} \, dt = 0 \\
\int_0^t \left(\delta\boldsymbol{\lambda}^c - \boldsymbol{\lambda}^c, \mathbf{u}_1^s - \mathbf{u}_2^s \circ \chi^s\right)_{\Gamma_c} \, dt = 0
\end{aligned} \tag{2.59}$$

for all $\left(\delta\mathbf{u}_1^s, \delta\mathbf{u}_2^s, \delta\boldsymbol{\lambda}^c\right) \in L^2\left(I, H_0^1\left(\Omega_{s,1}\right)^3\right) \times L^2\left(I, H_0^1\left(\Omega_{s,2}\right)^3\right) \times L^2\left(I, M_\lambda\right)$

2.7.3. Discretization of the contact constraints

To find a well-suited spatial discretization for the Lagrange multipliers, the mortar finite element method, cf. [202, 153], is applied to the dual field. However, in the presence of inequality constraints, the application of a so-called active set strategy is generally required to find a solution of the overall problem. To avoid this requirement, the strategy in [207, 154] is applied, and the system is regularized by assuming a linear relationship between the gap and the Lagrange multiplier field. As the Lagrange multipliers can be interpreted as the contact pressure, this corresponds to the assumption of a linear relationship between the contact pressure p_c and the gap g_n.

Therefore, the Lagrange multiplier field $\boldsymbol{\lambda}_h^{\mathrm{c}}$ is approximated via n^{lm} suitable shape functions ϕ_k, $k \in \left[n^{lm}\right]$ and the nodal Lagrange multiplier values $\hat{\boldsymbol{\lambda}}_h^{\mathrm{c},k}$ as

$$\boldsymbol{\lambda}_h^{\mathrm{c}} := \sum_{k=1}^{n^{lm}} \phi_k \hat{\boldsymbol{\lambda}}_h^{\mathrm{c},k}. \tag{2.60}$$

Using the notation

$$\langle x \rangle = \begin{cases} x, & \text{for } x \leq 0 \\ 0, & \text{for } x > 0 \end{cases}, \tag{2.61}$$

and assuming a linear relationship between the contact pressure and the gap, the nodal DoFs of the Lagrange multiplier field can be rewritten using the gap function, or equivalently the displacement functions of the two contacting bodies, as

$$\boldsymbol{\lambda}_h^{\mathrm{c}} := \sum_{k=0}^{n^{lm}} \epsilon_c \left\langle -\phi_k \left(\mathbf{u}_{h,1}^s - \mathbf{u}_{h,2}^s \right) \cdot \mathbf{n}_{c,h,1} \right\rangle. \tag{2.62}$$

Here, ϵ_c describes the slope of the linear relationship and $\mathbf{n}_{c,h,1}$ denotes the discretized outer normal vector field on the surface γ_c.

Inserting (2.62) and the shape functions $N_{j,1}$, $j \in [n_1^s]$ and $N_{i,2}$, $i \in [n_2^s]$ for the displacement field on the first and second body, respectively, into (2.59), and integrating the coupling contributions, gives rise to the following mortar matrices:

$$\begin{aligned} \mathbf{D}^c(k,j) = \int_{\Gamma_c} \phi_k N_{j,1} \, \mathrm{d}s, \quad \mathbf{M}^c(k,i) = \int_{\Gamma_c} \phi_k N_{i,2} \circ \chi \, \mathrm{d}s, \\ \text{for} \quad k \in [n^{lm}], j \in [n_1^s], i \in [n_2^s]. \end{aligned} \tag{2.63}$$

Use of these matrices and the indices $\mathcal{S}_1$ and $\mathcal{S}_2$ for quantities related to $\Omega_{s,1}$ and $\Omega_{s,2}$, respectively, leads to the following semi-discrete nonlinear system for the Problem 2.20:

$$\begin{bmatrix} \mathbf{A}_{\mathcal{S}_1\mathcal{S}_1} + \epsilon_c \left(\mathbf{M}^c\right)^T \boldsymbol{\kappa}^{-1} \mathbf{M}^c & -\epsilon_c \left(\mathbf{M}^c\right)^T \boldsymbol{\kappa}^{-1} \mathbf{D}^c \\ -\epsilon_c \left(\mathbf{D}^c\right)^T \boldsymbol{\kappa}^{-1} \mathbf{M}^c & \mathbf{A}_{\mathcal{S}_2\mathcal{S}_2} + \epsilon_c \left(\mathbf{D}^c\right)^T \boldsymbol{\kappa}^{-1} \mathbf{D}^c \end{bmatrix} \begin{bmatrix} \hat{\mathbf{u}}_{h,1}^s \\ \hat{\mathbf{u}}_{h,2}^s \end{bmatrix} = \begin{bmatrix} \mathbf{f}_1^{\mathcal{S}} \\ \mathbf{f}_2^{\mathcal{S}} \end{bmatrix}. \tag{2.64}$$

Here $\mathbf{A}_{\mathcal{S}_1\mathcal{S}_1}$ and $\mathbf{A}_{\mathcal{S}_2\mathcal{S}_2}$ denote the nonlinear matrices introduced in 2.37, arising from the structure continuum equations. The normalization matrix

$$\boldsymbol{\kappa}\left(m,m\right)=\int_{\Gamma_c}\phi_m\,\mathrm{d}s,\quad m\in[n^{lm}], \tag{2.65}$$

is required for the method to fulfill simple patch tests. In favor of a compact notation, the explicit statement of dependencies of nonlinear matrices is dropped within the remainder of this thesis.

2.8. Fluid-structure interaction

One of the big challenges in classical FSI simulations is the question of how to deal with the different points of view commonly adopted when simulating the fluid and structural domain, respectively. In fluid mechanics, the behavior of the flow field is commonly described from a fixed point of view, in Eulerian coordinates $\mathbf{x}(\mathbf{x}_0,t)$. In structural mechanics on the other hand, the observer follows the deformation of the solid in dependence of a fixed reference domain, accordingly adopting a Lagrangian perspective. To overcome this discrepancy, the Arbitrary Lagrangian-Eulerian (ALE) approach has been developed [83, 42]. The ALE frame introduces an extension function of the structural displacement to the fluid domain to "transform the Navier-Stokes equations to the reference domain" [51, p.34].

This section is meant to recapitulate the ALE approach for solving the Navier-Stokes equations on moving meshes, the FSI coupling conditions, their enforcement through a mortar finite element approach, and to review the concepts of strong and weak coupling algorithms and related challenges. The interested reader is referred to [161] for a comprehensive review of FSI in general, and to [105] and the thesis [129] for the application of mortar finite element-based mesh tying to FSI systems.

2.8.1. Fluid formulation on deforming meshes

As stated above, an ALE observer is used to describe the fluid field governed by the incompressible Navier-Stokes equations on a moving domain. The ALE approach can be interpreted as a compromise between the Eulerian and Lagrangian framework. Here, the fluid domain is successively updated, similar to the Lagrangian frame, but the mesh does not follow the movement of the fluid particles everywhere. Instead, a mesh velocity somewhere between the one of the Lagrangian and the Eulerian frame is applied. The ALE mapping

$$\boldsymbol{\mathcal{A}}(\boldsymbol{x},t):\Omega_f^0\times I\rightarrow\Omega_f\left(t\right),\boldsymbol{x}\mapsto\boldsymbol{x}+\boldsymbol{u}^f(\boldsymbol{x},t), \tag{2.66}$$

is used to compute the updated mesh, effectively mapping the reference domain Ω_f^0 to the current domain $\Omega_f\left(t\right)$ at time t. The mapping relies on the fluid mesh displacement $\boldsymbol{u}_f$,

which is computed via the mesh motion PDE (MMPDE). For a suitable semi-linear form $\mathbf{a}^{mmpde}(\cdot;\cdot)$ and the space of admissible functions

$$\mathcal{W}_{\mathcal{F}}^{u} := \{\mathbf{u} \in L^2\left(I, H_0^1(\Omega_f)^3\right) : \mathbf{u} = \hat{u}_s|_{\Gamma_i} \text{ on } \Gamma_i \times I\},\ \frac{\partial \mathbf{u}}{\partial t} \in L^2\left(I, L^2(\Omega_f)^3\right),$$

the MMPDE reads as follows:

Problem 2.21 *Find $\boldsymbol{u}^f \in \mathcal{W}_{\mathcal{F}}{}^u$ such that*

$$\int_I \mathbf{a}^{mmpde}\left(\boldsymbol{u}^f; \delta\boldsymbol{u}^f\right)\, dt = 0 \tag{2.67}$$

for all $\delta\boldsymbol{u}^f \in L^2\left(I, H_0^1(\Omega_f)^3\right)$.

A typical PDE to compute the fluid displacement $\boldsymbol{u}^f$ for the ALE transformation defined above is the Laplace problem

$$\mathbf{a}^{mmpde} := \left(\nabla \boldsymbol{u}^f, \nabla \delta\boldsymbol{u}^f\right). \tag{2.68}$$

However, also other equations are possible. In general, the MMPDE should be as simple as possible to be efficiently solved, while a smooth solution is desirable. In Chapter 4, for instance, a hyperelastic constitutive law will be used to extend the displacements from the FSI interface to the fluid mesh.

In order to compute the Navier-Stokes equations on a moving mesh, the mesh velocity

$$\boldsymbol{v}^{\text{ale}} := \frac{\partial \boldsymbol{u}^f}{\partial t}, \tag{2.69}$$

is necessary Based on the mesh velocity the semi-linear form for the Navier-Stokes equations on moving meshes can ca be written as

$$\begin{aligned}\mathbf{a}_{ale}^{f}\left(\mathbf{v}^f, p^f; \delta\mathbf{v}^f, \delta p^f\right) := \rho_f \left(\frac{\partial \mathbf{v}^f}{\partial t}, \delta\mathbf{v}^f\right)_{\Omega_f} + 2\gamma_f \left(\boldsymbol{\mathcal{E}}\left(\mathbf{v}^f\right), \boldsymbol{\nabla}\mathbf{v}^f\right)_{\Omega_f} - \left(p^f, \boldsymbol{\nabla}\cdot\delta\mathbf{v}^f\right)_{\Omega_f} \\ + \rho_f \left(\left(\left(\mathbf{v}^f - \boldsymbol{v}^{\text{ale}}\right)\cdot\boldsymbol{\nabla}\right)\mathbf{v}^f, \delta\mathbf{v}^f\right)_{\Omega_f} + \left(\boldsymbol{\nabla}\cdot\mathbf{v}^f, \delta p^f\right)_{\Omega_f}.\end{aligned} \tag{2.70}$$

For the Navier-Stokes equations on a moving mesh, evaluation of the integrals over the trial and test functions in (2.70) leads to the nonlinear system of equations

$$\boldsymbol{A}_{\mathcal{F}\mathcal{F}}^{ale}\left(\hat{\mathbf{v}}_h^f, \hat{\mathbf{u}}_h^f\right)\begin{pmatrix}\hat{\mathbf{v}}_h^f \\ \hat{\mathbf{p}}_h^f\end{pmatrix} = \mathbf{f}_h^{\mathcal{F}}, \tag{2.71}$$

where the vectors of unknowns and forces are as introduced in Section 2.6. Note that the fluid matrix $\boldsymbol{A}_{\mathcal{F}\mathcal{F}}^{ale}$ contains an additional dependency compared to the matrix arising from the Navier-Stokes equations computed on a fixed mesh, namely the dependence on the fluid mesh displacement $\hat{\mathbf{u}}_h^f$.

2.8.2. Fluid-structure interaction coupling conditions

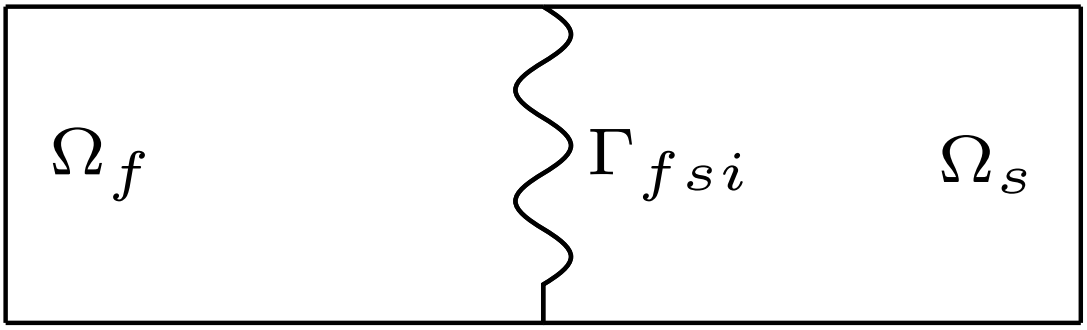

Figure 2.5.: Depiction of the fluid and structure domains Ω_f and Ω_s, respectively, and the FSI interface Γ_{fsi}

Finally, the Navier-Stokes equations in ALE formulation as recounted in Section 2.8.1 have to be coupled to the nonlinear elastodynamics equations. To model the interaction between the two domains as defined in Figure 2.5, meaningful coupling conditions need to be enforced on the FSI boundary. Here, the coupling is enforced by a collection of continuity conditions.

The first such condition is the geometric coupling condition

$$\boldsymbol{u}^f = \mathbf{u}^s \text{ on } \Gamma_{fsi} \times I, \tag{2.72}$$

which ensures continuity of the displacement variable on the FSI interface. Since the displacement also describes the mesh movement, this geometric condition also ensures matching domains and physically meaningful geometries.

Secondly, the kinematic coupling condition

$$\mathbf{v}^f = \mathbf{v}^s \text{ on } \Gamma_{fsi} \times I, \tag{2.73}$$

ensures continuity of the velocity across the interface.

Last but not least, the surface traction on the fluid boundary has to equal the one on the solid boundary in order to achieve an equilibrium of forces. This leads to the dynamic coupling condition

$$\boldsymbol{h}^f = \boldsymbol{h}^s \text{ on } \Gamma_{fsi} \times I. \tag{2.74}$$

Following the approach in [105, 130], relating $\boldsymbol{u}^f$ and $\mathbf{v}^f$ on the interface Γ_{fsi}, and enforcing the geometric coupling condition (2.72) using a Lagrange multiplier approach, gives rise to the following continuous problem:

Problem 2.22 *Find* $\left(\mathbf{v}^f, p^f, \boldsymbol{u}^f, \mathbf{u}^s, \boldsymbol{\lambda}^{fsi}\right) \in \mathcal{W}_{\mathcal{F}}^v \times \mathcal{W}_{\mathcal{F}}^p \times \mathcal{W}_{\mathcal{F}}^u \times \mathcal{W}_{\mathcal{S}} \times L^2\left(I, H^{-\frac{1}{2}}\left(\Gamma_{FSI}\right)^3\right)$, *with* $\mathbf{v}^f = \mathbf{v}_0$, $\boldsymbol{r}^b = \boldsymbol{r}_0$ *a.e. for* $t = 0$, *such that*

$$\begin{aligned}
&\int_0^T \mathbf{a}_{ale}^f\left(\mathbf{v}^f, p^f; \delta\mathbf{v}^f, \delta p^f\right) - \mathbf{b}^f\left(\delta\mathbf{v}^f\right)_{\Gamma_{fsi}} - \left(\frac{\partial \boldsymbol{u}^f}{\partial t} - \mathbf{v}^f, \delta\mathbf{v}^f\right) dt = 0,\\
&\int_0^T \mathbf{a}^s\left(\mathbf{u}^s; \delta\mathbf{u}^s\right) - \mathbf{b}^s\left(\delta\mathbf{u}^s\right) - \left(\boldsymbol{\lambda}^{fsi}, \delta\mathbf{u}^s\right)_{\Gamma_{fsi}} dt = 0,\\
&\int_0^T \left(\mathbf{u}^s - \boldsymbol{u}^f, \delta\boldsymbol{\lambda}^{fsi}\right)_{\Gamma_{fsi}} dt = 0\\
&\int_0^T \mathbf{a}^{mmpde}\left(\boldsymbol{u}^f; \delta\boldsymbol{u}^f\right) + \left(\boldsymbol{\lambda}^{fsi}, \delta\boldsymbol{u}^f\right)_{\Gamma_{fsi}} dt = 0
\end{aligned} \tag{2.75}$$

for all $\left(\delta\mathbf{v}^f, \delta p^f, \delta\boldsymbol{u}^f, \delta\mathbf{u}^s, \delta\boldsymbol{\lambda}^{fsi}\right) \in L^2\left(I, H_0^1\left(\Omega_f\right)^3\right) \times L^2\left(I, \mathcal{V}_p\right) \times L^2\left(I, H_0^1\left(\Omega_f\right)^3\right) \times L^2\left(I, H_0^1\left(\Omega_s\right)^3\right) \times L^2\left(I, H^{-\frac{1}{2}}\left(\Gamma_{fsi}\right)^3\right)$,

where $\mathbf{u}_D^f$ represents a Dirichlet boundary condition on the fluid mesh displacement $\mathbf{u}^f$.

Remark 2.23 *It is noteworthy that the solution also fulfills the dynamic coupling condition* (2.74) *via the Lagrange multiplier. In contrast, the kinematic coupling condition* (2.73) *is not naturally built-in to the system. Instead, combination of the geometric coupling condition and the relationship*

$$\frac{\partial \boldsymbol{u}^f}{\partial t} = \mathbf{v}^f \quad \text{a.e. on } \Gamma_{fsi}, \tag{2.76}$$

ensures fulfillment of the kinematic coupling condition as

$$\begin{aligned}
\mathbf{u}^s &= \boldsymbol{u}^f && \text{a.e. on } I \times \Gamma_{fsi}\\
\Rightarrow \frac{\partial \mathbf{u}^s}{\partial t} &= \frac{\partial \boldsymbol{u}^f}{\partial t} && \text{a.e. on } I \times \Gamma_{fsi}\\
\Rightarrow \frac{\partial \mathbf{u}^s}{\partial t} &= \mathbf{v}^f && \text{a.e. on } I \times \Gamma_{fsi}
\end{aligned} \tag{2.77}$$

2.8.3. Discretized nonlinear system of equations

In the following, the discrete system, discretized in space and time, is presented. Following the approach in [105, 130], the Lagrange multiplier field is discretized according to the mortar finite element method. The mortar matrices are build analogously to the case of contact mechanics in Section 2.7, cf. (2.63). Analogously to the continuous case, the mortar finite element method ensures enforcement of the geometric and dynamic coupling conditions. In addition, the discretized version of (2.76) reads

$$\hat{\boldsymbol{u}}_h^{f,n+1} := \hat{\boldsymbol{u}}_h^{f,n} + \tau_{\mathcal{AF}} \left(\hat{\mathbf{v}}_h^{f,n+1} - \hat{\mathbf{v}}_h^{f,n} \right), \tag{2.78}$$

where $\tau_{\mathcal{AF}}$ constitutes a parameter that depends on the employed time integration scheme. Using this relation, discretization and integration of (2.75) in time and space leads to the following nonlinear system of equations:

$$\begin{bmatrix} \mathbf{A}_{\mathcal{FF}}^{ale}\left(\hat{\mathbf{v}}_h^f, \hat{\boldsymbol{u}}_h^f\right) & 0 & 0 & 0 \\ 0 & \mathbf{A}_{\mathcal{AA}} & 0 & -\left(\mathbf{D}^{fsi}\right)^T \\ 0 & 0 & \mathbf{A}_{\mathcal{SS}}\left(\hat{\mathbf{u}}_h^s\right) & \left(\mathbf{M}^{fsi}\left(\hat{\mathbf{u}}_h^s, \hat{\boldsymbol{u}}_h^f\right)\right)^T \\ 0 & -\tau_{\mathcal{AF}}\mathbf{D}^{fsi} & \mathbf{M}^{fsi}\left(\hat{\mathbf{u}}_h^s, \hat{\boldsymbol{u}}_h^f\right) & 0 \end{bmatrix}_{n+1} \begin{bmatrix} \begin{pmatrix} \hat{\mathbf{v}}_h^f \\ \hat{\mathbf{p}}_h^f \end{pmatrix} \\ \hat{\boldsymbol{u}}_h^f \\ \hat{\mathbf{u}}_h^s \\ \hat{\boldsymbol{\lambda}}^{fsi} \end{bmatrix}_{n+1} = \begin{bmatrix} \mathbf{f}_h^{\mathcal{F}} \\ -\mathbf{f}_h^{\mathcal{AF}} \\ \mathbf{f}_h^{\mathcal{S}} \\ -\mathbf{f}_h^{\Lambda\mathcal{F}} \end{bmatrix}_{n+1}. \tag{2.79}$$

Here, the subscript $\mathcal{AA}$ highlights MMPDE related quantities, mixed subscripts $\mathcal{AF}$ denote quantities coupling the fluid velocities to the mesh motion displacement.

Remark 2.24 *In* (2.78)*, the employed time integration scheme is used to relate the displacement to the velocity in a strong manner. Due to the flexibility of using different time integration schemes for the various fields the kinematic coupling condition will, therefore, not be exactly fulfilled, even in a weak sense. For more details, the interested reader is referred to the thesis [129].*

2.8.4. Solution algorithms

In general, solution schemes for FSI can be classified into two categories: **strongly** and **loosely coupled algorithms**. The application of loosely coupled algorithms may lead to artificial oscillations in the solution variables. The reason for these numerical instabilities is the neglect of the added mass effect. Due to the incompressibility of the considered flow, the fluid has to move along with every displacement of the solid. This added mass is not taken into account when solving the solid problem separately. Especially for structure models with small mass, i.e., because of a low density compared to the fluid density, these loose coupling schemes are not suitable. Instead, a strongly coupled algorithm is required to avoid these spurious effects.

To some extent related to the notion of strong and loose coupling is the division of FSI algorithms into **monolithic** and **partitioned** solution procedures. Monolithic solution schemes solve the entire global system of nonlinear equations at once, and always constitute strongly coupled algorithms. The added mass effect is naturally accounted for by the applied nonlinear solutions algorithm, such as the Newton Raphson method. However, a consistent linearization for all terms is required to ensure an efficient treatment, and the generally

large system size makes the application of scalable linear iterative solvers such as algebraic multigrid (AMG) methods unavoidable. Due to the saddle-point like structure of matrices arising from FSI problems, advance preconditioning is necessary to ensure the efficiency of such iterative linear solvers.

Within partitioned solution schemes, the single fields are solved sequentially based coupling information exchanged between the two fields. The most common partitioned scheme is the classical Dirichlet-Neumann algorithm. Here, the fluid represents the Dirichlet partition, for which the mesh displacement on the FSI boundary $\hat{\boldsymbol{u}}_h^f\Big|_{\Gamma_{fsi}}$, based on the structure displacement solution $\hat{\mathbf{u}}_h^s$, is prescribed as a Dirichlet boundary condition. The structure partition, conversely, serves as the Neumann partition, for which the interaction force $\mathbf{f}_h^{s,fsi}$, based on the previous fluid solution, is applied on the interface Γ_{fsi}. If each field is only solved once in each time step, the method constitutes a loosely coupled algorithm that may lead to oscillation effects as described above. However, to recover strong coupling, a staggered approach can be used. In such solution algorithms, the procedure of solving the two subsystems in a staggered manner is repeated until a user-prescribed stopping criterion is fulfilled. Nevertheless, models with particularly light structures may still present a challenge, since the neglect of the added mass effect generally leads to convergence problems of the resulting fixed-point iteration. To facilitate and accelerate convergence in these cases, an acceleration technique can be employed. Two such acceleration techniques in the context of FBI will be shown in Section 3.3.

In the case of mortar mesh tying, and particularly for mortar dual shape functions, the interface variables are easily calculated via the following equations:

$$\hat{\boldsymbol{u}}_h^f = \boldsymbol{D}_{fsi}^{-1}\boldsymbol{M}_{fsi}\hat{\mathbf{u}}_h^s, \tag{2.80}$$

and

$$\mathbf{f}_h^{s,fsi} = \boldsymbol{M}_{fsi}^T\hat{\boldsymbol{\lambda}}^{fsi} = -\boldsymbol{M}_{fsi}^T\boldsymbol{D}_{fsi}^{-T}\mathbf{f}_h^{f,fsi}, \tag{2.81}$$

where $\mathbf{f}_h^{f,fsi}$ represents the interaction force acting on the fluid mesh. For more information on the solution procedure in the context of FSI, the interested reader is referred to Chapter 4 and [105].

Part I.

Fluid-beam interaction: a computational framework

In the area of FSI, the IBM [148, 149, 99] constitutes a well-studied method for mixed-dimen-sional interactions. Nearly five decades ago, Peskin first explored the idea of embedding a 1D body representing the response of a thin structure within a 2D fluid domain to simulate the blood flow in the vicinity of a heart valve [148]. At the time, Peskin modeled the blood flow via the incompressible Navier-Stokes equations spatially discretized with a FD method. The force exerted by the heart valve on the fluid around it was modeled as a direct linear response to the fluid velocity. The interpolation of the fluid velocity and force response between the two meshes was realized by using so-called delta functions as numerical approximations of Dirac functions.

Since that time a significant amount of research has been conducted on the extension and application of the IBM to fully resolved equal-dimensional 2D and 3D FSI problems based on fictitious domain methods, cf. [157, 81, 9, 124, 59], among others. In such methods, the domain occupied by the immersed structure is filled by a fictitious fluid volume. This usually leads to a coupling of the involved FSI values on the fictitious domain volume and/or its surface. An exception represents the work of Baaijens in [9], in which applications of his proposed fictitious domain/mortar finite element methods to slender bodies are shown. The slender bodies are modeled with continuum-based equations, while the coupling interface is reduced to only one side of the fictitious domain. Comparisons with fully coupled ALE-based methods show the validity of this simplification.

In the context of mixed-dimensional methods, beam formulations based on 1D equations are embedded in a 2D fluid in [122, 198, 8]. In [122], the coupling of the fluid and the beam is realized with moving composite meshes interacting on the beam surface, while an IBM-type coupling of the beam surface with the background mesh is presented in [198], and body-fitted meshes in combination with remeshing are employed in [8]. Finally, Huang et al. [91] present results for an IBM-type method coupling a 1D beam formulation with a 3D fluid. Again, the beam is coupled with the Navier-Stokes equations on the reconstructed beam surface, making all of the mentioned approaches surface-to-volume coupling schemes as categorized in [177]. In contrast, in the work of Tschisgale et al. [192], classical regularized delta functions are used to add FBI forces to the overall problem. This method, nevertheless, also necessitates the use of finely resolved background meshes.

Figure 2.6 shows representative fluid mesh resolutions for the different FBI approaches discussed above. Here, the fibers are assumed to be modeled via a 1D model. Though, Figure 2.6a shows the reconstruction of the beam's actual surface and a subsequent fictitious meshing, as in the coupling used in [91, 122, 8]. Figure 2.6b shows a mesh with approx. 3-5 fluid elements over the beam diameter as commonly required for IBM-type methods, for which discrete delta functions are applied to approximate the beam diameter. Such an approach can be found in [192, 198, 99]. Figure 2.6c depicts a representative mesh as used within the FBI approach first proposed for a multi-physics problem in the author's previous work [75]. The model is based on the assumption of small beam radii compared to the background elements and couples the two fields only along the beams' centerline instead of its surface. This leads to the possibility of relatively coarse, and, therefore, computationally efficient background meshes. The method is, thus, one of the first to be able to capture the actual physical interaction of the slender bodies with fluid flow while maintaining the complexity reduction with regard to the DoFs gained through the

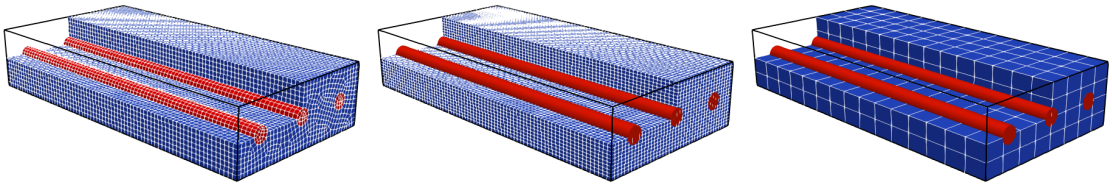

(a) Representative mesh for a surface-to-surface coupled method

(b) Representative mesh for a surface-to-volume coupled method

(c) Representative mesh for the centerline-to-volume coupling schemes used within this thesis

Figure 2.6.: Representative meshes for various mixed-dimensional coupling strategies

employment of reduced-dimensional beam theory.

Nevertheless, the solution of mixed-dimensional FSI problems leads to additional algorithmic difficulties which require treatment. Because of their considerable slenderness and susceptibility to external forces, immersing beams within fluid flow generally leads to numerical challenges with respect to the well-known added mass effect. Strong coupling of the fluid and structure field is, thus, essential for the stability of the simulation. As introduced in Section 2.8, strong coupling can be achieved by solving the full monolithic multi-physics problem or by means of a staggered partitioned approach. In the past, not much research has been devoted to the solution of linear systems arising from such mixed-dimensional monolithic problems. In particular, the linear systems to be solved for the beam field, as introduced in Section 2.5, are usually not diagonally-dominant, leading to the need for advanced preconditioning. In addition, the mixed-dimensional nature of the problem calls for specially tailored preconditioning for the overall monolithic problem as analyzed in [113, 26, 84]. In order to use well-established solution techniques for the two single fields, a staggered partitioned solution approach is chosen instead. In general, an acceleration technique is needed to guarantee convergence of the staggered scheme [164, 117, 63, 143, 122].

A further algorithmic difficulty stems from the fact that general applications of the envisioned FBI problems exhibit large displacements, making an IBM-type approach the methodology of choice. Such methods have also been used in the context of mixed-dimensional methods in [205, 198, 192, 112]. In contrast to classical ALE-based FSI approaches, for IBM-type methods it is not possible to track the interaction interface. Instead, the interface needs to be captured as the beams move through the fluid's background mesh. In particular, for large numbers of immersed beams and parallel high-performance computing (HPC), this gives rise to the need for efficient computationally-parallel search algorithms to find the current beam position.

Once identified, coupling quantities have to be exchanged between the beam mesh and the fluid's background mesh. Mesh tying is part of many numerical applications ranging from mesh partitioning approaches [202] to the simulation of multi-physics problems such as FSI [105]. As detailed in Section 2.2, for such surface-coupled problems, the mortar finite element method represents a mathematically sound, stable approach to transfer coupling quantities from one mesh to the other. Successful applications include the case of contact mechanics as well as ALE-based FSI [105, 153, 130, 9]. In the case of surface-

to-volume coupling, as applied in IBM-type methods, this simple choice of shape functions for inf-sup stable Lagrange multipliers is not guaranteed anymore. Nevertheless, in terms of smoothness and robustness of the problem solution, such problems can still benefit from using a mortar-type STS coupling approach. Examples of this are illustrated for fictitious domain/Lagrange multiplier methods in the context of FSI in [9, 41, 17]. For a mixed-dimensional mesh tying problem of 1D beam equations embedded into a 3D solid volume, the STS approach's advantages have recently been demonstrated in [177, 179]. This motivates the use of such a mortar-type discretization approach for the simulation of slender structures interacting with incompressible fluid flow.

In combination with the author's previous work in [75], the following analysis constitutes the first rigorous numerical study of a truly mixed-dimensional 1D-3D coupling approach to capture global effects of the interaction of nonlinear beam elements with 3D fluid flow in a manner that enables the use of a relatively coarse background mesh compared to the diameter of the slender beam. The method, thus, allows for a very efficient solution of the FBI problem in terms of the required number of unknowns.

3. Fluid-beam interaction

The aim of this chapter is the development of an efficient computational framework to capture the interactions between slender bodies modeled using geometrically exact beam theory and 3D fluid flow. To this end, first, the weak form of the overall FBI problem based on a true 1D-3D coupling approach as well as its requirements and challenges are stated. Afterward, two numerical coupling strategies, a GPTS and a mortar-type coupling, and the arising nonlinear matrices after spatial integration with the finite element method, are introduced. In order to ensure an efficient solution of these matrices, a specially tailored partitioned algorithm for the solution of the FBI problem is presented, and potential challenges arising from the high slenderness of the beam structures, are discussed. In the end, the nature of the 1D-3D coupling, the numerical and algorithmic building blocks, and the method's overall suitability for practically-relevant applications, are extensively validated by numerical examples. Major parts of this chapter have already been published in [75].

3.1. Weak formulation

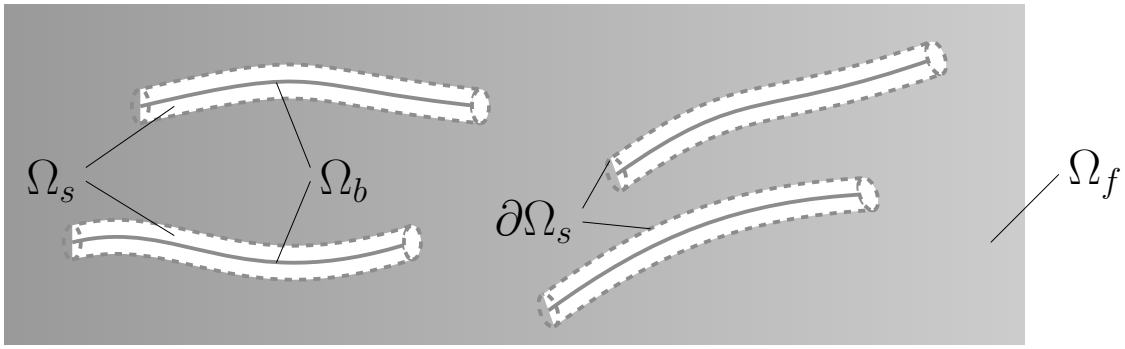

Figure 3.1.: Domain of a fluid-beam interaction problem. Figure is taken from the author's article [75].

The single field equations introduced within Chapter 2 can now be used to formulate the coupled fluid-beam interaction problem. In the following, the notation introduced in Chapter 2 and visualized in Figure 3.1 will be used, and the fluid domain will be denoted by Ω_f, the time-dependent beam domain by Ω_s, and the time-dependent beam centerline position will be denoted by Ω_b. Additionally, $\partial\Omega_s$ shall represent the surface of Ω_s. From a continuum mechanics point of view, the interaction of the fluid and structure fields takes place on the shared coupling interface $\Gamma^* := \overline{\Omega}_s \cap \overline{\Omega}_f$ defined as the intersection of the

respective closures of Ω_s and Ω_f. To model this interaction, the multi-physics nature of FSI problems leads to additional challenges compared to single field equations. Among these challenges is the fact, that the single field equations are based on different primal variables, i.e., the velocity field $\mathbf{v}^f$ for the Navier-Stokes equations, and the displacement field or, more accurately in the present case, the beam position $\mathbf{r}$ for the structure.

As presented in Section 2.8, it is thus customary to introduce the structure velocity $\mathbf{v}^s$ in order to formulate the kinematic coupling condition

$$\mathbf{v}^f = \mathbf{v}^s \qquad \text{a. e. on } \Gamma^*, \tag{3.1}$$

to ensure continuity of the velocity on the coupling interface Γ^*.

In the case of immersed or fictitious domain methods the FSI interface Γ^* is not a priori known but has to be captured as the embedded structures move through the fluid domain. For IBM-type methods the coupling interface is commonly defined by the surface of the structure domain moving through the fluid domain, i.e., $\Gamma^* := \partial\Omega_s$, while the fluid domain Ω_f spans the whole computational domain. Thus, for IBM-type methods, (3.1) leads to a surface-to-volume coupling approach, as adopted in [91, 122]. This holds in the sense that the constraints are enforced on the structure surface, while no a priori fluid surface can be defined and the coupling, thus, takes place within the fluid volume domain.

The aim of the proposed FBI method is to yield a computationally-efficient approach that does not require the geometrical resolution of the embedded fibers by the background mesh as in [122, 192, 193, 198]. Instead, the immersed fibers are assumed to be highly slender, also compared to the background mesh. Under the assumption of sufficiently small beam radii, the following simplifications can be argued to be valid:

$i)$ The coupling of the two fields can be realized directly on the 1-dimensional beam centerline, as it is done in [9, 177, 205, 110, 149].

$ii)$ Rotational effects on the fluid flow are negligible.

Such a beam centerline-to-volume coupling approach, in contrast to the above mentioned surface-to-volume coupling, reduces the complexity in the computations of the coupling conditions due to the reduced dimensionality of the coupling interface as well as the fact that no reconstruction of the beam surface is necessary.

For the beam velocity $\mathbf{v}^b := \dot{\mathbf{r}} : [0, l] \to \Omega_b$, (3.1) can be rewritten as

$$\mathbf{v}^f = \mathbf{v}^b \circ \mathbf{r}^{-1} \qquad \text{a. e. on } \Omega_b, \tag{3.2}$$

where $\mathbf{r}^{-1} := \mathbf{r}^{-1}(t, \cdot) : \Omega_b \to [0, l]$ represents the inversion of the beam centerline curve, and serves as projection of the beam's current geometry Ω_b in 3-dimensional space onto the beam parameter space $[0, l]$. Equivalently, this condition can be written as

$$\mathbf{v}^f \circ \mathbf{r} = \mathbf{v}^b \qquad \text{a. e. on } [0, l], \tag{3.3}$$

on the parameter space $[0, l]$.

Meanwhile, the dynamic coupling condition ensuring continuity of tractions takes the form

$$(\mathbf{f}, \delta\mathbf{r})_{\mathcal{B}} + \lim_{\partial\Omega_s \to \Omega_b} \left(\boldsymbol{\sigma}\left(\mathbf{v}^f\right) \cdot \mathbf{n}, \delta\mathbf{v}^f\right)_{\partial\Omega_s} = 0. \tag{3.4}$$

It is not obvious how the result of the second term looks in the limit case. However, using the restriction operator $\mathbf{\Pi} : H^1(\Omega_f)^3 \to L^2(\Omega_b)$, it is assumed that the second term in (3.4) leads to a 1-dimensional integral in the limit case, i.e.,

$$\int_{\Omega_b} \mathbf{f}_{fbi}^f\left(\mathbf{v}^{\mathbf{f}}\right) \cdot \mathbf{\Pi}\delta\mathbf{v}^f \, \mathrm{d}s, \tag{3.5}$$

where the result of the operator

$$\mathbf{f}_{fbi}^f\left(\mathbf{v}^{\mathbf{f}}\right) : H^1(\Omega_f)^3 \to L^2(\Omega_b),$$

represents a line force acting on the fluid. For the treatment via the penalty method, postulating the existence of such a line force suffices. Nevertheless, for coupling via a range of regularized Lagrange multiplier methods such as Nitsche type methods, further analysis of the exact form of the resulting line force is necessary. This question is closely related to the existence of a sufficiently smooth restriction operator $\mathbf{\Pi}$, which represents the 1D-3D analogon to the projection postulated by the trace theorem, Theorem 2.6. The restriction operator is required as the fluid variable $\mathbf{v}^f$ is a priori not well defined on the 1D beam centerline. The role and importance of $\mathbf{\Pi}$ is further discussed in Remark 3.3.

Due to its impact on the divergence condition, strong enforcement of the kinematic condition may lead to spurious effects on the fluid pressure field for immersed boundary methods. This condition will, thus, be denoted in a weak sense. Within this thesis, the enforcement via the two constraint enforcement techniques introduced in Section 2.2 will be investigated: the penalty and the Lagrange multiplier method. The FBI problem's weak form resulting from application of the two methods are presented in the following.

3.1.1. Lagrange multiplier-based constraint enforcement approach

Here, the Lagrange multiplier method is applied to enforce the kinematic coupling condition. Other works based on the application of Lagrange multipliers in the context of FSI include [105, 9, 130], among others. In the present case, the Lagrange multiplier approach is applied to enforce the kinematic equation, i.e., the continuity of beam and fluid velocities $\mathbf{v}^b$ and $\mathbf{v}^f$, respectively. This leads the overall FBI problem:

Problem 3.1 *Find* $\left(\mathbf{v}^f, p^f, \boldsymbol{r}^b, \boldsymbol{\lambda}\right) \in \mathcal{W}_{\mathcal{F}^v} \times \mathcal{W}_{\mathcal{F}^p} \times \mathcal{W}_{\mathcal{B}} \times L^2(I, \mathcal{V}_{\mathcal{B}})$, *with* $\mathbf{v}^f = \mathbf{v}_0$, $\boldsymbol{r}^b = \boldsymbol{r}_0$

a.e. for $t = 0$*, and* $\|\mathbf{r}'(0,\cdot)\|_{\mathbb{R}^3} = 1$*, such that*

$$\begin{aligned}
&\int_0^T \mathbf{a}^f\left(\mathbf{v}^f, p^f; \delta\mathbf{v}^f, \delta p^f\right) - \mathbf{b}^f\left(\delta\mathbf{v}^f\right) + \int_0^L \boldsymbol{\lambda}\boldsymbol{\Pi}\delta\mathbf{v}^f \circ \mathbf{r}^b ds\, dt = 0,\\
&\int_0^T \mathbf{a}^b\left(\boldsymbol{r}^b; \delta\boldsymbol{r}^b\right) - \mathbf{b}^b\left(\delta\boldsymbol{r}^b\right) - \int_0^L \boldsymbol{\lambda}\delta\mathbf{r}^b ds\, dt = 0,\\
&\int_0^T \int_0^L \left(\mathbf{v}^f - \mathbf{v}^b\right)\delta\boldsymbol{\lambda} ds\, dt = 0,
\end{aligned} \tag{3.6}$$

for all $\left(\delta\mathbf{v}^f, \delta p^f, \delta\boldsymbol{r}^b, \delta\boldsymbol{\lambda}\right) \in L^2\left(I, H_0^1(\Omega_f)^3\right) \times L^2(I, \mathcal{V}_p) \times L^2(I, \mathcal{V}_\mathcal{B}) \times L^2(I, \mathcal{V}_\mathcal{B})$.

Here, λ is the Lagrange multiplier. Analogously to the dynamic condition ensuring the continuity of traction, λ can be interpreted as a line load ensuring the equilibrium of forces here. Nevertheless, analogously to [149, 203, 9] the choice of coupling domain as the 1-dimensional beam centerline effectively introduces a singularity into the continuous system of equations. The handling of this singularity in the numerical system and its effect on the numerical behavior has been demonstrated in the author's previous work [75] and will be discussed in Section 3.4.

Remark 3.2 *In general, for embedded finite element methods, the form of an inf-sup stable Lagrange multiplier space depends on the position of the embedded mesh relative to the background mesh [28, 79]. For the case of mixed-dimensional problems, the form of such stable Lagrange multipliers is not yet well-studied. Alternatively, analogous to Nitsche's method for classical equal-dimensional embedded finite element problems [166, 79], stabilized Lagrange multiplier methods can also be applied to mixed-dimensional embedded finite element problems [112, 97]. Here, a mortar penalty regularization approach will be applied to the discrete problem in Section 3.2.2.*

Remark 3.3 *In* (3.6)*,* $\boldsymbol{\Pi}$ *is necessary since the integral over the 1-dimensional curve* Ω_b *is obviously not well-defined for* $\delta\mathbf{v}^f \in H_0^1(\Omega_f)^3$*. In contrast to well-known trace theorems such as [93], which postulate existence of such a trace operator on smooth boundaries of codimension one, existence conditions on the restriction operator* $\boldsymbol{\Pi}$ *in the context of a greater dimensionality gap are not yet well-studied [113]. As one of the first publications addressing the lack of trace-type theorems for mixed-dimensional problems with codimension two, Kuchta et al. [112] show sufficient regularity of such a restriction operator in the context of a mixed-dimensional model problem via averaging over a 3-dimensional domain around the embedded manifold.*

Even though a theoretical analysis of the well-posedness of the continuous problem in weak form would certainly represent a firm basis for further work, a sound theoretical existence and regularity analysis is out of te scope of this thesis. Instead, the choice of the coupling domain will be validated and its challenges illustrated by selected numerical examples in Section 3.4.

3.1.2. Penalty method-based constraint enforcement approach

Analogously to the Lagrange multiplier approach applied above, the kinematic coupling condition (3.2) is imposed weakly via the penalty method and a penalty parameter ϵ. This method comes with the advantage of simplicity of the implementation and, more importantly, robustness with regard to stability, independently of the position of the beam, and the well-known disadvantages such as deterioration of the condition number of the arising system matrix as already stated in Section 2.2.2.

The constraint (3.3) is introduced using a penalty contribution, that scales linearly with respect to the constraint violation, by building the derivatives of an abstract quadratic penalty functional:

$$\frac{\epsilon}{2} \int_0^l \left(\mathbf{\Pi} \boldsymbol{v}^f \circ \mathbf{r} - \mathbf{v}^b \right) \cdot \left(\mathbf{\Pi} \boldsymbol{v}^f \circ \mathbf{r} - \mathbf{v}^b \right) \, \mathrm{d}s. \tag{3.7}$$

This leads to the following full definition of the coupled problem:

Problem 3.4 *Find* $\left(\mathbf{v}^f, p^f, \boldsymbol{\eta}^b\right) \in \mathcal{W}_{\mathcal{F}^v} \times \mathcal{W}_{\mathcal{F}^p} \times \mathcal{W}_{\mathcal{B}}$, *with* $\mathbf{v}^f = \mathbf{v}_0$, $\boldsymbol{\eta}^b = \boldsymbol{\eta}_0$ *a. e. for* $t = 0$, *and* $\|\mathbf{r}'(0, \cdot)\|_{\mathbb{R}^3} = 1$ *a. e. on* $[0, l]$, *such that*

$$\begin{aligned} \int_0^T \mathbf{a}^f \left(\mathbf{v}^f, p^f; \delta\mathbf{v}^f, \delta p^f \right) - \mathbf{b}^f \left(\delta\mathbf{v}^f \right) + \epsilon \int_0^l \left(\mathbf{\Pi} \boldsymbol{v}^f \circ \mathbf{r} - \mathbf{v}^b \right) \cdot \mathbf{\Pi} \delta\mathbf{v}^f \circ \mathbf{r} \, ds \, dt = 0, \\ \int_0^T \mathbf{a}^b \left(\boldsymbol{\eta}^b; \delta\boldsymbol{\eta}^b \right) - \mathbf{b}^b \left(\delta\boldsymbol{\eta}^b \right) - \epsilon \int_0^l \left(\mathbf{\Pi} \boldsymbol{v}^f \circ \mathbf{r} - \mathbf{v}^b \right) \cdot \delta\mathbf{r} \, ds \, dt = 0, \end{aligned} \tag{3.8}$$

for all $\left(\delta\mathbf{v}^f, \delta p^f, \delta\boldsymbol{\eta}^b\right) \in L^2\left(I, H_0^1(\Omega_f)^3\right) \times L^2(I, \mathcal{V}_p) \times L^2(I, \mathcal{V}_{\mathcal{B}})$.

3.2. Discretization & numerical treatment

Within this section, the discretization of the coupling contributions is discussed. As for the single field equations, all spatial discretizations are based on the finite element method. After discretization of both, the 3-dimensional incompressible isothermal Navier-Stokes equations and the beam formulation, two distinct non-matching meshes emerge. The fixed fluid mesh takes on the role of a background mesh. The beam mesh, oriented along the beams' centerlines, is superimposed, leading to the use of an embedded mesh approach. The weak enforcement of the coupling constraint, either by the penalty method or by the use of Lagrange multiplier, leads to the additional contribution of coupling terms. These coupling contributions are collected in coupling matrices $\mathbf{C}_{\mathcal{FF}}$, $\mathbf{C}_{\mathcal{FB}}$, $\mathbf{C}_{\mathcal{BF}}$ and $\mathbf{C}_{\mathcal{BB}}$, where $\mathcal{BB}$ and $\mathcal{FF}$ to denote beam and fluid contributions, respectively, and the mixed subscripts $\mathcal{FB}$ and $\mathcal{BF}$ refer to the mixed coupling contributions. The exact form of these coupling matrices is given in Sections 3.2.1 and 3.2.2, for the the penalty and Lagrange multiplier

case, respectively. In favor of a compact notation the dependencies of the nonlinear matrices are dropped from heron out. However, this change in notation does not change the form, particularly the nonlinearity, of the matrices itself.

In any case, Problems 3.1 and 3.4, both, lead to a monolithic system of the form

$$\left[\begin{array}{ccc} \mathbf{A}_{\mathcal{FF}}+\mathbf{C}_{\mathcal{FF}} & 0 & -\mathbf{C}_{\mathcal{FB}} \\ -\mathbf{C}_{\mathcal{BF}} & \mathbf{A}_{\mathcal{BB}} & \mathbf{C}_{\mathcal{BB}} \end{array}\right]_{n+1} \left[\begin{array}{c} \left(\begin{array}{c} \hat{\mathbf{v}}_h^f \\ \hat{\mathbf{p}}_h^f \end{array}\right) \\ \hat{\boldsymbol{\eta}}_h^b \\ \hat{\mathbf{v}}_h^b\left(\hat{\boldsymbol{\eta}}_h^b\right) \end{array}\right]_{n+1} = \left[\begin{array}{c} \mathbf{f}_h^{\mathcal{F}} \\ \mathbf{f}_h^{\mathcal{B}} \end{array}\right]_{n+1}. \tag{3.9}$$

Remark 3.5 *For the sake of brevity $\mathbf{A}_{\mathcal{FF}}$ is used to represent the entire fluid matrix including stabilization and pressure contributions as introduced in Section 2.6. Since the fluid pressure has no effect on the coupling, the respective terms in the coupling matrices $\mathbf{C}_{\mathcal{FF}}$, and $\mathbf{C}_{\mathcal{BF}}$ default to zero.*

Since the matrix operator (3.9) is rectangular, the system in its current form is not solvable. There are two ways to remedy this problem: i) add an additional constraint to the system, or ii) remove one of the unknowns. The obvious target for either of these strategies are the beam velocity unknowns. For the Generalized-α time integration scheme, i) leads to the addition of the line

$$\left[\begin{array}{cc} 0 & -\dfrac{\gamma}{\beta\Delta t}\mathbf{1} \quad \mathbf{1} \end{array}\right]_{n+1} \left[\begin{array}{c} \left(\begin{array}{c} \hat{\mathbf{v}}_h^f \\ \hat{\mathbf{p}}_h^f \end{array}\right) \\ \hat{\boldsymbol{\eta}}_h^b \\ \hat{\mathbf{v}}_h^b \end{array}\right]_{n+1} = \left[\begin{array}{c} \mathbf{f}_h^{\mathcal{B},n} \end{array}\right]_{n+1}, \tag{3.10}$$

where $\mathbf{f}_h^{\mathcal{B},n} = -\dfrac{\gamma}{\beta\Delta t}\boldsymbol{r}_n - \dfrac{\gamma-\beta}{\beta}\dot{\boldsymbol{r}}_n - \dfrac{\gamma-2\beta}{2\beta}\Delta t\ddot{\boldsymbol{r}}_n$. This line represents a weak enforcement of the time integration scheme.

However, within this thesis the more commonly used strategy ii) will be followed, and the time integration scheme will directly be used to express $\hat{\mathbf{v}}_h^b\left(\hat{\boldsymbol{\eta}}_h^b\right)$ in terms of $\hat{\boldsymbol{\eta}}_h^b$. In that case, (3.9) becomes

$$\begin{aligned} \left[\begin{array}{cc} \mathbf{A}_{\mathcal{FF}}+\mathbf{C}_{\mathcal{FF}} & -\dfrac{\gamma}{\beta\Delta t}\mathbf{C}_{\mathcal{FB}} \\ -\mathbf{C}_{\mathcal{BF}} & \mathbf{A}_{\mathcal{BB}}+\dfrac{\gamma}{\beta\Delta t}\mathbf{C}_{\mathcal{BB}} \end{array}\right]_{n+1} \left[\begin{array}{c} \left(\begin{array}{c} \hat{\mathbf{v}}_h^f \\ \hat{\mathbf{p}}_h^f \end{array}\right) \\ \hat{\boldsymbol{\eta}}_h^b \end{array}\right]_{n+1} \\ = \left[\begin{array}{c} \mathbf{f}_h^{\mathcal{F}} - \mathbf{C}_{\mathcal{FB}}\mathbf{f}_h^{\mathcal{B},n} \\ \mathbf{f}_h^{\mathcal{B}} + \mathbf{C}_{\mathcal{BB}}\mathbf{f}_h^{\mathcal{B},n} \end{array}\right]_{n+1}. \end{aligned} \tag{3.11}$$

(3.11) characterizes the complete monolithic nonlinear system of equations for the FBI problem in dependence of the coupling matrices $\mathbf{C}_{\mathcal{FF}}$, $\mathbf{C}_{\mathcal{FB}}$, $\mathbf{C}_{\mathcal{BF}}$, and $\mathbf{C}_{\mathcal{BB}}$. However, in this thesis a partitioned FSI solution scheme will be used instead. After providing the

exact form of the coupling matrices for the penalty and (regularized) Lagrange multiplier method in Sections 3.2.1 and 3.2.2, respectively, the employed algorithmic strategy to solve this type of nonlinear system of equations in a partitioned manner will be discussed in Section 3.3.

Remark 3.6 *As the present problem is transient, the time discretization for the single fields is also applied to the constraint. Aiming at a temporally consistent exchange of coupling information [130, 95], this leads to a linear combination of the coupling contributions* $\mathbf{C}_{\circ\circ}^{n}$*, evaluated at the old time step* n*, and* $\mathbf{C}_{\circ\circ}^{n+1}$*, at the new time step* $n+1$ *in dependence of the time integration parameters for the employed fluid and structure time integration schemes, respectively. Further information on the algorithmic details will be given in Section 3.3.*

Remark 3.7 *Note that the assumption of relatively small beam radii also extends to the fluid element sizes. The choice of enforcing the fluid-beam coupling on the beam centerline introduces a singularity to* (3.8) *and* (3.6)*. The fluid elements need to be large enough to not be able to resolve this singularity, effectively "smearing" the interface over the volume of the element as is common in classical immersed methods. The exact domain of applicability of the method with respect to the quotient of beam diameter and fluid element size also depends on the properties of the simulated fluid. The influence of the background mesh resolution on the fluid velocity resolution will be studied in section 3.4.*

3.2.1. Penalty-based Gauss-Point-to-Segment coupling approach

To discretize the FBI problem with penalty constraint, Problem 3.4, a GPTS approach, as introduced in Section 2.2 and commonly used in contact mechanics, is used. Here, the constraint equation (3.3) is evaluated at each quadrature point of the beam.

Summarizing the beam element shape functions at node k, including positional shape functions H_k^d and tangential shape functions H_k^t, as H_k, and inserting (2.45) and (2.50) into the coupling contributions introduced in Problem 3.4, leads to the following coupling matrices:

$$\begin{aligned}
\mathbf{C}_{\mathcal{BB}}(k,j) &:= \epsilon \int_0^l H_k H_j \,\mathrm{d}s, \qquad & \mathbf{C}_{\mathcal{FF}}(k,j) &:= \epsilon \int_0^l (N_k \circ \chi)(N_j \circ \chi) \,\mathrm{d}s, \\
\mathbf{C}_{\mathcal{BF}}(k,j) &:= \mathbf{C}_{\mathcal{FB}}(j,k) := \epsilon \int_0^l H_k (N_j \circ \chi) \,\mathrm{d}s.
\end{aligned} \tag{3.12}$$

Here, χ denotes the projection of a point in the parameter space of the beam centerline to the corresponding point in the parameter space of the discretized fluid volume. The projection χ is achieved by computing the current position $\mathbf{r}_h$ at each Gauss point of the discretized beam centerline curve. Thus, the projection χ introduces a hidden dependency on the current deformation of the beam, and adds an additional nonlinearity to the system. The algorithmic treatment of this nonlinearity will be discussed in Section 3.3.

3.2.2. Regularized Lagrange multiplier field & Segment-to-Segment coupling approach

The introduction of a Lagrange multiplier field to enforce the continuity of velocities on the coupling based on Problem 3.1, again, leads to a mixed finite element formulation. Generally, this introduces a constraint on the choice of Lagrange multiplier shape functions Φ_k as they have to adhere to the inf-sup condition. For classical surface-coupled meshes on conforming surfaces and the number of Lagrange multiplier DoFs n^{lm}, a simple choice of such inf-sup stable shape functions to represent the finite element approximation of the Lagrange multipliers

$$\boldsymbol{\lambda}_h^{\text{fbi}} := \sum_{k=1}^{n^{lm}} \Phi_k \hat{\boldsymbol{\lambda}}_h^{\text{fbi},k}, \tag{3.13}$$

is guaranteed by using the same shape functions as for the primal field, leading to the mortar finite element method [202, 153]. For these inf-sup stable Lagrange multipliers, the traditional mortar matrices, as they arise from inserting (3.13) into the coupling constraint in (3.8) and successive integration, look as follows:

$$\begin{aligned} \mathbf{D}(k,j) = \int_0^l \Phi_k H_j \, \mathrm{d}s, \quad \mathbf{M}(k,i) = \int_0^l \Phi_k N_i \circ \chi \, \mathrm{d}s, \\ \text{for} \quad k \in [n^{lm}], j \in [n^b], i \in [n^f]. \end{aligned} \tag{3.14}$$

Again, χ represents the projection of the beam centerline onto its current position in 3-dimensional space. In particular, the sparsity pattern of $\mathbf{M}$ will change as the beams move through the fluid mesh as the set of fluid elements, which contain a beam, will change throughout the simulation. Insertion of all discrete functions into Problem 3.1 directly leads to the following nonlinear system of equations:

$$\begin{bmatrix} \mathbf{A}_{\mathcal{FF}} & 0 & 0 & -\mathbf{M}^T \\ 0 & \mathbf{A}_{\mathcal{BB}} & 0 & \mathbf{D}^T \\ -\mathbf{M} & 0 & \mathbf{D} & 0 \end{bmatrix}_{n+1} \begin{bmatrix} \begin{pmatrix} \hat{\mathbf{v}}_h^f \\ \hat{\mathbf{p}}_h^f \end{pmatrix} \\ \hat{\boldsymbol{\eta}}_h^b \\ \hat{\mathbf{v}}_h^b\left(\hat{\boldsymbol{\eta}}_h^b\right) \\ \hat{\boldsymbol{\lambda}}_h^{\text{fbi}} \end{bmatrix}_{n+1} = \begin{bmatrix} \mathbf{f}_h^{\mathcal{F}} \\ \mathbf{f}_h^{\mathcal{B}} \\ 0 \end{bmatrix}_{n+1}. \tag{3.15}$$

However, in contrast to surface-coupled problems on conforming surfaces, constructing the required inf-sup stable finite elements to guarantee well-posedness of problems arising from immersed methods, particularly mixed-dimensional ones, is a complex task. Instead, the inf-sup condition is circumvented by applying a node-wise penalty regularization after mortar discretization, as for example employed in [207, 154], and a linear relationship between the Lagrange multipliers and the mismatch in velocities is assume. Here, the slope of the linear relationship is given by the penalty parameter ϵ:

$$\hat{\boldsymbol{\lambda}}_h^{\text{fbi}} := \epsilon \left(\mathbf{v}_h^f - \mathbf{v}_h^b \right). \tag{3.16}$$

In contrast to the classical GPTS-based penalty approach in Section 3.2.1, this regularization approach keeps the Lagrange multiplier shape functions to fulfill the coupling in a weak sense, and, consequently, introduce matrix-matrix products into the nonlinear system. The constraint discretization strategy can, thus, be characterized as a STS-based approach. Specifically, the arising system of equations based on the penalty regularization reads

$$\left[\begin{array}{ccc} \mathbf{A}_{\mathcal{FF}} + \epsilon \mathbf{M}^T \boldsymbol{\kappa}^{-1} \mathbf{M} & 0 & -\epsilon \mathbf{M}^T \boldsymbol{\kappa}^{-1} \mathbf{D} \\ -\epsilon \mathbf{D}^T \boldsymbol{\kappa}^{-1} \mathbf{M} & \mathbf{A}_{\mathcal{BB}} & \epsilon \mathbf{D}^T \boldsymbol{\kappa}^{-1} \mathbf{D} \end{array}\right]_{n+1} \left[\begin{array}{c} \left(\begin{array}{c} \hat{\mathbf{v}}_h^f \\ \hat{\mathbf{p}}_h^f \end{array}\right) \\ \hat{\boldsymbol{\eta}}_h^b \\ \hat{\mathbf{v}}_h^b \left(\hat{\boldsymbol{\eta}}_h^b\right) \end{array}\right]_{n+1} = \left[\begin{array}{c} \mathbf{f}_h^{\mathcal{F}} \\ \mathbf{f}_h^{\mathcal{B}} \end{array}\right]_{n+1}. \tag{3.17}$$

Here, the normalization with the matrix

$$\boldsymbol{\kappa}\,(m,m) = \int_0^l \Phi_m \,\mathrm{d}s, \quad m \in [n^{lm}], \tag{3.18}$$

is classically necessary to fulfill simple patch tests, and is used to weigh the penalty force exchanged between the two fields [207]. Thus, for the mortar penalty-type coupling the following coupling matrices are applied:

$$\begin{aligned} \mathbf{C}_{\mathcal{BB}} &:= \epsilon \mathbf{D}^T \boldsymbol{\kappa}^{-1} \mathbf{D}, & \mathbf{C}_{\mathcal{FF}} &:= \epsilon \mathbf{M}^T \boldsymbol{\kappa}^{-1} \mathbf{M}, \\ \mathbf{C}_{\mathcal{BF}} &:= \epsilon \mathbf{D}^T \boldsymbol{\kappa}^{-1} \mathbf{M} & \mathbf{C}_{\mathcal{FB}} &:= \epsilon \mathbf{M}^T \boldsymbol{\kappa}^{-1} \mathbf{D}, \end{aligned} \tag{3.19}$$

Based on these results, the partitioned solution algorithm applied to the general FBI problem will be discussed in Section 3.3.

3.3. Solution algorithm

This section introduces the partitioned algorithm used to solve the interaction problem (3.9) as visualized in Figure 3.2. First, the general partitioning and transfer of coupling variables between the fluid and beam partitions will be discussed in Section 3.3.1. Section 3.3.2 addresses the challenges arising from additional nonlinearities such as the dependence of the coupling matrices on the current state as well as the movement of the fibers relative to the background mesh. Particularly, the application of an acceleration technique to facilitate convergence of the partitioned algorithm will be examined. Finally, the application of two one-way coupled algorithmic variants for the cases of rigid fixed beams and light fibers, respectively, will be discussed.

Within the presented partitioned algorithm, the nonlinear problems arising from the single field equations are solved using a Newton-Raphson algorithm. Furthermore, in order to capture the motion of the beams relative to the background mesh, a search procedure and

successive segmentation to build the coupling matrices has to be performed within every coupling iteration. In particular for large numbers of immersed beams, and in the context of parallel high performance computing, this gives rise to the need for computationally efficient parallel search algorithms to find the current beam position within each step of the algorithm. Here, the parallel search is performed using a binning-based communication between processes, and an octree-based search on each shared-memory unit. This way, all fluid element nodes in a prescribed vicinity of the displaced beam element nodes are found. The segmentation procedure introduced in Section 2.2 is applied to all resulting pairs of intersecting beam and fluid elements. If a valid segment is found within such a pair, its contributions are added to the respective matrices in (3.12). Otherwise, the pair does not contribute to the coupling terms.

The binning strategy represents a geometric partitioning method that is tailored to models where interactions between high numbers of bodies have to be resolved as is commonly the case for the simulation of particle methods [159, 185, 47]. The interested reader is referred to [47] for a more detailed description of the employed binning implementation's advantages and special features.

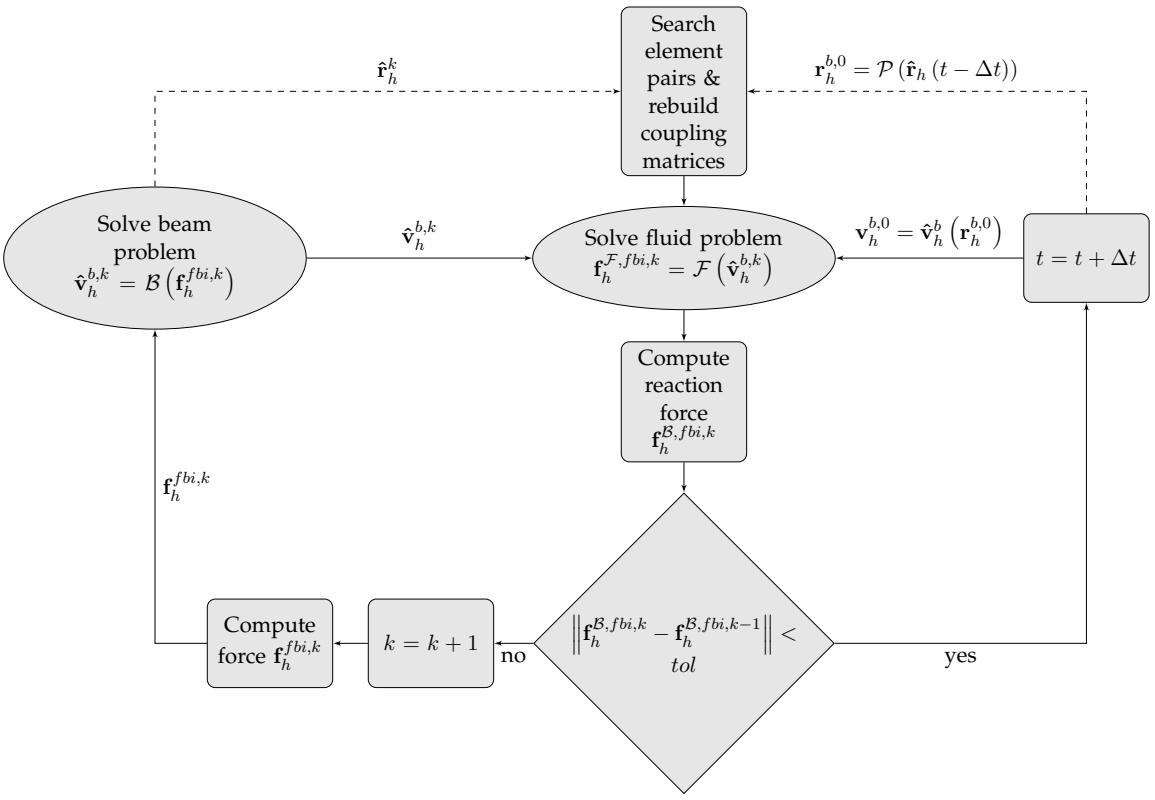

Figure 3.2.: Partitioned algorithm to solve the immersed FBI problem by evaluating the problem $\mathcal{F}\left(\hat{\mathbf{v}}_h^{b,k}\right)$ on the fluid partition, and the problem $\mathcal{B}\left(\mathbf{f}_h^{fbi,k}\right)$ in a staggered manner. At the start of each new time step, a predictor $\mathcal{P}$ is generally applied to the variables of interest.

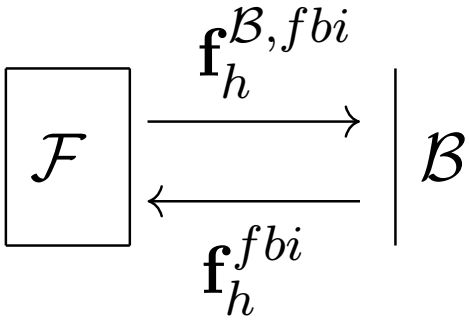

Figure 3.3.: Depiction of the FBI interaction forces between the non-matching geometries of the fluid field $\mathcal{F}$ and the beam field $\mathcal{B}$
. Figure is taken from the author's article [75].

3.3.1. Fluid-beam interaction coupling

As visualized in Figure 3.2, the partitioned algorithm is set up as a Dirichlet-Neumann-type algorithm, where the beam velocity is enforced as a Dirichlet condition on the fluid field, and a Neumann boundary condition is applied to the beam partition. Here, the kinematic constraint is enforced weakly on the fluid partition, resembling partitioned algorithms presented in [45] for two-body contact problems. In the following, the superscript k will be used to denote variables computed in the k^{th} FSI iteration. For the sake of a compact notation, this index will be dropped in equations only involving variables computed within the same FSI iteration.

To enforce the kinematic constraint for a given beam velocity $\hat{\mathbf{v}}_h^b$ in a weak sense on the fluid partition, the first line of the coupled system (3.11), namely

$$(\mathbf{A}_{\mathcal{FF}} + \mathbf{C}_{\mathcal{FF}}) \begin{pmatrix} \hat{\mathbf{v}}_h^f \\ \hat{\mathbf{p}}_h^f \end{pmatrix} = \mathbf{f}_h^{\mathcal{F}} + \mathbf{C}_{\mathcal{FB}} \hat{\mathbf{v}}_h^b, \tag{3.20}$$

is solved. This approach of weak enforcement of the kinematic coupling condition has the advantage that it naturally allows for fulfillment of the divergence condition also close to the immersed beams.

Similarly to the case of classical surface-coupled FSI methods on matching meshes, the interaction force required to attain an equilibrium of forces reads

$$\mathbf{f}_h^{\mathcal{F},fbi} := \mathcal{F}\left(\hat{\mathbf{v}}_h^b\right) := \mathbf{f}_h^{\mathcal{F}} - \mathbf{A}_{\mathcal{FF}} \begin{pmatrix} \hat{\mathbf{v}}_h^f \\ \hat{\mathbf{p}}_h^f \end{pmatrix} = \mathbf{C}_{\mathcal{FB}} \hat{\mathbf{v}}_h^b - \mathbf{C}_{\mathcal{FF}} \begin{pmatrix} \hat{\mathbf{v}}_h^f \\ \hat{\mathbf{p}}_h^f \end{pmatrix}. \tag{3.21}$$

However, in contrast to classical surface-coupled methods, an additional transfer to the beam mesh is required as visualized in Figure 3.3. As a result of the weak constraint enforcement methods, the interaction force required to keep the equations on the beam partition in equilibrium, as it acts on the beam mesh, is stated in the second line of the monolithic system (3.11), and has the form

$$\mathbf{f}_h^{\mathcal{B},fbi} = \mathbf{C}_{\mathcal{BF}} \begin{pmatrix} \hat{\mathbf{v}}_h^f \\ \hat{\mathbf{p}}_h^f \end{pmatrix} - \mathbf{C}_{\mathcal{BB}} \hat{\mathbf{v}}_h^b. \tag{3.22}$$

In the following, this interaction force is used and, in accordance with classical Dirichlet-Neumann algorithms, applied to the beam partition by solving

$$\mathbf{A}_{\mathcal{BB}} \hat{\mathbf{r}}_h = \mathbf{f}_h^{\mathcal{B}} + \mathbf{f}_h^{\mathcal{B},fbi}, \tag{3.23}$$

for a given fluid velocity $\hat{\mathbf{v}}_h^f$. In this form, (3.23) does not explicitly contain the beam velocity $\hat{\mathbf{v}}_h^b$. However, by solving the nonlinear system (3.23) for the the beams' current position vector

$$\hat{\mathbf{r}}_h := \mathbf{A}_{\mathcal{BB}}^{-1} \left(\mathbf{f}_h^{\mathcal{B}} + \mathbf{f}_h^{\mathcal{B},fbi} \right),$$

the current velocity $\hat{\mathbf{v}}_h^b := \hat{\mathbf{v}}_h^b \left(\hat{\mathbf{r}}_h \right)$ can be obtained through the application of a suitable time integration scheme $\mathcal{T}$ such that

$$\mathcal{B} \left(\mathbf{f}_h^{\mathcal{B},fbi} \right) := \mathcal{T} \left(\mathbf{A}_{\mathcal{BB}}^{-1} \left(\mathbf{f}_h^{\mathcal{B}} + \mathbf{f}_h^{\mathcal{B},fbi} \right), \hat{\mathbf{r}}_h \left(t - \Delta t \right), ... \right). \tag{3.24}$$

The beam velocity obtained through application of the time integration scheme can then be passed to the fluid partition for use in the subsequent iteration. In order to assess convergence of the solution, the following stopping criterion is chosen:

$$\left\| \mathbf{f}_h^{\mathcal{B},fbi,k} - \mathbf{f}_h^{\mathcal{B},fbi,k-1} \right\| < tol. \tag{3.25}$$

This completes the weak Dirichlet-Neumann-type algorithm for immersed beams, as sketched in Figure 3.2. However, in the case of highly slender fibers, a simple staggered approach as the one described so far may exhibit convergence problems. The upcoming section addresses this challenge and the choice of convergence acceleration technique.

3.3.2. Acceleration technique

Due to the partitioning, the applied interaction force remains constant during the solution of the structural problem, which leads to a neglect of the change in geometry of the beam, and therefore, the FBI interface. This nonlinearity is, thus, not treated within the Newton solver for the beam system but successively updated through the coupling iterations between the two fields. Especially for very slender and, therefore sensitive, structures this nonlinearity leads to convergence problems of the coupling iterations. Within this work, two different methods are applied to treat the nonlinearity, namely the Aitken relaxation method [92] as a representative of simple fixed-point iteration methods, and a matrix-free Newton Krylov (MFNK) method [106] as a representative of the somewhat more involved Quasi-Newton methods.

3.3.2.1. Aitken relaxation method

The idea behind the Aitken method is to relax the exchanged interface variable, classically the interface displacement, in order to avoid oscillations in the convergence behavior as described in [117]. The amount of relaxation is controlled via the relaxation parameter $\omega \in (0, 1)$, which is recomputed based on the current solution within every coupling step. In [143], a partitioned scheme for immersed shells was recently proposed, in which the relaxation is applied to the beam's acceleration before it is handed to the fluid solver. Motivated by the need to treat the nonlinearity contained in the interaction force applied to the beam, the interaction force is relaxed instead, and the relaxed force $\mathbf{f}_h^{fbi,k} = \omega \mathbf{f}_h^{\mathcal{B},fbi,k} + (1-\omega)\,\mathbf{f}_h^{\mathcal{B},fbi,k-1}$ is applied in the proper place, as visualized in Figure 3.2, instead. See also [116] for another application of a variant of the Aitken method based on force relaxation, and a detailed description of the computation of the relaxation parameter ω.

The computation of the relaxation parameter ω via the Aitken method defaults to a simple vector-vector product, making the method highly efficient with regard to the computational cost of the relaxation parameter. However, even though the Aitken relaxation method works well for many FSI problems, convergence is in general not guaranteed [117].

3.3.2.2. Quasi-Newton Krylov solver

Motivated by the fact that proper treatment of the interface nonlinearity may reduce the number of coupling iterations, a Quasi-Newton scheme is chosen to be applied to the residual

$$\mathbf{r}^{fbi,k} := \mathbf{f}_h^{\mathcal{B},fbi,k} - \mathbf{f}_h^{\mathcal{B},fbi,k-1}. \tag{3.26}$$

This means that the equation

$$\tilde{\mathbf{J}}_{fbi}^{k} \Delta \mathbf{f}_h^{\mathcal{B},fbi,k} = -\mathbf{r}^{fbi,k}, \tag{3.27}$$

is solved. $\tilde{\mathbf{J}}_{fbi}^{k}$ is an approximation of the linearization of (3.26). To solve the linear system in (3.27), a direct or an iterative linear solver can be used. Here, an iterative Krylov solver is applied, as in that case only the effect of the approximated Jacobian on the current residual, i.e. a matrix-vector product, needs to be known instead of the overall matrix. Based on [117], the effect of the sensitivity on a vector $\mathbf{y}$ can be approximated by

$$\tilde{\mathbf{J}}_{fbi}^{k}\mathbf{y} \approx \frac{\mathcal{F}\left(\mathcal{B}\left(\mathbf{f}_h^{\mathcal{B},fbi,k} + \gamma\left(\gamma + \frac{\left|\mathbf{f}_h^{\mathcal{B},fbi,k}\right|}{\mathbf{r}^{fbi,k}}\right)\mathbf{y}\right)\right) - \mathbf{f}_h^{\mathcal{B},fbi,k} - \gamma\left(\gamma + \frac{\left|\mathbf{f}_h^{\mathcal{B},fbi,k}\right|}{\mathbf{r}^{fbi,k}}\right)\mathbf{y} - \mathbf{r}^{fbi,k}}{\gamma\left(\gamma + \frac{\left|\mathbf{f}_h^{\mathcal{B},fbi,k}\right|}{\mathbf{r}^{fbi,k}}\right)}. \tag{3.28}$$

Here, γ is a user-selected parameter determining the finite differencing step size. The effect of the choice of γ will be discussed in detail in Section 3.4.3.2.

Compared to a direct solver, this choice of an iterative solver for (3.28) comes with the drawback that the residual (3.26) will have to be built m times per Quasi-Newton step, where m is the number of iterations of the Krylov solver, as visualized in Figure 3.4. Here, the residual evaluation is quite costly as it involves a full execution of the FBI algorithm presented in Figure 3.2. On the other hand, no full matrix has to be built or stored, and (3.28) can be directly used to approximate the effect of the sensitivity on the residuals, leading to a Matrix-free (Quasi-)Newton Krylov solver based on the Krylov subspace

$$\mathcal{K}_m^{fbi} := \mathbf{f}_h^{\mathcal{B},fbi,0} + \mathcal{K}_m\left(\tilde{\mathbf{J}}_{fbi}^k, \mathbf{r}^{fbi,0}\right). \tag{3.29}$$

For a comprehensive introduction to Krylov subspace methods and more information on linear solvers, the interested reader is referred to the literature, e.g., [21, 165].

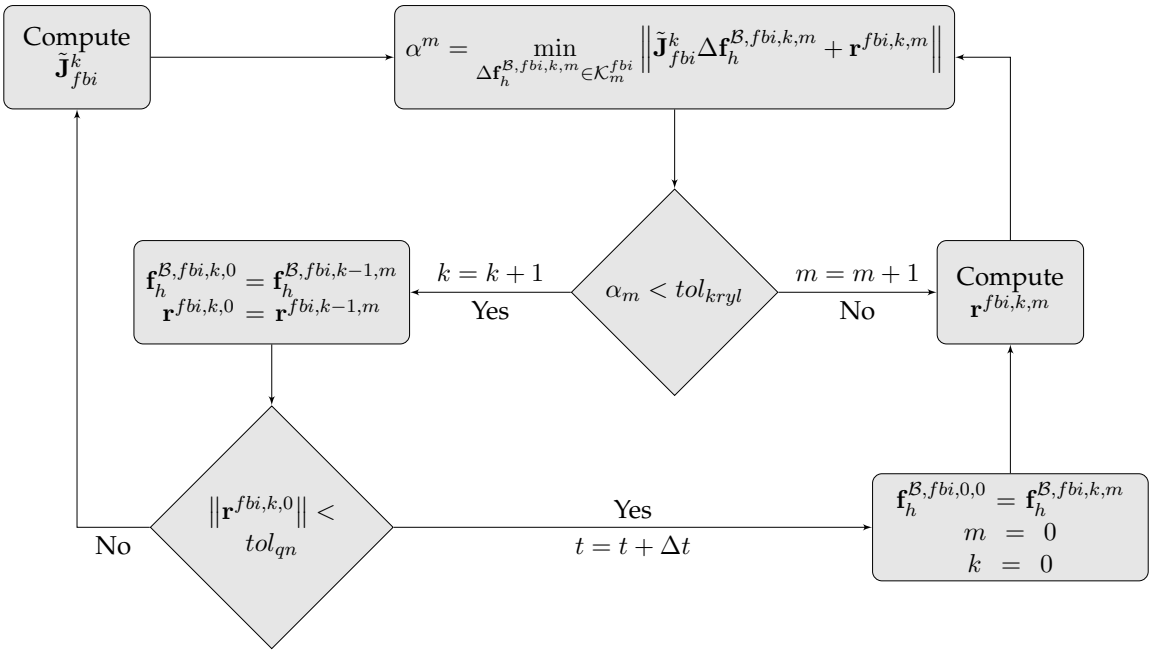

Figure 3.4.: Quasi-Newton Method

3.3.3. One-way coupling schemes

In the extreme cases of very light, flexible fibers and rigid, fixed beams, respectively, the algorithm presented above can be simplified. On the one hand, there exist numerous application scenarios, in which the one-way coupling variants proposed here represent valid models at rather low computational complexity. On the other hand, as will be shown in Section 3.4, this analysis serves as a validation of the different components of the fully two-way coupled fluid-beam interaction algorithm.

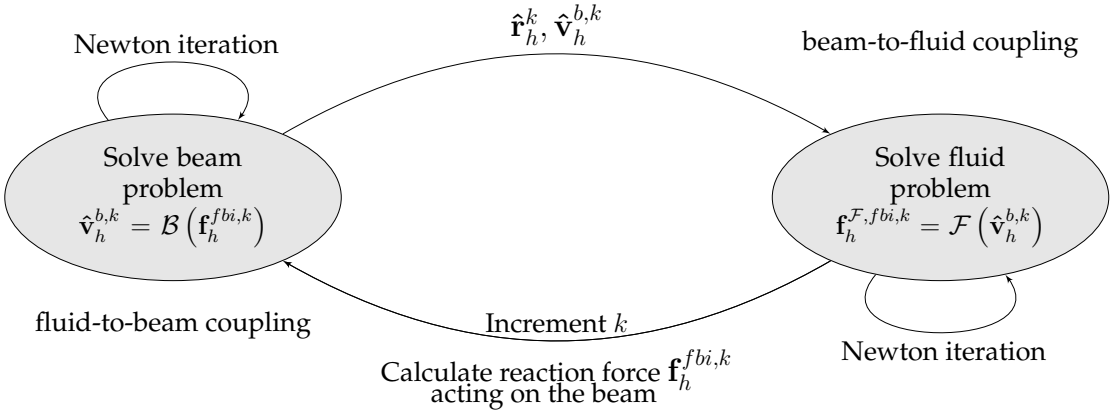

Figure 3.5.: Visualization of the one-way fluid and solid coupling schemes. In the visualization, $\mathcal{B}$, $\mathcal{F}$ represent suitable operators for the solution of the nonlinear beam problem, and for the solution of the nonlinear fluid problem, respectively.

3.3.3.1. One-way coupling for rigid beams

First, the special case of immersed rigid beams is analyzed. Assuming that the effect of the fluid flow on the beam is negligible allows to use a one-way coupling algorithm which only affects the fluid partition. In this coupling variant, the partitioned algorithm will converge after only one iteration leading to a simple staggered algorithm in which each field is only solved once. This one-way coupling scheme will be denoted as beam-to-fluid coupling variant within the remainder of this thesis.

Motivated by classical Dirichlet-Neumann partitioned schemes, where Ω_f acts as Dirichlet and Ω_b as Neumann Partition, the discrete penalty constraint at each time step

$$\mathbf{C}_{\mathcal{F}\mathcal{F}}\mathbf{v}_h^f = \mathbf{C}_{\mathcal{F}\mathcal{B}}\mathbf{v}_h^b, \tag{3.30}$$

is enforced on the fluid partition for a prescribed discrete beam velocity $\mathbf{v}_h^b$. Here, the coupling variable $\mathbf{v}_h^b$ is computed by the beam's time integration scheme. Constraint (3.30) can be interpreted as the weak enforcement of the Dirichlet constraint

$$\mathbf{v}_h^f = \bar{\mathbf{v}}_h^b := \left(\mathbf{C}_{\mathcal{F}\mathcal{F}}\right)^{-1}\mathbf{C}_{\mathcal{F}\mathcal{B}}\mathbf{v}_h^b, \tag{3.31}$$

where $\bar{\mathbf{v}}_h^b$ can be interpreted as the projection of the beam velocity onto the fluid mesh.

3.3.3.2. One-way coupling for light fibers

Conversely, the special case of freely moving, light fibers, for which the effect on the fluid flow can be neglected, is analyzed in the following. Within the remainder of this paper, this one-way coupling scheme will be denoted as the fluid-to-beam coupling variant. Within this coupling variant, generally multiple FSI iterations per time step are necessary to converge towards an equilibrium between the two separate fields.

Once more, motivated by classical Dirichlet-Neumann partitioned schemes, where the fluid domain is treated as Dirichlet partition, while the structure domain takes on the role of the Neumann partition, the coupling condition (3.3) is now applied to the beam in the form of the discrete interaction force

$$\mathbf{f}_h^{\mathcal{B},k+1} := \epsilon \mathbf{C}_{\mathcal{B}\mathcal{B}}^{k+1} \mathbf{v}_h^{b,k+1} - \epsilon \mathbf{C}_{\mathcal{B}\mathcal{F}}^{k+1} \mathbf{v}_h^{k}, \tag{3.32}$$

within every iteration $k+1$ of the partitioned algorithm.

Due to the partitioning, the applied interaction force is constant during the solution of the structure problem, which leads to a neglect of the change in geometry of the beam, and therefore, the FSI interface. This nonlinearity is thus not treated within the Newton solver for the beam system, but successively updated through the coupling iterations. The handling of the kinematic coupling constraint as a Neumann condition within a fixed-point iteration enables a flexible choice of the beam's time integration scheme as compared to a full Newton method, in which the velocity-displacement relationship would enter the linearization of the problem. Nevertheless, to ensure convergence of this one-way coupling scheme, one of the acceleration techniques previously presented in Section 3.3.2 has to be employed.

Remark 3.8 *Even if the assumptions of a perfectly rigid beam might not hold for a given physical setup, the numerical model of the beam-to-fluid coupling variant introduced in Section 3.3.3.1 still represents a physically meaningful and solvable situation. This is not necessarily the case for the fluid-to-beam coupling variant introduced in Section 3.3.3.2: The penalty force does not represent the FSI force in the fluid-to-beam coupling case. Instead, it is simply the scaled negative constraint violation, and should be interpreted as weak enforcement of the Dirichlet constraint* (3.3)*, for which the nonlinearity introduced by the change in geometry is treated by the Aitken relaxation instead of a Newton method. Since the beam is invisible to the fluid field, violation of the assumption of a perfectly soft, freely movable, light fiber may lead not only to unphysically large forces acting on the beam but also to a deterioration of convergence behavior of the given algorithm for large penalty parameters due to the ill-posedness of the underlying continuous problem. It is, thus, paramount to carefully check the modeling assumptions of this one-way coupling variant before considering applying the algorithm. The applicability of the proposed approach under no or even moderate violation of the fluid-to-beam coupling assumptions will be demonstrated in Section 3.4.*

3.4. Numerical examples

The numerical examples within this section are chosen to demonstrate the behavior of the proposed 1D-3D coupling approach and the performance of the presented computational framework in general. If not stated otherwise, all simulations include torsion-free beam elements, and the fluid is assumed to be initially at rest. All models are set up using the pre-processor MeshPy [178], and the simulations are performed with the in-house multi-physics research code BACI [1].

3.4.1. The one-way coupling variants & the Gauss-Point-to-Segment coupling approach

The following numerical examples are chosen to validate the proposed fluid-beam interaction approach in the special cases of very stiff slender bodies and very light fibers, cf. Sections 3.3.3.1 and 3.3.3.2. To this end, this section focuses on the analysis of the basic properties of the one-way coupling cases and the behavior of the 1D-3D coupling approach. Here, the GPTS approach presented in Section 3.2.1 is applied to all regarded examples.

3.4.1.1. Fixed obstacle immersed in a fluid channel

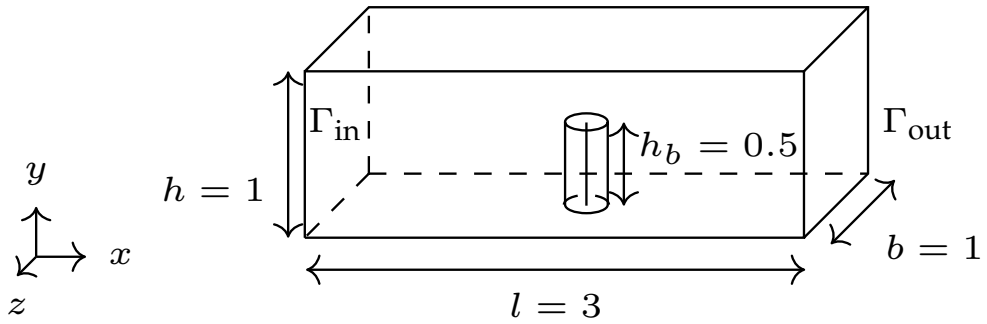

Figure 3.6.: Fixed obstacle immersed in a fluid channel

The purpose of the first example is twofold: its simplicity allows to easily compute the solution of a full 3D simulation to validate the proposed mixed-dimensional coupling approach and to study the convergence behavior of the resulting numerical error with respect to uniform mesh refinement. Secondly, the example is used to illustrate the dependence of the constraint violation within the fluid partition on the chosen penalty parameter. While numerical constraint enforcement via the penalty method is common practice in constrained optimization problems as well as applications such as contact dynamics, a use within computational fluid dynamics as presented within this work is not as common. This novelty warrants a closer look at the effect of this choice of constraint enforcement method.

Figure 3.6 shows the configuration of a fixed obstacle immersed in a mono-directional fluid flow. The time-dependent inflow velocity in x-direction $v_{in} = 0.5 \cdot (1 - \cos(10\pi t))$ for $t \in [0, 0.1]$, and $v_{in} = 1$ for $t > 0.1$, is prescribed on the surface Γ_{in}. On the surface Γ_{out}, a zero-traction condition is applied and perfect-sliding conditions are enforced on all other surfaces. The fixed beam obstacle is placed in the middle of the lower channel surface and is assumed to not be affected by the surrounding fluid. This allows to consider only one-way coupling from the fixed beam onto the fluid. The fluid is assumed to have a density of $\rho_f = 1$ and a dynamic viscosity of $\nu_f = 0.004$. The fluid domain is discretized by $96 \times 32 \times 32$ stabilized 8-noded hexahedral finite elements with equal-order interpolation, and the evolution in time is solved by the Crank-Nicolson method, i.e., the one-step-θ

method with $\theta = 0.5$, with time step size $\Delta t = 10^{-3}$. Note that for the proposed approach therefore neither the radius of the beam obstacle nor its material properties enter the simulation. Instead, only the effect of the applied Dirichlet conditions on the fluid solution in dependence on the penalty parameter is analyzed.

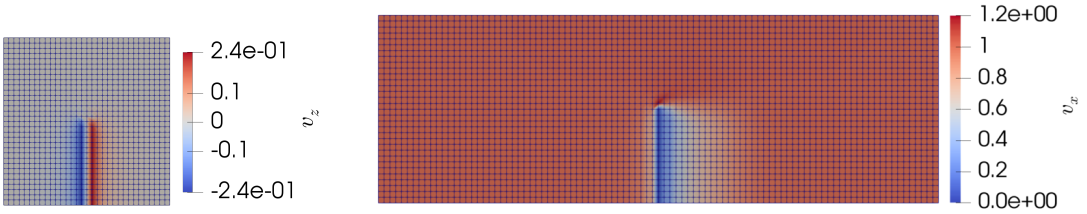

(a) Fluid velocity v_z around the obstacle

(b) Fluid velocity v_x in channel direction in the plane of the fixed obstacle

Figure 3.7.: Visualization of the effect of the obstacle on the fluid velocity in the channel. Figure is taken from the author's article [75].

The obstacle is expected to decelerate the fluid in its vicinity to a resting state, and thereby redirect the fluid flow to the sides and to the top. For a penalty parameter $\epsilon = 10^4$, simulation results illustrating this behavior are shown in Figure 3.7. The deceleration in x-direction as well as the deflection of the flow velocity in z-direction is clearly visible. In the regarded case of a fixed beam, the constraint violation after time step $n + 1$ is measured by calculating the L_2-norm of $\mathbf{K}_{\mathcal{FF}}^{n+1}\mathbf{v}_h^{f,n+1}$. Figure 3.8b shows the dependence of the constraint violation on the penalty parameter steady for the state solution at time $t = 0.5$.

In addition, Figure 3.8a allows a closer look at the L_2-norm of the computed penalty force $\mathbf{f}_h^{\mathcal{F},n+1} = \epsilon\mathbf{K}_{\mathcal{FF}}^{n+1}\mathbf{v}_h^{f,n+1}$ acting on the fluid at time $t = 0.5$. In Section 3.3, it was argued, that this penalty force will take on the amount of force necessary to fulfill the given FBI constraint, and thus can be interpreted as the interface force acting onto the fluid. For this

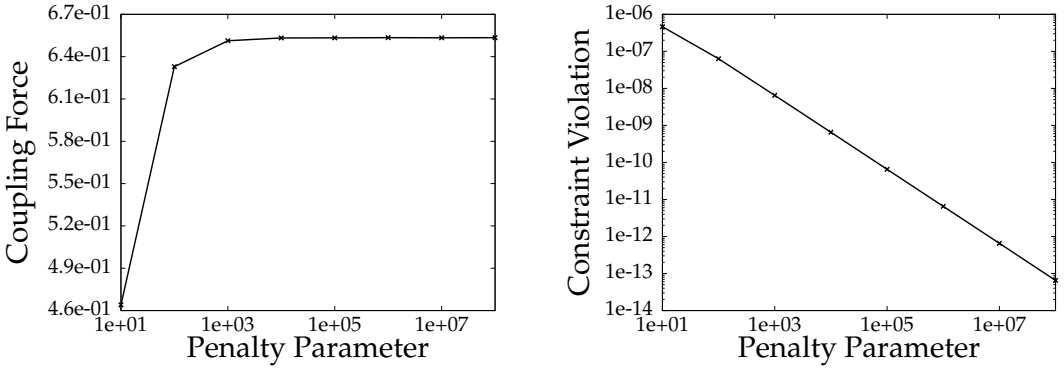

(a) Convergence behavior of the overall coupling force $\mathbf{f}_h^{\mathcal{F}}$

(b) Convergence behavior of the overall constraint violation

Figure 3.8.: Convergence behavior of the overall constraint violation with respect to the penalty parameter at time $t = 0.5$. Figure is taken from the author's article [75].

hypothesis to be valid, the penalty force needs to be practically independent of the chosen value of the penalty parameter, or equivalently, as the penalty parameter increases linear convergence of the constraint violation $\mathbf{K}_{\mathcal{FF}}^{n+1}\mathbf{v}_h^{f,n+1}$ towards zero is expected. Figure 3.8 suggests that both assumptions hold true for sufficiently large values of the penalty parameter. This is also an important basis for further work towards a fully coupled FBI framework, where the position of the beam centerline, and thus the geometry of the coupled problem, as well as the beam velocity, depend on the penalty force.

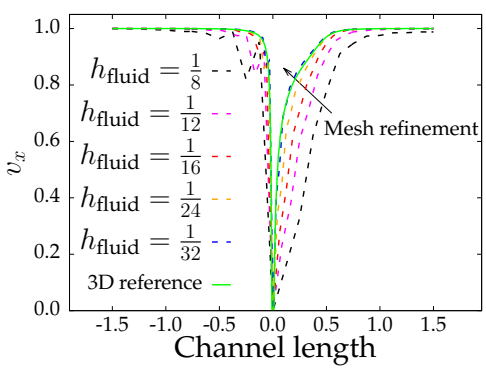

(a) Fluid velocity profile v_x over the channel length for different fluid element sizes h_{fluid} as well as a finely resolved 3D reference solution

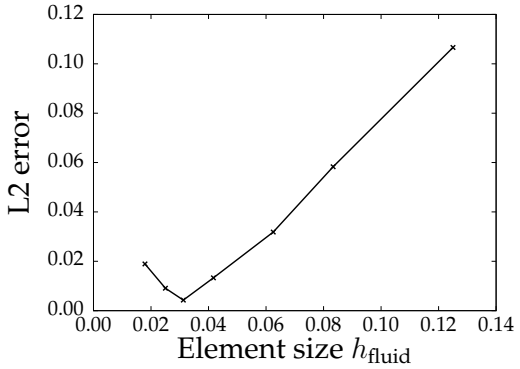

(b) L2 error of the fluid velocity in x-direction over the fluid element size h_{fluid} computed using a 3D CFD solution as reference

Figure 3.9.: Dependence of the fluid velocity on the mesh resolution. Figure is taken from the author's article [75].

Next, the behavior of the 1D-3D coupling solution with respect to the fluid mesh resolution is analyzed. Figure 3.9a shows the space-dependent steady state solution of $\mathbf{v}_x$ along the x-axis for different mesh resolutions. Here, the reference solution is computed using a full 3D CFD simulation, in which the 3-dimensional beam domain is cut out of the fluid domain, and no-slip boundary conditions are enforced on the newly generated beam surface. The fluid field for the reference solution is discretized using $641,928$ DoFs. This 3D reference solution is used to compute the L2 error of the 1-dimensional velocity profile plotted over the fluid element size h_{fluid} shown in Figure 3.9b.

Examining the fluid velocity profile over the channel length plotted in Figure 3.9a, the fluid flow is slowed down by the beam while the flow is undisturbed far from the obstacle, as expected. The kink in the FBI solutions just before the beam stems from the neglect of capturing the exact behavior of the pressure solution at the beam. As investigated by Baaijens in [9], the pressure would exhibit a jump at the beam, which cannot be represented within the discretization space of continuous piece-wise linear functions. Using appropriate discretization spaces allowing for pressure jumps on element boundaries as in [9], or even enhancing the space as in the extended finite element method in [171], can potentially solve this problem. Here, it is deliberately refrained from using such advanced fluid discretizations, since the target of this thesis is the development of an efficient solver for macroscopic effects in FBI, not a fine-scale resolution in the vicinity of the coupling interface. For now, note that refinement of the mesh near the obstacle can smooth these

kinds of kinks.

Further, it becomes evident that the fluid profile computed with the FBI method at a fluid element size of $h_{\text{fluid}} = \frac{1}{32}$ matches the 3D reference solution very well. As a more quantitative analysis, the L2 error of the 1D profiles with respect to the 3D CFD solution is shown in Figure 3.9b. The 1D-3D coupling approach exhibits a linear convergence behavior with respect to uniform mesh refinement, which is expected due to the fact that the beam radius does not enter the simulation, and instead, the area in which the fluid is slowed down is scaled by the fluid element size. This convergence behavior as well as the error values are in line with the results for general academic mixed-dimensional models reported in [112, 118], none of which exceeded linear convergence in the primary variable of the 3-dimensional field. It can also be seen, that for the proposed FBI approach, further mesh refinement of the fluid background mesh will lead to a narrowing of the affected fluid area and, thus, a growing error with respect to the 3D reference solution as evident in Figure 3.9b. This convergence behavior closely resembles the one that has been observed and discussed for a similar approach applied to mixed-dimensional solid-beam coupling in [177]. Such a behavior is to be expected, as the proposed 1D-3D coupling approach is only valid under the assumptions of relatively small beam radii compared to the fluid element size as elaborated in Remark 3.7. For problem setups, in which the model assumptions are violated, no further convergence can be expected and a different modeling technique should be chosen.

In conclusion, this example demonstrates that the FBI solution converges towards the reference solution within a spectrum of fluid element sizes, for which the model assumptions, as discussed in Remark 3.7, are fulfilled. While recovery of optimal convergence for 1D-3D coupling approaches is still a worthwhile topic of ongoing research, the matching of the solutions obtained with mixed-dimensional and fully resolved models satisfies the goals of this work and validates the general applicability of the proposed FBI model.

3.4.1.2. Light fiber in fluid flow

Having analyzed the one-way coupled case of rigid beams affecting fluid flow, this section is meant to investigate the effect of the penalty parameter on the coupling of a light fiber being transported by a fluid.

In this example, the fluid is again assumed to be contained in a hexahedron of dimensions $1 \times 1 \times 3$, as introduced in Section 3.4.1.1. Only now all DoFs in channel direction are set to be free, and a velocity of zero is prescribed in both other directions, leading to a pseudo 1-dimensional setup. In order to analyze the time-dependent behavior of the beam in dependence on the penalty parameter, an oscillatory inflow velocity

$$v_{in} = 0.5 \cdot (1 - \cos(\pi \cdot 10 \cdot t)) \tag{3.33}$$

in channel direction, is prescribed at the channel inlet.

The behavior of an immersed fiber with a density $\rho_b = 1$, a length $l = 0.5$, a cross-sectional area $A = 0.166$, and accordingly a mass of $m = 0.0880$, is regarded. Note that the other

material properties of the beam do not play a role in this example since the fluid flow is set up to be constant along the beam length such that the results can be analyzed as an immersed mass in dependence on the penalty parameter. The time step size is chosen as $\Delta t = 0.01$.

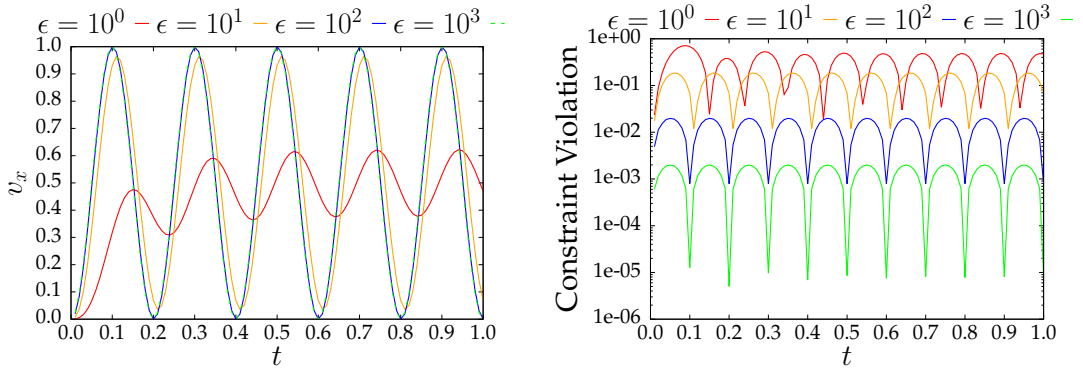

(a) Velocity of a rigid slender body immersed in a fluid channel for an oscillatory fluid inflow profile

(b) Absolute difference between the beam velocity and the prescribed fluid velocity over time

Figure 3.10.: Behavior of an immersed freely moving beam in dependence of the penalty parameter. Figure is taken from the author's article [75].

In the limit case of freely movable light fibers, the fiber is expected to be transported by the fluid exactly at the velocity of the fluid. Figure 3.10a shows velocity results for the beam in dependence on the penalty parameter. As argued in Remark 3.8, within the fluid-to-beam one-way coupling variant, the penalty force is used to introduce a weak Dirichlet constraint into the structure problem. Therefore, as in the case of the beam-to-fluid one-way coupling variant, linear convergence of the coupling violation towards zero is expected for sufficiently large penalty parameters. Figure 3.10b exhibits this expected behavior. This validates the treatment of the geometry-dependence by a fixed-point iteration as proposed in Figure 3.3 instead of a full Newton method.

3.4.1.3. Rotating lattice

After analyzing the behavior of the constraint violation itself, now global effects of slender bodies on fluid flow, as well as the proposed method's robustness under large displacements, are investigated. To this end, a rigid lattice of dimension $1.\bar{6} \times 1.\bar{6}$ made up of beams, as depicted in Figure 3.11a, is immersed in a cylindric tank filled with fluid at rest. The cylinder has a diameter $d = 1$, and a height of 2 in order to encompass the entire beam lattice. Furthermore, all surfaces are modeled with no-slip boundary conditions. The fluid is assumed to have a density $\rho_f = 1.0$, and a dynamic viscosity $\nu_f = 4$, while the beams are again assumed to not be affected by the fluid itself. The lattice starts rotating around the vertical axis of the cylinder as depicted in Figure 3.11b. The movement is described by the rigid body motion

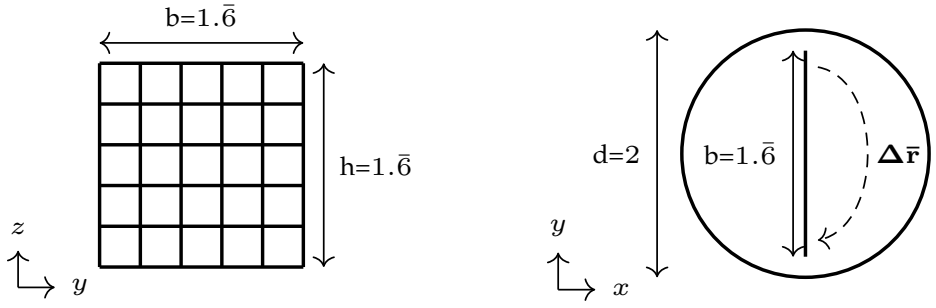

(a) Geometry of the beam lattice

(b) Top view of the immersed lattice

Figure 3.11.: Configuration of the rotating lattice immersed in a cylindrical fluid tank. Figure is taken from the author's article [75].

$$\boldsymbol{\Delta}\bar{\mathbf{r}} = \begin{pmatrix} \cos\left(2 \cdot \pi \cdot \bar{v}\right) \cdot x - \sin\left(2 \cdot \pi \cdot \bar{v}\right) \\ \sin\left(2 \cdot \pi \cdot \bar{v}\right) \cdot x + \cos\left(2 \cdot \pi \cdot \bar{v}\right) \end{pmatrix}, \tag{3.34}$$

with the time-dependent scaling factor $\bar{v} = 0.5 \cdot (1 - \cos(2\pi t))$ for $t \in [0, 0.5]$, and $\bar{v} = 1$ for $t \geq 0.5$. For this example, the time step is chosen as $\Delta t = 10^{-3}$, the evolution in time is discretized with the Backward Euler time stepping scheme, and the FBI constraint is enforced with a penalty parameter of $\epsilon = 100$. The entire fluid domain is discretized with $114,688$ hexahedral finite elements arranged into 64 layers along the height of the cylinder. The fluid mesh is depicted in Figure 3.13a.

It is expected that the beam lattice incites the fluid within the cylinder to start rotating. Herein, the fluid velocity in the vicinity of the beam matches the rigid body motion up to a penalty constraint violation while the velocity further away from the rotator is indirectly accelerated by the surrounding fluid.

Figures 3.12 and 3.13 depict the fluid solution after three quarters of a rotation of the lattice at time $t = 0.837$. Note that in the regarded time step, the velocity of the lattice in x-direction is negligible.

Figure 3.12a shows that the absolute velocity $\|\mathbf{v}\|_2$ follows the lattice structure of the beam geometry. Figure 3.12b offers a closer look at the velocity measured over the cylinder height at coordinates $x = 0.7$ and $y = 0$. It can be seen that the local velocity extrema of the fluid velocity v_y (black line) do not exactly match the beam positions (vertical lines). Instead, the fluid velocity in the vicinity of the beam struts is even a little higher than the prescribed rigid body velocity (blue line). This can be explained by the fact that, within the proposed coupling approach, the fluid solution is not enriched by additional shape functions to model gradient jumps within elements as is the case for extended finite elements as used in [171]. Thus, no sudden change in the fluid velocity within an element can be represented. The local extrema of the flow velocity thus fall to the finite element node closest to the beam, as seen in 3.12b, and lead to a discretization error near the interface, caused by the reduced complexity of the proposed approach.

Figure 3.13b shows the fluid velocity profile v_y, and thus the total velocity, in radial di-

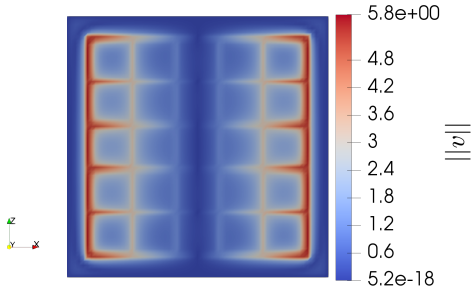

(a) Magnitude of the fluid velocity in the vicinity of the beam lattices induced by the prescribed lattice movement

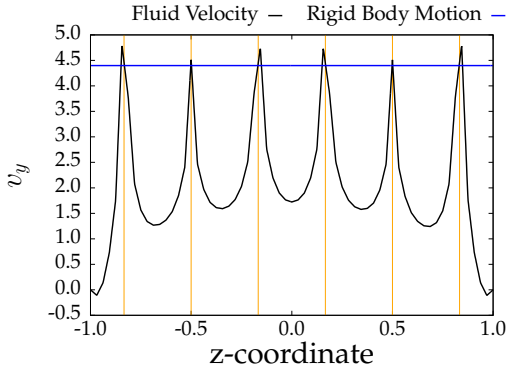

(b) Fluid velocity in y-direction over the lattice height in comparison to the prescribed rigid body motion

Figure 3.12.: Fluid velocity profile induced by the moving beam lattice along the height of the fluid cylinder. Figure is taken from the author's article [75].

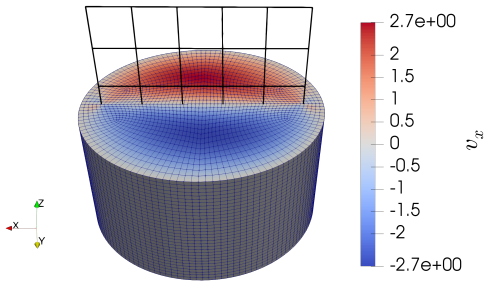

(a) Fluid velocity in x-direction after three quarters of a rotation of the beam lattice

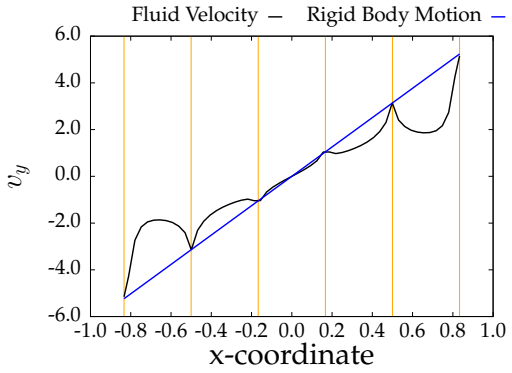

(b) Fluid velocity Magnitude over the beam lattice in radial direction

Figure 3.13.: Fluid velocity profile induced by the moving beam lattice. Figure is taken from the author's article [75].

rection along the x-axis cutting the beam lattice in a top and a bottom half. As expected from a physical point of view, it can be seen that the fluid velocity matches the rotational velocity very closely in the vicinity of the beam lattice while it lags behind within the holes of the mesh. Clearly, the discretization error due to missing enrichments of the underlying discretization space is less pronounced for this case of a less steep evolution of the fluid solution than in Figure 3.12b.

Figure 3.13a shows the fluid mesh, which was traversed via different cut scenarios of the overall beam lattice with the background mesh within each time step, until the presented state was reached. In the present case, the fluid mesh contains $114,688$ fluid elements, while the lattice is discretized using $1,200$ beam elements in order to force the the creation of numerous different integration segments by the segmentation procedure visualized in Figure 2.1. In this case, application of the segmentation procedure leads to the creation of

a number of different integration segments between $1,597$ and $1,940$ for each time step. Here, the exact number of segments for each time step depends on the position of the lattice relative to the background mesh and, thus, varies rather considerably over the course of the simulation due to the large lattice displacement and the numerous different cut scenarios stemming from the unsymmetric meshing of the fluid tank. Therefore, the regarded example also serves as a preliminary validation of the robustness of the applied segmentation procedure discussed in Section 2.2 and illustrated in Figure 2.1 with respect to varying intersection scenarios of the embedded with the background mesh.

3.4.2. Comparison of numerical variants of the fully coupled model

After validating the one-way coupling algorithms and analyzing the effect and limitations of the employed 1D-3D coupling approach in the previous subsection, the motivation of this subsection is the investigation of the influence of the numerical and algorithmic building blocks on the final solution. The influence of numerical parameter such as the constraint enforcement technique and the penalty parameter will be analyzed, and the performance of the proposed methodology for problems with large interface displacements will be demonstrated.

3.4.2.1. Single Elastic Beam

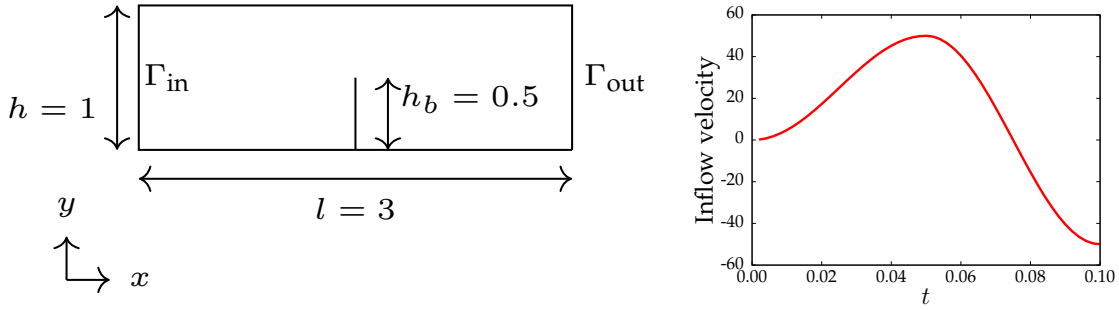

(a) Geometric setup of the quasi-2D example of an immersed elastic beam

(b) Maximum inflow velocity over time

Figure 3.14.: Problem setup for the single elastic beam immersed in a fluid channel

The intention of this example is to visualize the effect of the method's numerical parameters, namely penalty parameter, constraint enforcement technique, and, in the case of the mortar-type approach, Lagrange multiplier shape functions, on the solution of a fluid-beam system exhibiting large beam displacements. For this purpose, the problem is set up as pseudo quasi-2D in order to facilitate large displacements. The geometric setup of the channel and the beam is given in Figure 3.14a. The fluid inflow is prescribed on the left end of the fluid channel as a parabolic flow profile with respect to the channel height, and oscillating in time. The time evolution of the fluid velocity at the middle of the channel height is visualized in Figure 3.14b. inspired by the real physical properties of water, the

fluid has the density $\rho_f = 1$, and the viscosity $\nu_f = 0.004$. The channel has a height of 1, the length is 3, and the depth is 0.06 over two fluid elements. To allow for negative fluid velocities also on the Neumann boundary on the right, backflow boundary conditions, as analyzed in [14], are used. Non-penetration conditions are applied to all other channel surfaces. The immersed beam has a height $h_b = 0.5$, cross-sectional area $A = 10^{-4}$, density $\rho_b = 10$, Young's modulus $E_b = 10^7$, and is modeled using a hyperelastic material. Figure 3.15 illustrated the geometrical configuration as well as the fluid velocity in channel direction at different time snippets for the mortar-type method with linear Lagrange multiplier shape functions and a penalty parameter $\epsilon = 10^4$. The initial configuration can be found in Figure 3.15a. Figure 3.15b demonstrates the beam's deflection to the right, just before the flow direction changes, and Figures 3.15c- 3.15d show the beam's maximum deflection to the other side.

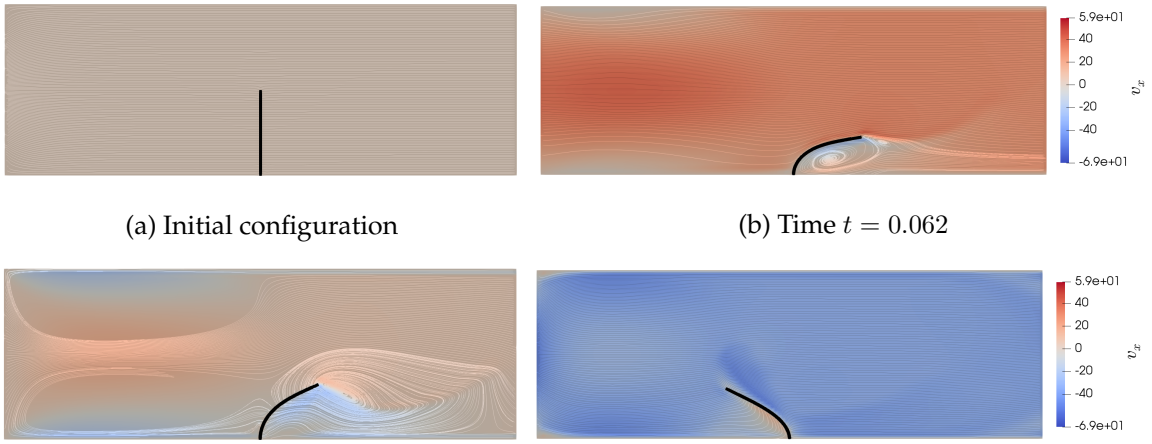

(a) Initial configuration

(b) Time $t = 0.062$

(c) Time $t = 0.074$

(d) Time $t = 0.1$

Figure 3.15.: Velocity solution in channel direction at different time steps

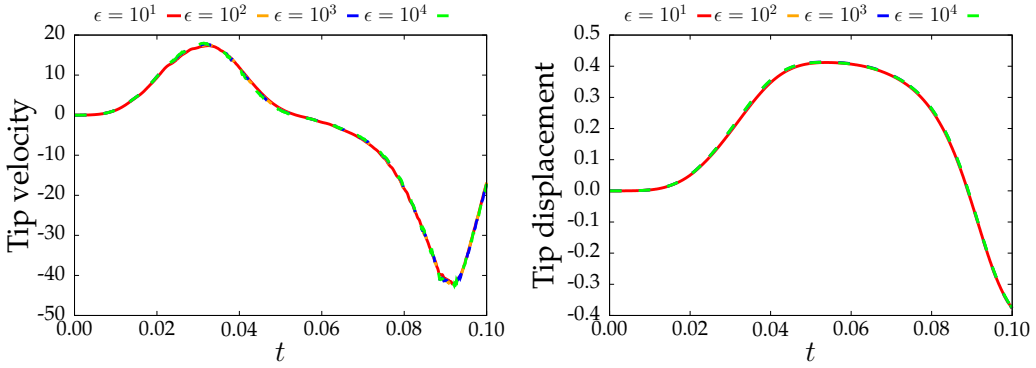

(a) Tip velocity in x-direction

(b) Tip displacement in x-direction

Figure 3.16.: The beam tip's velocity and displacement in x-direction for the mortar-type approach with linear Lagrange multiplier shape functions and different penalty parameter

$\frac{\left\|d^{\text{tip}}_{10^4}(t) - d^{\text{tip}}_{10^1}(t)\right\|_\infty}{\left\|d^{\text{tip}}_{10^4}(t)\right\|_\infty}$	$\frac{\left\|d^{\text{tip}}_{10^4}(t) - d^{\text{tip}}_{10^2}(t)\right\|_\infty}{\left\|d^{\text{tip}}_{10^4}(t)\right\|_\infty}$	$\frac{\left\|d^{\text{tip}}_{10^4}(t) - d^{\text{tip}}_{10^3}(t)\right\|_\infty}{\left\|d^{\text{tip}}_{10^4}(t)\right\|_\infty}$
2.33%	1.23%	0.49%

Table 3.1.: Relative differences in the tip displacement of an immersed elastic beam introduced by the penalty parameter for the mortar-type approach

$\frac{\left\|d^{\text{tip}}_{\text{cub}}(t) - d^{\text{tip}}_{\text{lin}}(t)\right\|_\infty}{\left\|d^{\text{tip}}_{\text{cub}}(t)\right\|_\infty}$	$\frac{\left\|d^{\text{tip}}_{\text{cub}}(t) - d^{\text{tip}}_{\text{quad}}(t)\right\|_\infty}{\left\|d^{\text{tip}}_{\text{cub}}(t)\right\|_\infty}$
0.48%	0.1%

Table 3.2.: Relative differences in the tip displacement of an immersed elastic beam introduced by the Lagrange multiplier shape functions

To analyze the effect of the penalty parameter on the simulation result, Figure 3.16 displays the beam tip velocity and tip displacement for a solution obtained with the mortar-type method and linear Lagrange multiplier shape functions for various penalty parameter values. Figure 3.16 demonstrates that, even for relatively small penalty parameters, the tip velocity as well as tip displacement is adequately captured without large mismatches between the different solutions over the whole duration of the simulation. The maximum relative differences in the tip displacement for low penalty parameters are shown in Table 3.1, using $d^{\text{tip}}_{10^4}$, computed with $\epsilon = 10^4$, as reference solution. As expected, for growing penalty values, this difference becomes smaller, suggesting convergence of the solution with respect to the penalty parameter. Furthermore, for the examined penalty values, the maximum difference stays below 2.5% even for the relatively large displacements and high velocities exhibited by the model problem.

Similarly, Table 3.2 contains the comparison of the tip displacement computed using $\epsilon = 10^2$ and cubic Lagrange multiplier shape functions with the solution for linear and quadratic shape functions. For the analyzed example, the difference introduced by the Lagrange shape functions stays well below 1%.

Analogously, the influence of the penalty parameter on the solution obtained with the GPTS based approach is analyzed in the following. To this purpose, Figure 3.17 shows the beam tip velocity and tip displacement for a solution obtained with linear Lagrange multiplier shape functions for various penalty parameter values. Noteworthy here is the fact that the simulation with the penalty parameter $\epsilon = 10^4$ terminates at time $t = 0.09$ because the iterative linear solver for the fluid field does not converge. Still, comparing the maximum error for solutions obtained for different penalty parameter until this point, shown

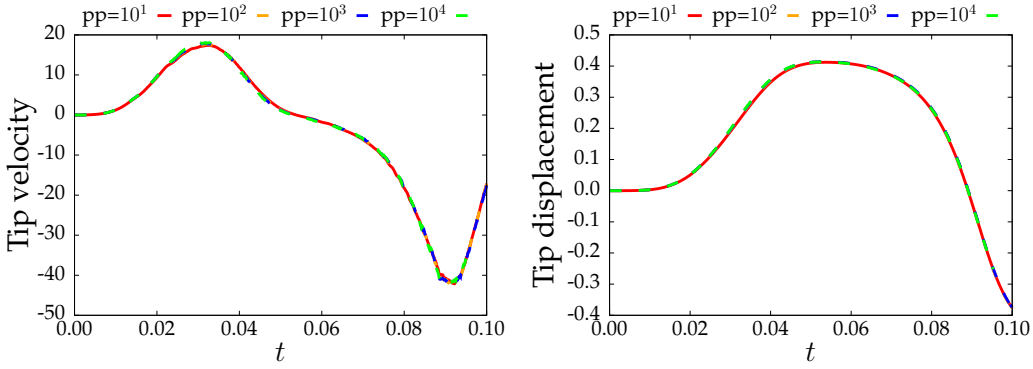

(a) Tip velocity

(b) Tip displacement

Figure 3.17.: Velocity and displacement for the penalty-based GPTS approach with different penalty parameter

$\frac{\left\|d^{\text{tip}}_{10^4}(t) - d^{\text{tip}}_{10^1}(t)\right\|_\infty}{\left\|d^{\text{tip}}_{10^4}(t)\right\|_\infty}$	$\frac{\left\|d^{\text{tip}}_{10^4}(t) - d^{\text{tip}}_{10^2}(t)\right\|_\infty}{\left\|d^{\text{tip}}_{10^4}(t)\right\|_\infty}$	$\frac{\left\|d^{\text{tip}}_{10^4}(t) - d^{\text{tip}}_{10^3}(t)\right\|_\infty}{\left\|d^{\text{tip}}_{10^4}(t)\right\|_\infty}$
2.58%	1.25%	0.79%

Table 3.3.: Relative differences in the tip displacement introduced by the penalty parameter for the GPTS-type approach

in Table 3.3, with the ones for the mortar method reported in Table 3.1, shows a slower convergence behavior. In particular for the difference of the solution obtained with the penalty parameters 10^3 and 10^4 exhibits a dramatical increase of over 50%. Nonetheless, even though not necessarily negligible, all the above reported numerical effects are well within the range of the modeling error reported in [215]. There, a beam based stent model was compared with a continuum mechanics based reference model, and a maximum displacement error of 4% was found.

In conclusion, the represented example exploring the effect of numerical parameter choices on the simulation results shows convergence of the solution with respect to the value of the penalty parameter as well as, in the case of the mortar-type method, the Lagrange multiplier shape functions. Besides convergence, the results for the mortar-type method suggest that also the use of moderate penalty parameters as well as linear Lagrange multiplier shape functions allows to sufficiently capture the overall solution even for large displacements. That constitutes a desirable result as these simple choices ease the solution procedure of the fields' resulting linear systems of equations due to the avoidance of ill-conditioning effects. In contrast, using the GPTS approach, the penalty parameter seems to have a more notable effect on the solution as well as the conditioning of the matrices. The improved robustness of the mortar-type method, compared to the GPTS, motivates the exclusive use of the mortar-type method in Section 3.4.3.

3.4.3. The fully coupled model & the mortar-type coupling approach

After analyzing the performance of the proposed one-way coupling schemes, the following numerical examples are chosen to investigate the performance of the introduced algorithmic building blocks, specifically the mortar-type coupling scheme and the overall Dirichlet-Neumann algorithm. First, the convergence behavior of the fully coupled FBI problem under uniform mesh refinement towards a reference solution, obtained with a fully resolved model, is analyzed. Afterwards, the performance of the employed acceleration methods are investigated. If not stated otherwise, the mortar-type interface discretization and TF beam elements will be applied.

3.4.3.1. Comparison to a 3D reference solution

Within this section, the spatial convergence behavior of the proposed fully-coupled mixed-dimensional method compared to a fully resolved ALE-based FSI approach as presented in [105, 130] is analyzed. To this end, the setup in Section 3.4.1.1 is followed, and a fluid channel with the dimensions $3 \times 1 \times 1$ is examined. An immersed beam of height 0.5, and with radius 0.01, is fixed in the middle of the bottom of the channel as sketched in Figure 3.6. The beam material is modeled using a hyperelastic material with the Young's modulus $E_n = E_s = 5 \cdot 10^9$ and the density $\rho_b = \rho_s = 10^1$ for both, the beam as well as the fully resolved model. Meanwhile, the fluid is modeled as a Newtonian fluid for different densities ρ_f and various constant viscosities ν_f. The simulations are run using the Generalized-α time integration method with a time step size $\Delta t = 10^{-4}$ and a spectral radius $\rho_\infty = 1$ for the structure fields [34], and a One-step-θ method with $\theta = 1.0$ for the fluid field. Within the first 500 steps, the inflow velocity is slowly accelerated until a parabolic inflow profile

$$\mathbf{v}_{in} = 1600 \cdot y \cdot (1 - y) \cdot z \cdot (1 - z)\,, \tag{3.35}$$

is reached. A zero traction boundary condition is prescribed on the outflow boundary and no-slip boundary conditions are enforced on all other sides. The FBI simulations are run with a penalty parameter $\epsilon = 10^4$ and linear Lagrange multiplier shape functions. The fully resolved 3D reference solution, in turn, is simulated with the Lagrange multiplier based ALE approach presented in [130, 105], using 2,183,072 and 10,240 linear hexahedral finite elements for the fluid and beam fields, respectively.

The obtained velocity solution for the FBI example with a fluid element size $\frac{1}{44}$ and the solution of the reference simulation with $\rho_f = 1.0$ and $\nu_f = 0.032$ are depicted in Figure 3.18a.

Figure 3.18b visualizes the relative L2 error of the fluid velocity solution compared to the fully resolved 3D reference solution under uniform mesh refinement and for different fluid material configurations, at time $t = 0.5$. Linear convergence can be observed for coarser meshes, which is in agreement with the results in [75] and Section 3.4.1.1, where linear convergence was recovered for a fixed beam obstacle.

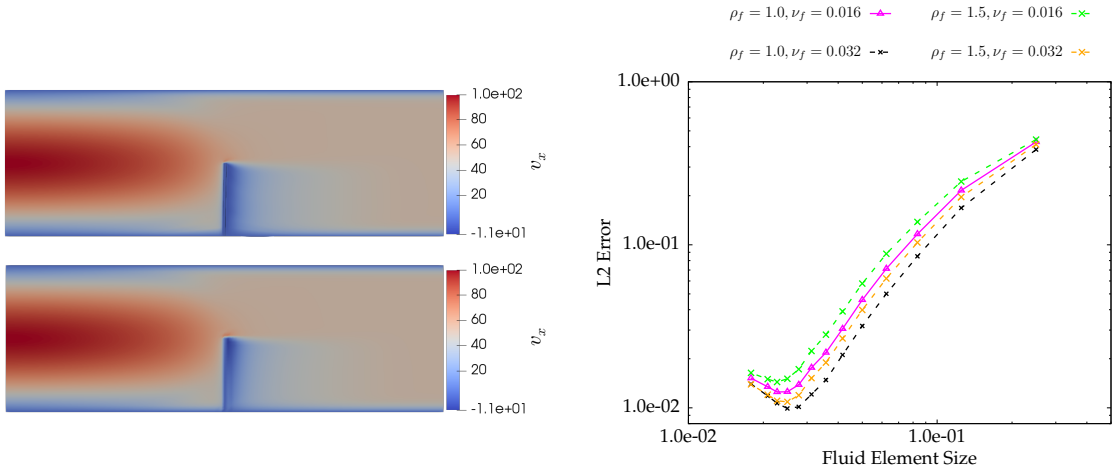

(a) Velocity of the reference solution (top), and the FBI solution with the fluid element size being equal to the beam diameter

(b) Behavior of the relative L2 error of the fluid velocity under uniform mesh refinement for varying Reynolds number

Figure 3.18.: Convergence behavior under uniform mesh refinement

In addition to the spatial discretization error, the shown L2 error contains the modeling difference introduced by using beam theory instead of continuum mechanics. Thus, spatial convergence can only be expected, firstly, as long a the modeling assumptions regarding the beam diameter are fulfilled, and secondly, as long as the error due to the spatial fluid field discretization is larger than the aforementioned modeling error.

While the convergence under uniform mesh refinement is limited by the modeling assumptions, it is important to note that the solution obtained with the presented mixed-dimensional approach converges against the computed 3D reference solution down to a point where the fluid element size nearly matches the beam diameter. In particular, no qualitative dependency of the convergence rate on the fluid material parameters can be observed. The L2-error for the optimum of any of the chosen material parameter sets falls under 1.5% while, at the same time, the mixed-dimensional approach reduces the number of DoFs to a fraction of $\frac{1}{25}$.

While a fully resolved 3D surface-coupled model is still recommended for applications where phenomena near the interface are of interest, this example shows that the solution obtained by the mixed-dimensional method converges against the reference solution and provides a globally matching solution at a fraction of the computational cost, thus validating the proposed methodology in a quire remarkable.

3.4.3.2. Comparison of partitioned solver strategies

Based on the example in Section 3.4.2.1 of an immersed elastic beam, within this example, the behavior of the FSI acceleration techniques in combination with the mortar-type discretization approach is compared. To this end, the setup and material parameters pre-

sented in Section 3.4.2.1 are reused, and the penalty parameter is fixed to $\epsilon = 10^3$. The convergence tolerance for the residuals of the single field equations is set to 10^{-8}, while the same tolerance is used within the nonlinear stopping criterion of the FSI algorithm. The Aitken relaxation technique is compared to the MFNK method with different values of γ. The sensitivity parameter γ influences the approximation quality of the matrix-free Jacobian as well as the input to the FSI operator $\mathcal{F}(B(\cdot))$ to compute the finite differences approximation.

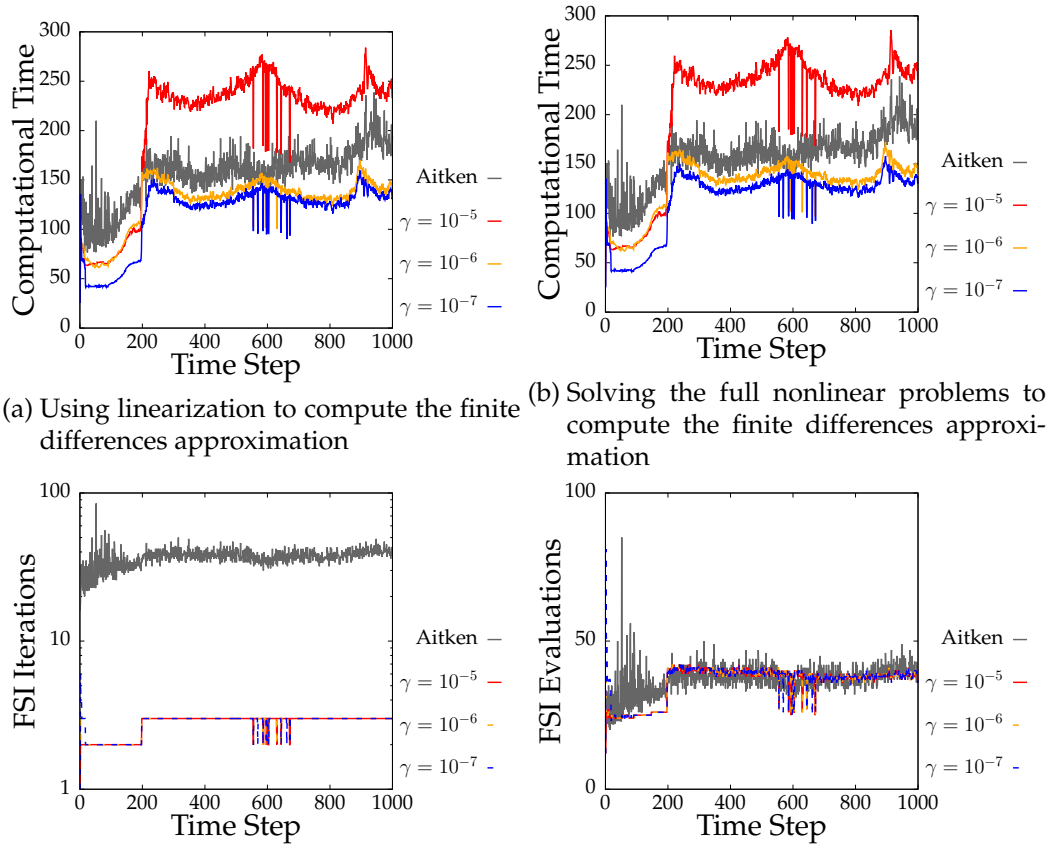

(a) Using linearization to compute the finite differences approximation

(b) Solving the full nonlinear problems to compute the finite differences approximation

(c) Using linearization to compute the finite differences approximation

(d) Number of FSI evaluations when using the linearized single field systems

Figure 3.19.: Analysis of the acceleration techniques

Figures 3.19a and 3.19b show the computational time required for the Aitken relaxation method compared to the MFNK approach with different values of γ. For the values visualized in Figure 3.19a, only the linearized single field equations were solved to compute the finite differences approximation of the Jacobian, while the time measurements for the case where the full nonlinear field equations are solved are depicted in 3.19b. It is notable in the current example that both, linearized and fully nonlinear approaches to approximate the finite differences, yield comparable computing times.

Figures 3.19a and 3.19b reveal that the MFNK solvers solve the considered problem faster than the Aitken relaxation method within the first 200 steps, independently of the used

γ. After 200 steps, the amount of required iterations increases for all MFNK solvers from 2 to 3 iterations. For the MFNK solver, each iteration contains a full Krylov solve and multiple evaluations of the residual (3.26). Therefore, this additional iteration increases the computation time significantly. Afterwards, the speed of the solver highly depends on the value of γ. This is not surprising, as the approximation of the Jacobian becomes better as γ tends to zero. As shown in Figure 3.19d, this is not the main reason for the speedup here, as the number of evaluations of the FSI residuum stays the same. Nevertheless, for each residual evaluation, the force $\mathcal{F}\left(\mathcal{B}\left(\mathbf{f}_h^{\mathcal{B},fbi} + \delta\mathbf{y}\right)\right)$ has to be evaluated. The smaller γ, the smaller the step length $\delta\mathbf{y}$, which can often be beneficial for the iterative linear solver applied to the fluid partition.

Looking at Figure 3.19c, it becomes evident that the MFNK solvers continuously stay below three iterations. The Aitken relaxation method, in contrast, shows large variations in the number of iterations, particularly within the first 200 time steps, where the maximum iteration count is 85.

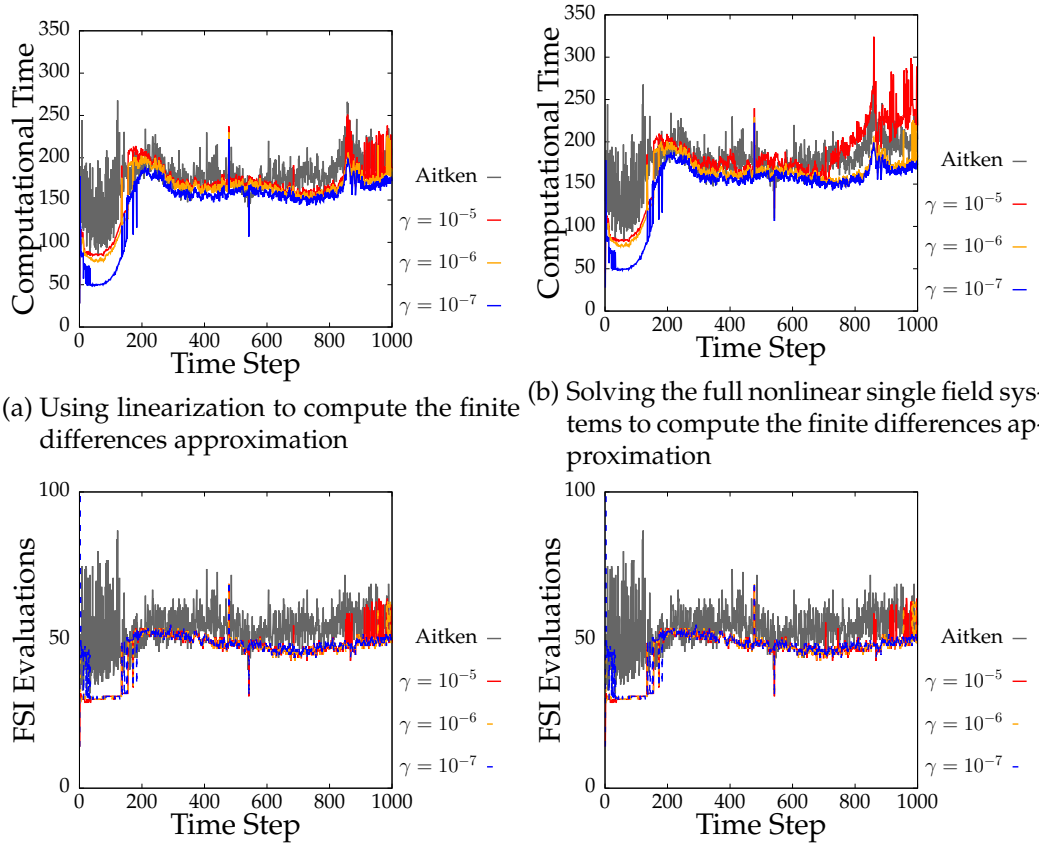

(a) Using linearization to compute the finite differences approximation

(b) Solving the full nonlinear single field systems to compute the finite differences approximation

(c) Number of FSI evaluations when using the linearized single field systems

(d) Number of FSI evaluations when solving the full nonlinear single field systems

Figure 3.20.: Analysis of the acceleration techniques for a light structure

Figure 3.20 visualizes the solver behavior for a variation of the problem above, where the

density of the beam is decreased by a factor of 2. For this somewhat more challenging setup, the typically required number of iterations, and with that the computational time of the Aitken relaxation technique, increases significantly compared to the example with higher density. Here, the MFNK method with any of the considered values for γ exhibits preferable computational times compared to the Aitken method when using the linearized single field equations to compute the finite differences approximation, as depicted in Figure 3.20a. In contrast, Figure 3.20b indicates that, for $\gamma = 10^{-5}$, solving the full single field equations leads to significantly higher computational times within the last 300 steps of the simulation. In any case, Figures 3.20c and 3.20d demonstrate that the number of FSI residuum evaluations required to solve the considered problem using the MFNK method is consistently lower than with the Aitken method, independently of the configuration.

As noted in [117], the Aitken relaxation method is a fairly simple and cheap method that often performs well in accelerating convergence. Nevertheless, choosing good parameters for the MFNK method can still speed up the convergence considerably. It is noteworthy that at least one parameter also has to be chosen for the Aitken relaxation method: the maximum number of allowed iterations until divergence is assumed. As shown in Figures 3.20c and 3.20d, the number of iterations can vary considerably, making this choice particularly difficult but integral for the robustness of the simulation.

3.4.4. Towards biomedical & engineering applications

Finally, the numerical examples within this section are chosen to examine the performance of the computational framework for application-inspired numerical experiments containing more complex geometries, additional nonlinearities in the single fields, and a large number of interacting fibers. In the following, the developed FBI method will be applied to the simulation of an immersed stent geometry and the computational investigation of a submerged vegetation patch containing $3,000$ fibers.

3.4.4.1. Submerged vegetation

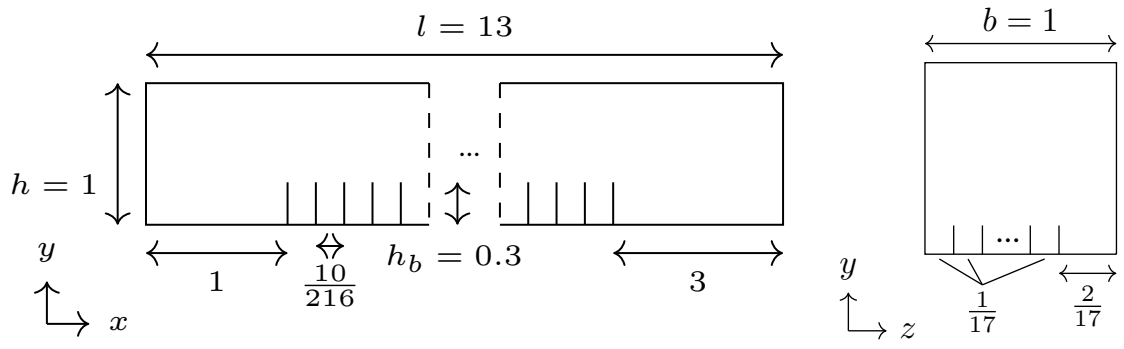

Figure 3.21.: Sketch of the configuration for the submerged vegetation example

Finally, this example serves as an application of the proposed approach to a problem inspired by a real-life research question: the behavior of a submerged vegetation patch and its impact on the coastal flow. Flexible terrestrial and aquatic plant canopies massively affect the flow formation in coastal water regions, and in open fields, as their interaction with the flow around them may lead to shear-layer formation and secondary currents. Additionally, plant canopies in water channels and river banks reduce the velocity and throughput of fluid, and can represent a technical challenge concerning the maintenance of the water supply. Studying and understanding the effect of such submersed vegetation patches is challenging. In [144, 142], these phenomena have been studied experimentally and, in [29, 44, 204], efforts have been made to quantify their effect on the flow around them by analytical solutions to roughness and density variation models. Recent numerical studies of submerged canopies include the analysis of rigid fixed submerged fibers [181, 186], 2D models of fluid flow interacting with submerged rod-like structures, as in [145, 54, 131], as well as immersed, 2D flaps interacting with the 3D flow around it, cf. [192, 193]. Due to the large number of fibers required to model such canopies realistically, the resolution of such setups in 3D poses a challenge regarding the model complexity. Additionally, the two geometrical scales pose an additional challenge concerning the complexity of the problem setup. Commonly, the displacements of the single beams, which in turn contribute to the patch's overall behavior, are significantly smaller than the channel length. Nevertheless, the behavior of flexible immersed canopies leads to highly interesting flow patterns, making it a prime target application for the proposed FBI approach.

As depicted in Figure 3.21, the submerged plant patch is modeled by 225×15 slender beams immersed within a 3-dimensional fluid channel with the dimensions $13 \times 1 \times 1$. The beams have the length $h_b = 0.3$, the radius $r_b = 10^{-2}$, and are modeled using a hyperelastic material with the Young's modulus $E_b = 10^7$ and the density $\rho_b = 10^1$. The beams are fixed to the floor of the channel with equal spacing of $\frac{10}{226}$ in the channel direction, starting at a distance of 1 to the inflow boundary. In the direction of the channel's depth, the beams are also spaced equally at an interval of $\frac{1}{17}$, with a distance of $\frac{1}{17}$ to the left wall and $\frac{2}{17}$ to the right wall. This setup leads to a slightly asymmetric behavior, which facilitates flow orthogonal to the channel's principal flow direction.

The fluid is modeled with the density $\rho_f = 1$, the dynamic viscosity $\nu_f = 0.004$, and a no-slip boundary condition is applied to the bottom surface. Non-penetration conditions are applied to the channel surfaces, and a backflow boundary condition is applied to the outflow. On the inflow boundary, the velocity

$$\mathbf{v}_{in} = 100 \cdot y \cdot (2 - y)\,,$$

is prescribed in channel direction, and the inflow is zero in both other directions.

The fully-coupled FBI method with mortar-type coupling discretization is applied using linear Lagrange shape functions, a penalty parameter $\epsilon = 10^2$, and a time step size $\Delta t = 2 \cdot 10^{-4}$. The fluid field is discretized with 491,520 finite elements yielding 2,095,236 DoFs, and the 3,375 fibers are discretized with 10,125 finite elements resulting in 81,000 DoFs.

Figure 3.22 depicts the solution of the fluid and beam fields at time $t = 0.24$. The effect of the beams' interaction on the fluid flow is illustrated in Figure 3.22a. The fluid is not only

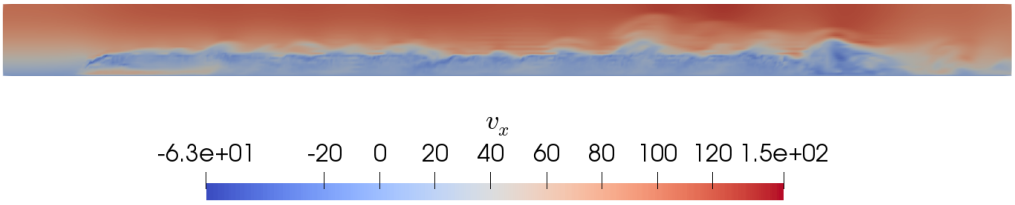

(a) Fluid velocity in channel direction on a slice through the channel's middle

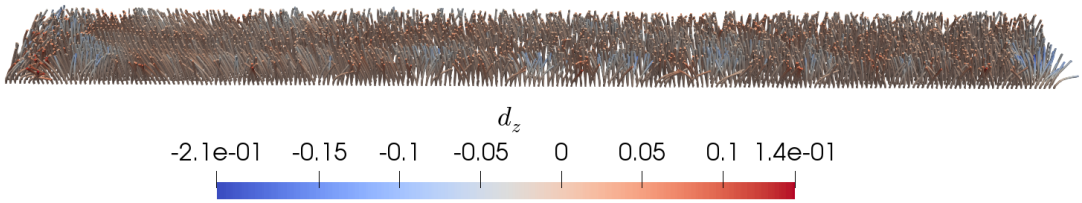

(b) Beam displacement orthogonal to the channel length

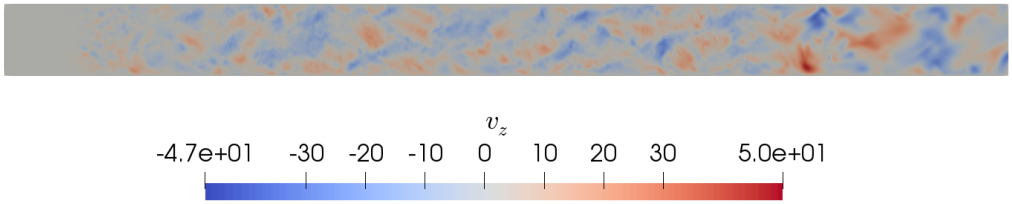

(c) Fluid velocity orthogonal to the principal channel direction at height $y = 0.3$

Figure 3.22.: Solution of the simulation of an immersed canopy

slowed down in the proximity of the fiber patch, but the flexible movement of the beams leads to the formation of monami-type fluid flow as also observed in [193, 144, 145]. As depicted in Figure 3.22b, this phenomenon goes hand in hand with displacement waves traveling through the beam patch. This behavior stems from the asymmetry of the model and the successive formation of fluid waves traveling orthogonal to the channel direction, as visualized for the beam displacement $\mathbf{d}$ in Figure 3.22c, and also observed in [193] for immersed flexible flaps. In contrast to 2D simulations, as reported in [145, 54], phenomena caused by flow orthogonal to the principle channel direction can be observed: the fluid pushes the beams in their wake to the sides, effectively increasing the unobstructed flow area in these regions, which in turn leads to variations in the fluid velocity. In contrast to the upper canopy layer of freely moving beam tips, this behavior does not occur near the ground where the beams are fully fixed. On the contrary, the fixation of the beam near the ground allows the formation of ground flow as hinted at in Figure 3.22a and Figure 3.23a.

The results of the shown example were obtained without the incorporation of beam-to-beam contact. Although an important phenomenon, note that the beams in the considered

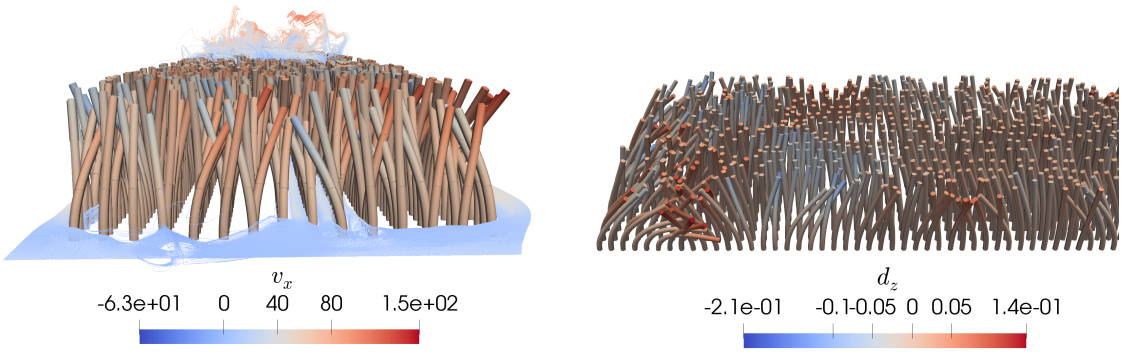

(a) Phenomenon of ground flow (b) Waves orthogonal to principal flow direction

Figure 3.23.: Captured flown features due to the simulation in three dimensions

example are only subjected to forces applied through interaction with the fluid flow. In this case, when using sufficiently large penalty parameters to enforce the FBI conditions, the beams interact implicitly through the fluid flow. Consequently, the impression of direct beam-to-beam interaction is created, as demonstrated in Figure 3.23b. However, a quantitative comparison with the solution of a beam-to-beam scheme such as the ones presented in [133, 136] is in order to assess the validity of the presented model. However, since this thesis focuses on the application of mixed-dimensional methods in the context of stenting procedures, further model extensions for the simulation of submerged vegetation are subject to future research.

As this example constitutes the first time that results of a 3D flexible submersed vegetation patch containing structures with high slenderness with respect to two directions were reported, a quantitative validation of the results is still out of the scope of this thesis. Nevertheless, this example showcases an envisioned target application of the proposed FBI approach and demonstrates its potential compared to alternatives, such as fully resolved or homogenized models, when it comes to the modeling of large amounts of fibers and their consequent interaction phenomena. This has been demonstrated by placing a large number of more than $3,000$ stems into the channel.

3.4.4.2. Immersed stent geometry

This example now addresses the use of the proposed FBI framework in the context of stenting procedures. To study the general applicability of the FBI approach to stenting-inspired examples, particularly to complex stent structures' interaction with fluid flow, the following example of an immersed stent geometry is set up. The material properties are inspired be the parameters reported in [139] for the Taxus Liberté, which is used for stenting of coronary arteries. Nevertheless, since the constitutive beam model is given by a hyperelastic material model, not considering plasticity or pre-stressing, these aforementioned material properties have been adapted such that the fully expanded stent will touch the fluid boundary.

The stent geometry itself, depicted in Figure 3.24a, is based on [5], has an initial radius

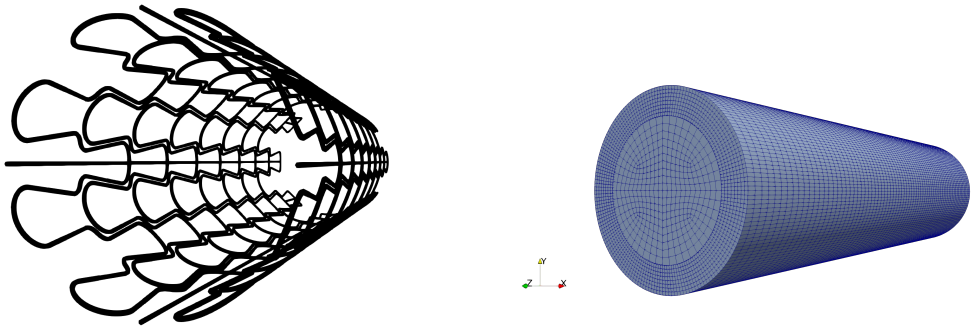

(a) Initial configuration of the beam centerline mesh in form of a stent structure

(b) Start configuration of the stent model problem with fluid at rest

Figure 3.24.: Geometric setup of the model problem of an immersed stent. Figure is taken from the author's article [75].

of $1.25\ \mathrm{mm}$, a length of $13\ \mathrm{mm}$, and is made up of $3,488$ SR beam elements. The beams have a Young's modulus $E_b = 6.2 \cdot 10^{10}\ \frac{\mathrm{g}}{\mathrm{mm} \cdot \mathrm{s}^2}$, a Poisson ratio $\nu_b = 0.3$, and a radius $r = 0.03\ \mathrm{mm}$. Figure 3.24 shows the setup of the model problem, for which the stent is half-way immersed in the fluid domain. The fluid domain consists of $113,800$ fluid elements, has a radius of $1.75\,\mathrm{mm}$, and a length of $15\,\mathrm{mm}$. The density is set to $\rho_f = 0.001\ \frac{\mathrm{g}}{\mathrm{mm}}$, the dynamic viscosity $\gamma_f = 0.003\ \frac{\mathrm{g}}{\mathrm{mm} \cdot \mathrm{s}}$, and the time step size $\Delta t = 0.001\ \mathrm{s}$ is used. The $113,800$ fluid elements are further subdivided into two independent meshes: a coarser inner cylinder mesh with a radius of $1.25\ \mathrm{mm}$ and a finer outer layer as visualized in Figure 3.24b. Both fluid meshes are then coupled using the mortar finite element method for surface coupling with condensed dual Lagrange multiplier shape functions as introduced in [46]. This mesh tying problem within the fluid field represents a rather complex application. This is to show that it is not only possible to include highly nonlinear phenomena within the structure field but that the flexibility of the proposed approach also allows for complex models of the fluid field. For the application at hand, this is especially beneficial since it is a priori known that the stent geometry will only move through the outer fluid layer, and it is expected that its effect on the fluid flow will also be restricted to this part of the fluid domain. Figure 3.25a depicts the initial position of the stent at the edge of the outer fluid mesh layer.

To model the extension of the stent by the balloon, the internal pressure is successively increased from $t = 0\ \mathrm{s}$ to $t = 0.1\ \mathrm{s}$ using the formula

$$\begin{pmatrix} \bar{p} \cdot x \cdot t \\ \bar{p} \cdot y \cdot t \end{pmatrix}. \tag{3.36}$$

For a fully expanded stent geometry, as shown in Figure 3.25b, $\bar{p} = 3.1 \cdot 10^3\ \frac{\mathrm{g}}{\mathrm{mm} \cdot \mathrm{s}^2}$ is used. For simplicity, the fluid is assumed to be at rest and oblivious to the stent for the entire expansion procedure, and the structure is simulated quasi-statically, thus neglecting

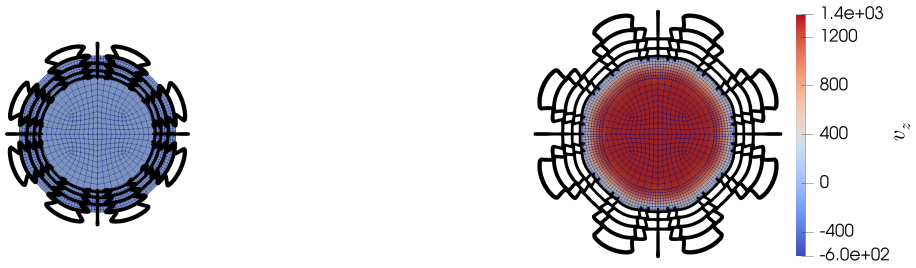

(a) Visualization of the initial position of the stent within the fluid pipe

(b) Effect of the stent on the fluid flow in axial direction

Figure 3.25.: Axial view of the fluid flow within the pipe in $\frac{\text{mm}}{\text{s}}$. Figure is taken from the author's article [75].

its inertia. Once the stent is in place, the spatially constant fluid inflow velocity prescribed at the inlet boundary to the right is ramped up during 50 time steps to a maximum velocity of $1000\ \frac{\text{mm}}{\text{s}}$, while no penetration, free slip boundary conditions are enforced on the cylinder barrel of the fluid domain. The interaction of the fluid with the stent structure is enforced using the beam-to-fluid coupling variant presented in Section 3.3.3.1 in combination with a GPTS coupling approach and the penalty parameter $\epsilon = 10^3$.

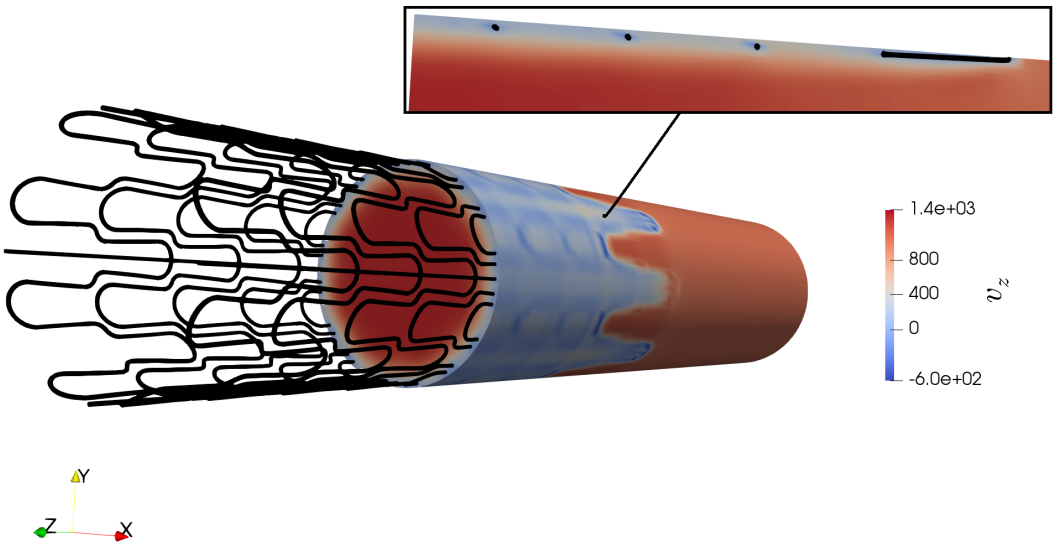

Figure 3.26.: Final configuration of the stent model problem showing the axial velocity in $\frac{\text{mm}}{\text{s}}$ and in a slice through the origin at a 45° angle

Figure 3.26 shows that the current method can capture the roughness introduced by the complex fully expanded stent geometry while considering the structure's material properties and expansion behavior. It is noteworthy that the exact location of stent wires/struts and, thus, the location of the imposed Dirichlet coupling conditions depends on the solution of the nonlinear beam problem modeling the stent and is, therefore, not known a priori as in the other examples. To this end, Figure 3.26 demonstrates that features of the expanded stent geometry translate directly to the fluid flow. The fluid flow far from the stent is unaffected, as expected. On closer inspection of the slice through the origin at a 45° angle, backflow appears in the vicinity of the stent struts (colored in black), while the fluid is partly slowed down in between the cross beams. Also, the expansion procedure leads to larger displacements at the outskirts of the stent system, whereas the stabilizers and cross struts lead to a stiffer behavior far from the axial edges. This effect leads to even more flowback of the fluid near the upstream edge of the stent while a boundary layer of decreased velocity is created downstream, where the stent geometry displays a smaller radial displacement.

Note that this model problem still represents a considerable simplification of the complex interactions present in a stented artery. In particular, the neglect of any vessel wall and corresponding boundary conditions poses an immense change in the dynamics of the system model. Nevertheless, the result serves as a proof of concept for the applicability of the FBI approach to models of stented arteries. Particularly, the example showcases the FBI scheme's ability to capture the effect of established stent models based on 1D beam equations, as proposed in [215, 183, 184], on the flow around it. This represents a sound starting point for extensions to a more complex model in Part III.

4. Fluid-beam-structure interaction

Within this chapter, the FBI approach presented in Chapter 3 is extended to its use on moving meshes and its combination with classical FSI between 3D fields. Even though IBMs have been the focus of research for many years, the literature on IBMs on moving meshes is still rather limited. Some work on this topic was reported in [72], where the movement of bubbles and droplets within a multiphase flow framework is studied. To model the multiphase flow, a level set method in combination with an ALE approach, which is used to improve the quality of the background mesh, is employed to capture the interface between different fluid phases. The mesh is kept completely free in order to follow the movement of various droplets. Additionally, an IBM method is applied to introduce boundaries of the computational domain and to capture the interaction with complex geometries of surrounding structures. The methodology is validated by various 2D examples and by a simulation of the passage of a 3D droplet through a periodically constricting pipe. The combination of Chamira methods with the application of an ALE approach to improve the FSI solution near the boundary is developed in [197, 65]. In this context, Chamira methods are classified as an IBM-type method in the sense that quantities of interest have to be exchanged between a patch and a non-matching background mesh. In [208], an IBM method on a moving mesh in 2D is proposed. The background mesh is moved to fit a structure's boundary and included into the fluid system using an ALE approach. This makes it a one-way coupled FSI approach.

It is noteworthy that this seemingly small change from fixed to moving background meshes fundamentally changes the requirements for the existence of solutions as well as the robustness of the numerical segmentation and search procedures. To the author's best knowledge, this thesis represents the first work on combining a full IBM-type coupling of immersed structures, here beams, with the full FSI coupling in ALE coordinates.

In the following, the combined Fluid-Beam-Structure interaction (FBSI) problem is stated in weak form, the resulting coupled system of equations is presented, and major differences to the pure FBI approach on fixed meshes are pointed out. Finally, the partitioned coupling algorithm applied to solve the problem is illustrated and the approach is validated with a numerical example.

4.1. Governing equations

Here, the overall system of equations is presented. The system does not only contain the fluid and solid fields but also the beams as well as the contributions stemming from interactions of the fluid with the beams, and the solid, respectively. The various components have already been introduced in Sections 2.4, 2.5, 3.1.2, and 2.8. The derivations in this

section, and the example in the upcoming section, are restricted to the GPTS approach introduced in Sections 3.1.2 and 3.2.1. Extension to the mortar penalty-type approach presented in Sections 3.1.2 and 3.2.2 are straight forward though.

The most significant change in comparison to the presented fbi approach developed in Chapter 3 is the fact that the fluid domain is now also time dependent. As presented in Section 2.8.1, the deformation of the fluid domain is governed by the ALE displacement $\boldsymbol{u}^f$, which, in turn, is computed based on the solid field displacement of the FSI interface via the MMPDE, i.e.,

$$\Omega_f = \Omega_f \left(t, \boldsymbol{u}^f \left(\mathbf{u}^s\right)\right). \tag{4.1}$$

As discussed above, this additional nonlinearity not only affects the existence of solutions to the problem, particularly the existence of a restriction operator $\mathbf{\Pi} : H^1 \left(\Omega_f\right)^3 \rightarrow L^2 \left(\Omega_b\right)$ since such a restriction operator now implicitly depends on the MMPDE, but it is also the root of additional algorithmic challenges that are further discussed in Section 4.2.

Combining all components for the FBI problem presented in Section 3.1.2 with the components of the FSI problem introduced in Section 2.8 in a straight-forward manner, the following FBSI system is obtained:

Problem 4.1 *Find* $\left(\mathbf{v}^f, p^f, \boldsymbol{u}^f, \mathbf{u}^s, \boldsymbol{\lambda}^{fsi}, \boldsymbol{\eta}^b\right) \in \mathcal{W}_{\mathcal{F}}^v \times \mathcal{W}_{\mathcal{F}}^p \times \mathcal{W}_{\mathcal{F}}^u \times \mathcal{W}_{\mathcal{S}} \times L^2 \left(I, H^{-\frac{1}{2}} \left(\Gamma_{FSI}\right)^3\right) \times \mathcal{W}_{\mathcal{B}}$, *with* $\mathbf{v}^f = \mathbf{v}_0$, $\mathbf{u}^s = \mathbf{u}_0^s$, $\boldsymbol{u}^f = \boldsymbol{u}_0^f$, $\boldsymbol{\eta}^b = \boldsymbol{\eta}_0$ *a. e. for* $t = 0$, *such that*

$$\begin{aligned}
&\int_0^T \mathbf{a}_{ale}^f \left(\mathbf{v}^f, p^f; \delta\mathbf{v}^f, \delta p^f\right) - \mathbf{b}^f \left(\delta\mathbf{v}^f\right) \\
&\qquad\qquad + \epsilon^{fbi} \int_0^l \left(\mathbf{\Pi}\boldsymbol{v}^f \circ \mathbf{r} - \mathbf{v}^b\right) \cdot \mathbf{\Pi}\delta\mathbf{v}^f \circ \mathbf{r}\, ds\, dt = 0, \\
&\int_0^T \mathbf{a}^s \left(\boldsymbol{r}^b; \delta\boldsymbol{r}^b\right) - \mathbf{b}^s \left(\delta\boldsymbol{r}^b\right) - \left(\boldsymbol{\lambda}^{fsi}, \delta\mathbf{u}^s\right)_{\Gamma_{fsi}} dt = 0, \\
&\int_0^T \mathbf{a}^b \left(\boldsymbol{\eta}^b; \delta\boldsymbol{\eta}^b\right) - \mathbf{b}^b \left(\delta\boldsymbol{\eta}^b\right) - \epsilon^{fbi} \int_0^l \left(\mathbf{\Pi}\boldsymbol{v}^f \circ \mathbf{r} - \mathbf{v}^b\right) \cdot \delta\mathbf{r}\, ds\, dt = 0, \\
&\int_0^T \left(\mathbf{u}^s - \boldsymbol{u}^f, \delta\boldsymbol{\lambda}^{fsi}\right)_{\Gamma_{fsi}} dt = 0 \\
&\int_0^T \mathbf{a}^{mmpde} \left(\boldsymbol{u}^f; \delta\boldsymbol{u}^f\right) + \left(\boldsymbol{\lambda}^{fsi}, \delta\boldsymbol{u}^f\right)_{\Gamma_{fsi}} dt = 0
\end{aligned} \tag{4.2}$$

for all $\left(\delta\mathbf{v}^f, \delta p^f, \delta\boldsymbol{u}^f, \delta\mathbf{u}^s, \delta\boldsymbol{\lambda}^{fsi}, \delta\boldsymbol{\eta}^b\right) \in L^2 \left(I, H_0^1 \left(\Omega_f\right)^3\right) \times L^2 \left(I, \mathcal{V}_p\right) \times L^2 \left(I, H_0^1 \left(\Omega_f\right)^3\right) \times L^2 \left(I, H_0^1 \left(\Omega_s\right)^3\right) \times L^2 \left(I, H^{-\frac{1}{2}} \left(\Gamma_{fsi}\right)^3\right) \times L^2 \left(I, \mathcal{V}_{\mathcal{B}}\right)$.

Here, all semi-linear and linear forms as well as all related quantities take the same form as presented in Sections 3.1.2 and 2.8. In the following, additional superscripts are introduced to highlight the interaction type of the constraint enforcement related quantities and matrices. This implies a change in notation for the FBI penalty parameter ϵ^{fbi} and the matrices $\mathbf{C}_{\mathcal{FF}}^{fbi}$, $\mathbf{C}_{\mathcal{FB}}^{fbi}$, $\mathbf{C}_{\mathcal{BF}}^{fbi}$, and $\mathbf{C}_{\mathcal{BB}}^{fbi}$ presented in Section 3.2.1 for FBI coupling.

4.2. Numerics & algorithmic aspects

After the derivation of the nonlinear system, the discretized nonlinear system of equations is presented, and alterations to the coupling algorithm in order to include the additional interactions between the fluid and solid fields are made.

As already pointed out in the previous section, the main difference compared to the nonlinear system for pure FBI is the introduction of a deformable ALE fluid domain. This results in the need for the beams to be coupled to a moving background mesh, for which its movement is governed by the MMPDE based on the solid field displacement. In turn, the projection χ, which was introduced in Section 3.2.1 for the integration of the FBI coupling matrices, no longer just depends on the movement of the beam centerline but also on the movement of the fluid mesh relative to the centerline. This results in an additional dependence of the FBI coupling matrices $\mathbf{C}_{\mathcal{FF}}^{fbi}$ and $\mathbf{C}_{\mathcal{FB}}^{fbi}$ on the fluid mesh displacement $\hat{\boldsymbol{u}}_h^f$.

Under consideration of the already defined coupling as well as single field matrices, spatial discretization by the FEM and numerical integration straightforwardly leads to the following discrete nonlinear system of equations:

$$\mathbf{A}^{fbsi}\left(\hat{\mathbf{v}}_h^f, \hat{\boldsymbol{u}}_h^f, \hat{\boldsymbol{\eta}}_h^b, \hat{\mathbf{u}}_h^s\right)\mathbf{x}^{fbsi} = \mathbf{f}^{fbsi}, \tag{4.3}$$

where the vector of unknowns for the fbsi system $\mathbf{x}^{fbsi}$ and the right hand side $\mathbf{f}^{fbsi}$ are given as

$$\mathbf{x}^{fbsi} := \begin{bmatrix} \begin{pmatrix} \hat{\mathbf{v}}_h^f \\ \hat{\mathbf{p}}_h^f \end{pmatrix} \\ \hat{\boldsymbol{u}}_h^f \\ \hat{\boldsymbol{\eta}}_h^b \\ \hat{\mathbf{u}}_h^s \\ \hat{\boldsymbol{\lambda}}^{fsi} \end{bmatrix}_{n+1}, \qquad \mathbf{f}^{fbsi} := \begin{bmatrix} \mathbf{f}_h^{\mathcal{F}} - \mathbf{C}_{\mathcal{FB}}^{fbi}\left(\hat{\mathbf{r}}_h, \boldsymbol{u}^f\right)\mathbf{f}_h^{\mathcal{B},n} \\ -\mathbf{f}_h^{\mathcal{AF}} \\ \mathbf{f}_h^{\mathcal{B}} + \mathbf{C}_{\mathcal{BB}}^{fbi}\left(\hat{\mathbf{r}}_h, \boldsymbol{u}^f\right)\mathbf{f}_h^{\mathcal{B},n} \\ \mathbf{f}_h^{\mathcal{S}} \\ -\mathbf{f}_h^{\Lambda\mathcal{F}} \end{bmatrix}_{n+1}. \tag{4.4}$$

Furthermore, the highly nonlinear monolithic system of equations for the FBSI coupling is given by:

$$\mathbf{A}^{fbsi}\left(\hat{\mathbf{v}}_h^f, \hat{\boldsymbol{u}}_h^f, \hat{\boldsymbol{\eta}}_h^b, \hat{\mathbf{u}}_h^s\right) :=$$

$$\begin{bmatrix} \mathbf{A}_{\mathcal{FF}}^{ale}\left(\hat{\boldsymbol{u}}_h^f\right) + \mathbf{C}_{\mathcal{FF}}^{fbi}\left(\hat{\mathbf{r}}_h, \hat{\boldsymbol{u}}_h^f\right) & 0 & -\frac{\gamma}{\beta\Delta t}\mathbf{C}_{\mathcal{FB}}^{fbi}\left(\hat{\mathbf{r}}_h, \hat{\boldsymbol{u}}_h^f\right) & 0 & 0 \\ 0 & \mathbf{A}_{\mathcal{AA}} & 0 & 0 & -\left(\mathbf{D}^{fsi}\right)^T \\ -\mathbf{C}_{\mathcal{BF}}^{fbi}\left(\hat{\mathbf{r}}_h, \hat{\boldsymbol{u}}_h^f\right) & 0 & \mathbf{A}_{\mathcal{BB}} + \frac{\gamma}{\beta\Delta t}\mathbf{C}_{\mathcal{BB}}^{fbi} & 0 & 0 \\ 0 & 0 & 0 & \mathbf{A}_{\mathcal{SS}} & \left(\mathbf{M}^{fsi}\right)^T \\ 0 & -\tau_{\mathcal{AF}}\mathbf{D}^{fsi} & 0 & \mathbf{M}^{fsi} & 0 \end{bmatrix}_{n+1} \tag{4.5}$$

Here, dependencies of the nonlinear operators on coupling quantities, i.e., the solution to other blocks, is highlighted while dependencies of $\mathbf{A}_{\mathcal{FF}}^{ale}$, $\mathbf{A}_{\mathcal{BB}}$, and $\mathbf{A}_{\mathcal{SS}}$, that are unrelated to the coupling of any fields, are dropped for the sake of brevity.

Due to the newly introduced additional interactions and nonlinearities, a specially tailored solution procedure is necessary to solve (4.3). Figure 4.1 illustrates the resulting partitioned FBSI algorithm. The monolithic system (4.3) is partitioned into three distinct solution procedures: the fluid partition, the structure partition containing the beam as well

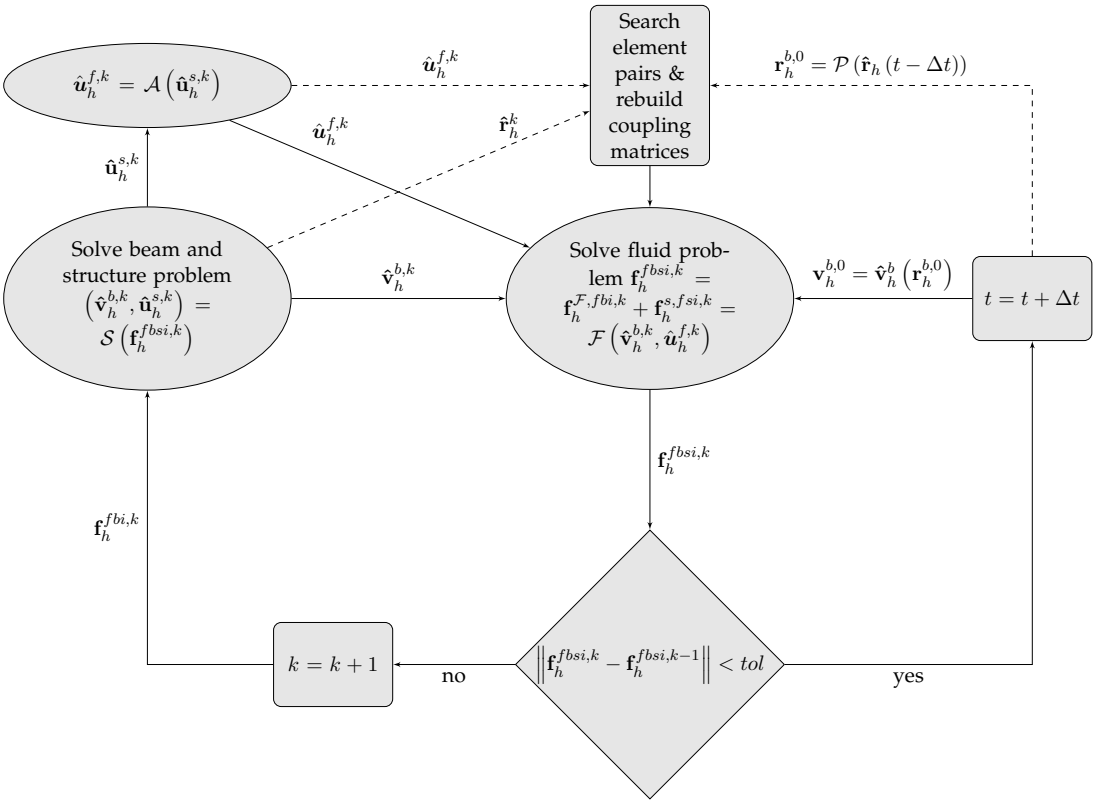

Figure 4.1.: Schematic of the Fluid-Beam-Structure Interaction Algorithm

as the solid systems, and the MMPDE. In the following, the problem to be solved for each of these partitions as well as their dependence on solution variables of other partitions are briefly recounted, and differences to the algorithm presented in Section 3.3 for the pure FBI problem are highlighted. As in Section 3.3, the superscript k is used to denote variables computed in the k^{th} FSI iteration. For the sake of a compact notation, this superscript is dropped where appropriate.

In contrast to Section 3.3, the fluid solution operator $\mathcal{F}$ now contains a dependency on the fluid mesh displacement $\hat{\boldsymbol{u}}_h^f$ in addition to its dependency on the beam velocity $\hat{\mathbf{v}}_h^b$. For the fluid partition, the first row of (4.3) is solved for the fluid state

$$\begin{pmatrix} \hat{\mathbf{v}}_h^f \\ \hat{\mathbf{p}}_h^f \end{pmatrix},$$

given a known beam velocity $\hat{\mathbf{v}}_h^b$ and the mesh displacement $\hat{\boldsymbol{u}}_h^f$. With the resulting fluid state, the forces acting on the beam and the FSI interface can be computed as introduced in Sections 3.3 and 2.8, respectively. Specifically, the interaction forces can be obtained as

$$\mathbf{f}_h^{s,fsi} := \boldsymbol{M}_{fsi}^T \hat{\boldsymbol{\lambda}}^{fsi}, \tag{4.6}$$

and

$$\mathbf{f}_h^{\mathcal{B},fbi} := \mathbf{C}_{\mathcal{B}\mathcal{F}} \begin{pmatrix} \hat{\mathbf{v}}_h^f \\ \hat{\mathbf{p}}_h^f \end{pmatrix} - \mathbf{C}_{\mathcal{B}\mathcal{B}} \hat{\mathbf{v}}_h^b, \tag{4.7}$$

and can be added up to recover the overall interaction force

$$\mathbf{f}_h^{fbsi} := \mathbf{f}_h^{\mathcal{B},fbi} + \mathbf{f}_h^{s,fsi}. \tag{4.8}$$

On the structure partition, the 3^{rd} and 4^{th} row of (4.3) is solved for $\hat{\boldsymbol{\eta}}_h^b$ and $\hat{\mathbf{u}}_h^s$, assuming a given interaction pressure $\hat{\boldsymbol{\lambda}}^{fsi}$ and fluid state

$$\begin{pmatrix} \hat{\mathbf{v}}_h^f \\ \hat{\mathbf{p}}_h^f \end{pmatrix}.$$

Specifically, the solid and beam equations are solved after applying the interaction force $\mathbf{f}_h^{fbsi,k}$ to the overall structure partition. From the solution $(\hat{\mathbf{r}}_h, \hat{\mathbf{u}}_h^s)$ of the structure partition, the input for the next steps can now be obtained. Namely, by application of a suitable time integration scheme $\mathcal{T}$, the beam velocity can be defined as

$$\hat{\mathbf{v}}_h^b := \mathcal{T}\left(\hat{\mathbf{r}}_h, \hat{\mathbf{r}}_h\left(t - \Delta t\right), ...\right), \tag{4.9}$$

and subsequently handed to the fluid partition. For inclusion of FSI, the mesh motion $\hat{\boldsymbol{u}}_h^f$ based on the restriction of the solid displacement to the FSI interface, $\hat{\mathbf{u}}_h^s|_{\Gamma_{fsi}}$, has to be computed. To do so, the MMPDE in the second row of (4.3) is solved. Instead of explicitly handing the Lagrange multiplier field $\hat{\boldsymbol{\lambda}}^{fsi}$ to the MMPDE, a condensed form of the

system, as presented in [130, 105], is used, and the projection of the restriction to the FSI interface of solid displacement is directly prescribed as Dirichlet boundary condition onto the MMPDE, i.e.

$$\hat{\boldsymbol{u}}_h^f\Big|_{\Gamma_{fsi}} := \boldsymbol{D}_{fsi}^{-1}\boldsymbol{M}_{fsi}\hat{\mathbf{u}}_h^s\Big|_{\Gamma_{fsi}}. \tag{4.10}$$

With that, the mesh motion solution $\hat{\boldsymbol{u}}_h^f$ can be extended to the fluid mesh, and subsequently used to compute the FBI coupling matrices. Both, the mesh motion solution $\hat{\boldsymbol{u}}_h^f$ and the FBI coupling matrices, can then be handed to the fluid partition again. In the presented algorithm, this loop of solving the three partitions is repeated until the change of the overall interaction force falls under a user-specified tolerance tol, i.e.

$$\left\|\mathbf{f}_h^{fbsi,k} - \mathbf{f}_h^{fbsi,k-1}\right\| = \left\|\mathbf{f}_h^{\mathcal{B},fbi,k} - \mathbf{f}_h^{\mathcal{B},fbi,k-1} + \mathbf{f}_h^{s,fsi,k} - \mathbf{f}_h^{s,fsi,k-1}\right\| < \text{tol}. \tag{4.11}$$

Note that the MFNK solver illustrated in Figure 3.4 can directly be applied to the overall interaction residual $\mathbf{f}_h^{fbsi,k} - \mathbf{f}_h^{fbsi,k-1}$ as described in Section 3.3.2.

Remark 4.2 *Note that* (4.3) *does not take interactions between the solid field and the beams into account. For simplicity, this special case is not taken into account by the notation in* (4.3)*. However, the overall methodology, as well as the algorithmic solution procedure presented here, can be easily applied to problems which take such contribution of potential interactions into account. The inclusion of interactions between the solid field and the beams is further discussed in Sections 4.3 and 5.1.1, and the presented algorithm is applied to a example containing such interactions in Chapter 7.*

4.3. Numerical example

Figure 4.2.: Geometrical setup of the FBSI model problem

As a proof of concept, the described FBSI algorithm is validated by its application to a numerical example. The following example is inspired by the opening and closing of a heart valve. Heart valves are usually made up of several leaflets which do not only interact with the fluid but their dynamics are greatly influenced by contact interactions between the

leaflets. Particularly the valves closing blocks blood from flowing back, thereby allowing for blood to be pumped from one heart chamber to the other. This behavior is not captured by the example presented here. However, the numerical experiment is sufficient to showcase a first use case of the developed FBI method on moving meshes and its interplay with classical continuum-based FSI methods.

For the example, fluid flow through a compliant pipe with radius 1 for the fluid part, and a thickness of 0.1 for the surrounding structure is set up. On the left boundary, a parabolic inflow profile is prescribed. The velocity is smoothly accelerated to a maximum of 100 in the middle of the parabolic inflow at time $t = 0.1$, and the velocity is then smoothly decelerated to a state of rest again. A backflow boundary condition as discussed in [14] is applied to the fluid outflow boundary and the structural part of the pipe is fixed in place at the artificially cut boundaries on both ends of the artery. The fluid is discretized using $34,350$ stabilized P1/P1finite elements, and the surrounding structure layer is discretized with one element over the thickness leading to a mesh with $4,320$ hexahedral elements with linear shape functions. At half distance to the axial ends of the pipe, 32 fibers are included in the simulation as illustrated in Figure 4.2. The fibers are equally spaced, orthogonal to the fluid flow, they are prescribed a length of 0.8, and they are made up of 10 TF beam elements each. The nodes at the beam ends, which coincide with the inner structure surface, are fixed in place. The fluid is modeled as Newtonian, using a fluid density $\rho_f = 1.0$ and a dynamic viscosity $\nu_f = 0.03$. The beams follow a hyperelastic constitutive law with the Young's modulus $E_b = 2 \cdot 10^9$, the density $\rho_b = 10$, the cross-sectional radius $r_b = 10^{-2}$, and the pipe's wall is modeled using a St.-Venant Kirchhoff material with the Young's modulus $E_s = 3 \cdot 10^6$, the density $\rho_s = 1.2$, and the Poisson ratio $\nu_s = 0.3$. The MMPDE for the ALE displacement is extended using the St.-Venant Kirchhoff constitutive law with the same parameters. Last but not least, a GPTS approach with the penalty parameter $\epsilon_{fbi} = 1$ is used for the FBI interaction, and the simulation is run for 200 time steps with a step length of $\Delta t = 10^{-3}$ using a Gen-α time integration scheme for all fields. For the structure components, the beams as well as the continuum field, a spectral radius $\rho_\infty = 1$ as defined in [34] is used, and the time stepping for the fluid field is based on the parameters $\alpha_f = \alpha_m = \gamma = 0.5$ as detailed in [130].

Due to the fluid flow, the fibers are expected to experience displacement with the maximum displacement occurring at the beam ends closest to the centerline of the pipe. This displacement behavior, in turn, effectively augments the unobstructed area between the tips of the beams. Subsequently, as the inflow velocity is decelerated, the beams are expected to move back into their resting position.

Figure 4.3 depicts the behavior of the beam cluster at times $t = 0.05$, $t = 0.01$, $t = 0.15$ and $t = 0.2$. Qualitatively, the beams behave as expected, and as stated above, tentatively validating the algorithm's ability to apply the correct interaction forces to the fibers

On the other hand, the displacement of the fibers, conversely, directly influences the behavior of the fluid flow. Therefore, the fluid velocity is expected to be highest in the center of the pipe, while it is slowed down in the areas close to the fibers. As the fibers are most densely packed at the beam tips, near the centerline of the pipe, the flow is diverted most noticeable in this area. Caused by the effective reduction in cross-sectional flow area by the obstructing beams, an acceleration of the fluid in the unobstructed region near the cen-

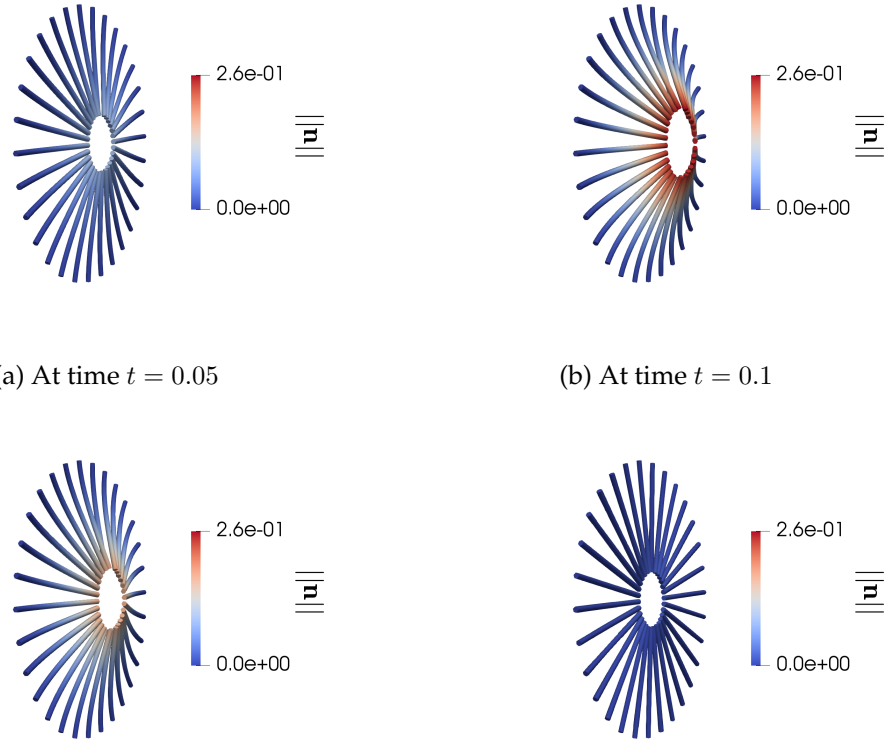

(a) At time $t = 0.05$

(b) At time $t = 0.1$

(c) At time $t = 0.15$

(d) At time $t = 0.2$

Figure 4.3.: Beam displacement for the immersed beams within a compliant pipe solved via the FBSI framework

terline of the pipe is expected. Furthermore, an effect of the fiber-based obstruction on the pressure is expected. As the cluster of fibers represents a relatively dense obstruction in the pipe, the pressure is expected to undergo a jump in the beams' vicinity. Furthermore, due to the inclusion of FSI interactions, flow induced deformation of the compliant pipe, such as in the benchmark in [63], is expected.

Figure 4.4 depicts the behavior of the fluid flow and its interactions with the immersed fibers at times $t = 0.05$, $t = 0.01$, $t = 0.15$, and $t = 0.2$. At all times, Figures 4.4a- 4.4d show a reduction in fluid velocity behind the beam obstruction while the fluid velocity in the unobstructed cross-section, close to the pipe's centerline, shows an increase. This behavior becomes even more evident in Figures 4.4b- 4.4d. As expected, particularly in Figures 4.4c and 4.4d it also becomes noticeable that the flow is slowed down most near the tips of the beams.

Additionally, Figure 4.5 demonstrates the effect of the fibers on the fluid pressure. A clear separation between the range of pressure values before and after the fiber obstruction can

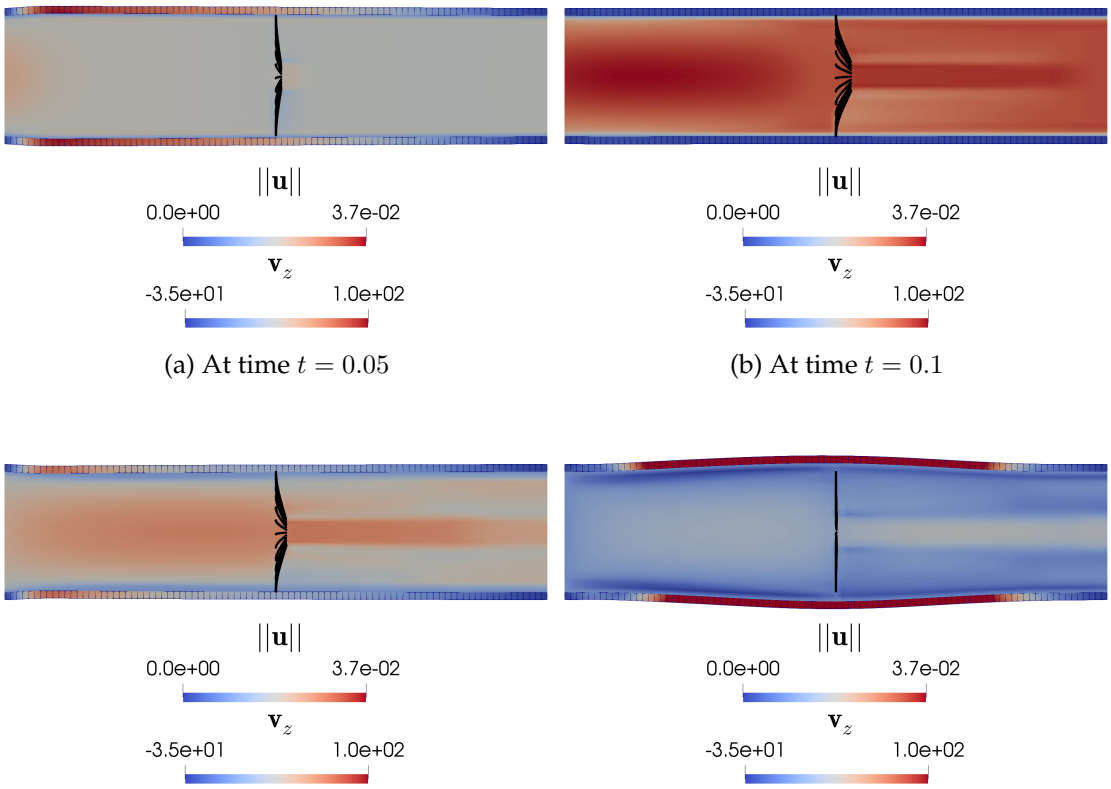

(a) At time $t = 0.05$

(b) At time $t = 0.1$

(c) At time $t = 0.15$

(d) At time $t = 0.2$

Figure 4.4.: Fluid velocity in channel direction for the fluid within a compliant pipe and a obstruction made up of fibers

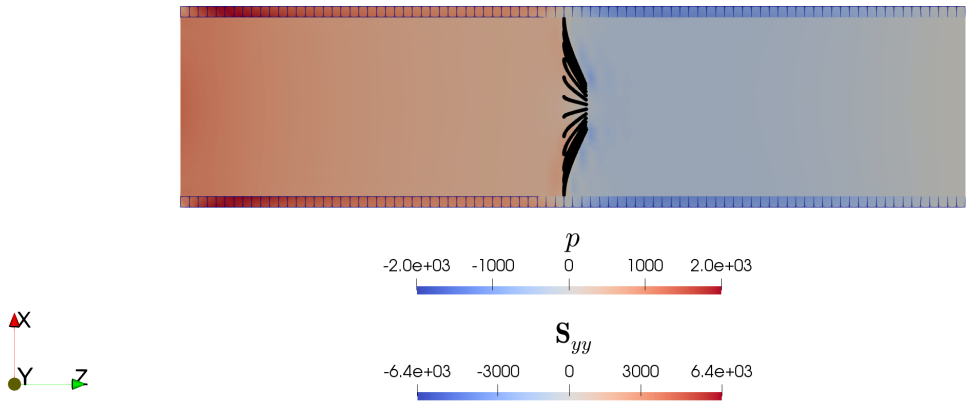

Figure 4.5.: FBSI Example Pressure and Stress at time $t = 0.1$

be observed. As the underlying model also captured the interaction of the fluid with the continuum structure, this jump directly translates to a change in stresses near the the fibers, most notable due to cross-sectional stretching of the solid layer. Figure 4.5 illustrated the principal stresses in tangential direction.

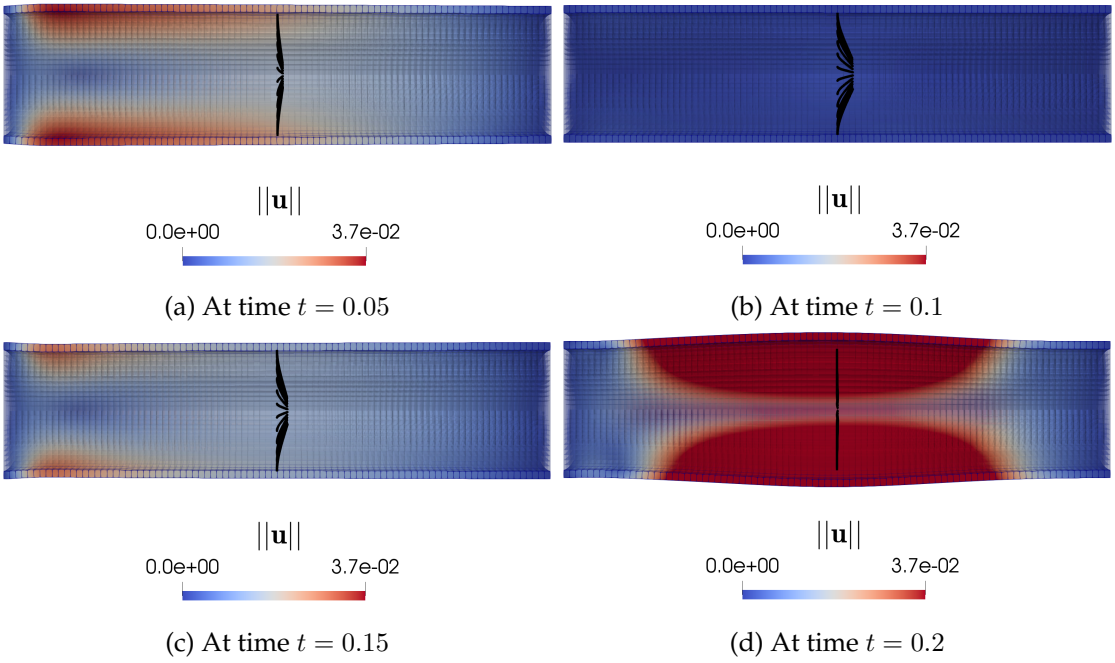

(a) At time $t = 0.05$ (b) At time $t = 0.1$

(c) At time $t = 0.15$ (d) At time $t = 0.2$

Figure 4.6.: Solid and fluid mesh displacements for the compliant pipe example solved via the FBSI framework

Figure 4.6 now depicts the magnitude of the continuum structure field's displacement as well as the fluid mesh displacement at times $t = 0.05$, $t = 0.01$, $t = 0.15$, and $t = 0.2$, particularly the smooth transition of displacement between the two fields.

The solution of the presented numerical experiment, thus, validates the behavior the presented FBSI framework with respect to the fluid flow as well as the fiber movement in a qualitative manner. Furthermore, Figure 4.6 demonstrated the fulfillment of the geometric coupling condition for the FSI interaction, effectively validating the fact that the FBIs as well as the FSIs can be captured by the proposed FBSI method.

Nonetheless, Figures 4.4d and 4.6d make it clear that the presented simulation represents a simplification of the regarded phenomena. It is notable that the model discrepancy, between the moving continuum structure and the fixed beam ends, leads to an unphysical gap between the two structures. In reality, for heart valve simulations, the beam ends are expected to interact with the pipe's wall, and to follow its movement. This motivates the development and application of structure mechanical interactions such as contact and mesh tying in order to adequately model biomechanical processes. Part II of this thesis, thus, focus on the development and application of such structure mechanical interactions, specifically in the context of balloon angioplasty.

Part II.

Modeling balloon angioplasty using geometrically exact beam theory

The application of computational methods to model biomedical procedures, particularly balloon angioplasty, has been a topic of research for many years. However, the state-of-the-art methods in numerical modeling of this complex procedure still leave questions unanswered and their use is not yet common in everyday practice. One of the reasons is certainly the complexity of each single component that interacts during balloon angioplasty.

The artery itself constitutes a complex living organ that adapts and grows with regard to the mechanical configuration it is subjected to. It exhibits an incompressible and anisotropic constitutive behavior that requires adequate modeling [87, 5]. Furthermore, because of its ability to adapt, the blood vessel in its examined geometrical configuration is generally not in a stress-free state. In order to capture a sufficiently realistic behavior of the artery for physically meaningful parameters, pre-stressing and pre-stretching of the artery are essential [90, 211]. In particular, the necessity of pre-stretching is substantiated in [211]. Zhang et al. conclude that pre-stretching is the main reason for the low magnitude in changes of vessel length, while generally rather large changes in the diameter are observed. There exist many formulations of varying complexity to pre-stress a geometry. The most common approach is inverse analysis [31, 68, 69, 125, 50]. In the case of inverse analysis, the stress-free state of the artery is found and on that basis, the stress in the current geometry is computed via physical considerations. A simpler approach is represented by the modified-updated Lagrangian formulation (MULF) [60, 61]. The MULF formulation is not as accurate as some other models, such as inverse analysis, but it represents a simple approach that delivers sufficiently accurate stress results and has been found to be robust also for real patient geometries [61].

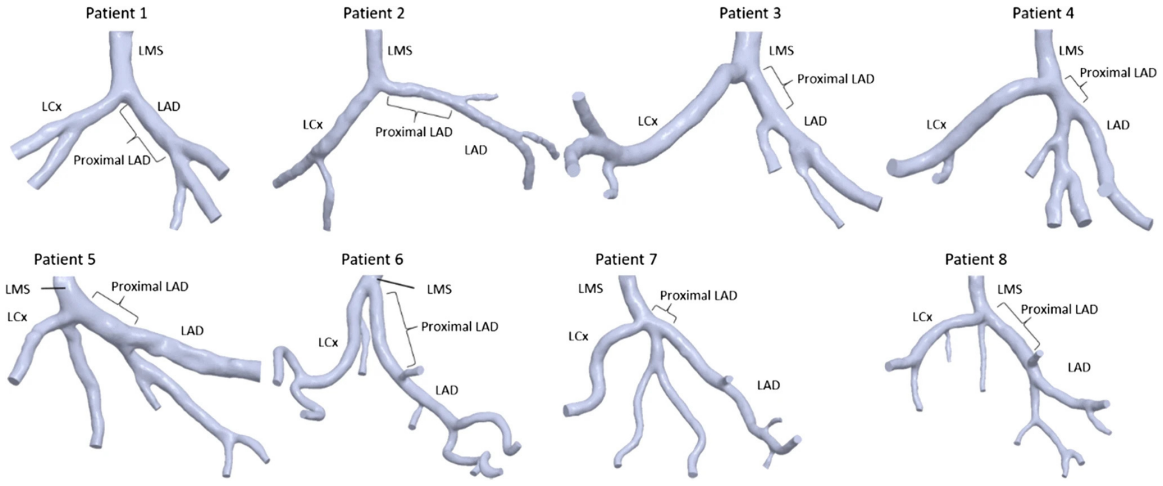

Figure 4.7.: Coronary artery geometries for 8 different patients. The geometry includes the left main stem (LMS), the left circumflex artery (LCx) and the left anterior descending artery (LAD). Taken from [151].

Since blood vessel geometries can significantly vary between patients, as demonstrated in Figure 4.7, the use of image-based geometries is crucial for the aid in patient-specifically tailored devices. However, the acquisition of real patient geometries leads to further re-

search questions and challenges. Information on the geometry of an artery is only available via, more or less high-quality, data obtained through image processing techniques. The extrusion of an accurate geometry from this data is non-trivial and may contain uncertainties [4, 66]. Even when information on the geometry of patient-specific data is available, usually very limited information on the plaque and stenotic regions of the diseased vessel is accessible. The formation of stenotic regions is generally caused by the formation of enclosed lipid pools or calcifications, mostly within the intimal layer. However, Shahidian et al. have shown the importance of suitable material models and accurate plaque geometry modeling for the investigation of potential ruptures and stress distributions close to the stenotic regions [173].

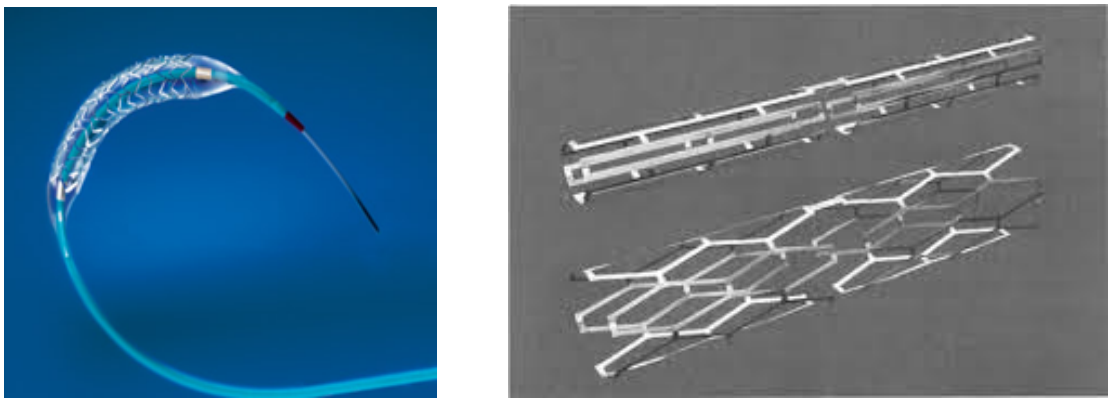

(a) Balloon catheter system. Taken from [10].

(b) Palmaz Schatz stent in crimped and expanded configuration. Taken from [53].

Figure 4.8.: Pictures of a balloon catheter and stent

The second component highly influencing the mechanics during balloon angioplasty is the balloon catheter, depicted in Figure 4.8a. The mechanics of the balloon catheter during the process of angioplasty are fairly complex. Generally, the ends of the balloon are fixed to the catheter and the balloon is folded in order to fit into the crimped stent. Once the air pressure within the balloon is increased, the balloon starts to unfold. The balloon material only starts to stretch after the balloon is fully unfolded, at which point the compliance begins to play a role. In literature, the complexity of the balloon model in simulations of endovascular intervention highly varies between contributions. Within a large number of publications, the balloon is neglected completely and Instead, the stent is simply expanded via strategically applied Neumann boundary conditions acting directly on the stent [163, 90, 137, 210], or via the displacement-driven expansion of a cylindrical shell [111, 90, 4]. However, the mechanics of angioplasty is heavily driven by the balloon inflation. The balloon does not only expand the stent but also exerts additional pressure on the vessel wall, guaranteeing further expansion of the lumen. It is, therefore, important to model the balloon and its inflation via an internal pressure. The initial balloon geometry can either be modeled as a cylindrical structure [103, 101, 102], or its intricate folding can be fully resolved [169, 139]. The latter is found to be necessary to capture expansion effects such as dog-boning, where the axial edges of the balloon-stent system are expanded faster than

its middle part [209, 39]. However, during unfolding, the contact regions between the stent and the balloon constantly change, thus, leading to a high numerical cost. Therefore, the use of cylindrical balloons is still widespread in the scientific community. Due to this simplification, the pressure applied to the inner surface of the balloon is generally required to be somewhat higher than in reality [62].

Particularly important for the long-term effect of balloon angioplasty and stent insertion is the quality of the stent model itself. As illustrated in Figure 4.8b, the stent undergoes large deformations during expansion, making the mechanics highly dependent on elastoplastic behavior [59, 4, 6]. In general, two different methods of geometry acquisition can be distinguished: the geometry may either be extracted from micro CT images [7, 139], or the geometry may be designed via a computer-aided cell-based procedure [6, 169]. In either case, the efficient meshing of these stent geometries poses a challenge and often requires rather finely resolved finite element meshes [163]. Additionally, for the investigation of the expansion procedure, the design of the stent in crimped configuration is essential [62, 108]. The complex geometries and high required mesh resolution motivate the use of beam theory to model the stent. In [183, 215], networks of beams are used to model stents and to capture their expansion behavior. Furthermore, the interaction of a beam-based stent network with a rigid arterial wall, based on point collision detection, is modeled in [16]. Finally, in [111], a beam-based stent model in combination with an elastoplastic constitutive law is used to capture the expansion behavior of a stent.

In addition to the precise modeling of the single components, their combination and the accurate capturing of the interactions between them determine the quality of a model for balloon angioplasty. A multitude of different computational methods and their application to various scenarios can be found in the literature. Some of these approaches and connected research questions are reviewed in the following. In [103], a numerical model for the free expansion behavior of an elastoplastic stent by a balloon is established. A cylindrically orthotropic model is used to reproduce characteristic pressure-diameter diagrams for balloon expandable stents. The interaction of the balloon and stent is captured via a penalty-based contact approach. The numerical model is, subsequently, applied to capture the expansion of six different stent designs and validated by practical experiments. In [49], an isotropic Mooney-Rivlin constitutive law is used to model the generically cylindrical vessel and the plaque. A cylindrical balloon is employed to expand the stent based on an elastoplastic material model. The vessel wall is pre-stressed via the application of a diastolic blood pressure. Furthermore, due to the assumption of symmetry, only a quarter model is simulated. The highest stresses after stenting are obtained at the axial stent ends and it is concluded that the highest risk of stent failure can be expected at the corners of stent cells. The declared aim of the work is the use of the developed computational method for the design of new stents. Similarly, in [206], symmetry constraints are applied to curved and straight cylindrical artery models, on top of which a stenotic layer is modeled. Both, vessel and plaque, are modeled using an isotropic Mooney–Rivlin material. After stenting, the conformity of the stent to the vessel geometry, the minimum lumen area, tissue prolapse between struts and principal stresses are compared between the straight and curved configuration. Increased stresses acting on the inner curvature of the curved vessel wall and a straightening effect are observed. A more complex model can be found in [139], where the performance of three different stent designs in a patient-specific

coronary bifurcation is compared. Within this work, the balloon is modeled as a folded membrane structure. The size of the stent meshes for the different designs varied between $21,000$ and $46,800$ finite elements. An artificial pressure is applied to the outer surface of the stent to mimic crimping. Contact between all components, i.e., artery, stent, balloon, and between catheter and guide wire, is modeled. Insertion of the stent is achieved via displacement conditions applied to the end of the catheter shaft. However, no pre-stressing or pre-stretching is applied to the arterial wall. Based on the numerical model, two modified stent designs are proposed to reduce values of maximum wall stresses after stenting.

Particularly the large size of stent meshes and the promising results of numerical experiments for the free stent expansion behavior of beam models motivates the development of a mixed-dimensional model for balloon angioplasty procedures. To the best of the author's knowledge, the following developments constitute the first application of a mixed-dimensional model to capture the full effects of balloon angioplasty and stent insertion, particularly the stent's interactions with the balloon and the vessel wall.

5. Developing an efficient model for computer-aided design of endovascular devices

This chapter is dedicated to the modeling of balloon angioplasty using a mixed-dimensional model. Specifically, a numerical method for the structure mechanical interactions between balloon, stent, and vessel wall, is developed. The model is qualitatively validated by chosen examples.

In the following, the main features of the applied mixed-dimensional interaction model for the coupling of geometrically exact beams with 3D solid surfaces, or beam-to-solid-surface (BTSS) coupling, are given. The model's suitability for applications in the context of balloon angioplasty is validated by comparison to the behavior of a fully resolved stent model during balloon inflation and stent expansion. After introduction of the mixed-dimensional coupling approach, the general composition of the arterial wall is reviewed and a realistic anisotropic constitutive law for its modeling is summarized. In the end, the resulting model for the simulation of balloon angioplasty is qualitatively validated by chosen numerical examples and comparison to adverse effects of angioplasty known from literature and practice. To the best of the author's knowledge, this constitutes the first application of a mixed-dimensional model to balloon angioplasty.

5.1. Numerical model for balloon angioplasty

Within this section, the considered model for angioplasty is developed. To that aim, the essential theoretical components of the model such as the BTSS coupling method and the employed anisotropic constitutive law for the artery are briefly recounted. Afterward, the considered geometric model for balloon angioplasty and all numerical and constitutive parameters are presented.

5.1.1. Beam-to-solid interaction

To model the interaction between the stent and the balloon or the vessel wall, the BTSS coupling framework, presented in the author's previous work [176], is used. Specifically, the consistent displacement coupling variant presented in the aforementioned work [176] is applied to the numerical examples within the remainder of this thesis. The fundamentals of this approach and the interaction model in weak form are briefly recounted here. The interested reader is referred to [176] for more details on the method.

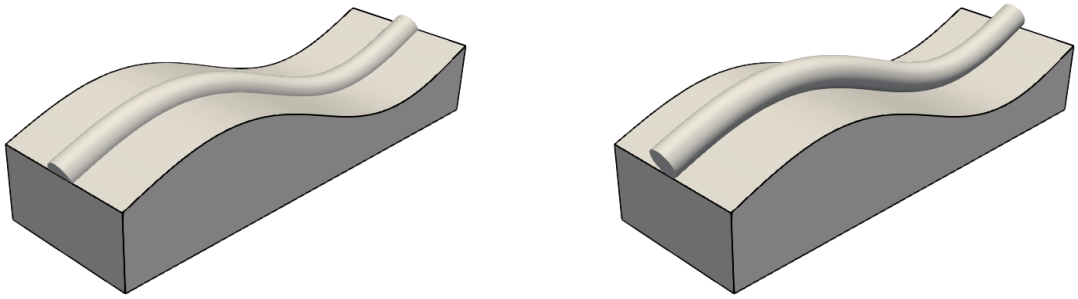

(a) Mesh tying of the beam centerline to the solid surface without offset

(b) Mesh tying of the beam centerline to the solid surface with offset

Figure 5.1.: Representation of two variations of beam-to-solid-surface mesh tying. Figure is taken from the author's article [176].

Similarly to the mixed-dimensional FBI approach introduced in Chapter 3, the BTSS approach relies on a beam centerline coupling, therefore, leading to a 1D-2D beam-centerline-to-surface coupling. A major novelty of the used approach is the possibility to couple the two components at a prescribed distance, i.e., an offset, from each other. The most obvious choice for such an offset is the beam radius, which ensures that the beam's surface, instead of its centerline, lies on the solid surface. In order to be able to capture this general case of an offset, as well as non-conforming discretizations, a distance function

$$d\left(\xi,\psi,s\right) := \left\|\mathbf{x}_s\left(\xi,\psi\right) - \hat{\mathbf{r}}_h\left(s\right)\right\|, \tag{5.1}$$

is introduced. Here, $(\xi,\psi) \in \Gamma^0_{btss}$ represent the solid coupling surface's configuration in the parameter space Γ^0_{btss}, while $s \in [0,l]$ represents the parametrization of the beam centerline in its reference configuration.

This definition of the distance function can be used to characterize the closest point projection $d_{btss} : [0,l] \to \mathbb{R}$ by the minimization problem

$$d_{btss}\left(s\right) := \min_{(\xi,\psi)\in\Gamma^0_{btss}} d\left(\xi,\psi,s\right) := d\left(\xi_{btss},\psi_{btss},s\right). \tag{5.2}$$

The minimal distance vector $\mathbf{x}_s\left(\xi_{btss},\psi_{btss}\right) - \hat{\mathbf{r}}_h\left(s\right)$ has to be orthogonal to the surface tangents, or in other words, has to be a linear combination of the surface normal

$$\mathbf{n}\left(\xi,\psi\right) = \frac{\dfrac{\partial \mathbf{x}_s\left(\xi,\psi\right)}{\partial\xi} \times \dfrac{\partial \mathbf{x}_s\left(\xi,\psi\right)}{\partial\psi}}{\left\|\dfrac{\partial \mathbf{x}_s\left(\xi,\psi\right)}{\partial\xi} \times \dfrac{\partial \mathbf{x}_s\left(\xi,\psi\right)}{\partial\psi}\right\|}. \tag{5.3}$$

These information lead to the following constraint on the BTSS coupling surface:

$$\mathbf{r}(s) - \mathbf{x}_s(\xi_{btss},\eta_{btss}) - d_c\left(\xi_{btss},\psi_{btss}\right)\mathbf{n}\left(\xi_{btss},\psi_{btss}\right) = 0 \quad \text{a.e. on} \quad \Gamma_{btss}, \tag{5.4}$$

where Γ_{btss} represents the solid body's coupling surface in the current configuration. Enforcing this coupling constraint with Lagrange multipliers leads to the following problem in weak form

Problem 5.1 *Find* $\left(\mathbf{u}^s, \boldsymbol{\eta}^b\right) \in \mathcal{W}_\mathcal{S} \times \mathcal{W}_\mathcal{B}$ *such that*

$$\begin{aligned} \mathbf{a}^s\left(\mathbf{u}^s; \delta\mathbf{u}^s\right) + \mathbf{a}^b\left(\boldsymbol{\eta}^b; \delta\boldsymbol{\eta}^b\right) - \mathbf{b}^s\left(\mathbf{u}^s\right) - \mathbf{b}^b\left(\boldsymbol{\eta}^b\right) + \int_{\Gamma_{btss}} \lambda^{btss}\left(\delta\mathbf{r} - \delta\mathbf{x}_s - d_{btss}\delta\mathbf{n}\right)\, ds = 0, \\ \int_{\Gamma_{btss}} \delta\lambda^{btss}\left(\mathbf{r} - \mathbf{x}_s - d_{btss}\mathbf{n}\right)\, ds = 0, \end{aligned} \tag{5.5}$$

for all $\left(\delta\mathbf{u}^s, \delta\boldsymbol{\eta}^b\right) \in L^2\left(I, H_0^1\left(\Omega_s\right)^3\right) \times L^2\left(I, \mathcal{V}_\mathcal{B}\right)$*, with* $\boldsymbol{\eta}^b = \boldsymbol{\eta}_0^b$ *and* $\mathbf{u}^s = \mathbf{u}_0^s$ *a.e. for* $t = 0$*, and* $\|\mathbf{r}'(0,\cdot)\|_{\mathbb{R}^3} = 1$ *a. e. on* $[0, l]$*.*

Here, the semilinear and linear forms $\mathbf{a}^s\left(\mathbf{u}^s; \delta\mathbf{u}^s\right)$, $\mathbf{b}^s\left(\mathbf{u}^s\right)$, and $\mathbf{a}^b\left(\boldsymbol{\eta}^b; \delta\boldsymbol{\eta}^b\right)$, $\mathbf{b}^b\left(\boldsymbol{\eta}^b\right)$, are as introduced in Section 2.4 for the continuum structure, and in Section 2.5, respectively.

The discretization of the single fields is straightforward and follows the derivations in Sections 2.4 and 2.5. Analogously to the FBI approach, a mortar penalty-type regularization is applied to the Lagrange multiplier field to circumvent the inf-sup condition. For more information on the computation of the discretized surface normals, or the closest point projection, as well as their consistent linearization the interested reader is referred to [176] for a comprehensive presentation and analysis of the employed BTSS coupling method.

5.1.2. Comparison with a fully resolved stent

For the comparison, the stent is modeled using a hyperelastic constitutive law with Young's Modulus $90,000\,\mathrm{MPa}$ and a Poisson ratio of 0.3. These parameters do not resemble the ones of stainless steel, as commonly used for bare-metal stents, but are closer to the parameters of copper. In both cases, the reduced-dimensional, as well as the fully resolved model, the balloon, and the stent, interact via normal contact instead of mesh tying in order to allow for sliding during the expansion procedure. Friction is neglected. In order to hold the stent in place, the stent nodes on one end of the stent are fixed as suggested in [103]. The balloon material is modeled using a hyperelastic constitutive law with Young's modulus $850\,\mathrm{MPa}$ and Poisson's ratio 0.4, and both ends are fixed in place. The balloon is modeled using linear hexahedral elements while the stent in the fully resolved case is modeled using linear tetrahedral finite elements. The pressure applied to the inner surface of the balloon is increased within 6 load steps until a pressure of $30\,\mathrm{MPa}$ is reached. The stent interacts with the balloon using a contact variation of the BTSS method introduced in Section 5.1.1, cf. [180], and the penalty parameter is chosen as $\epsilon_{\text{btss}} = 100$.

Figures 5.2a and 5.2b show the initial geometrical configuration of the balloon-stent system modeled using beam elements and a fully resolved stent model, respectively.

Figures 5.2c and 5.2d show the final configuration of the beam-based, and the fully resolved stent model, respectively. Figure 5.3, in turn, shows a comparison of the fully inflated stent for the beam model, in blue, and the 3D continuum model, in purple. The

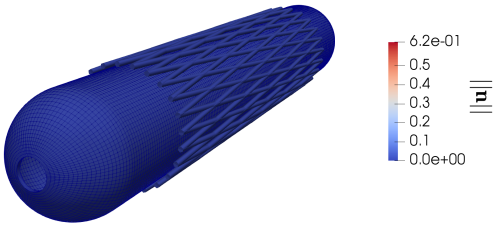

(a) Initial state of the 1D-3D model

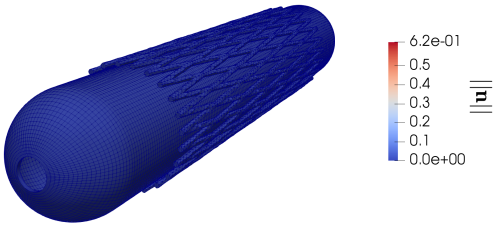

(b) Initial state of the 3D-3D model

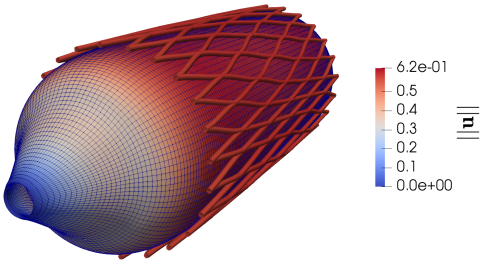

(c) Final state and displacement in mm of the 1D-3D model

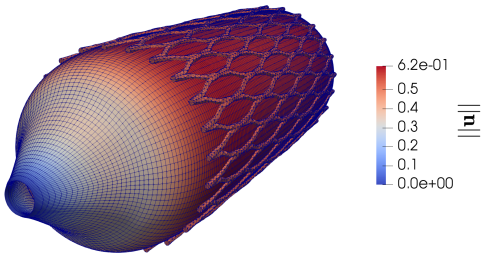

(d) Final state and displacement in mm of the 3D-3D model

Figure 5.2.: Comparison of the inflation of a balloon-stent system modeled as a network of SR beams and a fully resolved 3D stent model

maximum displacement in the radial direction for the beam model is 0.59, while the maximum displacement in that direction for the continuum model is 0.55. The stiffer behavior of the continuum model has various causes. Firstly, the strut connections have been modeled as rather wide to simplify the meshing of the stent geometry while the beams are only coupled point-wise at the intersection of the beam centerline. The use of linear tetrahedral elements additionally enhances this effect of the stiffer geometry model. Nevertheless, the difference constitutes a relative difference of approximately 7% in the maximum displacement. Considering the complexity of the problem, all present interactions, the differences in the initial geometry, and the fact that the beam-based stent is discretized with 95% less finite elements compared to the 3D model, this difference is in line with reports in [215].

The analyzed example shows that not only the stent expansion behavior itself can be adequately captured by a reduced-dimensional stent model, as reported in [215], but also its interaction with a balloon can be satisfactorily captured by the beam-to-solid-surface interaction formulation, first presented in [176], and reviewed in Section 5.1.1. This, in turn, further motivates the use of geometrically exact beam theory, and its interactions with 3D continuum fields, to efficiently model balloon angioplasty.

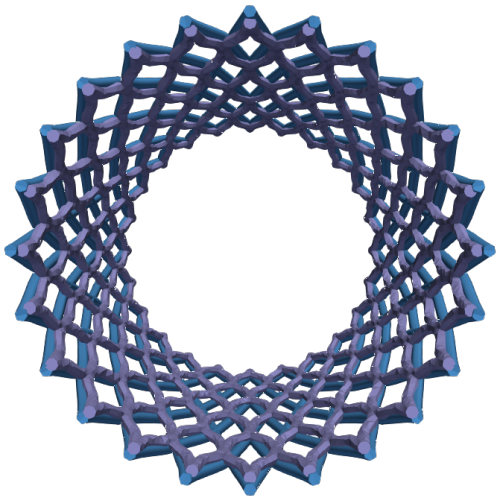

Figure 5.3.: Comparison of the end configuration of two stents, modeled with beam finite elements (blue) and 3D linear tetrahedral finite elements (purple)

5.1.3. Constitutive model for the arterial wall

In the following, the composition and essential constituents of the artery wall, and the arising constitutive response, are briefly recounted.

The arterial material is characterized by a high water content. A suitable material law should, therefore, reproduce the resulting incompressible material behavior. The microscopic structure of most human arteries consists of three different layers: adventitia, media, and intima. To model the passive mechanical response of the artery, these layers can be considered as a composite structure of two families of collagenous fibers arranged in symmetric spirals and embedded within an isotropic base material. The base material is associated with elastin. Under inner pressure, the artery vessel first shows a linear deformation-stress response due to the elastin matrix. As the load increases, an exponential stiffness response can be observed due to the gradual engagement of the collagen fibers. These observations suggest the use of an anisotropic material model. In fact, in [5], the response of an artery with anisotropic constitutive behavior is compared to an artery modeled using an isotropic constitutive law, and a mismatch of 600% in the maximum principle stresses was found. In the remainder of this thesis, the constitutive law applied to the artery model is, thus, based on the anisotropic material law presented in [87, 85]. This constitutive law is briefly reviewed in the following.

In the following, $\mathbf{g}_1$ and $\mathbf{g}_2$ denote the normalized direction vectors of the two families of fibers, and $\bar{\boldsymbol{C}} := \det\left(\mathbf{F}^{-\frac{2}{3}}\right)\mathbf{F}_e^T\mathbf{F}_e$ represents the modified right Cauchy-Green deformation tensor based on the elastic component $\mathbf{F}_e$ of the deformation tensor $\mathbf{F}$. In this case,

the strain energy function can be split into an isotropic and an anisotropic part:

$$\Psi\left(\bar{\boldsymbol{C}}, \boldsymbol{g}_1, \boldsymbol{g}_2\right) = \Psi_{iso}\left(\bar{\boldsymbol{C}}\right) + \Psi_{aniso}\left(\bar{\boldsymbol{C}}, \boldsymbol{g}_1, \boldsymbol{g}_2\right). \tag{5.6}$$

Using the shear modulus G, the isotropic part then takes the form

$$\Psi_{iso}\left(\bar{\boldsymbol{C}}\right) = \frac{G}{2\beta}\left(J^{-2\beta} - 1\right) + c_1\left(\mathrm{tr}\left(\bar{\boldsymbol{C}}\right) - 3\right), \qquad \beta = \frac{\nu}{1-2\nu}, \tag{5.7}$$

while the anisotropic part can be characterized by the material parameters k_1 and k_2, and has the form

$$\Psi_{aniso}\left(\bar{\boldsymbol{C}}, \boldsymbol{g}_1, \boldsymbol{g}_2\right) = \frac{k_1}{2k_2}\exp\left[k_2\left(\boldsymbol{g}_1\bar{\boldsymbol{C}}\boldsymbol{g}_1 - 1\right)^2\right] + \frac{k_1}{2k_2}\exp\left[k_2\left(\boldsymbol{g}_2\bar{\boldsymbol{C}}\boldsymbol{g}_2 - 1\right)^2\right] - 2. \tag{5.8}$$

Here, k_1 represents a linear scaling parameter of the energy function, and k_2 defines the exponential increase in the stress response as more and more collagen fibers become active.

Remark 5.2 *As the artery can be considered as nearly incompressible, the isotropic strain energy function in* (5.7) *can be simplified [85]. However, in this section, the form for the compressible Neo-Hookean constitutive model is given for generality.*

5.1.4. A mixed-dimensional simulation model for balloon angioplasty

Since the focus of the thesis lies in aiding in the understanding of the long-term effects of balloon angioplasty, the model suggested in this section is based on a quasi-static problem. The effect of inertia will therefore be neglected. Furthermore, parameters and geometries are based on coronary artery stenting. Nevertheless, the overall methodology is also transferable to the simulation of balloon angioplasty in other vessels.

Adventitia	$0.30\ \mathrm{mm}$
Media	$0.25\ \mathrm{mm}$
Intima	$0.20\ \mathrm{mm}$

Table 5.1.: Thickness of the arterial layers used in the coronary artery model

In the following, a simplified geometry of the artery is considered and depicted in Figure 5.4. The geometry can be interpreted as a tube with the radius $1.35\ \mathrm{mm}$ and the length $10\ \mathrm{mm}$. The three layers of the artery including the geometry parameters are stated in Table 5.1.

The values in Table 5.1 are based on measurements performed during autopsy of human left anterior descending arteries (LAD) and can be found in [88].

The stenosis is modeled as a stenotic layer on the inner surface of the artery, similarly to [168]. The stenosis has a length of $9.6\ \mathrm{mm}$, effectively decreasing the lumen diameter by $8\ \mathrm{mm}$ at its minimum. This corresponds to a reduction of the cross-sectional area

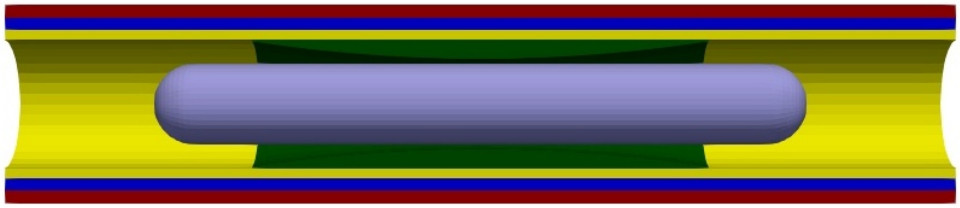

Figure 5.4.: Schematics of the base geometry used within the presented model of an angioplasty procedure. It contains the balloon (violet), the stenosis (green), the intima (yellow), media (blue), and adventitia (brown).

by 50%. In the current model, the simplified approach in [169] is followed and the overall constitutive behavior of the stenotic region is modeled as fibrous without fully modeling the geometry of its various components. In agreement with [89, 120], the fibrous tissue is modeled as a neo-Hookean material with Young's Modulus 115 MPa and Poisson's ratio 0.45.

Layer	G	k_1	k_2	Fiber orientation
Adventitia	7.56 kPa	38.57 kPa	85.03	67.00
Media	4.68 kPa	21.60 kPa	8.21	20.61
Intima	55.80 kPa	263.66 kPa	170.00	60.30

Table 5.2.: Constitutive parameter of the arterial layers

In order to pre-stress the artery, the diastolic blood pressure

$$p_{diastolic} = 80 \text{ mmHg} = 0.0107 \text{ MPa},$$

is applied to the lumen surface, and the resulting system is solved via the MULF algorithm presented in [61]. Further, a pre-stretch factor of 1.25, equaling a Dirichlet controlled displacement of 2 mm pulling on each artery end, is applied to the artery in order to stress the artery in the longitudinal direction.

The stent is modeled as a diamond-shaped structure, inspired by the Palmaz Schatz stent design, using 288 SR beam finite elements. A hyperelastic material with Young's modulus $E_b = 195,00$ MPa and Poisson's ratio $\nu_b = 0.3$ is applied to model stainless steel (SS316L). The stent struts itself have a radius of 0.04 mm, while the stents is modeled with a radius of 0.85 mm and a length of 6 mm in the crimped configuration. The stent is made up of 5 diamond-shaped cells in longitudinal strut direction, and 24 cells in circumferential direction, as illustrated in Figure 5.5.

The balloon is modeled as a cylinder of 12 mm length and an outer diameter of 1.7 mm with closures at both ends, as illustrated in Figure 5.4. The balloon thickness amounts

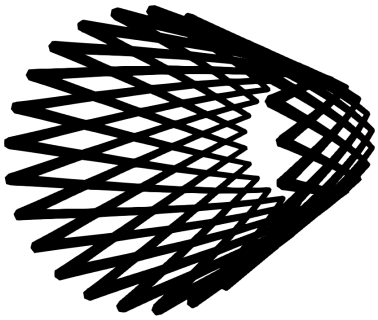

Figure 5.5.: Depiction of the applied diamond-shaped stent design

to $50\,\mathrm{micron}$. The balloon is discretized with one linear hexahedral element in the thickness direction, and a total of $5,568$ finite elements. The constitutive model of the balloon's homogeneous material is selected as an isotropic, hyperelastic St. Venant Kirchhoff material. The material parameters are chosen as $E_{balloon} = 850\,\mathrm{MPa}$ for the Young's modulus and $\nu_{balloon} = 0.4$ for the Poisson's ratio, and can be found in [139]. Furthermore, the catheter and the guide wire are neglected, and, instead, the position of the balloon is fixed at both ends.

If not stated otherwise, the balloon is expanded by applying an orthonormal pressure $p_{balloon}$ on the inner surface of the balloon. The pressure is successively increases up to $p_{balloon} = 30\,\mathrm{MPa}$ within 6 load steps. The balloon inflation serves two purposes: firstly, the balloon expands the stent and thereby puts it into place to later hold the artery open. Secondly, the balloon expands the plaque itself. In order to represent this complex process in a physically correct way, the numerical methods for contact mechanics and BTSS interaction, presented in Section 2.7 and Section 5.1.1, respectively, are used. The expansion of the stent by the balloon is modeled using the BTSS equations with the penalty parameter $\epsilon_{btss} = 100$, if not stated otherwise. The interaction of the balloon and the artery is modeled using the mortar penalty contact formulation with the penalty parameter $\epsilon_c = 20$. During the inflation phase, no interaction between the stent and the artery is taken into account, since the vessel expansion is assumed to be mainly driven by the balloon inflation.

The deflation phase is the last step, where the balloon is decoupled from the stent and coupled to the artery with the penalty parameter $\epsilon_{btss} = 100$. The inner pressure of the balloon is gradually lowered within 4 load steps. To overcome the limitations of employing a hyperelastic material law for the beam-based stent model, an artificial pressure is applied as a Neumann boundary condition to hold the stent open.

5.2. Captured effects

Within this section, the suitability of the developed simulation model for balloon angioplasty is demonstrated by validating the model's ability to capture well-known effects of

balloon angioplasty. The effects range from expected pre-stressing states over the stress distribution after stenting to the well-known straightening effect observed after stenting of curved vessels.

5.2.1. Pre-stressing & pre-stretching of the artery

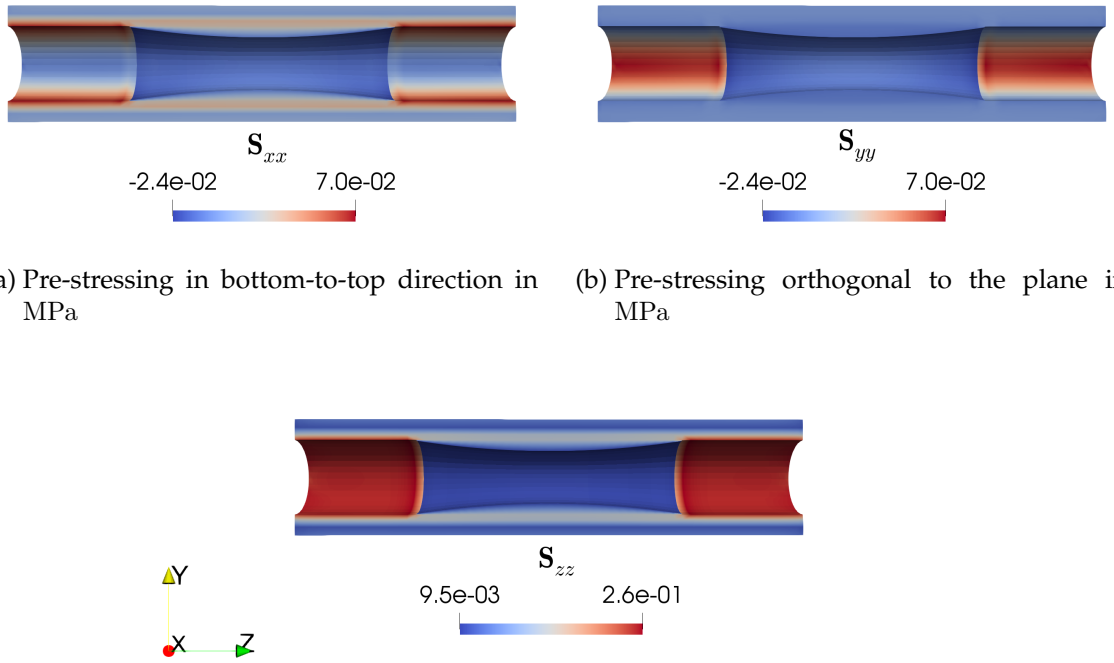

(a) Pre-stressing in bottom-to-top direction in MPa

(b) Pre-stressing orthogonal to the plane in MPa

(c) Pre-stressing in axial direction in MPa

Figure 5.6.: State of the vessel after pre-stressing and pre-stretching using the MULF method

In the following, the plausibility of the results after the pre-stressing and pre-stretching step is checked. As already stated in Section 5.1.4, a diastolic pressure is prescribed on the inner surface of the vessel while a displacement of 2 mm is applied to each end of the vessel. After the pre-stressing phase, the principle stresses in all directions are expected to be non-vanishing. In fact, the stresses due to pre-stressing are generally non-negligible, and prevent unrealistically large deformations during subsequent simulation phases [61, 188]. Furthermore, an influence of the different material properties of the various layers on the stress distribution is predicted due to the differing deformation-stress relationships. Particularly, the comparably high Young's modulus of the stenosed region leads to notable differences in the stress state as observed for a calcified vessel in [61].

Figure 5.6 depicts the result of the applied MULF pre-stressing and pre-stretching. The effect of pre-stressing is most notable within the innermost layer, the tunica intima, to

which the diastolic pressure is applied. Figures 5.6a and 5.6b show the vessel's stress state in the circumferential direction, and Figure 5.6c shows the stress in the axial direction. The depicted principal stresses are all non-negligible, and their influence on the material layer is notable in the presented figures. All in all, the results show an agreement with the expected effects after pre-stressing and pre-stretching.

5.2.2. Inflation of the balloon & contact interactions

Next, robustness and plausibility of the inflation behavior is validated. The balloon is expected to expand due to the internal pressure given in Section 5.1.4 and, in turn, to expand the stent. Once contact with the vessel wall is established an increase in the vessel lumen is anticipated.

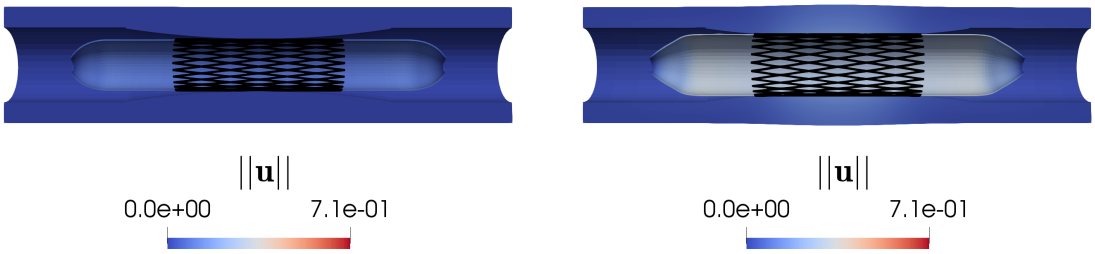

(a) Displacement state in mm during balloon inflation at pressure $p_{balloon} = 7.5$ MPa

(b) Displacement state in mm during balloon inflation at pressure $p_{balloon} = 15$ MPa

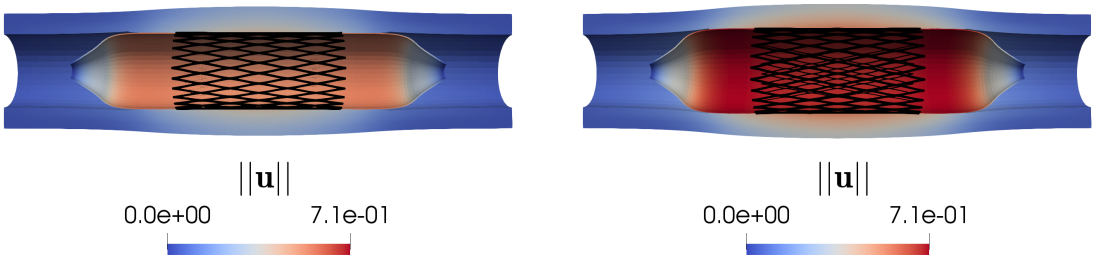

(c) Displacement state in mm during balloon inflation at pressure $p_{balloon} = 22,5$ MPa

(d) Displacement state in mm during balloon inflation at pressure $p_{balloon} = 30$ MPa

Figure 5.7.: Displacement behavior of balloon, stent, and vessel wall furing balloon inflation

Figure 5.7 shows the different stages of the balloon inflation phase. In Figure 5.7a, the balloon's inflation is not yet sufficient for contact with the artery to occur but the balloon already starts to expand the beam-based stent. In the next steps, the balloon comes into contact with the stenosis and slowly pushes it to the outside, effectively recovering the original lumen diameter, as demonstrated in Figures 5.7b and 5.7c. In Figure 5.7d, the

balloon inflation is finally sufficiently large to increase the lumen diameter. These results validate the robustness of the contact and mesh tying methods for the present generic geometry and demonstrate physically logical behavior throughout the inflation phase.

5.2.3. Balloon deflation & stress peaks

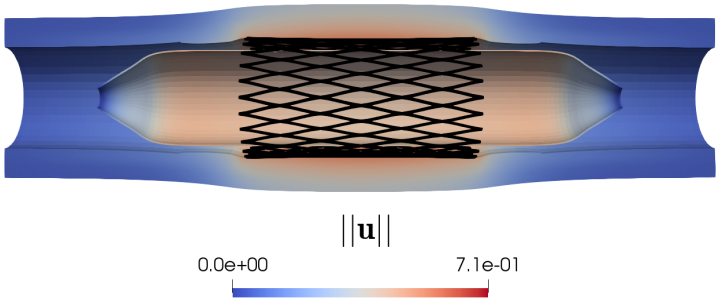

(a) Displacement state in mm during balloon deflation at pressure $p_{balloon} = 20$ MPa

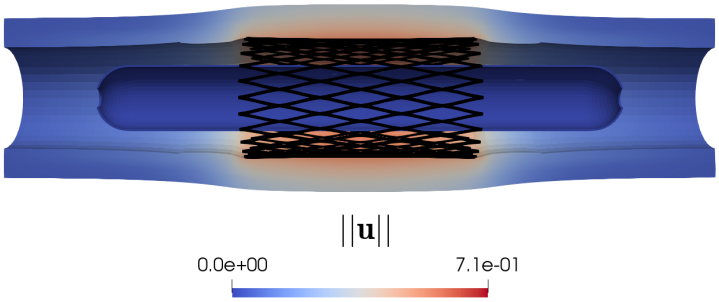

(b) Displacement state in mm during balloon deflation at pressure $p_{balloon} = 0$ MPa

Figure 5.8.: Displacement state during the stent deflation phase

After contact is established and the original lumen area is recovered, the balloon is deflated and the stent is left in place. Realistically, a recoil of the stent to its plasticized final state is expected. The stent in its plasticized state reinforces the vessel wall and keeps the lumen expanded. In contrast, the vessel wall in the unstented regions collapses, effectively decreasing the lumen area. The hight gradient of the artery-stent system's compliance in the transitional zone between stented and unstented regions lead to the development of stress peaks at the stent's edges [200, 139, 212, 100, 169].

The deflation phase represents the most crucial point in regard to the simplification of applying a hyperelastic constitutive law for the stent. However, this example is designed to illustrate the robustness of the employed BTSS method and to demonstrate its capturing of well-known phenomena in connection with balloon angioplasty, even under the model's current limitations.

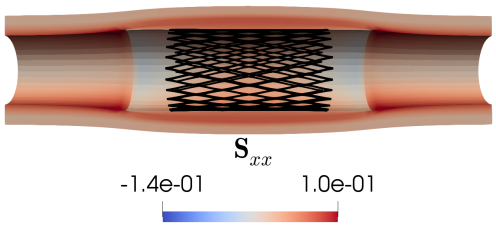

(a) Second Piola-Kirchhoff stress component $\mathbf{S}_{xx}$ in MPa at peak balloon inflation

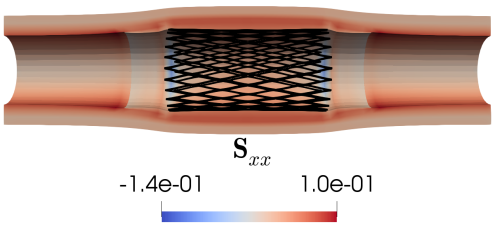

(b) Second Piola-Kirchhoff stress component $\mathbf{S}_{xx}$ in MPa after balloon deflation

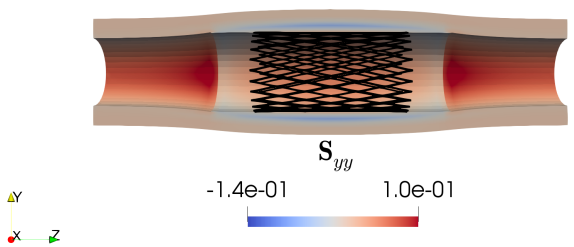

(c) Second Piola-Kirchhoff stress component $\mathbf{S}_{yy}$ in MPa at peak balloon inflation

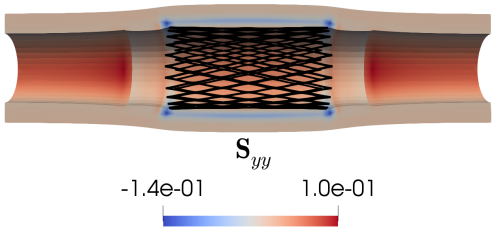

(d) Second Piola-Kirchhoff stress component $\mathbf{S}_{yy}$ in MPa after balloon deflation

Figure 5.9.: Comparison of the distribution of the second Piola-Kirchhoff stresses. The left column shows the circumferential and radial stresses in the artery before balloon deflation and the right column shows the circumferential and radial stresses after balloon deflation.

Figure 5.8 illustrates the results of the deflation phase. The stabilizing effect of the expanded stent on the artery is demonstrated. Additionally, the unstented vascular wall's protrusion into the lumen is illustrated by Figure 5.9. Furthermore, the formation of (negative) stress peaks in the principal stresses near the axial stent edges can be observed in the radial direction after balloon deflation, cf. Figures 5.9b and 5.9d. The obtained values are in the order of stress peaks observed in [139].

5.2.4. Straightening & edge effect for curved arteries

In contrast to the geometry treated up until now, real vessels are rarely perfectly straight but usually exhibit some amount of curvature. Stenting of such curved blood vessels generally leads to the so-called straightening effect. This effect has been observed in clinical studies in [74, 213, 132, 200], and has been captured through numerical experiments in [66, 94, 4, 169, 139, 212]. This straightening of the vessel affects the artery in two forms. On the one hand, the changed configuration of the vessel geometry may adversely affect the blood flow pattern and lead to recirculation zones and abnormal WSS [94, 213]. On

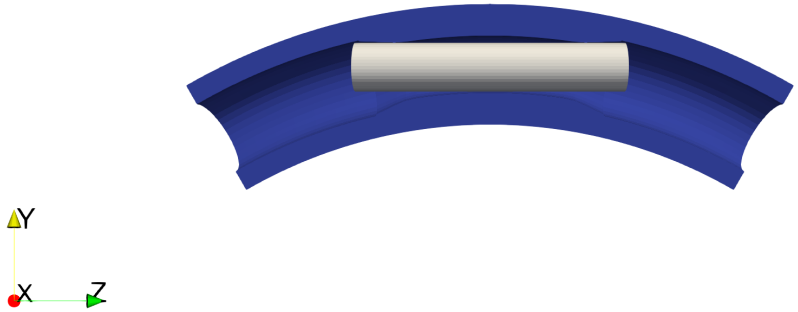

(a) Initial geometry of a straight balloon in a curved vessel

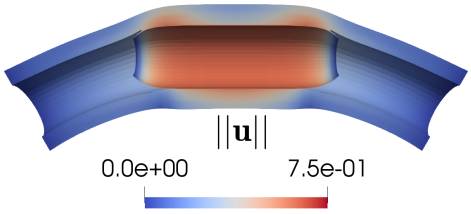

(b) Displacement in mm of a stenosed curved vessel and balloon at peak inflation of the balloon without stent

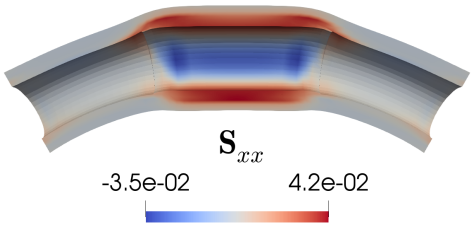

(c) Distribution of radial stresses in MPa within a stenosed curved vessel at peak inflation of the balloon without stent

Figure 5.10.: State at peak inflation of a balloon in a curved artery

the other hand, the poor fit of the stent in the artery may lead to vessel wall injury and inflammation due to high mechanical stress and angulation. This, in turn, precipitates edge restenosis near the stent edges [100, 74, 132]. Both effects have been linked to unfavorable long-term outcomes and in-stent restenosis.

In the following, the simulation model proposed in Section 5.1.4 is adapted and applied to model balloon angioplasty in a curved artery without stenting. To this end, the geometry of a straight balloon in a curved pipe is used. The initial geometry is depicted in Figure 5.10a. Furthermore, the pressure is slightly adapted to $48\ \mathrm{MPa}$ subdivided into 12 load steps. All other numerical parameters are taken directly from Section 5.1.4.

Figures 5.10b and 5.10c illustrate the simulation results. As expected, Figure 5.10b clearly exhibits straightening of the vessel due to the balloon expansion. Furthermore, Figure 5.10c demonstrates stress peaks near the stent edges, in radial as well as circumferential direction. These results demonstrate that both, the straightening effect as well as the mechanical stress peaks at the ends of the balloon, can be captured by the proposed methodology.

5.2.5. Inflation behavior of a curved balloon catheter device

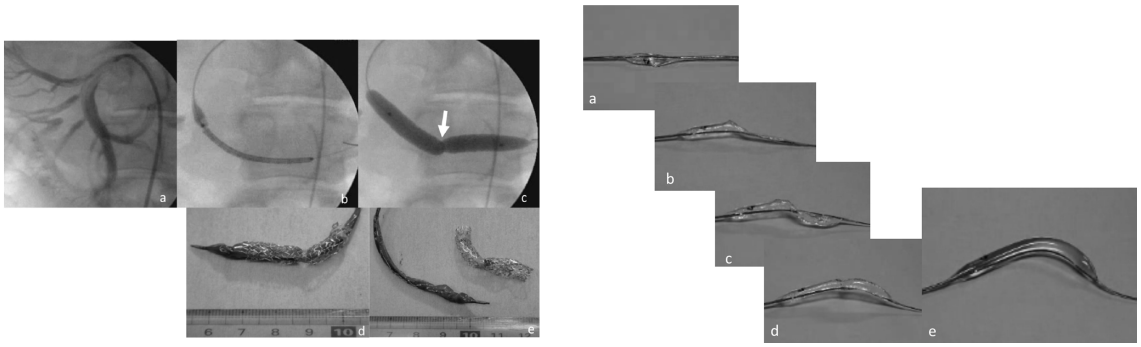

Figure 5.11.: Behavior of the curved GOKU balloon-catheter in practice. Figures are taken from [191].

The GOKU curve represents a balloon catheter that was specifically developed to treat acute-angled vessel portions and which is commercially available. During unfolding and inflation, the balloon transitions from a nearly straight configuration to a highly curved geometry. In [104], an in-vitro comparison to a conventional straight balloon was performed and significantly lower stresses for the insertion of the GOKU curve in an artificial curved vessel model were reported. Furthermore, "safety and effectiveness of catheter intervention in the early postoperative period have also been reported" [104, p.411]. In [58], a study with 45 patients was performed and the authors report that the GOKU curve performed better with respect to the reduction of complications. In addition, use of the GOKU curve contributed to better short-term outcomes after treatment of lesion angles between $70°$ and $110°$ compared to conventional straight stents. Its particular usefulness for lesion angles greater than $90°$ was hypothesized. Unfortunately, in [191], limited inflation of the GOKU balloon during the insertion of conventional straight stents of various lengths was observed in animal experiments. However, the GOKU curves suitability for acute-angled lesions stems from the particular inflation and bending behavior of the GOKU balloon catheter reported in [191] and visualized in Figure 5.11.

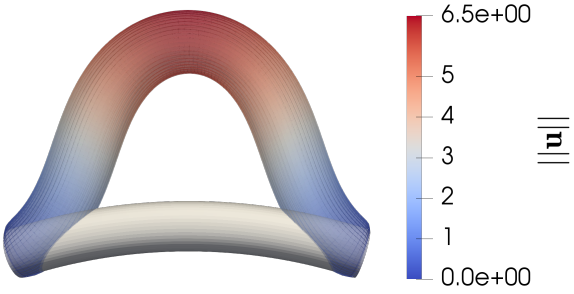

Figure 5.12.: Initial configuration of a curved balloon (gray) and displacement state of the balloon in mm after application of the inner pressure $p_{balloon} = 12\ \mathrm{MPa}$

Motivated by the success of the GOKU curve, the behavior of a slightly curved balloon under application of a uniform inner pressure is numerically investigated in the following. The goal of the simulation is the reproduction of the GOKU curves inflation behavior, i.e. its bending, as depicted in Figure 5.11. No stent nor artery is present in this simulation. Instead, the free inflation behavior of the curved balloon is analyzed. Only the balloon ends are constrained. The pressure is increased within 30 load steps, until a value of $p_{balloon} = 12\ \mathrm{MPa}$ is reached.

Figure 5.12 shows the initial geometry of the slightly curved balloon and the result of the inflation simulation. Similarly to the GOKU curve, the end configuration exhibits severe bending and only little inflation of the balloon geometry.

6. Computer-aided patient-specific design of endovascular devices

The focus of this chapter lies on the use of the model components developed in Chapter 5 for computer-aided design of patient-specific endovascular devices, specifically balloon catheters. The application of optimization procedures to aid in the design of endovscaular devices, particularly stents, is frequently encountered in the literature, cf. [199, 22, 194, 71, 70, 76, 174, 160], among others. Commonly used optimization parameters include stent features such as strut thickness, the number of cells, and material parameters. Stents are often optimized with respect to the reduction of unfavorable flow features, the reduction of stress peaks, or their geometric conformity with the vessel wall.

In the following, a novel balloon catheter technology based on an anisotropic balloon constitutive behavior is proposed. The direction of anisotropy is tailored to specific geometric scenarios to overcome challenges regularly encountered during angioplasty procedures. The combination of balloon catheter technology and the optimization of the balloon material itself constitute, to the author's best knowledge, a novel approach which targets the challenges faced during the stenting of curved blood vessels, cf. Sections 5.2.4 and 5.2.5.

6.1. Proposal of a novel patient-specific treatment for stenosed blood vessels

The favorable results reported for the use of GOKU balloons in in-vivo studies, cf. Section 5.2.5, suggests that the use of endovascular devices adapted to the geometrical features of the artery could aid in reducing negative consequences such as artery straightening and hinge effects. Already in [206], this idea was brought up: "Furthermore, we propose if the balloon were designed to expand in similar curvature as the vessel, the stent could be bent in advance and conform to the vessel better" [206]. To reduce the straightening effect and achieve a uniform stress distribution on vessel walls, the following section investigates the use of curved balloons and stents, as illustrated in Figure 6.1. Additionally, a patient-specific curved balloon technology, based on an anisotropic material that limits bending modes, is proposed to address limitations of the GOKU balloon catheter for stent insertion in slightly curved vessels.

Materials with directional properties can not only be found in nature but also in engineering. The production of inflatable devices taking on specific shapes upon inflation has recently been investigated by [146]. Here, inspired by the makeup of arteries, the proposed anisotropic balloon material is assumed to be a composite of a base material and two directional families of fibers. The modeling of such fiber reinforced composites was

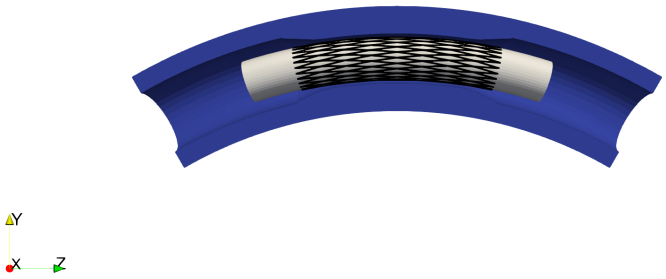

Figure 6.1.: Geometric configuration of a patient-specific curved balloon and stent

comprehensively treated in [85], and applied to a reinforced rubber material in [86]. The fiber properties utilized below are obtained from the hyperelastic material model in [86]. These properties impact the stress-strain relationship only during tension, and do not affect its behavior under compression, thus making it an appropriate choice for a balloon catheter. Table 6.1 summarizes the material properties of the proposed balloon, based on the anisotropic constitutive law presented in Section 5.1.3.

Fiber properties	k_1	161.5	MPa
	k_2	0.5	
Base material	$E_{balloon}$	850	MPa
	$\nu_{balloon}$	0.4	

Table 6.1.: Material properties of the proposed anisotropic balloon catheter

For the sake of realism, the material properties summarized in Table 6.1 is assumed to be fixed. The focus lies on studying the influence of the direction of anisotropy, i.e., the fibers, on the balloon behavior. To demonstrate the influence of the fiber direction on the undesired bending action of the device, Figure 6.2 shows the results of numerical experiments for various angles between the fiber directions and the normal in radial direction. The balloon ends are fixed and an orthonormal Neumann boundary condition is applied to the inner surface of the balloon to model the inner pressure of up to 64 MPa, which gradually increases during 16 load steps.

An angle of $0°$ corresponds to fibers in circumferential direction, leading to an activation of the fibers during circumferential stretching while stretching in axial direction is not restricted. Clearly, this configuration fails to limit the bending motion of the ballon, and may in fact amplify this behaviour. On the other end of the spectrum, a fiber angle of $90°$ leads to fibers running along the centerline of the balloon, thus, not restricting the inflation behavior while limiting the bending modes. The remaining fiber configurations exhibit behavior that falls somewhere between these two extremes, as depicted in Figure 6.2. For

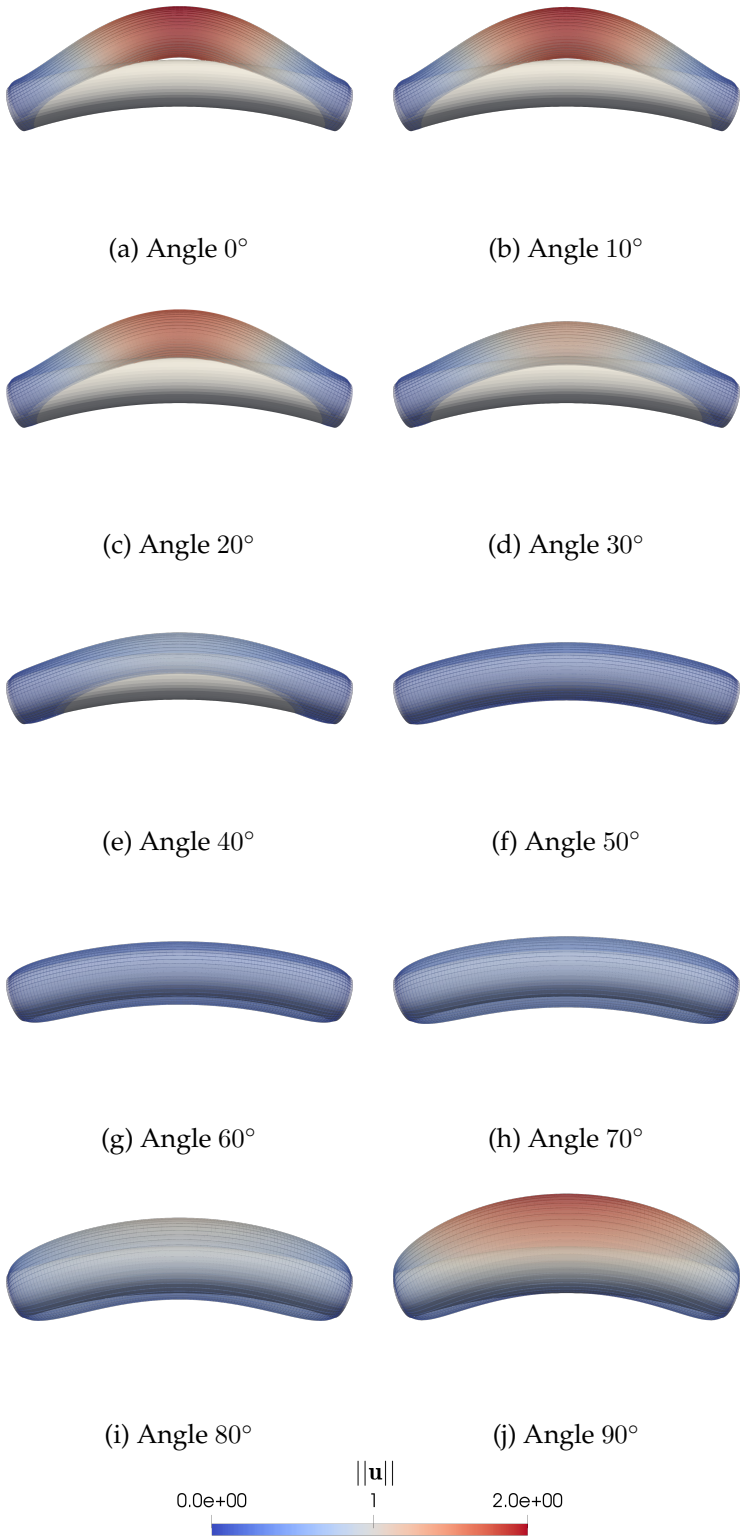

(a) Angle 0° (b) Angle 10°

(c) Angle 20° (d) Angle 30°

(e) Angle 40° (f) Angle 50°

(g) Angle 60° (h) Angle 70°

(i) Angle 80° (j) Angle 90°

Figure 6.2.: Parameter study on the influence of the direction of anisotropy on the novel curved balloon design. Displacement state in mm after application of an inner pressure of $64\ \mathrm{MPa}$

the given material properties and initial curvature of the balloon, a fiber angle between $60°$ and $70°$ seems to yield the most concentric inflation behavior, which is necessary for an uniform expansion of a blood vessel of the same curvature.

Evidently, the optimal fiber direction configuration of the anisotropic balloon to yield concentric inflation depends on the initial curvature of balloon and stent, which should be adapted to the curvature of the artery to be treated. Therefore, the anisotropy direction required patient-specific adaptation to achieve good conformity to the curvature of the blood vessel. For this purpose, an automatic procedure to find the best patient-specific fiber configuration for a given curvature is explored in the upcoming section.

6.2. Optimal balloon configuration for curved arteries

Within this section, the automatic optimization procedure for the fiber direction within the novel anisotropic balloon technology, presented in Section 6.1, is explored. In particular, the design is optimized with respect to various goal functions, and different geometric scenarios. All optimization procedures constitute optimal control problems, as introduced in Section 2.3, where the state of the problem is related to the parameter, i.e., the fiber direction, by the full numerical model at hand. All optimization procedures were performed using a BFGS variant and the open source library SciPy [195] to solve the optimal control problem. The gradient calculation was also outsourced to SciPy and performed via finite differences approximation. Where appropriate, the results of the optimization procedure are compared to commercially available devices, and their benefits are demonstrated.

6.2.1. Computational model & optimization procedure

Based on the proposed balloon design and the presented studies in Section 6.1, the aim of this optimization procedure is to find the fiber direction that leads to the most concentric expansion behavior of the balloon for a given pressure. To approximate this behavior, the integral of the displacement field in radial direction is chosen as the goal function. The integration surface Γ_{opt} is represented in x- and y-direction for Figure 6.1. This leads to the goal function

$$\frac{1}{2}\int_{\Gamma_{opt}} \mathbf{u}_x + \mathbf{u}_y \, \mathrm{d}\Gamma_{opt}. \tag{6.1}$$

It is worth noting that the goal function tends towards zero in the event of perfectly concentric inflation. Furthermore, a variant of the computational model for balloon inflation presented in Section 6.1 is used as state equation within the optimal control problem. To ensure that the simulation remains robust for all fiber orientations, the inner pressure of the balloon is reduced to $30\ \mathrm{MPa}$. Subsequently, 35 increments of increasing pressure are applied to reach this state. To investigate the robustness of the solution procedure with respect to low quality initial guesses, a fiber direction of $25°$ is prescribed for the initial guess. Furthermore, an absolute tolerance $tol_{opt} = 10^{-2}$ is enforced for the value of the Jacobian, and handed to the applied BFGS algorithm.

Iterations:	11
Function evaluations:	30
Gradient evaluations:	15
fun:	$2.3115396304074676e-07$
hess_inv:	0.0020231
jac:	0.00264692
x:	66.05565971

Table 6.2.: Behavior and solution of the BFGS algorithm for the optimization of the fiber direction in curved balloons

The solution as well as characterizing parameters of the optimal control procedure are summarized in Table 6.3b. The optimal value of $66.06°$ is well in line with the numerical study and observations in Section 6.1.

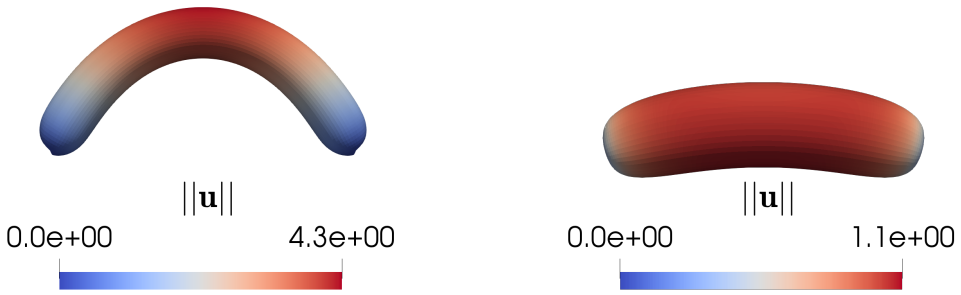

(a) Initial Guess (b) Optimal Solution

Figure 6.3.: Displacement solution in mm for the initial guess and optimized value of the BFGS algorithm for curved balloons at an inner pressure of $30\ \mathrm{MPa}$

Figure 6.3 depicts the balloon's configuration at an inner pressure of $30\ \mathrm{MPa}$. The solution for the initial estimate, with a fiber direction of $25°$, is illustrated in Figure 6.3a, while the optimal parameter, with a fiber direction of $66.06°$, is displayed in Figure 6.3b. A clear improvement in the inflation behavior, as well as a reduction in bending, is observable.

6.2.2. Comparison to commercial balloon catheter devices

An angioplasty simulation is set up to explore the advantages of the new patient-specific curved balloon technology when compared to a conventional straight balloon catheter. Figure 6.4 depicts the geometric setup for the optimized curved and the straight balloon. Both balloons are inflated until the stenosis no longer protrudes into the lumen. The numerical parameters for the simulation of the straight balloon are directly taken from Section 5.2.4. Note that the curved balloon requires a lower inner pressure, compared to the straight balloon, in order to fully push the stenosis out of the lumen. For the curved balloon, this leads to an inner pressure of $17.75\ \mathrm{MPa}$, increased within 18 load steps.

(a) Geometric configuration of a curved balloon in a curved artery

(b) Geometric configuration of a straight balloon in a curved artery

Figure 6.4.: Start configuration of a curved and straight balloon within a curved artery

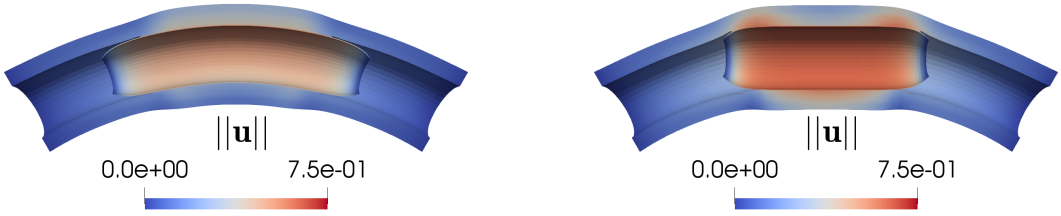

(a) Displacement solution in mm for the curved balloon expanded by an inner pressure of $17.75\ \mathrm{MPa}$ in a curved artery

(b) Displacement solution in mm for the straight balloon expanded by an inner pressure of $48\ \mathrm{MPa}$ in a curved artery

Figure 6.5.: End configuration of a curved and straight balloon within a curved artery

The result of the numerical experiments is shown in Figure 6.5. It is notable that the increased inflation of the straight balloon leads to larger displacements of the vessel wall at the upper edges of the stenosis and in the lower stenotic region. As expected, the curved balloon exhibits an uniform expansion and conforms well to the vessel geometry. In particular, little to no unfavorable straightening of the blood vessel occurs, resulting in a favorable geometric configuration.

The aforementioned displacement peaks lead to matching principal stress peaks in circumferential direction, as shown in Figure 6.6. While the principal stresses alone are surely not a definite measure of damage, stress peaks can indicate the potential for vessel injury. In this context, it is known from practice that injuries often occur near the balloon edges, leading to a candy-wrapper or edge restenosis effect [100, 74, 132]. This conforms to the locations of the captured principal stress peaks in the results of the presented numerical experiments. It stands to reason that lower and more uniform stresses may lessen the injury-induced restenosis leading to more favorable long-term outcomes.

Thus far, the numerical examples investigating the behavior of balloon angioplasty with

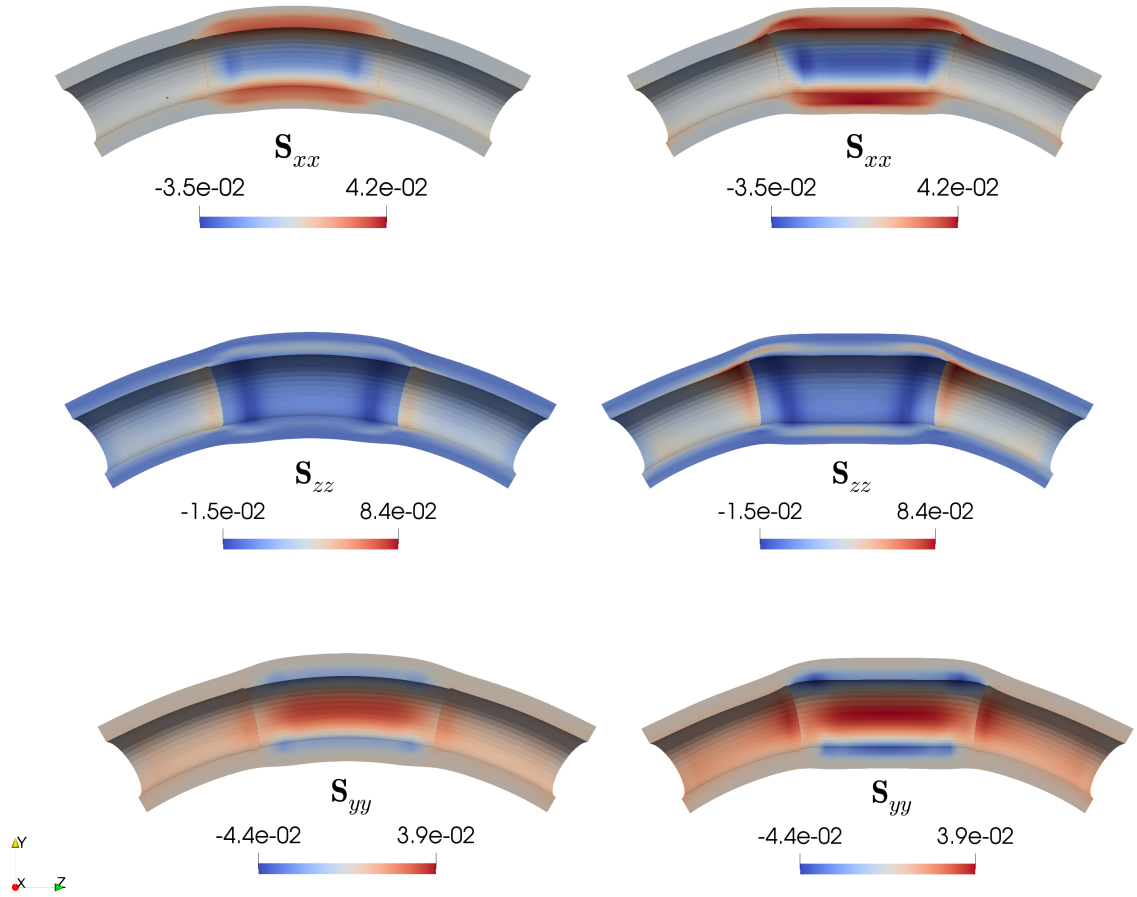

(a) Principal stresses for the curved balloon angioplasty

(b) Principal stresses for the straight balloon angioplasty

Figure 6.6.: Principal second Piola-Kirchhoff stresses in MPa for balloon angioplasty with a straight and an anisotropic curved balloon

the proposed anisotropic balloon have demonstrated a similar behavior to the one described in [104, 58]. Namely, the curved balloon conforms well with the curved artery and the resulting stress distribution is rather uniform. One difference to the commercially available curved GOKU balloon catheter is the range of application, specifically the curvature of the vessel sections. Although the GOKU curve was found to be most effective for acutely angled vessels [58], the proposed anisotropic balloon can be customized to suit various arteries, including those with only slight curvature. Further, the next numerical experiment is designed to investigate the GOKU curve's drawback of insufficient inflation of the balloon during stent insertion. To this end, the last simulation is adapted to additionally include a stent. The stent interacts with the balloon via the BTSS coupling method with the penalty parameter $\epsilon_{btss} = 100$. The contact between the artery and the balloon

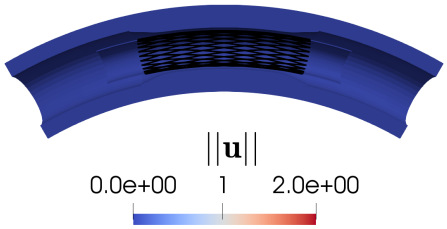

(a) Initial displacement state of a curved balloon-stent system in mm

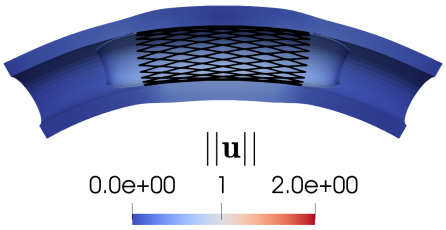

(b) Displacement state of a curved balloon-stent system in mm at an inner pressure of $16\ \mathrm{MPa}$

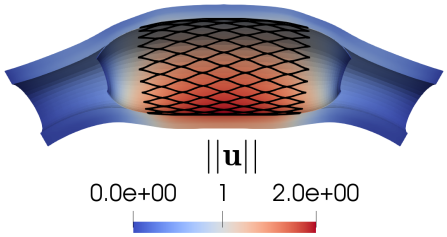

(c) Displacement state of a curved balloon-stent system in mm at an inner pressure of $26\ \mathrm{MPa}$

Figure 6.7.: Inflation of a curved balloon with curved stent

is modeled using the regularized Lagrange multiplier approach with the penalty parameter $\epsilon_c = 10$. The inner pressure is successively increased to a value of $26\ \mathrm{MPa}$ within 30 load steps. The initial configuration is illustrated in Figure 6.7a.

Figures 6.7b and 6.7c illustrate the stent expansion at 16 and $26\ \mathrm{MPa}$, respectively, demonstrating the suitability of the novel curved balloon catheter also for balloon angioplasty with stent insertion.

In addition to edge restenosis, plaque rupture is another potential complication of balloon angioplasty that is associated with stresses in the vessel wall. During plaque rupture, parts of the stenosis break of and enter the blood stream, thus, increasing the risk of embolism [196, 73]. The presented numerical examples demonstrate that the use of the proposed anisotropic curved balloon catheter may reduce stress peaks and lead to a more uniform stress contribution, which may reduce risks of both complications, restenosis and plaque rupture. However, to predict plaque rupture, the material of the plaque as well as the resultant stresses acting on the plaque play an important role. A study of the full patient-specific model including the arterial makeup is, therefore, necessary to recommend an improved balloon, and stent, design. The setup of such a model, and the influence of asymmetric stenotic regions on the stent expansion, is the topic of the next section.

6.3. Optimal balloon configuration for asymmetrically stenosed arteries

In general, blood vessels are not only curved but also exhibit cross-sectional asymmetry. These asymmetries can be inherent to the vessel's geometry or due to the asymmetric formation of stenosis. Asymmetric cross-sections, especially in the presence of calcification, can represent a challenge for conventional endovascular devices.

Medical studies conducted on sheep and human patients have revealed a positive association between restenosis and cross-section or stent asymmetry [141, 182, 172]. In [141], a study with 23 patients has shown that "[i]n-stent neointimal proliferation is more likely to occur in stented coronary arteries with a more oval than rounded cross-section, and particularly within the more curved portion of the oval cross-section" [141, p. 491]. Furthermore, in [182], post-procedural stent asymmetry is found to be related to higher event rates. This is especially troublesome as stent symmetry can in general not be confirmed by standard angiography [172]. One explanation for this correlation is given by the observation that the less diseased perimeter, with thinner plaque deposits, expands more and, therefore, experiences higher strains and stresses [169, 212]. Furthermore, a relationship between plaque composition and the probability of inadequate treatment of stenosis is reported in [169]. The increased risk is hypothesized to be caused by non-uniform stent expansion. In [212], the effect of curvature and asymmetric plaque formation on self-expandable Nitanol stents is studied. The artery is modeled as homogeneous, hyperelastic, and isotropic. As expected from mechanical considerations as well as clinical practice, higher compression and, consequently, higher stresses are found to be present on the sides where the stenosis is least pronounced. From experiments on rabbits, it is known that these factors, namely the extent of plaque and medial compression, are positively correlated with neointimal hyperplasia which, in turn, leads to in-stent restenosis. Zhao et al. have found through numerical experiments that highly asymmetric plaque formation may lead to underexpansion and malapposition of stents [212].

All the aforementioned problems of commercially available balloon catheters and stents, with respect to the long-term success of endovascular intervention, motivate the need for a circumferentially varying pressure distribution on the lumen wall. A circumferentially varying pressure distribution may aid in ensuring a uniform stent expansion even in the presence of cross-sectional asymmetry. To this end, the behavior of a heterogeneous balloon catheter, made up of four distinct material patches based on the anisotropic material model proposed in Section 6.1, is investigated in the following.

6.3.1. Optimal balloon design for a simplified artery model

Within this section, the proposed optimal control problem is first set up with a simplified state equation in order to investigate the relationship between the optimization parameter and the goal function in this simpler scenario. In particular, the vessel wall cross-section is modeled as homogeneous and isotropic. By this rather strong simplification, the mechanics of the system change drastically. In order to recover the expected behavior of the

system, artificially chosen parameters for the constitutive laws, and the pressures, are applied. Since these values do not correspond to physical parameters, but have been chosen to analyze the mathematical behavior of the optimal control problem, the use of units is abandoned for the length of this example.

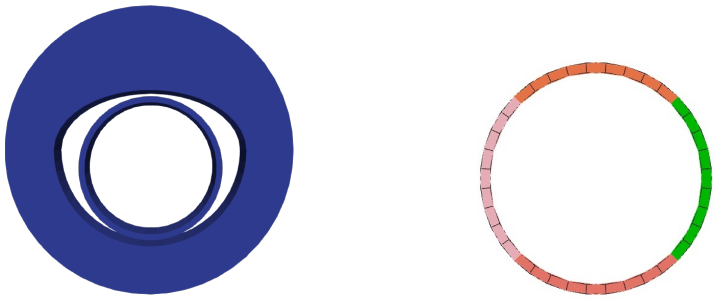

(a) Geometry of the idealized vessel cross-section

(b) Balloon made up of four anisotropic material patches

Figure 6.8.: Geometrical model of the generic quasi-2D arterial cross-section and the heterogeneous balloon

Figure 6.8a shows the geometry of the considered quasi-2D arterial problem and Figure 6.8b illustrates the makeup of the heterogeneous balloon consisting of four material patches. The outer surface is modeled as a quasi-2D cylinder with radius 1. The upper half of the lumen is modeled as elliptic and represents a stenotic lesion. The lower arterial region, on the other hand, is considered to be healthy and assumed to be perfectly round with the radius 0.8. This geometry is inspired by the representative artificial cross-sectional geometries in [173, 212]. As in Section 5.1.4, the balloon is assumed to be perfectly round in the initial configuration. A quasi-static simulation is performed. For the quasi-2D problem at hand, the displacement orthogonal to the plane is forced to zero via Dirichlet boundary conditions. On the outer surface of the artery, spring-dashpot conditions are applied, where the spring stiffness is set to $K_{sd} = 10^1$. The spring-dashpot conditions remove rigid body modes from the system and, at the same time, allow for some amount of displacement of the outer wall. Similarly, spring-dashpot conditions with the stiffness $K_{bsd} = 2 \cdot 10^1$ are applied to the balloon's artificially cut surfaces to mimic the catheters stabilizing effect on it. Additionally, an orthonormal pressure of up to $p = 3.15 \cdot 10^3$, slowly increased within 80 load steps, is applied to the inner surface of the balloon in order to inflate it. The vessel wall is modeled using a St. Venant-Kirchhoff material with the Young's modulus $E_s = 10^5$ and the Poisson ratio $\nu_s = 0.495$. The material parameters for the anisotropic balloon are taken from Section 6.1. Contact is modeled using the penalty mortar finite element method, presented in Section 2.7, using the penalty parameter $\epsilon_c = 2 \cdot 10^1$.

The result for the above described simulation with a conventional homogeneous, isotropic balloon material, and the novel anisotropic balloon with a fiber direction of $90°$, i.e., fibers in circumferential direction, is depicted in Figure 6.9. The figure showcases the influence of the fiber direction on the inflation behavior of the balloon and the overall system. Fig-

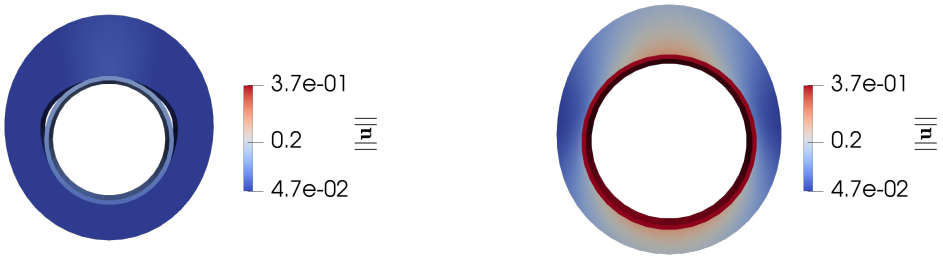

(a) Homogeneous, anisotropic balloon material (b) Homogeneous, isotropic balloon material

Figure 6.9.: Simulation result of the simplified model for a homogeneous, anisotropic balloon material with fiber direction $90°$, and a conventional homogeneous, isotropic balloon

ure 6.9a illustrates the expansion behavior of a fiber-reinforced balloon for which the fibers lie in circumferential direction, and effectively completely restrict the inflation behavior. The balloon's diameter in the expanded state is, thus, smaller compared to a balloon without fiber reinforcement. Figure 6.9b, in turn, shows the undesirable displacement of the lower, healthy, arterial region.

The aim of the following optimization is now the reduction of the deformation in the lower arterial region, and the recapture of the lumen shape of the healthy vessel, by tuning the fiber directions in all four balloon patches. In the idealized vessel at hand, the cross-section of the healthy geometry can be assumed as a perfect circle with radius $R_{\text{circle}} = 0.8$. These considerations lead to the following goal function, which quantifies the difference between the assumed position of the idealized healthy vessel and the position of the lumen wall after the balloon inflation procedure:

$$\int_{\Gamma_{opt}} ||\mathbf{x}^2 + \mathbf{y}^2|| - R_{\text{circle}}^2 \, \mathrm{d}\Gamma_{opt}, \tag{6.2}$$

where Γ_{opt} represents the inner surface of the quasi-2D artery.

In contrast to the optimization procedure applied to the curved balloon in Section 6.2, here the limited-memory BFGS (L-BFGS) algorithm [123] is applied to solve the optimization problem instead of the classical BFGS algorithm. The main difference between the two algorithms lies in the storage requirement for the Hessian inverse, which is of particular benefit for optimization problems with many optimization parameters. In practice, the main difference is that the L-BFGS implementation provided by SciPy directly allows for the application of bounds on the optimization parameter, which the BFGS algorithm does not. Furthermore, in order to normalize the problem description, the optimization parameter, i.e., the fiber angle, is scaled from $[0°, 90°]$ to $[0, 1]$ while the goal function is scaled by a factor of 200, and the appropriate bounds are set. In the following, the symmetry of the arterial cross-section is exploited, and the left and right patch are assumed to to be made up of the same material. This leads to three optimization parameters. The initial guess is

set to $60°$ for the lower patch, and $30°$ for both other patches, while an absolute tolerance $tol_{opt} = 10^{-3}$ is enforced for the norm of the Jacobian and handed to the applied L-BFGS algorithm.

`Iterations:`	1
`Function evaluations:`	8
`Gradient evaluations:`	2
`fun:`	0.206487
`jac:`	$[-0.00052485, 0.00096037, -0.00043162]$
`x:`	$[1., 0.16600637, 0.21601355] \cdot 90$

Table 6.3.: Optimization behavior of the hyperelastic arterial surrogate model

Table 6.3 summarizes the solution and characteristic numbers of the optimization procedure. For the problem at hand, the L-BFGS algorithm converges after only one iteration and two gradient evaluations. Note that multiple function evaluations are necessary, though, in order to compute the finite differences approximation of the gradient with respect to all three parameters. The optimal fiber direction of the lower patch is $90°$, for the upper patch it takes the value $14.94°$, and $19.44°$ for the two remaining patches.

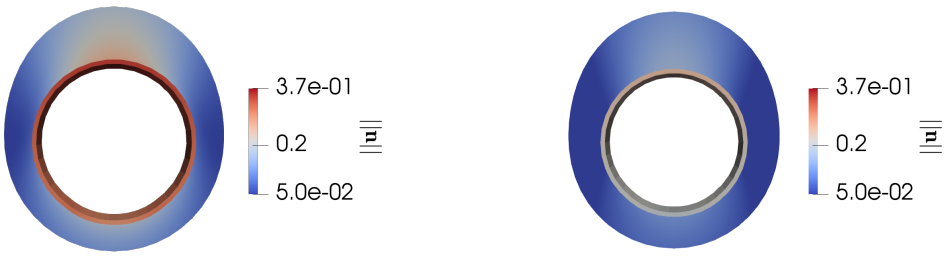

(a) Expanded balloon configuration corresponding to the initial guess

(b) Expanded balloon configuration for the optimized fiber diection

Figure 6.10.: Initial guess and final configuration after optimization of the fiber direction in all patches with a hyperelastic artery

The end configuration of the expanded balloon, for the parameters of the initial guess as well as the setup with the optimized fiber directions, is depicted in Figure 6.10.

The novel endovascular device design is based on a specific placement within the artery, which is generally very difficult to achieve during endovascular intervention. To study the sensitivity of the goal functional on the placement of the optimized balloon, the balloon is rotated in equidistant increments of $5°$ around its axis for $35°$ in each direction. Changes of less than 2% in the value of the goal functional are obtained for all of these configurations. This suggests the applicability of the proposed technology also under moderate misalignment.

6.3.2. Optimal balloon design for an anisotropic artery model with plaque

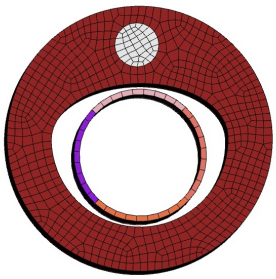

Figure 6.11.: Geometry of the arterial cross-section model with plaque occlusion

As a next step, the optimization procedure presented in the previous section is extended to a more realistic model for the artery. Particularly, an anisotropic material law for the artery model, realistic constitutive parameters for a coronary artery, and calcified plaque occlusions are included in the simulation. For the artery, the material parameters introduced in 5.1.4 are used. The geometry of the calcified plaque occlusion is depicted in Figure 6.11. The plaque is modeled as a Neo-Hookean material with the Young's modulus $E_{plaque} = 10\,\mathrm{MPa}$ and the Poisson ratio $\nu_{plaque} = 0.3$. The pressure is successively increased, within 90 load steps, until a pressure of $p = 22.5\,\mathrm{MPa}$ is reached. The spring-dashpot conditions are applied with the spring stiffnesses $K_{sd} = 10^{-2}$ and $K_{bsd} = 2 \cdot 10^{-2}$, on the arterial and balloon surface, respectively.

`Iterations:`	4
`Function evaluations:`	90
`Gradient evaluations:`	18
`fun:`	0.24707
`jac:`	$[0.00100506269, -0.00214809539, -0.00609041706]$
`x:`	$[1., 0.30354471, 0.16088478] \cdot 90$

Table 6.4.: Optimization behavior for the anisotropic arterial model with plaque occlusion

The characteristic numbers collected in Table 6.4 show that the relationship between the optimization parameter and the goal function has become more nonlinear as compared to the simplified approach. Now, four iterations of the L-BFGS, and 18 gradient evaluations to build up the BFGS approximation of the Hessian, are necessary. Even though the constitutive parameters are very different from the ones used in the previous section, the optimized fiber directions are very similar to the ones reported in Table 6.3 for the simplified model.

6.3.3. Optimal balloon design for an anisotropic artery model with plaque and truly asymmetric geometry

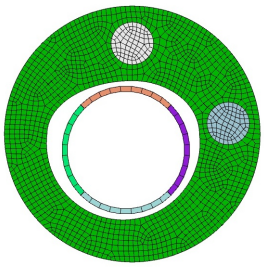

Figure 6.12.: Geometry of the asymmetric arterial cross-section model with multiple plaque occlusions

Last but not least, the optimization procedure is applied to a different cross-sectional geometry. All constitutive parameters are kept the same as in the previous example. Figure 6.12 depicts the adapted cross-sectional geometry, which now also exhibits stenosed thickening and a plaque occlusion on the right side of the artery. The pressure is successively increased within 70 load steps, until a pressure of $17,5\ \mathrm{MPa}$ is reached. Due to the lack of symmetry, the optimization is performed for the fiber direction of all four material patches, and the tolerance 10^{-4} is handed to the L-BFGS algorithm. As initial guess, the fiber direction for all balloon patches is set to $60°$.

`Iterations:`	3
`Function evaluations:`	20
`Gradient evaluations:`	4
`fun:`	0.09196
`jac:`	$[0.0000225597319, 0.0000655475674, -0.0000719424516, 0.0000756728014]$
`x:`	$[0., 0., 1., 0.] \cdot 90$

Table 6.5.: Optimization behavior for the truly asymmetric anisotropic arterial model with multiple plaque occlusion

The expanded state for the optimized balloon configuration is illustrated in Figure 6.13, and the result of the optimization procedure is shown in Table 6.5. The solution converged to the fiber angle $90°$ for the left patch, and a fiber direction $0°$ everywhere else. The numbers characterizing the optimization procedure demonstrate a convergence behavior that is very similar to the one for the previous geometry: three iterations are performed and four gradient evaluations are necessary. Contrary to the last example, here, more function evaluations are necessary since the gradient has to be built with respect to all four optimization parameters. However, the overall convergence behavior of the optimal control

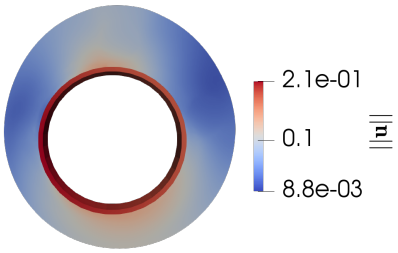

Figure 6.13.: Final displacement solution in mm after optimization of the fiber direction in all patches for an asymmetric arterial cross-section with anisotropic arterial model and multiple plaque occlusions

problem, which is the focus of the current section, is unchanged. This observation suggests that the robustness of the optimization procedure is not dependent on the geometry of the vessel cross-section, and concludes the chapter on optimal control as a tool for the patient-specific design of endovascular devices.

Part III.

Towards a computational model for stented arteries including blood flow

Numerical investigations into the influence of stents on the blood flow through arteries represents a further tool to gain insights into the long-term effects of balloon angioplasty since regions of altered WSSs are one of the main stent-induced effects linked to in-stent restenosis [94, 147]. "In fact, a flow effect on [in-stent restenosis] may be larger than local mechanics of stent contact. [...] the non-conformity between the stent and the vessel could generate unwanted turbulence in the blood stream while favoring the creation of thrombosis." [206, p. 2584]

The application of CFD and FSI simulations to study the blood flow through arteries is a well-established research field. However,such simulations still pose challenges with respect to accuracy and efficiency, cf. [64, 52, 11, 190], among others. Past works include the study of stent design and its influence on the velocity profile, recirculation zones, and WSS for 3D models and CFD, or FSI, simulations, cf. [147, 33, 94, 128], among others, and Figure 6.14. As for the case of stent insertion, the complexity of the models varies significantly. In [147] and [94], CFD simulations are run to investigate the effect of various stent designs on an artery. Specifically the formation of recirculation zones, regions of low and disturbed fluid velocities and low, or oscillating, WSSs are analyzed. Both models include pulsatile inflow profiles based on doppler ultrasound, or doppler velocimeter, data. In [147], however, the vessel geometry is modeled as a symmetric straight pipe and a zero pressure condition is applied to the outflow boundary. In contrast, the geometry in [94] is based on a patient-specific carotid artery bifurcation and patient-specific calibrated Windkessel models are applied as outflow boundary conditions. On top of that, in [147], the expanded stent configuration is directly included in the simulation while in [94], a virtual implantation procedure is used to insert the stent into the patient-specific vessel geometry. Subsequently, the fluid mesh is locally refined near the stent struts yielding a mesh size of $7,000,000$ finite elements. Furthermore, the blood flow is accurately modeled as non-Newtonian fluid in [94].

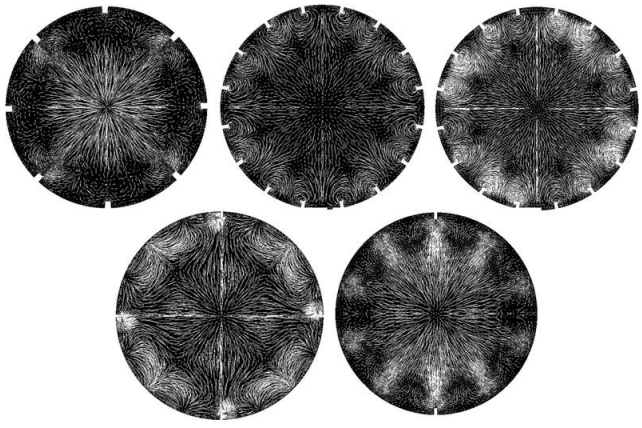

Figure 6.14.: Recirculation zones on a cross section perpendicular to the flow direction for different stent designs resulting from numerical experiments. Taken from [147].

In contrast, in [33] and [128], the simulation methodology is extended to an FSI approach in order to capture the effect of wall compliance on hemodynamics. While the geometry

in [128] is taken from computed tomography (CT) images of a left anterior descending artery (LAD), a straight pipe geometry is considered in [33]. Both numerical experiments consider the vessel wall to be isotropic and homogeneous, the fluid to be Newtonian, and the stent to exhibit a purely elastic behavior in the considered deformation range. In [128], the wall compliance is found to substantially affect the hemodynamic-induced WSSs. The non-negligible wall deformation may have also posed a challenge in [33], where the maximum iteration count for the FSI algorithm is set to $1,000$ iterations and a compute time of approximately 500 hours is required to simulate one cardiac cycle. Furthermore, the fluid mesh includes $1,121,130$ finite elements and the structure part is meshed with $899,710$ elements, partly because "the device adds complexity to the geometry and needs to be correctly refined" [33, p.219].

The excessive size of the required meshes and the long computing time motivates the use of mixed-dimensional modeling for the investigation of flow disturbances caused by the presence of stents. To the best of the author's knowledge, the following example, in combination with the author's own works [176] and [75], constitute the first application of a mixed-dimensional multi-physics model in the context of stenting procedures. Moreover, the following example represents the first application of a mixed-dimensional model that captures not only the interactions between hemodynamics and stent but also the interactions between the blood flow and the vessel wall.

7. Capturing the effect of a stented artery on blood flow and vice versa

Within this chapter, the behavior of an idealized stented vessel is investigated. The presented model and corresponding examples further demonstrate the applicability of the novel 1D-3D coupling approaches in the context of balloon angioplasty and stented vessels. In the following, the novel FBSI framework presented in Chapter 4, and the BTSS coupling approach sketched in 5.1.1, are applied to an example inspired by a stented blood vessel. The applied model and its parameters are summarized. Afterward, the modeling approach is validated by comparing the results of the numerical investigations with well-known phenomena from literature and practice.

7.1. Fluid-beam-structure interaction model for stented arteries

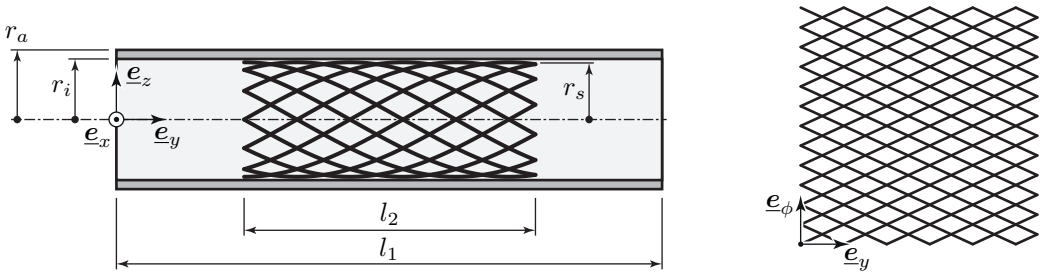

(a) Geometric configuration of stent and artery

(b) Unwrapped stent geometry

Figure 7.1.: Initial geometry of the stented elastic pipe. Figure is taken from the author's article [176] and modified.

The following problem setup is adapted from the author's previous work [176] to capture the effect of the stent on the fluid flow, in addition to the BTSS and continuum-based FSI interactions. The model constitutes a variant of the well-known FSI benchmark problem of a pressure wave traveling through an elastic tube, which was originally proposed in [63] to validate the suitability of FSI algorithms for blood flow simulations. In addition to the original FSI problem, a diamond-shaped stent structure is added to the geometrical setup. Figure 7.1a illustrates the problem setup. The FBI and BTSS coupling methodologies are applied in order to account for the stent's interaction with its surroundings. To solve the resulting problem, the FBSI algorithm introduced in Chapter 4 is employed. In the present case, the structure partition contains the beam equations as well as the solid continuum field, and represents a coupled problem itself.

As in the original benchmark problem, a constant pulse p_{in} is applied for $3 \cdot 10^{-3}\,\text{s}$ at the fluid inlet. Furthermore, a zero traction condition is applied to the fluid outflow boundary on the right end of the pipe and the displacement at both ends of the pipe is fixed via Dirichlet boundary conditions. Classical no-slip conditions are enforced on the FSI boundary. The beam centerline geometry depicted in Figure 7.1b is wrapped around a cylinder with a radius of $r_s = r_i - R$ to create the used diamond-shaped stent geometry. The stent, thus, perfectly fits into the pipe structure up to an offset the size of the beam radius. As the stent only experiences relatively small deformations, the application of a hyperelastic material model is a valid assumption [94, 33].

The Generalized-α Lie group time integration method is applied to all structural degrees of freedom. The parameters for the Generalized-α Lie group time integration method are chosen to obtain a fully implicit scheme, and a time step size $\Delta t = 10^{-4}\,\text{s}$ is used. To the fluid field, a classical second-order accurate Generalized-α time integration scheme, with the same time step size as for the structure field, is applied. The BTSS method is used with linear shape functions for the Lagrange multiplier fields and with the penalty parameter $\epsilon_{btss} = 10$. The FBI constraints are enforced by a GPTS-based penalty method with the penalty parameter $\epsilon_{fbi} = 10^{-5}$. The overall FBSI algorithm is run with the absolute tolerance of $tol_{fbi} = 3.5 \cdot 10^{-12}$. To discretize the problem, 264 Reissner beam elements, $5{,}760$ solid shell elements, and $51{,}193$ stabilized P1/P1 fluid finite elements, are employed. All dimensions and material parameters of the problem setup are summarized in Table 7.1.

Geometry	r_i	$1.25\,\text{mm}$
	r_a	$1.375\,\text{mm}$
	r_s	$1.246\,\text{mm}$
	l_1	$15\,\text{mm}$
	l_2	$6\,\text{mm}$
Beam	E_B	$9 \cdot 10^2\,\text{MPa}$
	ρ_B	$7.8\text{g}/\text{mm}^3$
	ν_B	0.3
	R	$0.04\,\text{mm}$
Solid	E_S	$3 \cdot 10^{-1}\,\text{MPa}$
	ρ_S	$1.2\,\text{g}/\text{mm}^3$
	ν_S	0.3
Fluid	p_{in}	$5 \cdot 10^{-4}\,\text{MPa}$
	ρ_F	$1.0\,\text{g}/\text{mm}^3$
	η_F	$0.3\,\text{g}/(\text{mm} \cdot \text{s})$

Table 7.1.: Table containing the parameters for the stented elastic pipe problem

7.2. Captured effects

Within this section, the various consequences of the stent placement for the blood vessel and the blood flow through that vessel are investigated. The considered effects demon-

strate the mixed-dimensional method's ability to capture these perturbations from the healthy configuration. The example, thus, serves as a proof of concept for the employment of mixed-dimensional modeling to investigate the intervention's long-term effects on the hemodynamics.

7.2.1. Stiffening of the artery & blood flow in stented regions

The main effect of a stent on the vessel is the introduction of a stiffer material response in the stented regions. The effect of this altered response is twofold. Firstly, this change in compliance may change the flow pattern and lead to regions of unfavorable flow behavior [94]. Secondly, the large change in compliance between the stented and unstented regions generally leads to stress peaks in these transitional zones. Both effects have been linked to the occurrence of in-stent restenosis and are of high interest when analyzing the suitability of endovascular devices and their effect on the patient [100, 35, 107].

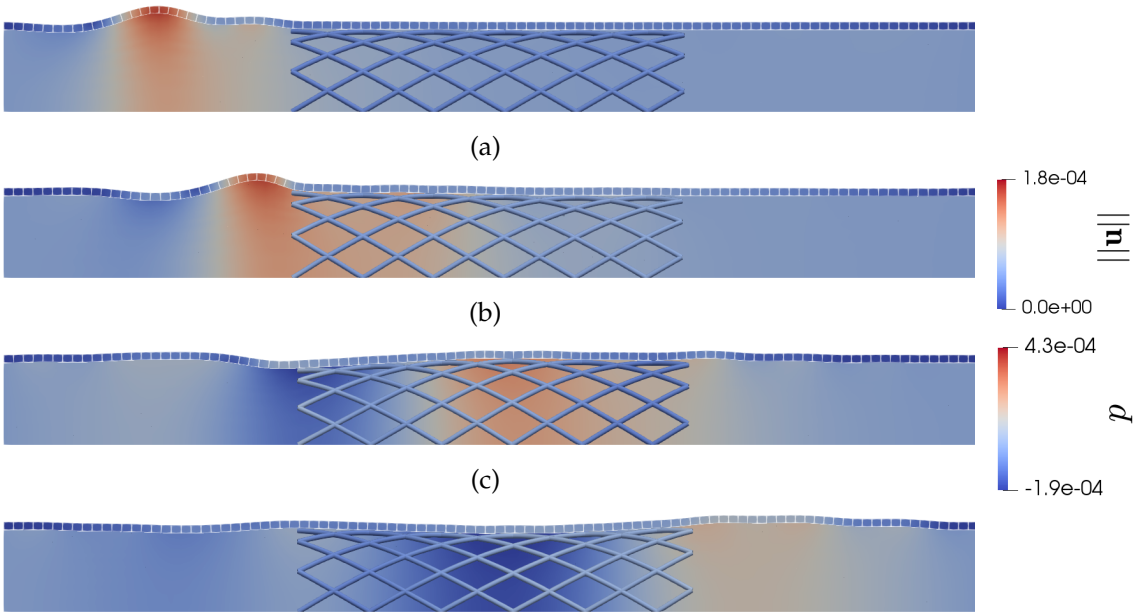

Figure 7.2.: Deformed configuration of the stented elastic pipe problem at various simulation times – the snapshots are taken at $t = 0.01\,\mathrm{s}$ (a), $t = 0.016\,\mathrm{s}$ (b), $t = 0.024\,\mathrm{s}$ (c) and $t = 0.03\,\mathrm{s}$ (d) respectively. The norm of the displacements in mm is shown in the solid and the pressure in MPa is shown in the fluid. The displacements are scaled with a factor of 15.

Figures 7.2a- 7.2d depict the structural displacement, scaled with a factor of 15, and the fluid pressure after $0.01\,\mathrm{s}$, $0.016\,\mathrm{s}$, $0.024\,\mathrm{s}$ and $0.030\,\mathrm{s}$. Figure 7.2 shows that the wall displacement, caused by the pressure wave, is smaller in the stiffer stented region than in the unstented region.

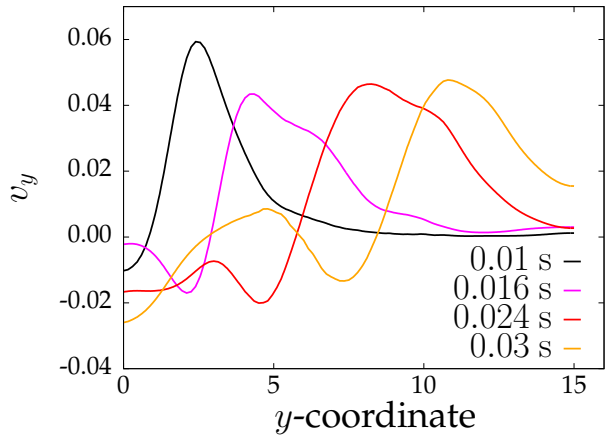

Figure 7.3.: Plot of the fluid velocity v_y in $\frac{\text{mm}}{\text{s}}$ in channel direction along the pipe's centerline

The altered stiffness response, in turn, affects the flow velocity. To maintain a constant flow throughput, an increase in the velocity within the stented region is required. Figure 7.3 illustrates the fluid velocity v_y in channel direction along the pipe's centerline. The fluid velocity plot demonstrates a slight increase in the flow velocity and the broadening of the wave within the stented region. This alteration of the fluid flow is still visible after the pressure wave leaves the stented region, and may potentially lead to a remodeling response of the vessel wall.

7.2.2. Flow perturbation due to the stent

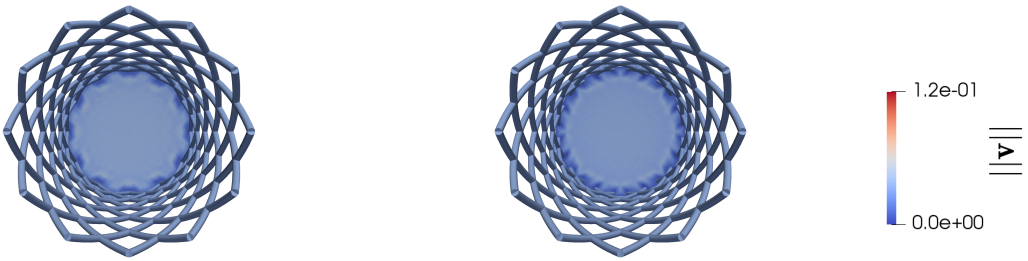

(a) (b)

Figure 7.4.: Velocity in channel direction in $\frac{\text{mm}}{\text{s}}$ at time $t = 0.016\,\text{s}$, at a distance of $4.7\ \text{mm}$ (a), and $5\ \text{mm}$ (b) from the channel inflow

The stent not only has an indirect effect on the flow but also affects the flow patterns directly. As already observed in Section 3.4.4.2, the stent struts slow down the fluid in its vicinity, effectively introducing some roughness to the vessel wall [147]. This fact leads to differing pressure distributions acting on the vessel wall that, in turn, may lead to differing stress responses correlated to growth and remodeling behavior of the artery. The extent of

the flow perturbation and the formation of recirculation zones is highly dependent on the stent design. Due to its correlation to in-stent restenosis, the quantification of these flow effects may represent an important metric for the quality of stent designs.

Figures 7.4a and 7.4b represent cross-sectional views of the fluid flow in channel direction at a distance of $4.7\,\mathrm{mm}$, and $5\,\mathrm{mm}$, from the channel inflow boundary, respectively. The figures demonstrate that the flow is slowed down near the stent struts, and that the flow pattern follows the stent geometry. Namely, following the stent's cross-section geometry, the cross-sectional flow pattern differs between the positions along the channel length, as illustrated by a comparison of Figure 7.4a and Figure 7.4b.

7.2.3. Forces acting on the stent

In contrast to homogenized approaches, the proposed mixed-dimensional model allows to additionally quantify the forces interchanged on the coupling interface.

Figures 7.5a- 7.5d illustrate the coupling interactions, i.e., the line loads exerted on the beam system by the vessel wall, as directly obtained via the regularized Lagrange multiplier contributions to the BTSS method. In general, it can be observed that the interaction force is highest at the ends of the stent, i.e., at the transition between a compliant and a very stiff region. This is particularly notable in Figure 7.5b, where the pressure wave reaches

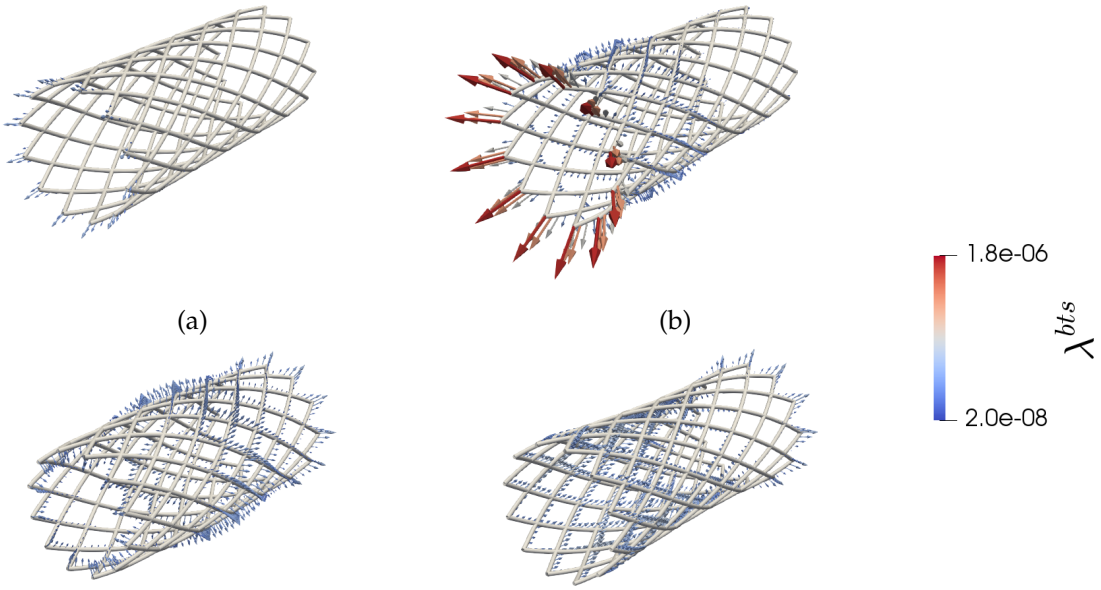

(a) (b)

(c) (d)

Figure 7.5.: Negative coupling line loads for beam-to-solid surface coupling at various simulation times – the snapshots are taken at $t = 0.01\,\mathrm{s}$ (a), $t = 0.016\,\mathrm{s}$ (b), $t = 0.024\,\mathrm{s}$ (c) and $t = 0.03\,\mathrm{s}$ (d) respectively.

the stent edge.

The presented simulation results serve as proof of concept for the proposed computational model, based on the FBSI framework developed in Chapter 4 and the BTSS coupling approach presented in Secion 5.1.1, to model stented arteries. The method's ability to capture important phenomena that may provide insight into the long-term success of vascular angioplasty has been demonstrated.

8. Conclusion & outlook

8.1. Summary of achievements

Within this thesis, a mixed-dimensional approach to modeling balloon angioplasty and stented arteries was developed. As a first step, an embedded finite element method to submerse 1-dimensional beam equations in 3-dimensional fluid flow was developed. The resulting continuous fluid-beam interaction (FBI) system, based on the Lagrange multiplier as well as the penalty method, was presented. The introduced kinematic constraint was enforced directly on the beam centerline, therefore, making it a truly mixed-dimensional 1D-3D coupling problem as well as a highly efficient modeling strategy for immersed slender structures regarding computational complexity as well as mesh creation. Two different discretization strategies, a Gauss-Point-to-Segment penalty approach and a mortar finite element-type Segment-to-Segment strategy-based on regularized Lagrange multipliers, were applied to the discretized interface problem. To solve the arising multi-physics problem, a specifically tailored novel strongly coupled Dirichlet-Neumann partitioned algorithm, based on the weak enforcement of the Dirichlet condition, as well as corresponding one-way coupling schemes were implemented. All algorithms were specifically designed for the efficient use on multi-core computing architectures and their convergence behavior was enhanced by the use of established Quasi-Newton-based acceleration techniques. For all cases, the one-way coupling schemes as well as the stable two-way coupling algorithm, the convergence of the resulting system solution with respect to the penalty parameter as well as the robustness of the segmentation algorithm were shown. The spatial convergence behavior of the fluid-beam solution under uniform mesh refinement with respect to the solution of corresponding fully resolved 3-dimensional models was shown and the approach was, thus, validated. Further effects of the proposed computational building blocks such as the coupling discretization strategy and the acceleration technique for the partitioned solver have been studied with numerical examples. The general possibility of modeling highly complex nonlinear problems such as mesh tying within the structure and/or fluid domain, and thus the flexibility of the proposed approach, was demonstrated by selected examples. In addition, limitations of the proposed coupling strategy such as the exact capturing of interface phenomena have been pointed out and the method's range of application has been studied. To demonstrate the efficiency and suitability of the proposed algorithms also for large examples and application-oriented problems, a fluid channel containing more than $3,000$ submerged fibers was set up to model the behavior of a submerged vegetation patch. Differences to the solution obtained with existing homogenized, 1D-2D, and 2D-3D coupling strategies have been pointed out. The method and solution algorithms were subsequently extended to their use on moving meshes and combined with established mortar finite element techniques for the solution of classical equal-

dimensional fluid-structure interaction problems. The resulting fluid-beam-structure interaction algorithm's ability to capture large displacements of beams and 3-dimensional structures was validated by a biomedically inspired numerical example.

In the second part of this thesis, a structure mechanical model for balloon angioplasty and stent insertion was developed. The model was based on a novel mixed-dimensional method capturing the interactions of geometrically exact beams with 2-dimensional surfaces and mortar finite element-based modeling of contact mechanics. Its ability to reproduce phenomena connected to post-interventional restenosis and the behavior of commercially available endovascular devices was demonstrated. Based on these observations, a novel patient-specific balloon catheter technology, on the basis of an anisotropic material, for the intervention in curved vessels was proposed. An optimal control procedure for the patient-specific tailoring of the technology for the treatment of curved as well as asymmetrically stenosed blood vessels, including suitable design goals and optimization parameters, was presented.

In the end, the novel fluid-beam-structure interaction algorithm was combined with the presented mixed-dimensional beam-to-solid-surface coupling method and applied to a numerical example inspired by the setup of a stented artery. The mixed-dimensional model's result served as proof of concept for the framework's suitability in the context of complex multi-physics-based simulations for post-interventional outcomes. At the same time, the simulation demonstrated the computational framework's flexibility and efficiency when it comes to the modeling of numerous intricate interaction phenomena.

In summary, an efficient computationally-parallel mixed-dimensional framework has been extended to capture multi-physics phenomena and was applied to real-life applications in the context of balloon angioplasty and stented arteries.

8.2. Outlook & future work

Even though considerable advances toward the efficient computational modeling of post-operative outcomes of balloon angioplasty by sophisticated mixed-dimensional coupling approaches have been made, there still exists a multitude of open research questions and possible model improvements. Future work can be categorized into numerical and algorithmic improvements of the multi-purpose fluid-beam interaction (FBI) framework, on the one hand, and further exploration and improvement of the mixed-dimensional model for the simulation of balloon angioplasty and subsequent outcomes, on the other hand.

The efficiency and overall benefits of the proposed FBI framework have been demonstrated by large-scale numerical examples and the comparison to classical methods with respect to characteristic mesh sizes. However, the computational framework can benefit from further improvement of the algorithmic components in the future. Two main areas of interest in this regard are the partitioned algorithm itself as well as the massively parallel search strategy. The employed search, based on a binning strategy in combination with an octree search, does not take into account the special features of beam geometries, particularly their large slenderness ratio. For a more efficient search and presorting of potential interaction pairs, a bounding-box-based search that is specifically tailored to beam geome-

tries, as investigated in [56], could lead to a significant speedup in the future. Furthermore, while an acceleration in solver time could be achieved by the application of sophisticated matrix-free Quasi-Newton-type methods to the interface residual, a change to a monolithic solver could further mitigate challenges with regard to slow convergence due to the added-mass effect. Though, such a change is only reasonable if specially-tailored preconditioning techniques, allowing an efficient scalable solution of the overall system via algebraic multigrid (AMG) methods, are available. On this subject, Kuchta et. al have already made some strides in the preconditioning of trace-coupled 1D-3D systems [113], and Firmbach et. al have recently proposed an efficient preconditioner for the monolithic coupling of geometrically exact beam theory with a 3D solid continuum [56]. Furthermore, the strategical employment of advanced discretization approaches and model adaptivity could alleviate the identified limitations of the proposed FBI approach. Particularly, the Non-Uniform Rational B-Splines-based (NURBS) discretization of the fluid field could potentially lead to a smoother fluid velocity solution, thus, reducing the solution's dependence, with respect to an integration error, on the background mesh. An adaptive choice of coupling strategy, based on the fulfillment of the presented model assumptions, and a potential switch to a volume-to-surface coupled or fully resolved model when necessary, can aid in overcoming the model's restrictions with regard to its application range.

Moreover, the extension of the current numerical model for balloon angioplasty and stented arteries to its use as a patient-specific digital organ twin requires its enhancement and further investigation in various areas. In particular, to accurately model the stent's expansion behavior, following [111], the geometrically exact beam's implementation needs to be enhanced by a phenomenological elasto-plastic material law, and a relationship between the constitutive parameters of continuum theory and the phenomenological material law has to be established. Additionally, the presence of broad strut intersection areas within stent geometries still limits the current modeling approach for beam-based stent structures as only point-to-point can be incorporated. An extension to line-to-line based mesh tying on the basis of the contact framework presented in [133] can increase the flexibility with respect to geometry creation in the future. A further step towards the model's use as a digital twin is the incorporation of patient-specific parameters such as vessel geometries obtained from computed tomography (CT) data, realistic fluid boundary conditions based on 0-dimensional (0D) models and doppler ultrasound data, as well as the blood's more accurate modeling based on a non-Newtonian behavior. To improve the accuracy of the interaction of the various components, the beam-to-solid-surface interaction model could be adapted from a mesh tying implementation to a full contact model such as recently proposed in the thesis [180]. In any case, to further assess the accuracy of the developed model, its validation by quantitative comparison with experimental and medical data is essential.

Last but not least, the proposed novel balloon technology for patient-specific treatment represents a compelling idea that could be further evaluated. Particularly, aspects such as the efficient production of such patient-specific devices as well as the complexity of their accurate placement in practice pose further fascinating research perspectives.

Bibliography

[1] Baci: A comprehensive multi-physics simulation framework. https://baci.pages.gitlab.lrz.de/website

[2] Ulster university. https://www.ulster.ac.uk/cardiovascular/cvd-prevalence

[3] World health organization. https://www.who.int/health-topics/cardiovascular-diseases

[4] F. Auricchio, M. Conti, M. De Beule, G. De Santis, B. Verhegghe: Carotid artery stenting simulation: From patient-specific images to finite element analysis. *Medical Engineering & Physics* **33**(3), 281–289 (2011)

[5] F. Auricchio, M. Conti, A. Ferrara, S. Morganti, A. Reali: Patient-specific finite element analysis of carotid artery stenting: A focus on vessel modeling. *International Journal for Numerical Methods in Biomedical Engineering* **29**(6), 645–664 (2012)

[6] F. Auricchio, M. Conti, M. Ferraro, S. Morganti, A. Reali, R. Taylor: Innovative and efficient stent flexibility simulations based on isogeometric analysis. *Computer Methods in Applied Mechanics and Engineering* **295**, 347–361 (2015)

[7] F. Auricchio, M. Conti, M. Ferraro, A. Reali: Evaluation of carotid stent scaffolding through patient-specific finite element analysis. *International journal for numerical methods in biomedical engineering* **28**(10), 1043–1055 (2012)

[8] R.F. Ausas, C.G. Gebhardt, G.C. Buscaglia: A finite element method for simulating soft active non-shearable rods immersed in generalized newtonian fluids. *Communications in Nonlinear Science and Numerical Simulation* **108**, 106213 (2022)

[9] F.P. Baaijens: A fictitious domain/mortar element method for fluid-structure interaction. *International Journal for Numerical Methods in Fluids* **35**(7), 743–761 (2001)

[10] M. Balghith: Artery bypass versus pci using new generation des. In: W.S. Aronow (ed.) Artery Bypass, chap. 19. IntechOpen, Rijeka (2013)

[11] D. Balzani, S. Deparis, S. Fausten, D. Forti, A. Heinlein, A. Klawonn, A. Quarteroni, O. Rheinbach, J. Schröder: Numerical modeling of fluid–structure interaction in arteries with anisotropic polyconvex hyperelastic and anisotropic viscoelastic material models at finite strains. *International journal for numerical methods in biomedical engineering* **32**(10), e02756 (2016)

[12] J.R. Barber: Contact mechanics. Springer (2018)

[13] S. Beier, J. Ormiston, M. Webster, J. Cater, S. Norris, P. Medrano-Gracia, A. Young, B. Cowan: Hemodynamics in idealized stented coronary arteries: important stent design considerations. *Annals of Biomedical Engineering* **44**, 315–329 (2016)

[14] C. Bertoglio, A. Caiazzo, Y. Bazilevs, M. Braack, M. Esmaily, V. Gravemeier, A. L. Marsden, O. Pironneau, I. E. Vignon-Clementel, W. A. Wall: Benchmark problems for numerical treatment of backflow at open boundaries. *International Journal for Numerical Methods in Biomedical Engineering* **34**(2), e2918 (2018)

[15] A. Beudin, T.S. Kalra, N.K. Ganju, J.C. Warner: Development of a coupled wave-flow-vegetation interaction model. *Computers & Geosciences* **100**, 76–86 (2017)

[16] B. Bisighini, M. Aguirre, M.E. Biancolini, F. Trovalusci, D. Perrin, S. Avril, B. Pierrat: Machine learning and reduced order modelling for the simulation of braided stent deployment (2023). `https://arxiv.org/abs/2301.08511`

[17] L. Boilevin-Kayl, M.A. Fernández, J.F. Gerbeau: Numerical methods for immersed fsi with thin-walled structures. *Computers and Fluids* **179**, 744–763 (2019)

[18] J. Bonari, M.R. Marulli, N. Hagmeyer, M. Mayr, A. Popp, M. Paggi: A multi-scale fem-bem formulation for contact mechanics between rough surfaces. *Computational Mechanics* **65**(3), 731–749 (2019)

[19] W.M. Boon, J.M. Nordbotten, J.E. Vatne: Functional analysis and exterior calculus on mixed-dimensional geometries. *Annali di Matematica Pura ed Applicata (1923-)* **200**(2), 757–789 (2021)

[20] C.P. Bradley, N. Emamy, T. Ertl, D. Göddeke, A. Hessenthaler, T. Klotz, A. Krämer, M. Krone, B. Maier, M. Mehl, et al.: Enabling detailed, biophysics-based skeletal muscle models on hpc systems. *Frontiers in physiology* **9**, 816 (2018)

[21] D. Braess: Finite elements: Theory, fast solvers, and applications in solid mechanics. Cambridge University Press (2007)

[22] N.W. Bressloff, G. Ragkousis, N. Curzen: Design optimisation of coronary artery stent systems. *Annals of Biomedical Engineering* **44**, 357–367 (2016)

[23] F. Brezzi, K.J. Bathe: A discourse on the stability conditions for mixed finite element formulations. *Computer Methods in Applied Mechanics and Engineering* **82**(1-3), 27–57 (1990)

[24] O. Brüls, A. Cardona: On the use of lie group time integrators in multibody dynamics. *Journal of Computational and Nonlinear Dynamics* **5**(3) (2010)

[25] O. Brüls, A. Cardona, M. Arnold: Lie group generalized-α time integration of constrained flexible multibody systems. *Mechanism and Machine Theory* **48**, 121–137 (2012)

[26] A. Budisa, W.M. Boon, X. Hu: Mixed-dimensional auxiliary space preconditioners. *SIAM Journal on Scientific Computing* **42**(5), A3367–A3396 (2020)

[27] E. Burman, P. Hansbo, M.G. Larson, A. Massing: Cut finite element methods for partial differential equations on embedded manifolds of arbitrary codimensions. *ESAIM: Mathematical Modelling and Numerical Analysis* **52**(6), 2247–2282 (2018)

[28] E. Béchet, N. Moës, B. Wohlmuth: A stable lagrange multiplier space for stiff interface conditions within the extended finite element method. *International Journal for Numerical Methods in Engineering* **78**(8), 931–954 (2009)

[29] F. Carollo, V. Ferro, D. Termini: Flow resistance law in channels with flexible submerged vegetation. *Journal of hydraulic engineering* **131**(7), 554–564 (2005)

[30] D. Cerroni, F. Laurino, P. Zunino: Mathematical analysis, finite element approximation and numerical solvers for the interaction of 3d reservoirs with 1d wells. *GEM-International Journal on Geomathematics* **10**, 1–27 (2019)

[31] P. Chadwick: Applications of an energy-momentum tensor in non-linear elastostatics. *Journal of Elasticity* **5**(3-4), 249–258 (1975)

[32] T.Y. Chang, H. Taniguchi, W.F. Chen: Nonlinear finite element analysis of reinforced concrete panels. *Journal of Structural Engineering* **113**(1), 122–140 (1987)

[33] C. Chiastra, F. Migliavacca, M.A. Martínez, M. Malvè: On the necessity of modelling fluid-structure interaction for stented coronary arteries. *Journal of the mechanical behavior of biomedical materials* **34**, 217–230 (2014)

[34] J. Chung, G. Hulbert: A time integration algorithm for structural dynamics with improved numerical dissipation: The generalized-α method. *Journal of Applied Mechanics* **60**(2), 371–375 (1993)

[35] M. Colombo, Y. He, A. Corti, D. Gallo, F. Ninno, S. Casarin, J. Rozowsky, F. Migliavacca, S. Berceli, C. Chiastra: In-stent restenosis progression in human superficial femoral arteries: Dynamics of lumen remodeling and impact of local hemodynamics. *Annals of Biomedical Engineering* **49**, 2349–2364 (2021)

[36] M.A. Crisfield, G. Jelenić;: Objectivity of strain measures in the geometrically exact three-dimensional beam theory and its finite-element implementation. *Proceeding of the Royal Society of London* **455**(1983), 1125–1147 (1999)

[37] C. D'angelo, A. Quarteroni: On the coupling of 1d and 3d diffusion-reaction equations: application to tissue perfusion problems. *Mathematical Models and Methods in Applied Sciences* **18**(08), 1481–1504 (2008)

[38] S.L. Dawson, S. Cotin, D. Meglan, D.W. Shaffer, M.A. Ferrell: Designing a computer-based simulator for interventional cardiology training. *Catheterization and Cardiovascular Interventions* **51**(4), 522–527 (2000)

[39] M. De Beule, P. Mortier, S.G. Carlier, B. Verhegghe, R. Van Impe, P. Verdonck: Realistic finite element-based stent design: The impact of balloon folding. *Journal of Biomechanics* **41**(2), 383–389 (2008)

[40] H. Delingette, S. Cotin, N. Ayache: A hybrid elastic model allowing real-time cutting, deformations and force-feedback for surgery training and simulation. In: Proceedings Computer Animation 1999, pp. 70–81 (1999)

[41] N. Diniz Dos Santos, J.F. Gerbeau, J.F. Bourgat: A partitioned fluid-structure algorithm for elastic thin valves with contact. *Computer Methods in Applied Mechanics and Engineering* **197**(19-20), 1750–1761 (2008)

[42] J. Donea, A. Huerta, J.P. Ponthot, A. Rodríguez-Ferran: Arbitrary Lagrangian-Eulerian Methods. In: E. Stein, R. de Borst, T.J.R. Hughes (eds.) Encyclopedia of Computational Mechanics, vol. 1: Fundamentals, chap. 14, pp. 1–25. John Wiley & Sons, Ltd, New York (2004)

[43] D. Durville: Finite element simulation of the mechanical behaviour of textile composites at the mesoscopic scale of individual fibers. *Textile composites and inflatable structures II* pp. 15–34 (2008)

[44] A. D'Ippolito, F. Calomino, G. Alfonsi, A. Lauria: Flow resistance in open channel due to vegetation at reach scale: A review. *Water* **13**(2) (2021)

[45] C. Eck, B. Wohlmuth: Convergence of a contact-neumann iteration for the solution of two-body contact problems. *Mathematical Models and Methods in Applied Sciences* **13**(08), 1103–1118 (2003)

[46] A. Ehrl, A. Popp, V. Gravemeier, W. Wall: A dual mortar approach for mesh tying within a variational multiscale method for incompressible flow. *International Journal for Numerical Methods in Fluids* **76**(1), 1–27 (2014)

[47] J.F. Eichinger, M.J. Grill, I.D. Kermani, R.C. Aydin, W.A. Wall, J.D. Humphrey, C.J. Cyron: A computational framework for modeling cell–matrix interactions in soft biological tissues. *Biomechanics and Modeling in Mechanobiology* **20**(5), 1851–1870 (2021)

[48] A.E. Elwi, T.M. Hrudey: Finite element model for curved embedded reinforcement. *Journal of Engineering Mechanics* **115**(4), 740–754 (1989)

[49] N. Eshghi, M. Hojjati, M. Imani, A. Goudarzi: Finite element analysis of mechanical behaviors of coronary stent. *Procedia Engineering* **10**, 3056–3061 (2011)

[50] V.D. Fachinotti, A. Cardona, P. Jetteur: Finite element modelling of inverse design problems in large deformations anisotropic hyperelasticity. *International Journal for Numerical Methods in Engineering* **74**(6), 894–910 (2008)

[51] L. Failer: Optimal control for time dependent nonlinear fluid-structure interaction. Ph.D. thesis, Technische Universität München (2017)

[52] L. Failer, P. Minakowski, T. Richter: On the impact of fluid structure interaction in blood flow simulations: Stenotic coronary artery benchmark. *Vietnam Journal of Mathematics* **49**, 169–187 (2021)

[53] J. Fajadet, J. Marco, B. Cassagneau, G. Robert, M. Vandormael: Coronary Stenting with the Palmaz-Schatz Stent: The Clinic Pasteur Interventional Cardiology Unit Experience, pp. 57–77. Springer Berlin Heidelberg, Berlin, Heidelberg (1992)

[54] Z. Fang, C. Gong, A. Revell, J. O'Connor: Fluid–structure interaction of a vegetation canopy in the mixing layer. *Journal of Fluids and Structures* **109**, 103467 (2022)

[55] J. Favier, A. Dauptain, D. Basso, A. Bottaro: Passive separation control using a self-adaptive hairy coating. *Journal of Fluid Mechanics* **627**, 451–483 (2009)

[56] M. Firmbach, A. Popp, M. Mayr, I. Steinbrecher: Computational challenges in mixed-dimensional beam/solid coupling. *Proceedings in Applied Mathematics & Mechanics* (2023)

[57] L.P. Franca, S.L. Frey: Stabilized finite element methods: Ii. the incompressible Navier-Stokes equations. *Computer Methods in Applied Mechanics and Engineering* **99**(2-3), 209–233 (1992)

[58] T. Fujii, H. Tomita, K. Nagaoka, T. Shimizu, N. Oyama, H. Kise, S. Tarui, Y. Miyahara, K. Ishino: Use of the novel curved goku balloon catheter for acute-angled lesions in palliative surgery for congenital heart disease: comparison with a conventional straight balloon. *Heart and vessels* **36** (2021)

[59] M. Gay, L. Zhang, W.K. Liu: Stent modeling using immersed finite element method. *Computer Methods in Applied Mechanics and Engineering* **195**(33-36), 4358–4370 (2006)

[60] M. Gee, C. Reeps, H. Eckstein, W. Wall: Prestressing in finite deformation abdominal aortic aneurysm simulation. *Journal of biomechanics* **42**(11), 1732–1739 (2009)

[61] M.W. Gee, C. Förster, W.A. Wall: A computational strategy for prestressing patient-specific biomechanical problems under finite deformation. *International Journal for Numerical Methods in Biomedical Engineering* **26**(1), 52–72 (2010)

[62] M.A. Geith, K. Swidergal, B. Hochholdinger, T.G. Schratzenstaller, M. Wagner, G.A. Holzapfel: On the importance of modeling balloon folding, pleating, and stent crimping: An fe study comparing experimental inflation tests. *International Journal for Numerical Methods in Biomedical Engineering* **35**(11), e3249 (2019)

[63] J.F. Gerbeau, M. Vidrascu: A quasi-newton algorithm based on a reduced model for fluid-structure interaction problems in blood flows. *ESAIM: Mathematical Modelling and Numerical Analysis* **37**(4), 631–647 (2003)

[64] J.F. Gerbeau, M. Vidrascu, P. Frey: Fluid–structure interaction in blood flows on geometries based on medical imaging. *Computers & Structures* **83**(2), 155–165 (2005)

[65] L.N.A. Ghantasala: Coupling procedures for fluid-fluid and fluid-structure interaction problems based on domain decomposition methods. Dissertation, Technische Universität München, München (2021)

[66] F. Gijsen, F. Migliavacca, S. Schievano, L. Socci, L. Petrini, A. Thury, J. Wentzel, A. van der Steen, P. Serruys, G. Dubini: Simulation of stent deployment in a realistic human coronary artery. *Biomedical engineering online* **7**, 23 (2008)

[67] H.M. Gomes, A.M. Awruch: Some aspects on three-dimensional numerical modelling of reinforced concrete structures using the finite element method. *Advances in Engineering Software* **32**(4), 257–277 (2001)

[68] S. Govindjee, P.A. Mihalic: Computational methods for inverse finite elastostatics. *Computer Methods in Applied Mechanics and Engineering* **136**(1-2), 47–57 (1996)

[69] S. Govindjee, P.A. Mihalic: Computational methods for inverse deformations in quasi-incompressible finite elasticity. *International Journal for Numerical Methods in Engineering* **43**(5), 821–838 (1998)

[70] T.J. Gundert, A.L. Marsden, W. Yang, J. LaDisa John F.: Optimization of cardiovascular stent design using computational fluid dynamics. *Journal of Biomechanical Engineering* **134**(1) (2012)

[71] T.J. Gundert, A.L. Marsden, W. Yang, D.S. Marks, J.F. LaDisa Jr: Identification of hemodynamically optimal coronary stent designs based on vessel caliber. *IEEE Transactions on Biomedical Engineering* **59**(7), 1992–2002 (2012)

[72] E. Gutiérrez, F. Favre, N. Balcázar, A. Amani, J. Rigola: Numerical approach to study bubbles and drops evolving through complex geometries by using a level set – moving mesh – immersed boundary method. *Chemical Engineering Journal* **349**, 662–682 (2018)

[73] D.E. Gutstein, V. Fuster: Pathophysiology and clinical significance of atherosclerotic plaque rupture. *Cardiovascular Research* **41**(2), 323–333 (1999)

[74] M. Gyöngyösi, P. Yang, A. Khorsand, D. Glogar: Longitudinal straightening effect of stents is an additional predictor for major adverse cardiac events. *Journal of the American College of Cardiology* **35**(6), 1580–1589 (2000)

[75] N. Hagmeyer, I. Steinbrecher, M. Mayr, A. Popp: One-way coupled fluid-beam interaction: capturing the effect of embedded slender bodies on global fluid flow and vice versa. *Advanced Modeling and Simulation in Engineering Sciences* **9** (2022)

[76] Y. Han, W. Lu: Optimizing the deformation behavior of stent with nonuniform poisson's ratio distribution for curved artery. *Journal of the Mechanical Behavior of Biomedical Materials* **88**, 442–452 (2018)

[77] P. Hansbo, A. Szepessy: A velocity-pressure streamline diffusion finite element method for the incompressible Navier-Stokes equations. *Computer Methods in Applied Mechanics and Engineering* **84**(2), 175–192 (1990)

[78] S.R. Hauck, A. Kupferthaler, M. Stelzmüller, W. Eilenberg, M. Ehrlich, C. Neumayer, F. Wolf, C. Loewe, M.A. Funovics: Endovascular stent-graft repair of the ascending aorta: Assessment of a specific novel stent-graft design in phantom, cadaveric, and clinical application. *CardioVascular and Interventional Radiology* **44**(9), 1448–1455 (2021)

[79] M. Hautefeuille, C. Annavarapu, J.E. Dolbow: Robust imposition of dirichlet boundary conditions on embedded surfaces. *International Journal for Numerical Methods in Engineering* **90**(1), 40–64 (2011)

[80] R. He, L. Zhao, V. Silberschmidt, Y. Liu: Mechanistic evaluation of long-term in-stent restenosis based on models of tissue damage and growth. *Biomechanics and Modeling in Mechanobiology* **19** (2020)

[81] C. Hesch, A. Gil, A. Arranz Carreño, J. Bonet, P. Betsch: A mortar approach for fluid–structure interaction problems: Immersed strategies for deformable and rigid bodies. *Computer Methods in Applied Mechanics and Engineering* **278**, 853–882 (2014)

[82] M. Hinze, R. Pinnau, M. Ulbrich, S. Ulbrich, S. Ulbrich: Analytical background and optimality theory. *Optimization with PDE Constraints* pp. 1–95 (2009)

[83] C.W. Hirt, A.A. Amsden, J.L. Cook: An arbitrary Lagrangian-Eulerian computing method for all flow speeds. *Journal of Computational Physics* **14**(3), 227–253 (1974)

[84] E. Hodneland, X. Hu, J.M. Nordbotten: Well-posedness and discretization for a class of models for mixed-dimensional problems with high-dimensional gap. *SIAM Journal on Applied Mathematics* **81**(5), 2218–2245 (2021)

[85] G. Holzapfel: Nonlinear Solid Mechanics. A Continuum Approach for Engineering, second print edn. John Wiley Sons (2001)

[86] G. Holzapfel, T. Gasser: A viscoelastic model for fiber-reinforced composites at finite strains: Continuum basis, computational aspects and applications. *Computer Methods in Applied Mechanics and Engineering* **190**, 4379–4430 (2001)

[87] G. Holzapfel, T. Gasser, R. Ogden: A new constitutive framework for arterial wall mechanics and a comparative study of material models. *Journal of Elasticity* **61**, 1–48 (2000)

[88] G.A. Holzapfel, G. Sommer, C.T. Gasser, P. Regitnig: Determination of layer-specific mechanical properties of human coronary arteries with nonatherosclerotic intimal thickening and related constitutive modeling. *American Journal of Physiology-Heart and Circulatory Physiology* **289**(5), H2048–H2058 (2005)

[89] G.A. Holzapfel, G. Sommer, P. Regitnig: Anisotropic mechanical properties of tissue components in human atherosclerotic plaques. *Journal of Biomechanical Engineering* **126**(5), 657–665 (2004)

[90] G.A. Holzapfel, M. Stadler, T.C. Gasser: Changes in the mechanical environment of stenotic arteries during interaction with stents: Computational assessment of parametric stent designs. *Journal of Biomechanical Engineering* **127**(1), 166–180 (2005)

[91] D.Z. Huang, P. Avery, C. Farhat: An embedded boundary approach for resolving the contribution of cable subsystems to fully coupled fluid-structure interaction. *International Journal for Numerical Methods in Engineering* (2020)

[92] B.M. Irons, R.C. Tuck: A version of the aitken accelerator for computer iteration. *International Journal for Numerical Methods in Engineering* **1**(3), 275–277 (1969)

[93] D.S. Jerison, C.E. Kenig: The neumann problem on lipschitz domains. *Bull. Amer. Math. Soc.* **4**(2), 203–208 (1981)

[94] N. Johari, M. Hamady, X. Xu: A computational study of the effect of stent design on local hemodynamic factors at the carotid artery bifurcation. *Artery Research* **26**, 161 – 169 (2020)

[95] M. Joosten, W. Dettmer, D. Perić: On the temporal stability and accuracy of coupled problems with reference to fluid-structure interaction. *International Journal for Numerical Methods in Fluids* **64**(10-12), 1363–1378 (2010)

[96] J.A. Kaufman: Endovascular intervention: basic concepts and techniques. *Journal of Vascular Surgery* **34**(3), 576 (2001)

[97] P. Kerfriden, S. Claus, I. Mihai: A mixed-dimensional cutfem methodology for the simulation of fibre-reinforced composites. *Advanced Modeling and Simulation in Engineering Sciences* **7**(1), 1–26 (2020)

[98] U. Khristenko, S. Schuß, M. Krüger, F. Schmidt, B. Wohlmuth, C. Hesch: Multidimensional coupling: A variationally consistent approach to fiber-reinforced materials. *Computer Methods in Applied Mechanics and Engineering* **382**, 113869 (2021)

[99] Y. Kim, C.S. Peskin: Penalty immersed boundary method for an elastic boundary with mass. *Physics of Fluids* **19**(5), 053103 (2007)

[100] Y.G. Kim, I.Y. Oh, Y.W. Kwon, J.K. Han, H.M. Yang, K.W. Park, H.Y. Lee, H.J. Kang, B.K. Koo, H.S. Kim: Mechanism of edge restenosis after drug-eluting stent implantation. *Circulation Journal* **77**, 2928–2935 (2013)

[101] D. Kiousis, T. Gasser, G. Holzapfel: A numerical model to study the interaction of vascular stents with human atherosclerotic lesions. *Annals of biomedical engineering* **35**, 1857–69 (2007)

[102] D. Kiousis, T. Gasser, G. Holzapfel: Smooth contact strategies with emphasis on the modeling of balloon angioplasty with stenting. *International journal for numerical methods in engineering* **75**(7), 826–855 (2008)

[103] D.E. Kiousis, A.R. Wulff, G.A. Holzapfel: Experimental studies and numerical analysis of the inflation and interaction of vascular balloon catheter-stent systems. *Annals of Biomedical Engineering* **37**(2), 315–330 (2009)

[104] H. Kise, A. Miyata, H. Tomita, T. Fujii, K. Fujimoto, H. Kiguchi, N. Oyama, T. Soga, Y. Hata, M. Hirata, A. Itoh, K. Ishino, Y. Hasebe, M. Hoshiai: Novel curved balloon catheter for dilating postoperative angled lesions associated with congenital heart disease. *Journal of Interventional Cardiology* **27**(4), 408–413 (2014)

[105] T. Klöppel, A. Popp, U. Küttler, W.A. Wall: Fluid–structure interaction for nonconforming interfaces based on a dual mortar formulation. *Computer Methods in Applied Mechanics and Engineering* **200**(45-46), 3111–3126 (2011)

[106] D.A. Knoll, D.E. Keyes: Jacobian-free newton–krylov methods: a survey of approaches and applications. *Journal of Computational Physics* **193**(2), 357–397 (2004)

[107] T.R. Kohler, A. Jawień: Flow affects development of intimal hyperplasia after arterial injury in rats. *Arteriosclerosis and Thrombosis : a Journal of Vascular Biology* **12**, 963–71 (1992)

[108] G. Kokot, W. Kuś, P. Dobrzyński, M. Sobota, A. Smola, J. Kasperczyk: A project of bioresorbable self-expanding vascular stents. the crimping process numerical simulation. In: AIP Conference Proceedings, vol. 1922, p. 070004 (2018)

[109] A. Konyukhov, K. Schweizerhof: On some aspects for contact with rigid surfaces: Surface-to-rigid surface and curves-to-rigid surface algorithms. *Computer Methods in Applied Mechanics and Engineering* **283**, 74–105 (2015)

[110] J. Kremheller, A. Vuong, B.A. Schrefler, W.A. Wall: An approach for vascular tumor growth based on a hybrid embedded/homogenized treatment of the vasculature within a multiphase porous medium model. *International Journal for Numerical Methods in Biomedical Engineering* **35**(11), e3253 (2019)

[111] C. Krewcun, L. Sarry, N. Combaret, E. Péry: Fast simulation of stent deployment with plastic beam elements. In: 2019 41st Annual International Conference of the IEEE Engineering in Medicine and Biology Society (EMBC), pp. 6968–6974 (2019)

[112] M. Kuchta, F. Laurino, K.A. Mardal, P. Zunino: Analysis and approximation of mixed-dimensional pdes on 3d-1d domains coupled with lagrange multipliers. *SIAM Journal on Numerical Analysis* **59**(1), 558–582 (2021)

[113] M. Kuchta, K. Mardal, M. Mortensen: Preconditioning trace coupled 3d -1d systems using fractional laplacian. *Numerical Methods for Partial Differential Equations* **35**(1), 375–393 (2018)

[114] S. Kunze, C. Brücker: Control of vortex shedding on a circular cylinder using self-adaptive hairy-flaps. *Comptes Rendus Mécanique* **340**(1-2), 41–56 (2012)

[115] A. König, T.M. Schiele, J. Rieber, K. Theisen, M. Harald, K. Volker: Influence of stent design and deployment technique on neointima formation and vascular remodeling. *Clinical Research in Cardiology* **91**, 98–102 (2002)

[116] U. Küttler, C. Förster, W. Wall: A solution for the incompressibility dilemma in partitioned fluid–structure interaction with pure dirichlet fluid domains. *Computational Mechanics* **38**, 417–429 (2006)

[117] U. Küttler, W.A. Wall: Fixed-point fluid–structure interaction solvers with dynamic relaxation. *Computational Mechanics* **43**(1), 61–72 (2008)

[118] F. Laurino, P. Zunino: Derivation and analysis of coupled pdes on manifolds with high dimensionality gap arising from topological model reduction. *ESAIM: Mathematical Modeling and Numererical Analysis* **53**(6), 2047–2080 (2019)

[119] T.A. Laursen: Computational contact and impact mechanics: fundamentals of modeling interfacial phenomena in nonlinear finite element analysis. Springer Science & Business Media (2003)

[120] R.T. Lee, S.G. Richardson, H.M. Loree, A.J. Grodzinsky, S.A. Gharib, F.J. Schoen, N. Pandian: Prediction of mechanical properties of human atherosclerotic tissue by high-frequency intravascular ultrasound imaging. an in vitro study. *Arteriosclerosis and Thrombosis: A Journal of Vascular Biology* **12**(1), 1–5 (1992)

[121] J. Lenoir, S. Cotin, C. Duriez, P. Neumann: Interactive physically-based simulation of catheter and guidewire. *Computers & Graphics* **30**(3), 416–422 (2006)

[122] L. Li, W. Henshaw, J. Banks, D. Schwendeman, A. Main: A stable partitioned fsi algorithm for incompressible flow and deforming beams. *Journal of Computational Physics* **312**, 272–306 (2016)

[123] D.C. Liu, J. Nocedal: On the limited memory bfgs method for large scale optimization. *Mathematical Programming* **45**(1), 503–528 (1989)

[124] W.K. Liu, D.W. Kim, S. Tang: Mathematical foundations of the immersed finite element method. *Computational Mechanics* **39**(3), 211–222 (2005)

[125] J. Lu, X. Zhou, M.L. Raghavan: Inverse elastostatic stress analysis in pre-deformed biological structures: demonstration using abdominal aortic aneurysms. *Journal of Biomechanics* **40**(3), 693–696 (2007)

[126] D.G. Luenberger, Y. Ye: Linear and nonlinear programming, vol. 1, 4 edn. Springer Publishing Company, Incorporated (2016)

[127] W.H. Maisel, W.K. Laskey: Drug-eluting stents. *Circulation* **115**(17), e426–e427 (2007)

[128] M. Malvè, A. García, J. Ohayon, M. Martínez: Unsteady blood flow and mass transfer of a human left coronary artery bifurcation: Fsi vs. cfd. *International Communications in Heat and Mass Transfer* **39**(6), 745–751 (2012)

[129] M. Mayr: A monolithic solver for fluid-structure interaction with adaptive time stepping and a hybrid preconditioner. Dissertation, Technische Universität München, München (2016)

[130] M. Mayr, T. Klöppel, W.A. Wall, M.W. Gee: A temporal consistent monolithic approach to fluid-structure interaction enabling single field predictors. *SIAM Journal on Scientific Computing* **37**(1), B30–B59 (2015)

[131] M. Maza, J.L. Lara, I.J. Losada: A coupled model of submerged vegetation under oscillatory flow using Navier–Stokes equations. *Coastal Engineering* **80**, 16–34 (2013)

[132] M.C. McDaniel, H. Samady: The sheer stress of straightening the curves. *JACC: Cardiovascular Interventions* **4**(7), 800–802 (2011)

[133] C. Meier, M.J. Grill, W.A. Wall, A. Popp: Geometrically exact beam elements and smooth contact schemes for the modeling of fiber-based materials and structures. *International Journal of Solids and Structures* **154**, 124–146 (2018)

[134] C. Meier, A. Popp, W.A. Wall: An objective 3d large deformation finite element formulation for geometrically exact curved kirchhoff rods. *Computer Methods in Applied Mechanics and Engineering* **278**, 445–478 (2014)

[135] C. Meier, A. Popp, W.A. Wall: A locking-free finite element formulation and reduced models for geometrically exact kirchhoff rods. *Computer Methods in Applied Mechanics and Engineering* **290**, 314–341 (2015)

[136] C. Meier, W.A. Wall, A. Popp: A unified approach for beam-to-beam contact. *Computer Methods in Applied Mechanics and Engineering* **315**, 972–1010 (2017)

[137] F. Migliavacca, L. Petrini, M. Colombo, F. Auricchio, R. Pietrabissa: Mechanical behavior of coronary stents investigated through the finite element method. *Journal of Biomechanics* **35**(6), 803–811 (2002)

[138] Y. Mori, A. Rodenberg, D. Spirn: Well-posedness and global behavior of the peskin problem of an immersed elastic filament in stokes flow. *Communications on Pure and Applied Mathematics* **72**(5), 887–980 (2019)

[139] P. Mortier, G.A. Holzapfel, M. De Beule, D. Van Loo, Y. Taeymans, P. Segers, P. Verdonck, B. Verhegghe: A novel simulation strategy for stent insertion and deployment in curved coronary bifurcations: Comparison of three drug-eluting stents. *Annals of Biomedical Engineering* **38**(1), 88–99 (2009)

[140] J.W. Moses, M.B. Leon, J.J. Popma, P.J. Fitzgerald, D.R. Holmes, C. O'Shaughnessy, R.P. Caputo, D.J. Kereiakes, D.O. Williams, P.S. Teirstein, J.L. Jaeger, R.E. Kuntz: Sirolimus-eluting stents versus standard stents in patients with stenosis in a native coronary artery. *New England Journal of Medicine* **349**(14), 1315–1323 (2003)

[141] T. Murata, T. Hiro, T. Fujii, K. Yasumoto, A. Murashige, M. Kohno, J. Yamada, T. Miura, M. Matsuzaki: Impact of the cross-sectional geometry of the post-deployment coronary stent on in-stent neointimal hyperplasia: An intravascular ultrasound study. *Circulation journal* **66**, 489–93 (2002)

[142] E. Murphy, M. Ghisalberti, H. Nepf: Model and laboratory study of dispersion in flows with submerged vegetation. *Water Resources Research* **43**(5) (2007)

[143] A. Nitti, J. Kiendl, A. Reali, M.D. de Tullio: An immersed-boundary/isogeometric method for fluid–structure interaction involving thin shells. *Computer Methods in Applied Mechanics and Engineering* **364**, 112977 (2020)

[144] T. Okamoto, I. Nezu: Resistance and turbulence structure in open-channel flows with flexible vegetations. *Environmental Hydraulics - Proceedings of the 6th International Symposium on Environmental Hydraulics* **1**, 215–220 (2010)

[145] J. O'Connor, A. Revell: Dynamic interactions of multiple wall-mounted flexible flaps. *Journal of Fluid Mechanics* **870**, 189–216 (2019)

[146] J. Panetta, F. Isvoranu, T. Chen, E. Siéfert, B. Roman, M. Pauly: Computational inverse design of surface-based inflatables. *ACM Transactions on Graphics (TOG)* **40**(4), 1–14 (2021)

[147] S. Pant, N.W. Bressloff, A.I.J. Forrester, N. Curzen: The influence of strut-connectors in stented vessels: A comparison of pulsatile flow through five coronary stents. *Annals of Biomedical Engineering* **38**, 1893–1907 (2010)

[148] C.S. Peskin: Flow patterns around heart valves: A numerical method. *Journal of Computational Physics* **10**(2), 252–271 (1972)

[149] C.S. Peskin: The immersed boundary method. *Acta Numerica* **11**, 479–517 (2002)

[150] D.V. Phillips, O.C. Zienkiewicz: Finite element non-linear analysis of concrete structures. *Proceedings of the Institution of Civil Engineers* **61**(1), 59–88 (1976)

[151] N. Pinho, C.F. Castro, C.C. António, N. Bettencourt, L.C. Sousa, S.I.S. Pinto: Correlation between geometric parameters of the left coronary artery and hemodynamic descriptors of atherosclerosis: Fsi and statistical study. *Medical & Biological Engineering & Computing* **57**, 715–729 (2018)

[152] A. Popp: Mortar methods for computational contact mechanics and general interface problems. Ph.D. thesis, Technische Universität München (2012)

[153] A. Popp, M.W. Gee, W.A. Wall: A finite deformation mortar contact formulation using a primal–dual active set strategy. *International Journal for Numerical Methods in Engineering* **79**(11), 1354–1391 (2009)

[154] M.A. Puso, T.A. Laursen: A mortar segment-to-segment contact method for large deformation solid mechanics. *Computer Methods in Applied Mechanics and Engineering* **193**(6), 601–629 (2004)

[155] A. Ranjbaran: Mathematical formulation of embedded reinforcements in 3d brick elements. *Communications in Numerical Methods in Engineering* **12**(12), 897–903 (1996)

[156] R. Rannacher: Finite element methods for the incompressible Navier-Stokes equations. Springer (2000)

[157] A.D. Rauch, A.T. Vuong, L. Yoshihara, W.A. Wall: A coupled approach for fluid saturated poroelastic media and immersed solids for modeling cell-tissue interactions. *International Journal for Numerical Methods in Biomedical Engineering* **34**(11), e3139 (2018)

[158] E. Reissner: On one-dimensional finite-strain beam theory: The plane problem. *Journal of Applied Mathematics and Physics (ZAMP)* **23**(5), 795–804 (1972)

[159] C.E. Rhoades: A fast algorithm for calculating particle interactions in smooth particle hydrodynamic simulations. *Computer Physics Communications* **70**(3), 478–482 (1992)

[160] N.S. Ribeiro, J. Folgado, H.C. Rodrigues: Surrogate-based multi-objective design optimization of a coronary stent: Altering geometry toward improved biomechanical performance. *International Journal for Numerical Methods in Biomedical Engineering* **37**(6), e3453 (2021)

[161] T. Richter: Fluid-structure Interactions: Models, Analysis and Finite Elements. Lecture Notes in Computational Science and Engineering. Springer International Publishing (2017)

[162] C. Rogers, E.R. Edelman: Endovascular stent design dictates experimental restenosis and thrombosis. *Circulation* **91**(12), 2995–3001 (1995)

[163] T. Roy, A. Chanda: Computational modelling and analysis of latest commercially available coronary stents during deployment. In: Procedia Materials Science, vol. 5, pp. 2310–2319 (2014)

[164] B. Rüth, B. Uekermann, M. Mehl, P. Birken, A. Monge, H.J. Bungartz: Quasi-newton waveform iteration for partitioned surface-coupled multiphysics applications. *International Journal for Numerical Methods in Engineering* **122**(19), 5236–5257 (2021)

[165] Y. Saad: Iterative methods for sparse linear systems. SIAM (2003)

[166] J. Sanders, M.A. Puso: An embedded mesh method for treating overlapping finite element meshes. *International Journal for Numerical Methods in Engineering* **91**(3), 289–305 (2012)

[167] C. Schenk, D. Portillo, I. Romero: Linking discrete and continuum diffusion models: Well-posedness and stable finite element discretizations. *International Journal for Numerical Methods in Engineering* **124**(9), 2105–2121 (2023)

[168] A. Schiavone, T.Y. Qiu, L. Zhao: Crimping and deployment of metallic and polymeric stents – finite element modelling. *Vessel Plus* **1** (2017)

[169] A. Schiavone, L. Zhao: The importance of vessel factors for stent deployment in diseased arteries. *Journal of Integrative Cardiology* **1** (2015)

[170] A. Schiavone, L. Zhao, A. Abdel-Wahab: Effects of material, coating, design and plaque composition on stent deployment inside a stenotic artery—finite element simulation. *Materials Science and Engineering: C* **42**, 479–488 (2014)

[171] B. Schott, U. Rasthofer, V. Gravemeier, W. Wall: A face-oriented stabilized nitsche-type extended variational multiscale method for incompressible two-phase flow. *International Journal for Numerical Methods in Engineering* **104**(7), 721–748 (2014)

[172] C. Schulz, R. Herrmann, C. Beilharz, J. Pasquantonio, E. Alt: Coronary stent symmetry and vascular injury determine experimental restenosis. *Heart (British Cardiac Society)* **83**, 462–7 (2000)

[173] A. Shahidian, A. Ghorbannia: Stress analysis of internal carotid artery with low stenosis level: The effect of material model and plaque geometry. *Journal of Mechanics in Medicine and Biology* p. 1750098 (2017)

[174] X. Shen, H. Zhu, J. Jiang, Y. Deng, S. Ji: Multi-objective optimization design of balloon-expandable coronary stent. *Cardiovascular Engineering and Technology* **10**, 10–21 (2019)

[175] J. Simo: A finite strain beam formulation. the three-dimensional dynamic problem. part i. *Computer Methods in Applied Mechanics and Engineering* **49**(1), 55–70 (1985)

[176] I. Steinbrecher, N. Hagmeyer, C. Meier, A. Popp: A consistent mixed-dimensional coupling approach for 1d cosserat beams and 2d solid surfaces (2022). `https://arxiv.org/abs/2210.16010`

[177] I. Steinbrecher, M. Mayr, M.J. Grill, J. Kremheller, C. Meier, A. Popp: A mortar-type finite element approach for embedding 1d beams into 3d solid volumes. *Computational Mechanics* **66**(6), 1377–1398 (2020)

[178] I. Steinbrecher, A. Popp: Meshpy – a general purpose 3d beam finite element input generator. https://compsim.gitlab.io/codes/meshpy

[179] I. Steinbrecher, A. Popp, C. Meier: Consistent coupling of positions and rotations for embedding 1d cosserat beams into 3d solid volumes. *Computational Mechanics* **69**(3), 701–732 (2022)

[180] I.S. Steinbrecher: Mixed-dimensional finite element formulations for beam-to-solid interaction. Ph.D. thesis, Universität der Bundeswehr München (2022)

[181] T. Stoesser, G.P. Salvador, W. Rodi, P. Diplas: Large eddy simulation of turbulent flow through submerged vegetation. *Transport in Porous Media* **78**(3), 347–365 (2009)

[182] P. Suwannasom, Y. Sotomi, Y. Ishibashi, R. Cavalcante, F.N. Albuquerque, C. Macaya, J.A. Ormiston, J. Hill, I.M. Lang, M. Egred, J. Fajadet, M. Lesiak, J.G. Tijssen, J.J. Wykrzykowska, R.J. de Winter, B. Chevalier, P.W. Serruys, Y. Onuma: The impact of post-procedural asymmetry, expansion, and eccentricity of bioresorbable everolimus-eluting scaffold and metallic everolimus-eluting stent on clinical outcomes in the absorb ii trial. *JACC: Cardiovascular Interventions* **9**(12), 1231–1242 (2016)

[183] J. Tambača, M. Kosor, S. Čanić, D.P. M.D.: Mathematical modeling of vascular stents. *SIAM Journal on Applied Mathematics* **70**(6), 1922–1952 (2010)

[184] J. Tambača, S. Čanić, D. Paniagua: A novel approach to modeling coronary stents using a slender curved rod model: A comparison between fractured xience-like and palmaz-like stents. In: W. Fitzgibbon, Y. Kuznetsov, P. Neittaanmäki, J. Périaux, O. Pironneau (eds.) Computational Methods in Applied Sciences, pp. 41–58. Springer Netherlands, Dordrecht (2009)

[185] Y.H. Tang, G.E. Karniadakis: Accelerating dissipative particle dynamics simulations on gpus: Algorithms, numerics and applications. *Computer Physics Communications* **185**(11), 2809–2822 (2014)

[186] H. Tariq, U. Ghani, N. Anjum, G.A. Pasha: 3d numerical modeling of flow characteristics in an open channel having in-line circular vegetation patches with varying density under submerged and emergent flow conditions. *Journal of Hydrology and Hydromechanics* **70**(1), 128–144 (2022)

[187] C.A. Taylor, T.J. Hughes, C.K. Zarins: Finite element modeling of blood flow in arteries. *Computer Methods in Applied Mechanics and Engineering* **158**(1-2), 155–196 (1998)

[188] C.A. Taylor, J. Humphrey: Open problems in computational vascular biomechanics: hemodynamics and arterial wall mechanics. *Computer Methods in Applied Mechanics and Engineering* **198**(45-46), 3514–3523 (2009)

[189] T.E. Tezduyar: Stabilized finite element formulations for incompressible flow computations. *Advances in Applied Mechanics* **28**, 1–44 (1991)

[190] M.P. Thon, A. Hemmler, A. Glinzer, M. Mayr, M. Wildgruber, A. Zernecke-Madsen, M.W. Gee: A multiphysics approach for modeling early atherosclerosis. *Biomechanics and Modeling in Mechanobiology* **17**, 617–644 (2018)

[191] H. Tomita, T. Higaki, T. Kobayashi, T. Fujii, K. Fujimoto: Stenting for curved lesions using a novel curved balloon: Preliminary experimental study. *Journal of Cardiology* **66**(2), 120–124 (2015)

[192] S. Tschisgale, J. Fröhlich: An immersed boundary method for the fluid-structure interaction of slender flexible structures in viscous fluid. *Journal of Computational Physics* **423**, 109801 (2020)

[193] S. Tschisgale, B. Löhrer, R. Meller, J. Fröhlich: Large eddy simulation of the fluid–structure interaction in an abstracted aquatic canopy consisting of flexible blades. *Journal of Fluid Mechanics* **916** (2021)

[194] S. Čanić, L. Grubišić, D. Lacmanović, M. Ljulj, J. Tambača: Optimal design of vascular stents using a network of 1d slender curved rods. *Computer Methods in Applied Mechanics and Engineering* **394**, 114853 (2022)

[195] P. Virtanen, R. Gommers, T.E. Oliphant, M. Haberland, T. Reddy, D. Cournapeau, E. Burovski, P. Peterson, W. Weckesser, J. Bright, S.J. van der Walt, M. Brett, J. Wilson, K.J. Millman, N. Mayorov, A.R.J. Nelson, E. Jones, R. Kern, E. Larson, C.J. Carey, İ. Polat, Y. Feng, E.W. Moore, J. VanderPlas, D. Laxalde, J. Perktold, R. Cimrman, I. Henriksen, E.A. Quintero, C.R. Harris, A.M. Archibald, A.H. Ribeiro, F. Pedregosa, P. van Mulbregt, SciPy 1.0 Contributors: SciPy 1.0: Fundamental Algorithms for Scientific Computing in Python. *Nature Methods* **17**, 261–272 (2020)

[196] A.C. van der Wal, A.E. Becker: Atherosclerotic plaque rupture–pathologic basis of plaque stability and instability. *Cardiovascular Research* **41**(2), 334–344 (1999)

[197] W.A. Wall, P. Gamnitzer, A. Gerstenberger: Fluid–structure interaction approaches on fixed grids based on two different domain decomposition ideas. *International Journal of Computational Fluid Dynamics* **22**(6), 411–427 (2008)

[198] M. Wang, E.J. Avital, X. Bai, C. Ji, D. Xu, J.J. Williams, A. Munjiza: Fluid–structure interaction of flexible submerged vegetation stems and kinetic turbine blades. *Comp. Part. Mech.* **7**(5), 839–848 (2019)

[199] T. Watson, M. Webster, J. Ormiston, P. Ruygrok, J. Stewart: Long and short of optimal stent design. *Open Heart* **4**, e000680 (2017)

[200] J.J. Wentzel, D.M. Whelan, W.J. van der Giessen, H.M. van Beusekom, I. Andhyiswara, P.W. Serruys, C.J. Slager, R. Krams: Coronary stent implantation changes 3-d vessel geometry and 3-d shear stress distribution. *Journal of Biomechanics* **33**(10), 1287–1295 (2000)

[201] C.H. Whiting, K.E. Jansen: A stabilized finite element method for the incompressible Navier–Stokes equations using a hierarchical basis. *International Journal for Numerical Methods in Fluids* **35**, 93–116 (2001)

[202] B.I. Wohlmuth: A mortar finite element method using dual spaces for the lagrange multiplier. *SIAM journal on numerical analysis* **38**(3), 989–1012 (2000)

[203] C.Y. Wong, P.H. Trinh, S.J. Chapman: Shear-induced instabilities of flows through submerged vegetation. *Journal of Fluid Mechanics* **891** (2020)

[204] F.C. Wu, H. Shen, Y.J. Chou: Variation of roughness coefficients for unsubmerged and submerged vegetation. *Journal of Hydraulic Engineering* **125** (1999)

[205] M.C.H. Wu, H. Muchowski, E. Johnson, M.R. Rajanna, M.C. Hsu: Immersogeometric fluid-structure interaction modeling and simulation of transcatheter aortic valve replacement. *Computer Methods in Applied Mechanics and Engineering* **357**, 112556 (2019)

[206] W. Wu, W.Q. Wang, D.Z. Yang, M. Qi: Stent expansion in curved vessel and their interactions: A finite element analysis. *Journal of Biomechanics* **40**(11), 2580–2585 (2007)

[207] B. Yang, T.A. Laursen, X. Meng: Two dimensional mortar contact methods for large deformation frictional sliding. *International Journal for Numerical Methods in Engineering* **62**(9), 1183–1225 (2005)

[208] D. Young, Y. Jan, C. Chiu: A novel immersed boundary procedure for flow and heat simulations with moving boundary. *Computers Fluids* **38**(6), 1145–1159 (2009)

[209] H. Zahedmanesh, D. John Kelly, C. Lally: Simulation of a balloon expandable stent in a realistic coronary artery—determination of the optimum modelling strategy. *Journal of Biomechanics* **43**(11), 2126–2132 (2010)

[210] H. Zahedmanesh, C. Lally: Determination of the influence of stent strut thickness using the finite element method: Implications for vascular injury and in-stent restenosis. *Medical biological engineering computing* **47**, 385–93 (2009)

[211] W. Zhang, C. Herrera, S.N. Atluri, G.S. Kassab: The effect of longitudinal pre-stretch and radial constraint on the stress distribution in the vessel wall: A new hypothesis. *Molecular Cellular Biomechanics* **2**(1), 41–52 (2005)

[212] S. Zhao, L. Gu, S. Froemming: Performance of self-expanding nitinol stent in a curved artery: Impact of stent length and deployment orientation. *Journal of Biomechanical Engineering* **134** (2012)

[213] H. Zhu, J.J. Warner, T.R. Gehrig, M.H. Friedman: Comparison of coronary artery dynamics pre- and post-stenting. *Journal of Biomechanics* **36**(5), 689–697 (2003)

[214] O.C. Zienkiewicz, R.L. Taylor, J.Z. Zhu: The finite element method: Its basis and fundamentals, seventh edn. Butterworth-Heinemann (2013)

[215] P. Zunino, J. Tambača, E. Cutrì, S. Čanić, L. Formaggia, F. Migliavacca: Integrated stent models based on dimension reduction: Review and future perspectives. *Annals of Biomedical Engineering* **44**(2), 604–617 (2015)